Development of Micro-Macro Continuum-Discontinuum Coupled Numerical Method

THÈSE N^{O} 4807 (2010)

PRÉSENTÉE LE 24 SEPTEMBRE 2010
À LA FACULTÉ ENVIRONNEMENT NATUREL, ARCHITECTURAL ET CONSTRUIT
LABORATOIRE DE MÉCANIQUE DES ROCHES
PROGRAMME DOCTORAL EN MÉCANIQUE

ÉCOLE POLYTECHNIQUE FÉDÉRALE DE LAUSANNE

POUR L'OBTENTION DU GRADE DE DOCTEUR ÈS SCIENCES

PAR

Gaofeng ZHAO

acceptée sur proposition du jury:

Prof. I. Botsis, président du jury
Prof. J. Zhao, Dr J. Fang, directeurs de thèse
Prof. F. Darve, rapporteur
Prof. S. Jeon, rapporteur
Prof. L. Laloui, rapporteur

ÉCOLE POLYTECHNIQUE
FÉDÉRALE DE LAUSANNE
Suisse
2010

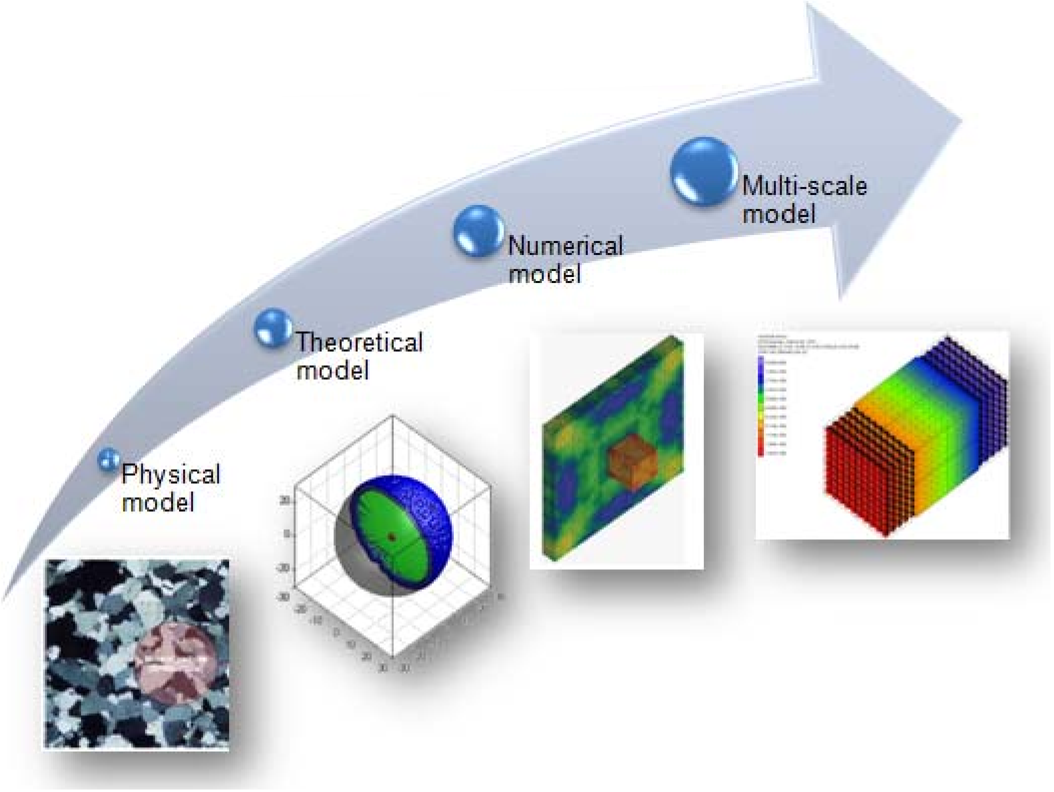

To my parents

Acknowledgments

I would like to express my infinite gratitude and sincere thanks to those who supported and influenced my work and assisted me during my PhD study and thesis writing process.

Professor Zhao J, my supervisor, for his supervision and encouragements during the whole research and the writing of this thesis. Without his effort, the thesis will surely not be able to be accomplished.

Dr. Fang JN, my co-supervisor, for his useful discussions and suggestions on the research context and the English expression during the writing of this thesis.

Professor Laloui L and Professor Molinari JF, members of the qualification examination committee, for their comments and suggestions on the development of the numerical method.

Professor Botsis J, my mentor, for his comments on the thesis and be serving as the chairman of the PhD defense jury.

Professor Hudson JA, Professor Tang CA, Professor Carranza-Torres C and Professor Li XZ, for their useful suggestions on development of the numerical method in this thesis.

Dr. Shi GH for his valuable comments, suggestions and discussions on the numerical numerical manifold method.

Professor Ma GW, for providing the chance for me to study the numerical manifold method at NTU.

Professor Zhao XB for providing useful suggestions on wave propagation simulations.

Zhu JB, for his help on testing the DLSM code on wave propagation through single joint case.

Kazerani T, for cooperations on implementation of full-rate dependency constitutive model into DLSM and useful discussions.

ROJAS FUENTES R and Dr. Liu XL, my roommates and colleagues, for their supporting during life time and useful discussions on the research topic.

Ye YG, Gong FQ, Gong MZ, Man K, Yang WM, Shi L, Ma HS, Duan YY, You S, Yin LJ, Sun L, Peng Q, Li JC, Xu T and all colleagues in LMR and LMS for their support during my study and life time.

Prof Darve F and Prof Jeon S for reviewing and evaluating this dissertation.

Prof Song HW, Prof Zhou GQ, Prof Jing HW, Prof Yang RM for their supports during my PhD application process.

The Education Affairs Office of the Embassy of the People's Republic of China in Switzerland for their support during the study and life time.

The China Scholarship Council and Swiss National Science Foundation for their financial support during my PhD study.

Unknown reviewers on the paper of DLSM for their critical and useful suggestions.

Abstract

A micro-macro and continuum-discontinuum coupled model and corresponding computer codes are developed in this thesis for rock dynamics study.

Firstly, a new micromechanical model for describing the elastic continuum based on the underlying microstructure of material is proposed. The model provides a more general description of material than linear elasticity.

Then, a numerical model Distinct Lattice Spring Model (DLSM) is developed based on the RMIB theory. The new proposed model has the advantages of being meshless, and automatic continuum description through underlying discontinuum structure and directly using macroscopic elastic parameters.

Following this, the multi-scale DLSM (m-DLSM) is proposed to combine DLSM and NMM. The proposed model uses a tri-layer structure and the macro model can be automatically released into micro model during calculation.

Forth ward, the ability of DLSM on modeling dynamic failure is studied. A damage based micro constitutive law is developed. Relationships between the micro constitutive parameters and the macro mechanical parameters of material are provided. The micro parameters can directly be obtained from macro experimental results, i.e., tensile strength and fracture energy, through these equations.

Moreover, the ability of DLSM on modeling wave propagation is enhanced and verified. Non-reflection boundary condition and methods to represent discontinuity in DLSM are developed.

Finally, the parallelization of DLSM and 2D implicit DLSM are introduced. The main achievements of the whole PhD work and future research works are summarized and prospected in the conclusion part of the thesis.

Keywords: rock dynamics; numerical model; microstructure; RMIB; DLSM; m-DLSM; NMM; multi-scale; dynamic failure; wave propagation; Open MP; MPI; parallelization; implicit; MLS.

Résumé

Un modèle micro-macro et continu discontinu couplé et les codes informatiques correspondants sont développés dans cette thèse pour a dynamique des roches.

Tout d'abord, un nouveau modèle micromécanique pour décrire le continu élastique basée sur la microstructure des matériaux sous-jacents est proposé. Le modèle fournit une description plus générale de la matière que l'élasticité linéaire.

Ensuite, un modèle numérique Distinct Lattice Spring Model (DLSM) est développé basé sur la théorie RMIB. Le nouveau modèle proposé a l'avantage de ne pas avoir besoin de maillage, et une description du continuum au moyen d'une structure discontinue directement en utilisant des paramètres macroscopiques élastiques.

Suite à cela, l'DLSM multi-échelle (m-DLSM) est proposé pour combiner DLSM et NMM. Le modèle proposé utilise une structure tri-couche et le macro de le modèle être automatiquement transformé dans le modèle micro pendant le calcul.

Ensuite, la capacité de DLSM sur la modélisation de la rupture dynamique est étudiée. Un micro basée sur dédommagement loi de comportement est développé. Les relations entre les paramètres micro constitutive et les paramètres macro mécaniques des matériaux sont fournis. Les micro paramètres peuvent être directement obtenus à partir de macro résultats expérimentaux, à savoir, résistance à la traction et l'énergie de rupture, par le biais de ces équations.

En outre, la capacité de DLSM pour la modélisation de la propagation des ondes de modélisation est améliorée et vérifiée. Des non condition de réflexive et des méthodes pour représenter une discontinuité dans DLSM sont développés.

Enfin, la parallélisation des DLSM et 2D DLSM implicites sont introduits. Les principales réalisations de l'ensemble du travail de thèse et de travaux de recherche futurs sont résumés dans la partie conclusion de la thèse.

Mots-clés: dynamique des roches; modèle numérique; microstructure; RMIB; DLSM; m-DLSM; NMM; multi-échelle; rupture dynamique; propagation des ondes; Open MP; MPI; parallélisation; implicite; MLS.

Table of Contents

List of figures

List of tables

List of symbols

Roman alphabet

A : the area of the joint plane
$\bar{A}$: the equivalent area of the particle
$\mathbf{b}$: the body force per unit mass
$\mathbf{B}_e$: the interpolation matrix of strain
$b_{ji}(\mathbf{x})$: the basis of the displacement function
$[\mathbf{C}]$: the damping matrix
c_{ijnm} : the elastic tensor
$c_j(\mathbf{x})$: the displacement function of the jth physical cover
C_p : the P-wave velocity
C_R : the Reyleigh surface wave velocity
C_S : the S-wave velocity
d : the thickness of the weak material layer
$\mathbf{D}$: the elastic matrix
$D(u_n)$: the damage variable function for normal spring
D^{bond} : the damage variable of bond
D^n : the damage variables for normal spring
D^s : the damage variables for shear spring
E : the Young’s modulus
E^{cpu} : the efficiency of a parallel code
$\mathbf{F}^{(t)}$: the vector of external force
$f(u_n)$: the spring interaction force
$\mathbf{F}_i^{\mathrm{ME}}$: the transferred force to the ith PMM element
G : the shear elastic modules

G_f : the macro fracture energy

G_f^* : the fracture energy of the representative spring

$H_m^{(n)}(x)$: Hankel function

k : the normal/shear spring stiffness

K : the bulk elastic modules

$[\mathbf{K}]$: the stiffness matrix

k_0 : the initial stiffness

$\bar{k}(u_n)$: the secant modulus

$\mathbf{K}^{\text{bond}}$: the bond stiffness matrix in local coordinate

K_{IC} : the fracture toughness for mode-I crack

K_{Id}^c : the dynamic fracture toughness

$\dot{K}_{Id}$: the average loading rate for dynamic fracture toughness test

$\mathbf{K}_{ij}^b$: the stiffness matrix of lattice bond in global coordinate

$\mathbf{K}_i^{\text{PME}}$: the stiffness matrix of PMM element

k_n : the normal stiffness of the bond

k_n^{bond} : the normal stiffness of the bond cut by virtual joint plane

k_n^j : the inputted normal stiffness of the discontinuity

K^{red} : the dimensionless parameter to identify the damage variable function

k_s : the shear stiffness of the bond

k_s^{bond} : the shear stiffness of the bond cut by virtual joint plane

k_s^j : the inputted normal stiffness of the discontinuity

l : the original length of the bond

l^* : the representative spring length in DLSM (equal to the mean particle size)

lr : the mesh ratio of DLSM/UDEC model.

$[\mathbf{M}]$: the diagonal mass matrix

$\mathbf{M}_i^{\text{PME}}$: the mass matrix of PMM element

$\mathbf{n}$: the outward normal vector on the boundary surface

n^{cut} : the number of bonds cut by the plane

$\mathbf{N}_e$: the interpolation matrix of displacement

np : number of processors used in the parallel simulation

np_x : the number of dividing in x direction

np_y : the number of dividing in y direction

np_z : the number of dividing in z direction

S : the speedup of a parallel code

t : time

$\bar{t}$: the prescribed traction on the corresponding boundaries

$|T_1|$: the transmission coefficient across a single fracture

t_n : the normal viscous traction

t_{s1} : the shear viscous traction

t_{s2} : the shear viscous traction

$\mathbf{u}$: the vector of particle displacement

$\bar{\mathbf{u}}$: the prescribed displacement on the corresponding boundaries

$\ddot{\mathbf{u}}$: the accelerate

u_c^* : the ultimate compressive deformation of the bond

$\mathbf{u}_{ij}^{\mathrm{LS}}$: the mapped displacement from PMM model to the linked particle

$\mathbf{u}_{ij}^{\mathrm{ME}}$: the displacement vector of the PMM element

u_{ji} : the general DOFs of the cover

u_n : the normal deformation of the bond

u_n^* : the ultimate tensile deformation of the bond

u_s : the shear deformation of the bond

u_s^* : the ultimate shear deformation of the bond

V_L : limiting crack propagation velocity

v_n : the normal components of the velocity of the particle

v_{s1} : the shear components of the velocity of the particle

v_{s2} : the shear components of the velocity of the particle

z : the P-wave/S-wave impedance

Greek symbols

α : the damping constant

α^{2D} : the microstructure geometry coefficient of 2D lattice model

α^{3D} : the microstructure geometry coefficient of 3D lattice model

δ_1 : the dimensionless parameter to identify the damage variable function

δ_2 : the dimensionless parameter to identify the damage variable function

ε_1 : the maximum main strain of the PMM element

ε_{ij} : the components of strain tensor

ε_t^* : the ultimate strain of the model

ϕ_j : the weight function

Φ : the potential function

φ : the relative shear displacement of the bond

γ : the reduction factor for criteria releasing the PMM into DLSM in m-DLSM

ν : the Poisson's ratio

ρ : the density

$\boldsymbol{\sigma}$: the Cauchy stress

σ_{ij} : the components of stress tensor

σ_t^{macro} : the macroscopic uniaxial tensile strength

σ_c^{macro} : the macroscopic uniaxial compressive strength

σ_{hydro}^{macro} : the macroscopic hydrostatic compressive strength

ω : the angular frequency of the harmonic wave

ξ : the direction vector of the bond spring

Miscellaneous symbols

Δ : the prescribed displacement load

Δt_{n} : the time step used in DLSM model.

∇ : the gradient operator

Π_b : the strain energy of the bond

List of abbreviations

BCM   Boundary Contour Method

BEM   Boundary Element Method

BPM   Bonded-Particle Model

CDEM   Continuum-based Discrete Element Method

CDM   Continuum Damage Mechanics

CLSM   Conventional Lattice Spring Model

CPU   Central Processing Unit

CZM   Cohesive Zone Model

DDA   Discontinuous Deformation Analysis

DEM   Discrete Element Method

DEM*   Diffuse Element Method

DLSM   Distinct Lattice Spring Model

DCM Distinct Motion Code

EFG   Element Free Galerkin

FCM   Finite Cover Method

FD-HMM   Finite Difference Heterogeneous Multi-scale Method

FDM   Finite Difference Method

FDTD   Finite-Difference Time-Domain method

FEEM   Finite Edge Element Method

FEM   Finite Element Method

FPM   Finite Point Method

FVM   Finite Volume Method

GBEM   Galerkin Boundary Element Method

GFDM   Generalized Finite Difference Method

GFEM   Generalized Finite Element Method

GIMP   Generalized Interpolation Material Point method

GPU   Graphics Processing Unit

GTN   Gurson Tvergaard Needleman

LSM   Lattice Spring Model

MD   Molecular Dynamics

m-DLSM   multi-scale DLSM

MLS   Moving Least Square

MPI   Message Passing Interface

MsFEM   Multiscale Finite Element Method

NEM   Natural Element Method

NMM   Numerical Manifold Method

OpenMP   Open Multi-Processing

PC   Personal Computer

PDEs   Partial Differential Equations

PFC Particle Flow Code

PHPC   Personal High Performance Computing

PMM   Particle based Manifold Method

PU   Partion of Unity

PUM   Partion of Unity Method

QC   Quasicontinuum

QM   Quantum Mechanics

ReaxFF   Reactive Force Field

RKPM   Reproducing Kernel Particle Method

RMIB   Real Multi-dimensional Internal Bond model

SPH   Smoothed Particle Hydrodynamics

TBB   Threading Building Blocks

TBM   Tunnel Boring Machine

XFEM   Extend Finite Element Method

Chapter 1

Introduction

1.1 Rock dynamics and numerical modeling

Rock dynamics is the science of studying mechanical behavior of rock under dynamic loading. Rock in general is a term representing rock material and rock mass, so the research object in rock dynamics includes both rock material and rock mass. Unlike any other man-made material, rock usually has undergone a geological history involving appreciable mechanical, thermal and chemical actions over millions of years. Both rock material and rock mass have complex structures as shown in Figure 1.1, which make the mechanical properties of rock much more complex than those of other man-made materials. The structural complexity of rock plays an important role in determine the mechanical property of rock material and rock mass. There are two issues in rock dynamics. The first one is the failure of rock, which is one of the most important research issues. Because it is related to the economy and safety of structures built in/on rocks and is also the key element in the solution of many engineering problems involving dynamic loading conditions. Wave propagation across rock mass is another study issue of rock dynamics, and it is important to be able to predict wave attenuation across fractured rock masses.

The failure of rock generally refers to a rock suffers permanent damage which affects its ability to sustain a load. For rock dynamics, the fracture pattern and mechanical properties are influenced by strain rate. This strain rate dependency is the most concerned topic in rock dynamics. Results of a series of dynamic triaxial compression tests on granite samples showed that the dynamic compressive strength increases with the stain rate [1-3]. The rate dependent behavior may be influenced by many factors including rock type, porosity, and water content and confining pressure. Mechanism governing the rate-dependent behavior of rock materials was explained by different kinds of models, such as heat activation theory [4], spring-dashpot models [5, 6], sliding crack model [7] and inertial effect [8, 9]. However, the real mechanism of the dynamic effect is still not clear now. Recently, the microstructure of rock material is considered as one of the influence factors of the dynamic effect. However, when microscopic scale is concerned, both analytical method and experimental method are limited. The analytical solution is not suitable to solve problems of complex geometry and existing experimental facilities, e.g., the microscopic scale scanning electron microscope (SEM) and X-ray CT, are not sensitive enough to detect the dynamic fracturing process of rock material under high loading rates. Fortunately, with the rapid advancement of computing technology, numerical methods provide the alternative tool for studying the mechanisms of dynamic effect on rock materials.

(a) Microstructure of sandstone, field view of 3.5mm [10] .

(b) Joint pattern of rock mass, field of view around 10m [11]

Figure 1.1. The complex structure of rock at micro/macro scale.

Wave transmission is another research issue in rock dynamics. The wave transmission can be viewed as the transmission of dynamic loads through rocks. It is an important research issue for engineering purpose, as the damage criteria of rock structures are generally regulated according to threshold values of wave amplitudes, such as peak displacement, peak particle velocity and peak acceleration [12, 13]. The prediction of wave attenuation across fractured rock masses is very important in solving problems in geophysics, seismic investigation, rock dynamics, rock protective engineering, and earthquake engineering. Many researchers use wave scattering theories and displacement discontinuity theories to study the wave propagation through rock joints (e.g. [14, 15]). Interface wave propagation through a single fracture and one set of fractures has been examined by many researchers (e.g. [16-18]). In those studies, the wave attenuation is the most concerned study context. In practice, there commonly exist several sets of fractures in fractured rock masses. The intersecting fractures produce intersecting reflection interfaces. Wave attenuation across intersecting fractures will be more complicated than that across a set of fractures, where the reflection interfaces are parallel. Analytical method is very difficult to be applied for the complex geometry condition. Again, numerical methods are promising solutions for wave propagation problems in rock dynamics.

There exist a large number of numerical methods which have been applied to rock mechanics and rock engineering. In order to solve rock dynamics problems, the numerical model is required to satisfy the following requirements:

- Used parameters can be obtained directly from the exiting standard experiments.
- Failure of material and energy transmission can be explicitly modeled.
- The macroscopic continuum behavior before failure can be precisely modeled.
- The microscopic discontinuum response after failure can be modeled.
- Complex geometry model at microscopic scale can be easily represented.

Unfortunately, so far, there does not exist a single numerical method which could satisfy all of them. A micro-macro and continuum-discontinuum coupled numerical method should be developed to satisfy these requirements. The methodology is shown in Figure 1.2, where the macro continuum is made up of micro discontinuum parts before failure and the macro continuum can be further broken into micro discontinuum parts after failure. The goal of this PhD thesis is to develop a numerical model based on this methodology and then use it to study rock dynamics problems related to rock failure and wave propagation.

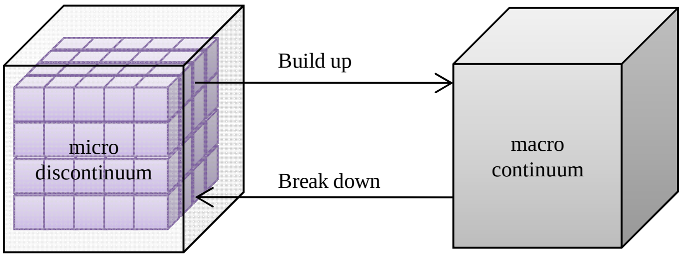

Figure 1.2. Micro-macro and continuum discontinuum methodology.

1.2 Objectives and scope of the thesis

The main objectives of this research are:

- To develop a micro-macro and continuum-discontinuum coupled model and computer codes.
- To validate the codes for numerical modeling study on wave propagation through rock material and rock mass, rock fracturing process and dynamic effect of rock material.

In order to achieve the objectives, the following works have been performed:

- Reviewing the existing numerical methods to find their advantages and disadvantages and conceptualizing the new numerical model.
- Developing a microstructure based **theoretical model** for macroscopic continuum.
- Developing a microstructure based **numerical model** and its computer code.
- Developing a **multiscale model** based on the proposed model and its computer code.
- Verifying the codes against analytical solutions and experimental results.
- Modeling the loading rate effect of rock material to validate the new model on dynamic fracturing simulation.
- Modeling wave propagation through rock material and rock mass to test the applicability of the developed code for wave propagation study.
- Applying high performance computing for the model and develop parallel codes.
- Investigating the explicit model and develop the implicit version of the model.

1.3 Structure of the thesis

This thesis is divided into 10 chapters. In **Chapter 1**, an general introduction of the thesis is given, including a discussion of rock dynamics and its requirements on the numerical modeling, and objectives and scope of the research.

Chapter 2 focuses on the literature review on different numerical methods. The literature review is not only focusing on the numerical methods used in rock mechanics but also concerning other methods used in areas such as nanostructure technology and metals. These numerical methods are reviewed in three groups: continuum based methods, discontinuum based methods and coupled methods. Following the literature review, the challenges and problems existing in the current numerical methods are listed and the possible solutions are discussed.

Chapter 3 presents a new micromechanical model, real multi-dimensional internal bond model (RMIB), for modeling elastic continuum. The continuum is assumed to have an underlying micro-structure consisting of discrete particles connected by multi-dimensional internal bonds (normal and shear springs), which has been demonstrated as a useful description for fracture modeling of materials such as rock and concrete. The proposed model provides a microscopic description of the rock material at macroscopic scale and also serves as the theoretical foundation for the new developed numerical model in Chapter 4.

Chapter 4 introduces a 3D distinct lattice spring model (DLSM). The model discretize the macroscopic continuum into microscopic discontinuum parts and is the computational realization of the RMIB theory in Chapter 3. It is a kind of lattice spring model, which is different from the conventional lattice spring models. It can represent the diversity of the Poisson’s ratio without violating the rotational invariance. The material parameters inputted in the model is the conventional material parameters, e.g., the elastic modules and the Poisson’s ratio. Relationships between microscopic spring parameters and macroscopic material constants are derived based on the RMIB theory. The new proposed model has the advantages of being meshless, and automatic continuum description through underlying discontinuum structure and directly using macroscopic elastic parameters. Numerical examples are presented to show the abilities and properties of DLSM in modeling elastic and dynamic failure problems.

Chapter 5 presents a multiscale numerical method (m-DLSM) which combines numerical manifold method (NMM) and DLSM. The proposed model use a tri-layer structure to couple the macroscopic NMM with the microscopic DLSM model. A new particle based manifold method (PMM) is proposed to bridge the two different methods. The coupled method is validated by several examples including one example of blasting wave propagation through a tunnel.

Chapter 6 focuses on the ability of DLSM to study dynamic failure of rock material. As a new developed numerical model, constitutive model used in DLSM is different from those used in the existing numerical methods. A general form of the micro constitutive law is proposed. Moreover, relationships between the micro constitutive parameters and the macro mechanical parameters of material are provided. By using these equations, micro parameters used in DLSM can directly be obtained from macro experimental results, i.e., tensile strength and fracture energy. Two examples are modeled by DLSM to show the ability of the new developed code on modeling dynamic failure problems.

Chapter 7 presents the applications of DLSM on the study of stress wave propagation through rock material and rock mass. Non-reflection boundary condition is implemented and tested. The influence of particle size on P-wave and S-wave propagation through rock are investigated through 1D and 2D wave propagation problems. Two methods are introduced in DLSM to represent discontinuity. Wave propagation through single joint is predicted by DLSM and compared with analytical solutions.

Chapter 8 describes the computational aspects of DLSM. The motivation of the study is to reduce computational time by parallel computing and solve scientific problems which are too big to handle by the serial DLSM code. This chapter is organized into two main sections. The first section presents the parallel implementation based on the OpenMP (Open Multi-Processing) programming interface. The second section describes the parallel implementation based on Message Passing Interface (MPI) for supercomputer.

Chapter 9 introduces the 2D implicit DLSM. The global stiffness matrix is assembled and static solution can be obtained by solving linear algebraic equations. The modeling results are compared with FEM results. It shows that the DLSM model is numerically stable, which is an important feature. Moreover, it is easy to treat heterogeneity and does not require integration. These features make the method advantageous than some existing meshless methods.

In the final chapter, **Chapter 10**, the main achievements of the whole PhD work are summarized. Future research works are also prospected.

1.4 Reference

1. Masuda K., Mizutani H, Yamada I. Experimental-study of strain-rate dependence and pressure-dependence of failure properties of granite. J Phys Earth, 1987; 35:37-66.
2. Zhao J. Applicability of Mohr-Coulomb and Hoek-Brown strength criteria to the dynamic strength of brittle rock. Int. J. Rock Mech. & Min.Sci., 2000; 37: 1115-1121.
3. Zhao J, Li HB, Wu MB, Li TJ. Dynamic uniaxial compression tests on a granite. Int. J. Rock Mech. & Min.Sci., 1999; 36:273-277.
4. Kumar A. Effect of stress rate and temperature on strength of basalt and granite. Geophysics, 1968; 33: 501-510.
5. Chong KP, Boresi AP. Strain rate dependent mechanical-properties of new-albany reference shale. Int. J. Rock Mech. & Min.Sci., 1990; 27: 199-205.
6. Chong KP, Hoyt PM, Smith JW, Paulsen BY. Effects of strain rate on oil-shale fracturing. Int. J. Rock Mech. & Min.Sci., 1980; 17: 35-43.
7. Li HB, Zhao J, Li TJ. Micromechanical modelling of the mechanical properties of a granite under dynamic uniaxial compressive loads. Int. J. Rock Mech. & Min.Sci., 2000; 37: 923-935.
8. Li QM, Lu YB, Meng H. Further investigation on the dynamic compressive strength enhancement of concrete-like materials based on split Hopkinson pressure bar tests. Part II: Numerical simulations. Int. J. Impact Eng. 2009; 36: 1327-1334.
9. Chambart M. An anisotropic delay-damage model to simulate reinforced concrete structures in dynamics. Proc of 1st EPFL Doct Conf Mech, 2010; 21-25.
10. Waters DJ. http://www.earth.ox.ac.uk/~oesis/micro/index.html, 2010.
11. Hoek E. Practical rock engineering, lecture notes, 2007.
12. Mohanty B. Physics of exploration hazard. forensic investigation of explosions. S. Beveridge, ed., Taylor and Francis, 1998; 15-44.
13. Stacey T. Seismic assessment of rock masses. Proc. Symp. on exploration for rock Engng, Johannesburg, A. A. Balkema, 1976; 113-7.
14. Cai JG, Zhao J. Effects of multiple parallel fractures on apparent attenuation of stress waves in rock masses. Int. J. Rock Mech. & Min.Sci., 2000; 37: 661-682.
15. Hudson J. Wave speeds and attenuation of elastic waves in material containing cracks. Geophys J Roy Astron Soc, 1981; 64:133-50.
16. Gu B. Interface waves on a fracture in rock, Ph.D.Thesis, University of California, Berkeley, USA, 1994.
17. Pyraknolte LJ, Nolte DD. Wavelet analysis of velocity dispersion of elastic interface waves propagating along a fracture. GRL, 1995; 22:1329-1332.
18. Zhao J, Cai JG, Zhao XB, Li HB. Experimental study of ultrasonic wave attenuation across parallel fractures. J Geomech Geoengrg, 2006; 1: 87-103.

Chapter 2

Review of present state of numerical methods

With the improvement of modern computers on computing power, numerical methods have become extremely useful in scientific research. It has been proven that, in addition to experimental method, computer simulation using numerical methods is a powerful and effective tool for the study of rock mechanics. For example, numerical modeling has been used to study dynamic response of fractured rock masses [1, 2], fracturing propagation in rock and concrete [3-9], wave propagation in jointed rock masses [10, 11], and acoustic emission in rock [12]. There exist a large number of numerical methods, e.g., Finite Element Method (FEM), Finite Difference Method (FDM), Finite Volume Method (FVM) and Discrete Element Method (DEM). Generally numerical methods used in rock mechanics can be classified into continuum based method, discontinuum based method and coupled continuum/discontinuum method [13]. Based on this classification, this chapter will review the existing methods with more focuses on new developed methods and those not covered by [13], e.g., Smoothed Particle Hydrodynamics (SPH), Molecular Dynamics (MD) and combined FEM/DEM method. This chapter attempts to obtain a global view for each class of methods and find the advantages and disadvantages of each. Finally, some ideas of how to design the suitable numerical method for rock dynamics are proposed.

2.1 Continuum based methods

2.1.1 Finite Difference Method (FDM)

FDM is one of the oldest numerical techniques used for the solution of sets of PDEs. The implementation of FDM is simple in both three dimensional and two dimensional cases. It does not need trial (or interpolation) functions like any other methods. However, the conventional FDM with regular grid system does suffer the inflexibility in dealing with fractures, complex boundary conditions and material heterogeneity. This shortcoming constrains its application in rock mechanics. Development of FDM targets at getting rid of the shortcoming. For example, the Finite Volume Method (FVM) is considered as an extended FDM which not only removes the regular mesh constrain but also specially fits to the simulation of non-linear behavior of solid materials [14]. Finite-difference time-domain (FDTD) method [15] is a direct development of FDM. It adopts a two layer grid-based differential time-domain methodology. FDTD was widely used for processing electromagnetic data in rock mechanics, e.g., the imaging of electromagnetic data for cross-borehole [16-18]. FDTD was also used for determining the hydraulic conductivity of rocks [19] and solving wave propagation problems in homogeneous and heterogeneous medium [20-25]. Inhomogeneous problems are solved by FDTD using the double grid methodology.

Based on the basic idea of FDM, some truly meshless methods are proposed recently, such as the generalized finite difference method (GFDM) [26] and the finite point method (FPM) [27]. Indeed, the basic idea of FDM has been widely used to discretize time domain in many numerical methods, especially for dynamic analysis, e.g., DEM and MD.

2.1.2 Boundary Element Method (BEM)

Boundary element method (BEM) seeks a weak solution at the global level through a numerical solution of an integral equation derived from the original PDE using Betti's reciprocal theorem and Somigliana's identity. As only the boundary surface of modeling domain is needed, BEM reduces the problem dimension by one. This leads to a fast computing speed and easy mesh generation. BEM is more suitable for solving problems of homogeneous and linearly elastic bodies [28-30]. Recent development of BEM includes the Boundary Contour Method (BCM) [31] and the Fast Multipole BEM (FMBEM) [32] with further reduction of computational time, the Galerkin BEM (GBEM) [33, 34] which paves the way for the variation formulation of BEM for solving non-linear problems, and meshfree BEM [35, 36] which overcomes the drawbacks related to the use of boundary element in the conventional BEM. In general, BEM is not as efficient as FEM in dealing with material heterogeneity, non-linear material behavior and damage evolution process.

2.1.3 Finite Element Method (FEM)

The FEM [37] term was first used by Clough for plane stress problems, now it has become the mainstream numerical tool in engineering sciences, including rock mechanics. FEM has great robustness and flexibility in the treatment of material heterogeneity, non-linear deformability, complex boundary conditions, in situ stresses and gravity. These merits make the FEM becoming the most successful numerical method used in engineering and science research [14]. Special development of FEM for problems in rock mechanics is the idea of joint elements [38-41] which was introduced for the simulation of jointed rock mass. In rock mechanics, the most difficult thing faced by FEM is the simulation of fracturing process. This subsection will focus on this aspect. A survey of the literatures on FEM modeling of fracturing progress found that the available methods can be classified into two groups: the element degradation approach and the element boundary breaking approach.

The idea of the element degradation approach is to treat the fracturing process as a sequence of element degradation. The deletion technique provided in ABAQUS [42] is an example of this kind of approach, which removes the elements where the failure criterion is locally reached. Elements deleted can be visualized to mimic the crack progress. The most representative method in this group is the continuum damage mechanics (CDM) based FEM, which was widely used for brittle fracturing analysis [43-45]. When combined with the Weibull distribution for representing heterogeneity and some statistical failure criteria, it was applied to describe damage evolution and crack propagation in rock and concrete under static and dynamic loading conditions [3-9]. Based on the equivalent continuum concept, another degradation technique was realized by modeling cracks and joints as elastic degradation and/or softening plasticity [46]. Crack smeared model is one representative of this method, which was first introduced by Rashid [47]. The crack smeared model is commonly used in concrete fracture analysis, and it is being far more popular because of its computational convenience [48]. Applications of the crack smeared model include, to just name a few, fracturing analysis of concrete under high strain rates [49], simulation of the thermo-mechanical behavior and failure of ceramic refractory materials [50], and damage analysis of reinforced concrete structures [51]. This technique has also been used in commercial FEM codes, e.g., ANSYS [52] and ATENA [53], to simulate the fracture/crack process of concrete-like materials. Element degradation method has the advantages of no requirement of re-meshing and not adding new degrees of freedom in the calculation process. However, this method cannot give explicit description of the fracture surface and has mesh size and orientation dependency.

The element boundary breaking approach represents the fracturing process by the separation of inter-element boundaries. The method inserts interface elements along the inter-element boundaries. It was used for crack propagation in concrete and rock materials [54-56]. Failure of an inter-element boundary can be based on the fracture mechanics or failure criteria of the corresponding interface element. Fracture mechanics based methods are used in several FEM codes such as ABQUS [42], FRANC [57] and MARC [58] to deal with crack propagation problems. The most successful development of the element boundary breaking approach is the Cohesive Zone Model (CZM) which dates back to the work of Hillerborg et al. [59] and Belytschko et al. [60] for brittle materials. The CZM has been successfully used in simulation of fracture and fragmentation in brittle materials, multiple discrete crack propagation and dynamic crack growth in ceramic materials [61-65]. Normally, this technique should be coupled with re-meshing techniques to eliminate the element dependence and the problem of stress singularity which exists in the crack tip [63]. However, re-meshing techniques [66-69] requires a rather complex software package to be developed and the use of re-meshing techniques also accumulates the calculation errors through mapping of variables. The worse fact is that adaptive re-meshing can hardly be used to simulate complex crack development, such as crack coalescence and crack bifurcation.

There also exist some shortcomings in FEM, e.g., the continuum assumption in FEM makes it unsuitable to deal with complete detachment and large-scale fracture opening problems [13, 14], which are the most concerned issues in rock mechanics. Locking effects which include numerical locking and element locking during simulation are other pitfalls of the traditional FEM [70-74]. Some of these shortcomings have been solved by the derived FEMs to be reviewed in the following subsection.

2.1.4 Derived FEM

After the Partition of Unity (PU) [75] was proposed by Babuska and Melenk, researchers of different numerical methods can find their theoretical base through it. Based on PU, a priori knowledge about the solution can be added into the approximation space of the numerical solution. Numerical methods based on PU are usually called as derived FEMs. The typical derived FEMs are Numerical Manifold Method (NMM) [76], eXtend FEM (XFEM) [77], Generalized FEM (GFEM) [78] and Finite Cover Method (FCM) [79, 80]. The review in this subsection will focus on these methods.

NMM was developed to integrate Discontinuous Deformation Analysis (DDA) and FEM. NMM employs two sets of cover system [76]. One is mathematical cover which is used to build approximation and independent of the problem domain. Another is physical cover which contains the geometry information of the problem domain and is used to define the integration fields. The advantages of NMM are releasing the task of meshing and combining continuum and discontinuum problems into one framework. For this reason, NMM is suitable for fracture progress simulation [81, 82]. NMM has several advantages over classical FEM, e.g., it is more suitable for modeling dynamic crack growth problem [81] and micropolar elasticity [82]. FCM [78] is an extension of NMM to modeling of heterogeneous materials by using Lagrange multipliers. Recently, FCM has been extended to three-dimension by Terada and Kurumatani [83]. The NMM is proposed much earlier than the PU theory and other derived FEMs. Recently, it is also called as cover-based generalized FEM [80]. Actually, the solver in manifold code is very similar with that in standard FEM and the distinct parts in NMM are the mesh generation technique and the half element technique. NMM can be regarded as a special derived FEM designed for rock mechanical problems which contain large numbers of discontinuities.

The XFEM [77] and GFEM [78] are other well known derived FEMs. GFEM and XFEM use exactly the same technique, but GFEM targets at solving problems in complex geometry with less error and less computer resources [84, 85], while XFEM focuses on crack propagation problems. For this reason, only XFEM is addressed here.

XFEM treats cracks at element level by using the level sets technique [86]. Usually, Heaviside function and asymptotic functions are used to deal with the discontinuity and singularity. Compared with the classical FEM, XFEM has several advantages in aspect of mesh independence. In XFEM, elements containing a crack are not required to conform to crack edges, and mesh generation is much simpler than in classical FEM. The most important aspect of XFEM is that it can perform extending crack without any re-meshing and the singularity can well be captured. Because of these advantages, XFEM was successfully used in the simulation of crack propagation [87], dynamic crack propagation [88] and three-dimensional crack propagation [89, 90]. Recent development of XFEM includes dealing with cohesive fracturing [91], explicit formulation of XFEM [92, 93], anisotropic XFEM [94] and considering contact between crack surfaces [95, 96].

These derived FEMs have the advantage of mesh independence and being able to deal with weak or strong discontinuities efficiently. These merits make them very suitable for fracturing process analysis. Nevertheless, they also have their own disadvantages. For example, in some cases the implementation of boundary conditions is as difficult as that in meshless methods [97]. The global stiffness matrix will become singular if the crack passes a very tiny part of XFEM element [98], which is an existing problem for all derived FEMs including NMM and GFEM. Implementation of XFEM into available commercial FEM code is difficult [99] because additional degrees of freedom are introduced. Moreover, all of these methods would suffer ill-conditioned problems when higher order cover functions (trial functions) are used. There are methods to reduce the singularity, but with the price of sacrificing the description of discontinuity inside enriched elements. In spite of these drawbacks, these derived FEMs are still the most promising methods. This is mainly attributed to the successful succession of the standard FEM idea and its inherent merits, e.g., robust and easy to deal with complex geometry, various loading and material conditions.

2.1.5 Meshless methods

In recent years, a large family of meshless methods with the aim of getting rid of mesh constraints has been developed. Their requirements for model generation are only generation and distribution of discrete nodes without fixed element-node topological relations as in FEM. Compared to mesh generation, it is relatively simple to establish a point distribution and adapt it locally. A local approximation function for the PDEs is built based on points grouped together in ‘clouds’. There are many meshless methods, such as Smoothed Particle Hydrodynamics (SPH) [100, 101], Diffuse Element Method Nayroles [102], Element Free Galerkin (EFG) [103, 104], Reproducing Kernel Particle Method (RKPM) [105, 106], Hp Clouds [107], Partion of Unity Method (PUM) [108], Finite Point Method (FPM) [109], Method of Finite Spheres [110], Natural Element Method (NEM) [111]. Review on these methods is given in [13] and [112]. Depending on the methodology used to discretize the partial differential equations (PDEs), meshless methods can be classified into two major categories: meshless strong-form methods and meshless weak-form methods. Most of meshless weak-form methods such as EFG [103] are 'meshless' only in terms of the numerical approximation of field variables and they have to use a background mesh to do numerical integration of a weak form over the problem domain, which is computationally expensive. Meshless strong-form methods such as GFDM [26] and FPM [109] often use the point collocation method to satisfy governing partial differential equations and boundary conditions. They are simple to be implemented and computationally efficient. Since they do not need any background mesh, they are truly meshless methods. In this subsection, only three representative meshless methods will be concerned, they are EFG, SPH and FPM.

EFG [103] is based on moving least square interpolations (MLS) which requires only nodal data and no element connectivity is needed. This meshless property is very suitable to model dynamic crack propagation problems. The application and development of the EFG method includes various fields, such as problems of fracture and static crack growth [104], dynamic problems [113], three-dimensional material non-linear dynamic problems [114], adaptive approach [115], dynamic propagation of arbitrary 3-D cracks [116], mixed-mode dynamic crack propagation in concrete and probabilistic fracture mechanics [117, 118], parallel EFG algorithm [119] and multiple cracks and cohesive crack growth [120]. Contact algorithm based on a penalty method is introduced in [121]. The EFG was also used for analysis of jointed rock masses with block-interface models [122]. The EFG method has the potential to be used in rock mechanics. Difficulty in implementing essential boundary conditions and additional computational cost caused by MLS are the main drawbacks of EFG.

SPH was first invented to deal with problems in astrophysics [100] and later extended for elastic problems [123]. Application of SPH is mainly in fragmentation analysis, such as dynamic fragmentation in brittle elastic solid [124, 125], high distortion impact computations [126, 127], concrete fragmentation under explosive loading [128], formation of cracks around magma chambers [129] and strain rate effect for heterogeneous brittle materials [130]. SPH exhibits an instability called the tensile instability and a problem known as the zero-energy mode. Both need special treatment in order to produce stable and accurate results [131]. Furthermore, the kernel function of SPH has great influence on the simulation results [132] and its accuracy is not as good as FEM. Overall speaking, SPH has advantage in simulation of dynamic fragmentation and is easy to implement. But the accuracy, computational time and contact treatment are still problematic in SPH, which hamper its further application in rock mechanics.

FPM [109] is a kind of meshless point collocation method which uses the weighted least squares (WLS) approximation within each point cloud. It can be easily constructed to have consistency of a desired order. Discrete equations are directly obtained from PDEs. It is easy to be implemented and boundary conditions can also be implemented by directly prescribing boundary conditions on points placed on boundaries. The most attractive point of FPM is that it can give more accurate stress results than FEM [133]. FPM with intrinsic enrichment was proposed for solving elastic crack problems. By the method, the local behavior of the near-tip stresses is successfully captured and the stress intensity factors can be accurately computed [134]. Furthermore, FPM is developed to simulate crack propagation under dynamic loading conditions [135]. Adaptive refinement process for FPM based on posteriori error estimator was presented [136]. However, the instability and the difficulty of dealing with heterogeneous media have handicapped its application to rock mechanics. Recently, the heterogeneous problem is partially solved [137], however, for arbitrary heterogeneous problem there is no good solution yet.

The main advantage of the meshless approaches is the sharply reduced demand for meshing compared with the standard FEM for both continuous and fractured bodies. Shortcomings of many meshless approaches are difficulty in enforcement of essential boundary conditions, stability problem and high computational cost. Generally speaking, meshless methods still do not outperform FEM in computing performance. Nevertheless, they have good potential for rock mechanics problems due to its flexibility in treatment of fractures and complex structures.

2.1.6 Drawbacks of continuum based methods

The continuum assumption in continuum based methods makes it not suitable for dealing with complete detachment and large-scale fracture opening problems [13], which are the most concerned issues in rock mechanics. It is difficult to apply continuum based methods to solve problems which involve complex discontinuity, such as jointed rock masses and rock in post-failure state. This is regarded as the intrinsic limit of continuum based methods. The continuum based methods use the idea of top-down methodology. Therefore, they cannot be used for exploring study on fundamental issues of mechanical problems, e.g., the microscopic mechanism of dynamic effect in rock materials.

2.2 Discontinuum based methods

2.2.1 Discrete Element Method (DEM)

DEM was invented for solving rock mechanics problems [138]. The key concept of DEM is to divide the modeling domain into an assemblage of rigid or deformable blocks/particles/bodies [139,140]. DEM is made for dealing with discontinuous bodies with large displacements and rotations, e.g., the progressive failure of blocky rock mass. DEM has undergone a long development since it was first proposed by Cundall [139]. DEM methods have been widely used in underground works [141-143], laboratory test simulations and constitutive model development [144-146], rock dynamics [147, 148], wave propagation in jointed rock masses [11], nuclear waste repository design and performance assessment [149], rock fragmentation process [150], and acoustic emission in rock [12].

According to the solution method used, DEM methods can be divided into two groups: explicit ones and implicit ones. For the explicit DEM methods, there exist two kinds of approaches: the dynamic relaxation method and the static relaxation method. The latter uses equations of equilibrium to obtain the displacement of blocks at the next time step. Examples of static relaxation based DEMs can be found in [140, 151]. The static relaxation method iterates faster and does not need damping. However, it cannot be used for dynamic problems. Dynamic relaxation based DEM use Newton’s second law to get the displacement of blocks at the next time step, and it is called as the distinct element method. The distinct element method can simulate the complex mechanical interactions of a discontinuous system. The most representative explicit

DEM codes are UDEC and 3DEC for two-dimensional and three-dimensional problems in rock mechanics [152,153] respectively. Making use of particles to simulate granular materials is another development direction of DEM [14, 154]. The most representative codes in this field are the Particle Flow Code (PFC) [155] and the Distinct Motion Code (DMC) [156]. Bonded Particle Model (BPM) [157, 158] was implemented in the particle DEM codes, which can describe the damage mechanism and time-dependent behavior of rock material at microscope. It has been used not only to simulate rock materials but also in shear-band simulation of metal material [159].

Contact detection and contact interaction are the most important issues in DEM, and many researchers think that DEM is distinct from other methods on the ability of detection new contacts during the calculation procedure. There are many contact detection algorithms which target at saving computing time and memory space, and detail information can be found in the book by Munjiza [160]. Mechanical interaction between two contacting blocks has a great influence on the final mechanical behaviors of DEM models. Usually it is modeled by a finite stiffness spring in the normal direction and a finite stiffness spring in the shear direction. Improvements of interaction modeling were reported, e.g., an interaction range and a modified Mohr Coulomb rupture criterion were introduced in DEM [161, 162] and a first order differential equation for joint cohesion was implemented into the UDEC code [163].

DDA [164] is a type of DEM originally proposed to analyze the mechanical behavior of blocky systems. It is similar to FEM, but can represent the interaction of individual blocks in rock masses. DDA is typically based on a work-energy method, and can be derived using the principle of minimum potential energy or the Hamilton's principle. The applications of DDA are mainly on landslides, tunneling, fracturing and fragmentation processes of geological and structural materials, and earthquake effects [165-167]. Developments of DDA include meshing the blocks with FEM meshes [168], dealing the contact as joint with stiffness and removing none penetration criterion to reduce the computation time and get fast convergence [169], coupled stress-flow problems [170], three-dimensional block system analysis [171], higher order elements [172], more comprehensive representation of the fractures [173], and viscous boundary for modeling stress wave propagation [167].

Mainly due to the explicit representation of fractures and joints, DEMs have been enjoying wide applications in rock mechanics and rock engineering. Furthermore, the theory of DEM methods is simple and easy to understand. Nevertheless, no method is perfect, there are also some shortcomings in DEM, e.g., the lack of knowledge of the geometry data of the rock fractures limits their applications [174]. Moreover, DEM is relatively new and many researchers regard it as “not yet proven” numerical method for analysis and design in rock mechanics.

2.2.2 Molecular Dynamics (MD)

MD is a form of computer simulation in which atoms and molecules are the basic elements. The system behavior is obtained through direct simulation of the motion of elements interacting under given physical laws. It is regarded as an interface between laboratory experiment and theory, and can be understood as a kind of "virtual experiment". MD was originally conceived within theoretical physics in the late 1950's [175]. Now it is widely used in material science and biochemistry science. It can help people to explain and find some phenomena at the atomic level. This review will only focus on the mechanical application of MD. Even in the early time, MD was used to study the crack properties and results obtained by MD agree well with those by continuum mechanics and fracture mechanics [176-179]. MD simulation was also used to study brittle to ductile transition of the propagation of a sharp crack and favorable crack propagation direction in crystallize material [180, 181], failure mechanism of micro granular material [182, 183], propagation of mode-I cracks in an icosahedral model quasi-crystal [184], and Yoffe's linear theory of dynamic brittle fracture [185].

Rock mechanics related problems solved by MD include interaction between complex granular particles [186], mechanical properties of poly-crystal materials [187], viscoelastic behavior of granite rock [188], and influence of porosity on elastic strength properties of polycrystalline specimens (sandstone) [189]. Potential function used in MD simulation has great influence on the simulation results, and it is also the core context of MD study. Potentials used for crack propagation study include the Lennard-Jones Potential [176,178], the Hooke’s Law (Harmonic Potential) [185], the EAM potentials [182, 183] and the ReaxFF reactive force field [190]. The Lennard-Jones Potential and the Hooke’s Law are simple but not very physically realistic. The EAM potentials could be successfully used in simulation of metal. However, they are not suitable for non-metal material such as silicon. The problem can be solved by using the ReaxFF reactive force field, which is computationally costly [190].

MD can be used to explain mechanical phenomena at atomic scale. It is a powerful tool for study mechanisms of crack propagation at microscopic level. However, long time simulations are mathematically ill-conditioned. Simple potential functions are not sufficiently accurate to reproduce the dynamics of molecular systems, while complex potential functions are usually computationally expensive. Furthermore, the atomic structures of rock materials are too complicated and can hardly be obtained. These limitations lead to the fact that MD still cannot be used for engineering problems in rock mechanics.

2.2.3 Lattice Model (LMs)

A family of methods coined as lattice models (LMs) have been developed in the past few decades. They are based, in principle, on the atomic lattice models originated from condensed matter physics. In these models, material is represented by a system of discrete units (e.g. particles) interacting via connecting elements. These discrete units are much coarser than the true atomic ones and may represent larger volumes of heterogeneities such as grains or clusters of grains. Compared to a true lattice model, the use of coarse lattices in lattice models dramatically reduces the number of degrees of freedom, and hence makes simulation of continuum systems affordable for medium-sized computers. Lattice models are more suitable for modeling fracture of materials than conventional FEMs because the former ones simulate fracture by either simply removing connecting elements that exceed the strength or successively degrading their mechanical properties according to cohesive laws. The spatial cooperative effects of crack formation and heterogeneities can be easily investigated through the use of LMs [191, 192].

There exist two different types of lattice models. In the first type models, the material is discretized as a network of springs or beams whose geometry is not related to the actual internal geometry of the material. Here the discrete units are merely lattice sites (nodes). This type of models can be further classified into lattice spring [193-197] and lattice beam [198-201] models according to the number of degrees of freedom per node and the mechanical properties of connecting elements. In a lattice spring model

(LSM), the unknowns are the nodal displacements and the connecting elements are one-dimensional springs. In a lattice beam model, the unknowns are the nodal displacements and rotations and the connecting elements are beams transferring normal forces, shear forces and bending moments. The second type models are based on the discrete element method originally developed for granular media with contact modeling [202]. For example, the rigid body-spring network model developed by Kawai [203] subdivides the material into rigid particles interconnected along their boundaries through normal and shear springs. It introduces additional rotational degrees of freedom on each particle and hence can be viewed as discretization of a micropolar continuum. Models in this category also include that of Zubelewicz and Bažant [204], the confinement-shear lattice model of Cusatis et al. [205], the bonded-particle model [206], the simple deformable polygonal discrete element model [207].

The origin of LSM may trace back to Hrennikoff [193]. The simplest LSM is the normal force model in which only central force interactions (normal springs) are considered. The normal force model has been extensively applied to investigate the elastic and failure properties of a disordered medium [194-199] or the fractal properties of crack [208]. It is also frequently used to study fracture or other issues of material science [209]. However, for the normal force model, it is known that the Poisson's ratio obtained by the model approaches, in the limit of an infinite number of particles, a fixed value, namely, 0.25 for three-dimensional cases and 0.33 for two-dimensional cases. Such restriction is not suitable for many materials and it can be overcome by introducing non-central force interactions (shear springs) between particles. There are different methods proposed to solve this problem, e.g., a method to modify the Poisson's ratio by introducing a harmonic potential for rotation of bonds from their initial orientation [210]. A non-central two-body interaction limiting the rotational freedom of bonds is introduced in the Born spring model [211, 212] to allow a broad choice of the Poisson's ratio. The Kirkwood-Keating spring model [213, 214] introduces angular springs to penalize the angular variations between the contiguous bonds incident onto the same node. Nevertheless, this problem cannot be solved ideally if only pair body interaction is considered, because in this case rotational invariance is often violated.

2.2.4 Drawbacks of discontinuum based methods

Discontinuum based methods treat rock material or rock mass as an assembled model of blocks, particles or bars. The fracturing process of rock is represented by the breakage of inter-block contacts or inter-particle bonds, which can be easily implemented in computer simulation. Discontinuum based methods can reproduce realistic failure process of rock. However they are not suitable for stress state analysis of pre-failure rock. This is the undesired aspect of discontinuum based methods.

2.3 Coupled Methods

2.3.1 Continuum and Discontinuum Coupled Methods

The continuum based methods are unsuitable to capture the post-failure discontinuous stage while the discontinuum based methods are unsuitable to capture the pre-failure stage of rock. A combination of continuum and discrete methods is required in many rock mechanics applications, such as predicting the formation and interaction of fragments for projectile penetration into rock [216]. Coupled continuum and discontinuum methods can take advantages of the strength of each method while avoiding its disadvantages. For fracturing simulation, a coupled method is required to be able to capture both the pre-failure and the post-failure behavior after collapse occurs [217]. Modeling the discontinuous zone with a discontinuum based method and the continuous zone with a continuum based method is a direct coupling methodology. Examples of this kind of coupling are hybrid DEM/BEM model [218], combinations of DEM, DFN and BEM approaches [219], and hybrid DEM/FEM model [220, 221]. To develop continuum-discontinuum coupled methods, most researchers incline to couple FEM with DEM. The review in this subsection will be limited to this approach.

Combined finite-discrete element method [160, 222] is a recently developed coupled FEM/DEM method which aims at modeling failing, fracturing and fragmenting of solids. In the combined finite-discrete element method, each body is represented by a single discrete element that interacts with other discrete elements that are close to it. In addition, each discrete element is divided into FEM elements, which can be broken into smaller blocks during calculation. Coupled FEM/DEM has been widely used to simulate fracture process of rock, e.g., Morris et al. [216] developed a FEM/DEM code, LDEC, to investigate the effect of explosive and impact loading on geological media, Karami and Stead [223] used a coupled FEM/DEM model to simulate crack propagation under mixed mode loading, and Ariffin et al. [224] applied a hybrid FEM/DEM code to investigate the processes of joint surface damage and near-surface intact rock tensile failure. Coupled FEM/DEM method is a powerful method to solve the fracturing process problems. However, implementing this method into a computer code needs complex skills and extensive efforts. There also exist some numerical methods which attempt to combine continuum and discontinuum methods into one single framework, e.g., NMM [77], the continuum-based discrete element method (CDEM) [225], the Peridynamic model [226], and the Finite Edge Element Method (FEEM) [227]. However, the basic ideas of these methods are similar to the FEM/DEM coupled methodology.

2.3.2 Multiscale Coupled Methods

Multiscale modeling was regarded as an exciting and promising methodology for simulation of fracturing process [228, 229]. Problems in rock mechanics are often multiscale, e.g., multiscale fracturing is regarded as the key to forecasting volcanic eruptions [230]. The purpose of multiscale modeling is reducing the computational time [231] and directly obtaining macro material response from micro mechanical interaction [232]. So far, there are three types of coupling methods. The first one is to couple models of different scales by using microscopic model only for parts of the modeling domain where it is needed and applying macroscopic model for other parts. This methodology is widely used in coupling MD with continuum mechanics. For example, FEM with MD [177], analytical solution with molecular dynamics [183] and the generalized interpolation material point (GIMP) method with molecular dynamics (MD) [233].

The second one is to use the same methodology, but adapted to different scales. For example, a two scale approach based on a refined global-local method is applied to the failure analysis of concrete structures [234]. In this approach, the FEM solution is split into two parts. The first part is a linear elastic analysis on a coarse mesh over the whole model. The second one is a non-linear analysis over a small part of the model. XFEM was used for simulating micro-macro crack evolution in heterogeneous materials in [235, 236]. It is realized by decomposing the solution into a coarse-scale description unchanged during the crack propagation and a fine scale computation which can be done independently of the coarse-scale computation. Examples of this kind of coupling method also include the three-scale computational method [237, 238], the multi-scale boundary element method [239], and the Voronoi cell FEM with a non-local Gurson Tvergaard Needleman (GTN) model [240].

The third one is the numerical method which includes multiscale function itself. For example, the multiscale finite element method (MsFEM) [241] was designed for solving a class of elliptic problems. The finite difference heterogeneous multi-scale method (FD-HMM) [242] was proposed for solving multi-scale parabolic problems. Quasicontinuum (QC) method is a coupled continuum and atomistic method which was initially proposed by Tadmor et al. [243] for simulating the mechanical response of polycrystalline materials. QC is used for the study of metal materials, e.g., the effects of structure and size on the deformation of bi-crystals in copper [244], the atomic scale fracture [245], and the deformation and failure of metal material [246]. There are also some wavelet based numerical methods, e.g., the wavelet based reproducing kernel particle method (RKPM) [247] and the multi-resolution finite element method based on the second generation wavelets [248, 249], which are of multiscale nature. The shortcoming of multiscale methods is that these methods are relatively new and no method is specially designed for rock mechanics.

2.4 Challenges and conclusions

Challenges exist in computational science include [250]:

(1) Explicitly and accurately model dynamic crack propagation problem.

(2) Multi-scale analysis.

(3) Multi-physics analysis.

There exist many numerical methods. Each of them has its own advantages and demerits. Table 2.1 lists the weakness and strength of the representative numerical methods in rock mechanics.

Table 2.1. Numerical methods for rock mechanics

Numerical methods	FEM	Derived-FEM	DEM	BPM/Lattice	MD	FEM/DEM	Multiscale methods
Pre-failure	✓	✓	×	×	×	✓	✓
Post-failure	×	×	✓	✓	✓	✓	☑
Ill-condition	✓	✓	×	×	✓	☑	☑
Calibration	×	×	×	✓	✓	☑	☑
Rock material	✓	✓	×	✓	×	✓	☑
Rock mass	×	☑	✓	×	×	✓	☑
Dynamic	✓	✓	✓	✓	✓	✓	✓
Wave propagation	✓	✓	✓	✓	✓	✓	✓
Implementation	✓	×	×	✓	✓	×	×

(✓: suitable/yes/easy; ×: unsuitable/no/difficult; ☑: theoretically suitable/yes)

It can be seen that there is not a numerical method satisfying all the requirements. Development of a micro-macro and continuum-discontinuum coupled numerical method is needed. The selection of the methods for coupling can be based on the information provided in Table 2.1. From which, the best choice in terms of efficiency and accuracy turns out to be the combination of the derived FEM and the BPM/Lattice model. As the degree of freedoms for each particle in BPM is not consistent with that in FEM, LSM is selected as the microscopic model in this thesis. However, for the LSM model, the limitation on the Poisson’s ratio and how to determine the model parameters are the problems need to be solved. In this thesis, a new LSM model will first be proposed to solve these problems. Then, a corresponding multiscale model will be developed by coupling LSM with NMM.

2.5 References

1. Chen SG, Cai JG, Zhao J, Zhou YX. Discrete element modelling of an underground explosion in a jointed rock mass. Geotech Geol Eng, 2000; 18: 59-78.
2. Hildyard MW, Young RP. Modelling seismic waves around underground openings in fractured rock. Pure Appl Geophys, 2002; 159: 247-276.
3. Bennett J. A Weibull brittle material failure model for the ABAQUS computer program. Contract: W-7405-ENG-36., 1991.
4. Du J, Kobayashi AS, Hawkins NM. FEM dynamic fracture analysis of concrete beams. J Eng Mech, 1989 ; 115: 2136-2149.
5. Kaiser PK, Tang CA. Numerical simulation of damage accumulation and seismic energy release during brittle rock failure-Part II: Rib Pillar Collapse. Int. J. Rock Mech. Min. Sci, 1998; 35:123-134.
6. Liang ZZ, Tang CA, Li HX., Zhang YB. Numerical simulation of the 3D failure process in heterogeneous rocks. Int. J. Rock Mech. Min. Sci, 2004; 41: 419-419.
7. Prisco M, Mazars J. Crush-crack a non-local damage model for concrete. Mech. Cohes.-Frict. Mater., 1996; 1:321-347.

8. Tang CA, Kaiser PK. Numerical simulation of cumulative damage and seismic energy release during brittle rock failure-Part I:Fundamentals. Int. J. Rock Mech. & Min.Sci, 1998; 35: 113-121.

9. Zhu WC, Tang CA. Numerical simulation of Brazilian disk rock failure under static and dynamic loading. Int. J. Rock Mech. & Min.Sci., 2006; 43: 236-252.

10. Chen SG, Zhao J. A study of UDEC modelling for blast wave propagation in jointed rock masses. Int. J. Rock Mech. & Min.Sci., 1998; 35: 93-99.

11. Lei WD, Teng, J, Hefny AM, Zhao J. Transmission ratio (T-n) in the radian direction normal to joints in 2-D compressional wave propagation in rock masses. J of Uni of Sci and Tech Beijing, 2006; 13: 199-206.

12. Hazzard JF, Young RP. Simulating acoustic emissions in bonded-particle models of rock. Int. J. Rock Mech. & Min.Sci., 2000; 37: 867-872.

13. Jing L. A review of techniques, advances and outstanding issues in numerical modelling for rock mechanics and rock engineering. Int. J. Rock Mech. & Min.Sci., 2003; 40: 283-353.

14. Jing L, Hudson JA. Numerical methods in rock mechanics. Int. J. Rock Mech. & Min.Sci., 2002; 39: 409-427.

15. Yee KS. Numerical solution of inital boundary value problems involving maxwell's equations in isotropic media. IEEE Trans. Antenn. Prop., 1966; 14: 302 - 307.

16. Ernst JR, Holliger K., Maurer H, Green AG. Realistic FDTD modelling of borehole georadar antenna radiation: methodolgy and application. Near Surf Geophys, 2006; 4: 19-30.

17. Holliger K, Musil M, Maurer HR. Ray-based amplitude tomography for crosshole georadar data: a numerical assessment. J Appl Geophys., 2001; 47: 285-298.

18. Yu L, Chouteau M, Boerner DE, Wang J. On the imaging of radio-frequency electromagnetic data for cross-borehole mineral exploration. Geophys J Int, 1998; 135: 523-541.

19. Lesnic D, Elliott L, Ingham DB, Clennell B, Knipe RJ. A mathematical model and numerical investigation for determining the hydraulic conductivity of rocks. Int. J. Rock Mech. & Min.Sci., 1997; 34: 741-759.

20. Barkhatov VA. Solving wave equations by the finite-difference time-domain method: Basic relationships for a two-dimensional problem. Russ J Nondestr Test., 2007; 43: 605-618.

21. JafarGandomi A, Takenaka H. Efficient FDTD algorithm for plane-wave simulation for vertically heterogeneous attenuative media. Geophys, 2007; 72: H43-H53.

22. Sato M. Finite-difference time-domain numerical analysis of elastic wave fields using both elastic and velocity potential variables. JJAP., 2006; 45: 4453-4461.

23. Schroder CT, Scott WR. A finite-difference model to study the elastic-wave interactions with buried land mines. Ieee Trans on Geosci and Remot Sens, 2000; 38: 1505-1512.

24. Schubert F, Peiffer A, Kohler B, Sanderson T. The elastodynamic finite integration technique for waves in cylindrical geometries. J. Acoust. Soc. Am., 1998; 104: 2604-2614.

25. Wang TL, Tang XM. Finite-difference modeling of elastic wave propagation: A nonsplitting perfectly matched layer approach. Geophys, 2003; 68: 1749-1755.

26. Liszka T, Orkisz J. The finite-difference method at arbitrary irregular grids and its application in applied mechanics. Comput Struct., 1980; 11: 83-95.

27. Onate E, Perazzo F, Miquel J. A finite point method for elasticity problems. Comput Struct., 2001; 79: 2151-2163.

28. Gray JP, Monaghan JJ. Numerical modelling of stress fields and fracture around magma chambers. J Volcanol Geoth Res., 2004; 135: 259-283.

29. Pan EN, Chen CS, Amadei B. A BEM formulation for anisotropic half-plane problems. Eng Anal Bound Elem., 1997; 20: 185-195.

30. Saez A, Dominguez J. Dynamic crack problems in three-dimensional transversely isotropic solids. Eng Anal Bound Elem., 2001; 25: 203-210.

31. Nagarajan A, Mukherjee S, Lutz E. The boundary contour method for three-dimensional linear elasticity. J Appl Math Mech., 1996;63: 278-286.

32. Nishimura N. Fast multipole accelerated boundary integral equation methods, Appl Mech Rev, 2002; 55: .299-324.

33. Bonnet M, Maier G, Polizzotto C. Symmetric Galerkin boundary element methods. Appl Mech Rev, 1998; 51: 669-703.

34. Maier G, Frangi A. Symmetric boundary element method for "discrete" crack modelling of fracture processes. CAMES, 1998; 5: 201-226.

35. Liu GR, Gu YT. Boundary meshfree methods based on the boundary point interpolation methods. Eng Anal Bound Elem., 2004; 28: 475-487.

36. Nicolazzi LC, Barcellos CS, Fancello EA, Duarte CAM. Generalized boundary element method for galerkin boundary integrals. Eng Anal Bound Elem., 2005; 29: 494-510.

37. Clough RW. The finite element method in plane stress analysis. Proc Secon ASCE Conf Elec Compu, Pittsburg, PA, 1960; 345.

38. Goodman R, Taylor R, Brekke T. A model for the mechanics of jointed rock. J Soil Mech Div ASCE 94, 1968; SM3: 37–59.

39. Katona. A simple contact–friction interface element with applications to buried culverts. Int J Numer Anal Methods Geomech, 1983; 7: 71–84.

40. Mahtab MA, Goodman RE. Three-dimensional finite element analysis of jointed rock slopes. Proc., Second Congress of the International Society of Rock Mechanics, Belgrade, 1970; 3:353-360.

41. Zienkiewicz OB, B. Dullage,C. Stagg, K. Analysis of nonlinear problems in rock mechanics with particular reference to jointed rock systems. Proc. Second International Congress on Rock Mechanics, Belgrade, 1970.

42. ABAQUS. Abaqus reference manuals, 2005.

43. Bonora N. A nonlinear CDM model for ductile failure. Eng Fract Mech (UK), 1997, 58: 11-28.

44. Brooker DC, Ronalds BF. Prediction of ductile failure in tubular steel members using ABAQUS. International Society of Offshore and Polar Engineers, P.O. Box 189, Cupertino, CA, 95015-0189, USA, 2001.

45. Kuna-Ciska, H, Skrzypek JJ. CDM based modelling of damage and fracture mechanisms in concrete under tension and compression. Eng Fract Mech, 2004; 71: 681-698.

46. Zienkiewicz OC, Hinton E, Biccanic N, Fejzo P. Computational models for the transient dynamic analysis of concrete dams. Dams and Earthquake, Inst. of Civil Engineers, London, 1980.

47. Rashid YR. Ultimate Srength analysis of pre-stressed concrete pressure vessels. Nucl Eng Des, 1968; 7: 334-344.

48. Abdollahi A. Investigation of objectivity in the application of the FEM to RC structures - II. Comput Struct, 1996; 58: 1183-1211.

49. Ali A. FEM analysis of concrete structures subjected to mode-I and mixed-mode loading conditions. Comput Struct, 1996; 61: 1043-1055.

50. Andreev K, Harmuth H. FEM simulation of the thermo-mechanical behaviour and failure of refractories - A case study. J Mater Process Tech, 2003; 143-144(1): 72-77.

51. Chambart M. An anisotropic delay-damage model to simulate reinforced concrete structures in dynamics. Proc of 1st EPFL Doct Conf Mech, 2010; 21-25.

52. Ansys Inc. http://www.ansys.com/, 2008.

53. Wolfel. ATENA Non-linear Simulation of Concrete and Reinforced Concrete. http://www.woelfel.de/wtpeng/atena/atena.hhtml, 2007.

54. Alfaiate J, Pires EB, Martins JAC. A finite element analysis of non-prescribed crack propagation in concrete. Comput Struct, 1997; 63: 17-26.

55. Cho SH, Kaneko K. Influence of the applied pressure waveform on the dynamic fracture processes in rock. Int. J. Rock Mech. & Min.Sci., 2004; 41: 771-784.

56. Cho SH, Ogata Y, Kaneko K. Strain-rate dependency of the dynamic tensile strength of rock. Int. J. Rock Mech. & Min.Sci., 2003; 40: 763-777.

57. Agrawal P, Sun CT. Fracture in metal-ceramic composites. Compos Sci Tech, 2004; 64: 1167-1178.

58. MSC.Software. What's New: Marc 2007 r1. http://www.mscsoftware.com/, 2007.

59. Hillerborg A, Modeer M, Petersson PE. Analysis of crack formation and crack growth in concrete by means of fracture mechanics and finite elements. Cem Concr Res 6, 1976: 773–782.

60. Belytschko T, Chiapetta RL, Bartel HD. Efficient large-scale nonlinear transient analysis by finite-elements. Int. J. Numer. Meth. Engng., 1976; 10: 579-596.

61. Camacho GT, Ortiz M. Computational modelling of impact damage in brittle materials. Int J Solid Struct, 1996; 33: 2899-2938.

62. Molinari JF, Gazonas G, Raghupathy R, Rusinek A, Zhou F. The cohesive element approach to dynamic fragmentation: The question of energy convergence. Int. J. Numer. Meth. Engng, 2007; 69: 484-503.

63. Yang ZJ, Chen J. Finite element modelling of multiple cohesive discrete crack propagation in reinforced concrete beams. Eng Fract Mech, 2005; 72: 2280-2297.
64. Zhou F, Molinari JF. Dynamic crack propagation with cohesive elements: A methodology to address mesh dependency. Int. J. Numer. Meth. Engng, 2004; 59: 1-24.
65. Zhou FH, Molinari JF, Ramesh KT. A cohesive model based fragmentation analysis: effects of strain rate and initial defects distribution. Int J Solid Struct, 2005; 42: 5181-5207.
66. Bocca P, Carpinteri A, Valente S. Size effects in the mixed mode crack propagation: Softening and snap-back analysis. Eng Fract Mech, 1990; 35: 159-170.
67. Bocca P, Carpinteri A, Valente S. Mixed mode fracture of concrete. Int J Solid Struct, 1991; 27: 1139-1153.
68. Molinari JF, Ortiz M. Three-dimensional adaptive meshing by subdivision and edge-collapse in finite-deformation dynamic-plasticity problems with application to adiabatic shear banding. Int. J. Numer. Meth. Engng, 2002; 53: 1101-1126.
69. Wawrzynek PA, Ingraffea AR. An interactive approach to local remeshing around a propagating crack. Finite Elem Anal Des, 1989; 5: 87-96.
70. Arnold DN. Discretization by finite-elements of a model parameter dependent problem. Num Math, 1981; 37: 405-421.
71. Babuska I, Suri M. On locking and robustness in the finite-element method. SINUM, 1992; 29: 1261-1293.
72. Chilton L, Suri M. On the selection of a locking-free hp element for elasticity problems. Int. J. Numer. Meth. Engng, 1997; 40: 2045-2062.
73. Suri M. Analytical and computational assessment of locking in the hp finite element method. Comput Meth Appl Mech Eng, 1996; 133: 347-371.
74. Szabo BA. The P-P and H-P versions of the finite-element method in solid mechanics. Comput Meth Appl Mech Eng, 1990; 80: 185-195.
75. Babuska I, Melenk JM. The partition of unity method. Int. J. Numer. Meth. Engng,1997; 40: 727-758.
76. Shi GH. Manifold method of material analysis. Transactions of the 9th Army Conference on App Math and Comput, U.S. Army Research Office, Minneapolis, MN, 1991; 57-76.
77. Belytschko T, Black T. Elastic crack growth in finite elements with minimal remeshing. Int. J. Numer. Meth. Engng, 1999; 45: 601-620.
78. Strouboulis T, Copps K, Babuska I. The generalized finite element method: an example of its implementation and illustration of its performance. Int. J. Numer. Meth. Engng, 2000; 47: 1401-1417.
79. Terada K, Asal M, Yamagishi M. Finite cover method for linear and non-linear analyses of heterogeneous solids. Int. J. Numer. Meth. Engng, 2003; 58: 1321-1346.
80. Terada K, Ishii T, Kyoya T, Kishino Y. Finite cover method for progressive failure with cohesive zone fracture in heterogeneous solids and structures. Comput Mech., 2007; 39: 191-210.
81. Chiou YJ, Lee YM, Tsay RJ. Mixed mode fracture propagation by manifold method. Int J Fract., 2002; 114: 327-347.
82. Zhao GF, Ma GW, Zhang HH, Zhao J. A numerical manifold method for plane micropolar elasticity, Int. J. Comput. Meth., 2010; 7(1): 151–166.
83. Terada K, Kurumatani M. An integrated procedure for three-dimensional structural analysis with the finite cover method. Int. J. Numer. Meth. Engng, 2005; 63: 2102-2123.
84. Strouboulis T, Zhang L, Babuska I. Generalized finite element method using mesh-based handbooks: application to problems in domains with many voids. Comput Meth Appl Mech Eng, 2003; 192: 3109-3161.
85. Strouboulis T, Zhang L, Babuska I. Assessment of the cost and accuracy of the generalized FEM. Int. J. Numer. Meth. Engng, 2007; 69: 250-283.
86. Prabel B, Combescure A, Gravouil A, Marie S. Level set X-FEM non-matching meshes: application to dynamic crack propagation in elastic-plastic media. Int. J. Numer. Meth. Engng, 2007; 69: 1553-1569.
87. Stolarska M, Chopp DL, Moes N, Belyschko T. Modelling crack growth by level sets in the extended finite element method. Int J Numer Meth Eng., 2001; 51: 943-960.

88. Grégoirea D, Maigrea H, Réthoréa J, Combescure A. Dynamic crack propagation under mixed-mode loading – Comparison between experiments and X-FEM simulations. Int J Solid Struc., 2007; 44: 6517-6534.

89. Pedro MAA, Belytschko T. Analysis of three-dimensional crack initiation and propagation using the extended finite element method. Int J Numer Meth Eng., 2005; 63:760-788.

90. Sukumar N, Chopp DL, Moran B. Extended finite element method and fast marching method for three-dimensional fatigue crack propagation. Eng Fract Mech., 2003; 70: 29-48.

91. Asferg JL, Poulsen PN, Nielsen LO. A consistent partly cracked XFEM element for cohesive crack growth. Int J Numer Meth Eng., 2007; 72: 464-485.

92. Menouillard T, Réthoré J, Combescure A, Bung H. Efficient explicit time stepping for the eXtended Finite Element Method (X-FEM). Int J Numer Meth Eng., 2006; 63: 911-939.

93. Menouillard T, Réthoré J, Moës N, Combescure A, Bung H. Mass lumping strategies for X-FEM explicit dynamics: Application to crack propagation. Int J Numer Meth Eng., 2008; 74: 447-474.

94. Asadpoure A, Mohammadi S, Vafai A. Modeling crack in orthotropic media using a coupled finite element and partition of unity methods. Finite Elem Anal Des, 2006; 42: 1165-1175.

95. Khoei AR, Nikbakht M. An enriched finite element algorithm for numerical computation of contact friction problems. Int J Mech Sci, 2007; 49: 183-199.

96. Ribeaucourt R, Baietto-Dubourg MC, Gravouil A. A new fatigue frictional contact crack propagation model with the coupled X-FEM/LATIN method. Comput Meth Appl Mech Eng, 2007 ; 196: 3230-3247.

97. Fernandez-Mendez S, Huerta A. Imposing essential boundary conditions in mesh-free methods. Comput Meth Appl Mech Eng, 2004; 193: 1257-1275.

98. Markus Peters KH. Numerical aspects of the eXtended Finite Element Method. PAMM., 2005; 5(1):355-356.

99. Stéphane B, Phu VN, Cyrille D, Hung ND, Amor G. An extended finite element library. Int J Numer Meth Eng., 2006; 2:1-33.

100. Monaghan JJ. An Introduction to Sph. Comput Phys Com., 1988; 48: 89-96.

101. Randles PW, Libersky LD. Smoothed particle hydrodynamics: Some recent improvements and applications. Comput Meth Appl Mech Eng, 1996; 139: 375-408.

102. Nayroles B, Touzot G, Villon P. Generalizing the finite element method: Diffuse approximation and diffuse elements. Comput Mech, 1992; 10: 307-318.

103. Belytschko T, Lu Y, Gu L. Element free Galerkin methods. Comput. Mech., 1992 ; 37: 229-256.

104. Belytschko T, Lu YY, Gu L. Element-free Galerkin methods. Int J Numer Meth Eng., 1994; 37: 229-256.

105. Liu WK, Chen Y, Uras RA, Chang CT. Generalized multiple scale reproducing kernel particle methods. Comput Meth Appl Mech Eng., 1996 ; 139: 91-157.

106. Liu WK., Hao W, Chen Y, Jun S, Gosz J. Multiresolution reproducing kernel particle methods. Computational Mechanics, 1997; 20: 295-309.

107. Liszka TJ, Duarte CAM, Tworzydlo WW. hp-Meshless cloud method. Comput Meth Appl Mech Eng, 1996; 139: 263-288.

108. Melenk JM, Babuska I. The partition of unity finite element method: Basic theory and applications. Comput Meth Appl Mech Eng, 1996; 139: 289-314.

109. Onate E, Idelsohn S, Zienkiewicz OC, Taylor RL. A finite point method in computational mechanics: Applications to convective transport and fluid flow. Int. J. Numer. Methods Eng, 1996; 39: 3839-3866.

110. De S, Bathe KJ. The method of finite spheres. Comput Mech, 2000; 25: 329-345.

111. Sukumar N, Moran B, Belytschko T. The natural element method in solid mechanics. Int. J. Numer. Methods Eng., 1998; 43: 839-887.

112. Belytschko T, Krongauz Y, Organ D, Fleming M, Krysl P. Meshless methods: An overview and recent developments. Comput Meth Appl Mech Eng, 1996; 139: 3-47.

113. Belytschko T, Lu YY, Gu, L, Tabbara M. Element-free galerkin methods for static and dynamic fracture. Int J Solid Struct, 1995; 32: 2547-2570.

114. Belytschko T, Krysl P, Krongauz Y. A three-dimensional explicit element-free Galerkin method. Int J Numer Meth Fluid, 1997; 24: 1253-1270.

115. Haussler-Combe U, Korn C. An adaptive approach with the Element-Free-Galerkin method. Comput Meth Appl Mech Eng., 1998; 162: 203-222.

116. Krysl P, Belytschko T. The Element Free Galerkin method for dynamic propagation of arbitrary 3-D cracks. Int. J. Numer. Methods Eng, 1999; 44: 767-800.

117. Rahman S, Rao BN. Probabilistic fracture mechanics by Galerkin meshless methods - part II: reliability analysis. Comput Mech, 2002; 28: 365-374.

118. Randles PW, Libersky LD. Smoothed particle hydrodynamics: Some recent improvements and applications. Comput Meth Appl Mech Eng., 1996; 139: 375-408.

119. Singh IV, Jain PK. Parallel EFG algorithm for heat transfer problems. Adv Eng Software, 2005; 36: 554-560.

120. Muravin B, Turkel E. Multiple crack weight for solution of multiple interacting cracks by meshless numerical methods. Int. J. Numer. Methods Eng, 2006; 67: 1146-1159.

121. Belytschko T, Fleming M. Smoothing, enrichment and contact in the element-free Galerkin method. Comput Struct, 1999; 71: 173-195.

122. Zhang X, Lu MW, Wegner JL. A 2-D meshless model for jointed rock structures. Int. J. Numer. Methods Eng., 2000; 47: 1649-1661.

123. Libersky LD, Petschek AG. Smooth particle hydrodynamics with strength of materials. Lecture notes with physics, 1991, 248-257.

124. Benz W, Asphaug E. Impact simulations with fracture .1. Method and Tests. Icarus, 1994; 107: 98-116.

125. Benz W, Asphaug E. Simulations of brittle solids using smooth particle hydrodynamics. Comp. Phys. Comm., 1995; 87: 253-265.

126. Johnson GR, Stryk RA, Beissel SR. SPH for high velocity impact computations. Comput Meth Appl Mech Eng., 1996; 139: 347-373.

127. Medina DF, Chen JK. Three-dimensional simulations of impact induced damage in composite structures using the parallelized SPH method. Compos Appl Sci Manuf, 2000; 31(8): 853-860.

128. Rabczuk T, Eibl J. Simulation of high velocity concrete fragmentation using SPH/MLSPH. Int. J. Numer. Methods Eng., 2003; 56: 1421-1444.

129. Gray JP, Monaghan JJ. Numerical modelling of stress fields and fracture around magma chambers. J Volcanol Geoth Res., 2004; 135: 259-283.

130. Ma G, Dong A, Li J. Modeling strain rate effect for heterogeneous brittle materials. Transactions of Tianjin University, 2006; 12 (SUPPL): 79-82

131. Dyka CT, Randles PW, Ingel RP. Stress points for tension instability in SPH. Int. J. Numer. Methods Eng., 1997; 40: 2325-2341.

132. Fulk DA, Quinn DW. An analysis of 1-D smoothed particle hydrodynamics kernels. J Comput Phys, 1996; 126: 165-180.

133. Onate E, Perazzo F, Miquel J. A finite point method for elasticity problems. Comput Struct, 2001; 79: 2151-2163.

134. Lee SH, Yoon YC. Meshfree point collocation method for elasticity and crack problems. Int. J. Numer. Methods Eng., 2004; 61: 22-48.

135. Kim HJ, Lee SH, Kim MK. Prediction of crack propagation under dynamic loading conditions by using the enhanced point collocation meshfree method. Key Eng Mater, 2006; 324-325 II: 1059-1062.

136. Perazzo F, Lohner R, Perez-Pozo L. Adaptive methodology for meshless finite point method. Adv Eng Software, 2008; 39: 156-166.

137. Zhao GF, Fang JN, Zhao J, Parriaux A. A double stage finite point method for elasticity problems in heterogeneous materials, Geomech Geoeng., 2010 (submitted).

138. Chappel, BA. The mechanics of blocky material, Australia National University, Canberra, 1972.

139. Cundall, PA. A computer model for simulating progressive, large scale movements in blocky rock systems. Proc. International Symposium on Rock Fracture, Nancy, 1971.

140. Williams JR, Mustoe GGW. Modal methods for the analysis of discrete systems. Comput Geotech, 1987; 4:1-19.

141. McNearny RL, Abel JrJF Large-scale two-dimensional block caving model tests. Int. J. Rock Mech. & Min.Sci., 1993; 30: 93-109.

142. Sofianos AI, Kapenis AP. Numerical evaluation of the response in bending of an underground hard rock Voussoir beam roof. Int. J. Rock Mech. & Min.Sci., 1998; 35(8), 1071-1086.

143. Souley M, Homand F, Thoraval A. The effect of joint constitutive laws on the modelling of an underground excavation and comparison with in situ measurements. Int. J. Rock Mech. & Min.Sci., 1997; 34: 97-115.

144. Jing L, Nordlund E, Stephansson O. A 3-D constitutive model for rock joints with anisotropic friction and stress dependency in shear stiffness. Int. J. Rock Mech. & Min.Sci., 1994; 31: 173-178.

145. Kulatilake PHSW, Liang J, Gao H. Experimental and numerical simulations of jointed rock block strength under uniaxial loading. J Eng Mech ASCE, 2001; 127: 1240-1247.

146.Min KB, Jing LR. Numerical determination of the equivalent elastic compliance tensor for fractured rock masses using the distinct element method. Int. J. Rock Mech. & Min.Sci., 2003; 40: 795-816.

147. Cai JG, Zhao J. Effects of multiple parallel fractures on apparent attenuation of stress waves in rock masses. Int. J. Rock Mech. & Min.Sci., 2000; 37: 661-682.

148. Zhao XB, Zhao J, Hefny AM, Cai JG. Normal transmission of S-wave across parallel fractures with Coulomb slip behavior. J Eng Mech ASCE, 2006; 132: 641-650.

149. Jing L, Tsang CF, Stephansson O. DECOVALEX - an international co-operative research project on mathematical models of coupled THM processes for safety analysis of radioactive waste repositories. Int. J. Rock Mech. & Min.Sci.,1995; 32: 389-398.

150. Gong QM, Zhao J. Influence of rock brittleness on TBM penetration rate in Singapore granite. Tunnel Under Spac Tech, 2007; 22: 317-324.

151. Taylor LM. BLOCKS, A block motion code for geomechanics studies. Sandia National Laboratories, 1983.

152. Cundall PA. Formulation of a three-dimensional distinct element model--Part I. A scheme to detect and represent contacts in a system composed of many polyhedral blocks. Int. J. Rock Mech. & Min.Sci.,1988; 25: 107-116.

153. Hart R, Cundall PA, Lemos J. Formulation of a three-dimensional distinct element model--Part II. Mechanical calculations for motion and interaction of a system composed of many polyhedral blocks. Int. J. Rock Mech. & Min.Sci., 1988; 25: 117-125.

154. Cundall PA, Strack ODL. A discrete numerical model for granular assemblies. Geotech , 1979; 29: 47-65.

155. ITASCA Consulting Group, I. PFC-2D and PFC-3D Manuals, 1995.

156. Taylor LM, Preece DS. Simulation of blasting induced rock motion using spherical element models. Engineering computations, 1992; 9: 243-252.

157. Potyondy DO. Simulating stress corrosion with a bonded-particle model for rock. Int. J. Rock Mech. & Min.Sci., 2007; 44: 677-691.

158.Yoon JS. Application of experimental design and optimization to PFC model calibration in uniaxial compression simulation. Int. J. Rock Mech. & Min.Sci., 2007, 44: 871-889.

159. Hu N, Molinari JF. Shear bands in dense metallic granular materials. Journal of the Mechanics and Physics of Solids, 2004; 52: 499-531.

160. Munjiza A. The combined finite-discrete element method, John Wiley&Sons, Ltd, University of London, 2004.

161. Donze F, Magnier SA. Formulation of a 3-D numerical-model of brittle behavior. Geophys J Int, 1995 ; 122: 790-802.

162. Hentz S, Donze FV, Daudeville L. Discrete element modelling of concrete submitted to dynamic loading at high strain rates. Comput Struct, 2004; 82: 2509-2524.

163. Kemeny J. Time-dependent drift degradation due to the progressive failure of rock bridges along discontinuities. Int. J. Rock Mech. & Min.Sci., 2005; 42: 35-46.

164. Shi GH. Discontinuous deformation analysis, a new numerical model for the statics and dynamics of block systems. PhD thesis, Univ. of California, Berkeley, Berkeley, Calif, 1988.

165. Hatzor YH, Arzi AA, Zaslavsky Y, Shapira A. Dynamic stability analysis of jointed rock slopes using the DDA method: King Herod's Palace, Masada, Israel. Int. J. Rock Mech. & Min.Sci., 2004; 41: 813-832.

166. Hsiung SM, Shi G. Simulation of earthquake effects on underground excavations using Discontinuous Deformation Analysis (DDA). Proc. 38th US Rock Mechanics Symposium, Washington, DC, 2001; 1413-1420.

167. Jiao YY, Zhang XL, Zhao J, Liu QS. Viscous boundary of DDA for modeling stress wave propagation in jointed rock. Int. J. Rock Mech. & Min.Sci., 2007; 44: 1070-1076.
168. Shyu K. Nodal-based discontinuous deformation analysis, PhD thesis. University of California, Berkeley, 1993.
169. Cheng YM. Advancements and improvement in discontinuous deformation analysis. Comput Geotech, 1998; 22: 153-163.
170. Kim YI, Amadei B, Pan E. Modeling the effect of water, excavation sequence and rock reinforcement with discontinuous deformation analysis. Int. J. Rock Mech. & Min.Sci., 1999; 36: 949-970.
171. Jiang QH, Yeung MR. A model of point-to-face contact for three-dimensional discontinuous deformation analysis. Rock Mech Rock Eng, 2004; 37: 95-116.
172. Hsiung SM. Discontinuous deformation analysis (DDA) with n^{th} order polynomial displacement functions. Rock mechanics in the national interest, Swets & Zeitlinger Lisse,2001; 1437–44.
173. Zhang X, Lu MW. Block-interfaces model for non-linear numerical simulations of rock structures. Int. J. Rock Mech. & Min.Sci.,1998; 35: 983-990.
174. Starfield AM, Cundall PA. Towards a methodology for rock mechanics modelling. Int. J, Rock Mech. Min. Sci. & Geomech., 1988; 25: 99-106.
175. Alder BJ, Wainwright TE. Studies in molecular dynamics. I. General Method. J. Chem. Phys, 1959; 31: 459.
176. Dienes GJ, Paskin A. Molecular dynamic simulations of crack-propagation. J Phys Chem Solid, 1987; 48: 1015-1033.
177. Mullins M, Dokainish MA. Simulation of the (001) plane crack in alpha-Iron employing a new boundary scheme. Philos Mag A., 1982; 46: 771-787.
178. Paskin A, Gohar A, Dienes GJ. Computer-simulation of crack-propagation. Phys. Rev., 1980; 44: 940-943.
179. Paskin A, Som DK, Dienes GJ. The dynamic properties of moving cracks. Acta Metallurgica, 1983; 31:1841-1848.
180. Cheung KS, Yip S. Brittle-ductile transition in intrinsic fracture-behavior of crystals. Phys. Rev., 1990; 65: 2804-2807.
181. Kohlhoff S, Gumbsch P, Fischmeister HF. Crack-propagation in bcc crystals studied with a combined finite-element and atomistic model. . Philos Mag A., 1991; 64(4), 851-878.
182. Farkas D, Van Swygenhoven H, Derlet PM. Intergranular fracture in nanocrystalline metals. Phys. Rev. B., 2002; 66: 601011-601014.
183. Hasnaoui A, Van Swygenhoven H, Derlet PM. Dimples on nanocrystalline fracture surfaces as evidence for shear plane formation. Sci, 2003; 300: 1550-1552.
184. Rosch F, Rudhart C, Roth J, Trebin HR, Gumbsch P. Dynamic fracture of icosahedral model quasicrystals: A molecular dynamics study. Phys. Rev. B., 2005; 72(1): 1-9.
185. Abraham FF. Unstable crack motion is predictable. J Mech Phys Solid, 2005; 53(5): 1071-1078.
186. Poschel T, Buchholtz V. Molecular-dynamics of arbitrarily-shaped granular particles. J De Physique I, 1995; 5:1431-1455.
187. Krivtsov AM, Wiercigroch M. Molecular dynamic simulation of mechanical properties for polycrystal materials. Mater Phys Mech, 2001; 3: 45-51.
188. Ichikawa Y, Kawamura K, Uesugi K, Seo YS, Fujii N. Micro- and macrobehavior of granitic rock: observations and viscoelastic homogenization analysis. Comput Meth Appl Mech Eng., 2001; 191: 47-72.
189. Krivtsov A.M. Molecular dynamics simulation of impact fracture in polycrystalline materials. Meccanica, 2003; 38: 61-70.
190. Buehler MJ, van Duin, ACT, Goddard WA. Multiparadigm modeling of dynamical crack propagation in silicon using a reactive force field. Phys. Rev. B., 2006; 96: 1-4.
191. Ostoja-Starzewski M, Sheng PY, Jasiuk I. Damage patterns and constitutive response of random matrix-inclusion composites. Eng Fract Mech 1997; 58(5-6):581-606.
192. Buxton GA, Care CM, Cleaver DJ. A lattice spring model of heterogeneous materials with plasticity. Modell Simul Mater Sci Eng 2001; 9(6):485-97.
193. Hrennikoff A. Solution of problems of elasticity by the framework method. ASME J. Appl. Mech. 1941; 8:A619-A715.

194. Lemieux MA, Breton P, Tremblay AMS. Unified approach to numerical transfer matrix methods for disordered systems: applications to mixed crystals and to elasticity percolation. J. Physique Lett. 1985; 46:1-7.

195. Ray P, Chakrabarti BK. A microscopic approach to the statistical fracture analysis of disordered brittle solids. Solid State Commun. 1985; 53(5):477-479.

196. Sahimi M, Goddard JD. Elastic percolation models for cohesive mechanical failure in heterogeneous systems. Phys. Rev. B 1986; 33:7848-7851.

197. de Arcangelis L, Hansen A, Herrmann HJ, Roux S. Scaling laws in fracture. Phys. Rev. B 1989; 40:877-880.

198. Lilliu G, van Mier JGM. 3D lattice type fracture model for concrete. Eng. Fract. Mech. 2003; 70:927-941.

199. Schlangen E, Garboczi EJ. Fracture simulations of concrete using lattice models: computational aspects. Eng. Fract. Mech. 1997; 57:319-332.

200. Karihaloo BL, Shao PF, Xiao QZ. Lattice modelling of the failure of particle composites. Eng. Fract. Mech. 2003; 70(17):2385-2406.

201. Liu JX, Deng SC, Zhang J, Liang NG. Lattice type of fracture model for concrete. Theor. Appl. Fract. Mech. 2007; 48(3):269-284.

202. Cundall PA, Strack ODL. Discrete numerical model for granular assemblies. Geotechnique 1979; 29(1):47-65.

203. Kawai T. New discrete models and their application to seismic response analysis of structures. Nucl Eng Des 1978; 48(1):207-229.

204. Zubelewicz A, Bažant, ZP. Interface element modeling of fracture in aggregate composites. J Eng Mech 1987; 113(11):1619-1630.

205. Cusatis G, Bažant ZP, Cedolin L. Confinement-shear lattice model for concrete damage in tension and compression: I. Theory. J Eng Mech 2003; 129(12):1439-1448.

206. Potyondy DO, Cundall PA. A bonded-particle model for rock. Int J Rock Mech Min Sci 2004, 41(8):1329-1364.

207. Mustoe GGW. Generalized formulation of the discrete element method. Engineering Computations 1992; 9(2):181-190.

208. Heermann HJ, Kertész J, De Arcangelis L. Fractal shapes of deterministic cracks. Europhys. Lett. 1989; 10:147-152.

209. Curtin WA, Scher H. Mechanics modeling using a spring network. J. Mater. Res. 1990; 5:554-562.

210. Hassold GN, Srolovitz DJ. Brittle fracture in materials with random defects. Phys. Rev. B 1989; 39(13):9273-81.

211. Caldarelli G, Castellano C, Petri A. Criticality in models for fracture in disordered media. Phys Stat Mech Appl., 1999; 270(1):15-20.

212. Parisi A, Caldarelli G. Self-affine properties of fractures in brittle materials. Phys Stat Mech Appl., 2000; 280(1):161-5.

213. Ostoja-Starzewski M, Sheng PY, Alzebdeh K. Spring network models in elasticity and fracture of composites and polycrystals. Computational Materials Science 1996; 7(1-2):82-93.

214. Schwartz LM, Feng S, Thorpe MF, Sen PN. Behavior of depleted elastic networks: Comparison of effective-medium and numerical calculations. Phys. Rev. B 1985; 32(7):4607-17.

215. Babadagli T. Analysis of the displacement in fractal lattices with different number of grids. Fractals, 2005; 13: 207-213.

216. Morris JP, Rubin MB, Block GI, Bonner MP. Simulations of fracture and fragmentation of geologic materials using combined FEM/DEM analysis. Int J Impact Eng, 2006; 33: 463-473.

217. Darve F, Servant G, Laouafa F, Khoa HDV. Failure in geomaterials: continuous and discrete analyses. Comput. Methods Appl. Mech. Engrg. 2004; 193:3057–3085.

218. Lorig LJ, Brady BHG, Cundall PA. Hybrid distinct element-boundary element analysis of jointed rock. Int. J. Rock Mech. & Min.Sci.,1986, 23: 303-312.

219. Wei L, Hudson JA. A hybrid discrete-continuum approach to model hydro-mechanical behaviour of jointed rocks. Eng Geol, 1988; 49: 317-325.

220. Chen SG, Zhao J. A study of UDEC modelling for blast wave propagation in jointed rock masses. Int. J. Rock Mech. & Min.Sci., 1998; 35: 93-99.

221. Pan XD, Reed MB. Coupled distinct element-finite element method for large deformation analysis of rock masses. Int. J. Rock Mech. & Min.Sci., 1991; 28: 93-99.

222. Munjiza A, Owen DRJ, Bicanic N. A combined finite-discrete element method in transient dynamics of fracturing solids. Eng Comput, 1995; 12: 145-174.

223. Karami A. Stead D. Asperity degradation and damage in the direct shear test: A hybrid FEM/DEM approach. Rock Mech Rock Eng, 2008; 41: 229-266.

224. Ariffin AK, Huzni S, Nor MJM, Mohamed NAN. Hybrid finite-discrete element simulation of crack propagation under mixed mode loading condition. Comput Meth Appl Mech Eng., 2006; 195:4579-4593.

225. Li SH, Zhao MH, Wang YN, Wang JG. A continuum-based discrete element method for continuous deformation and failure process. Comput Mech (Abstracts), WCCM VI in conjunction with APCOM’04, Tsinghua University Press & Springer-Verlag, Beijing, China, 2004.

226. Silling SA, Askari E. A meshfree method based on the peridynamic model of solid mechanics. Comput Struct, 2005; 83: 1526-1535.

227. Song HW, Zhao GF. Finite edge element method for united simulation of continuous-discontinuous problems. J of China Univ of Min & Tech, 2008; 37: 15-18 (in chinese).

228. Guidault PA, Allix O, Champaney L, Navarro JP. A two-scale approach with homogenization for the computation of cracked structures. Comput Struct, 2007; 85: 1360-1371.

229. Hettich T, Hund A, Ramm E. Modeling of failure in composites by X-FEM and level sets within a multiscale framework. Comput Meth Appl Mech Eng, 2008; 197: 414-424.

230. Kilburn CRJ. Multiscale fracturing as a key to forecasting volcanic eruptions. J Volcanol Geoth Res, 2003; 125: 271-289.

231. Wu CD, Lin JF. Multiscale particle dynamics in nanoimprint process. Appl Phys Mater Sci Process, 2008; 91(2): 273-279.

232. Sansoz F, Molinari JF. Size and microstructure effects on the mechanical behavior of FCC bicrystals by quasicontinuum method. Thin Solid Films, 2007; 515: 3158-3163.

233. Ma J, Lu H, Wang B, Hornung R, Wissink A, Komanduri R. Multiscale simulation using generalized interpolation material point (GIMP) method and molecular dynamics (MD). CMES, 2006; 14: 101-117.

234. Haidar K, Dube JF, Pijaudier-Cabot G. Modelling crack propagation in concrete structures with a two scale approach. Int J Numer Anal Meth Geomech, 2003; 27: 1187-1205.

235. Guidault PA, Allix O, Champaney L, Navarro JP. A two-scale approach with homogenization for the computation of cracked structures. Comput Struct, 2007; 85: 1360-1371.

236. Stefan Loehnert TB. A multiscale projection method for macro/microcrack simulations. Int. J. Numer. Meth. Engng, 2007; 71:1466-1482.

237. Takano N, Okuno Y. Three-scale finite element analysis of heterogeneous media by asymptotic homogenization and mesh superposition methods. Int J Solid Struct, 2004; 41(15): 4121-4135.

238. Vernerey FJ, Liu WK, Moran B, Olson G. A micromorphic model for the multiple scale failure of heterogeneous materials. J Mech Phys Solid, 2008; 56(4), 1320-1347.

239.Sfantos GK, Aliabadi MH. Multi-scale boundary element modelling of material degradation and fracture. Comput Meth Appl Mech Eng, 2007; 196(7): 1310-1329.

240. Hu C, Bai, J, Ghosh S. Micromechanical and macroscopic models of ductile fracture in particle reinforced metallic materials. Modelling Simul Mater. Sci. Eng., 2007 ; 15: S377–S392.

241. Hou, TY, Wu XH. A multiscale finite element method for elliptic problems in composite materials and porous media. J Comput Phys, 1997; 134(1): 169-189.

242. Abdulle, A., Weinan, E. Finite difference heterogeneous multi-scale method for homogenization problems. J Comput Phys, 2003; 191(1): 18-39.

243. Tadmor EB, Ortiz M, Phillips R. Quasicontinuum analysis of defects in solids. Philo Magaz A., 1996; 73(6): 1529-1563.

244. Sansoz F, Molinari JF. Size and microstructure effects on the mechanical behavior of FCC bicrystals by quasicontinuum method. Thin Solid Films, 2007 ; 515(6): 3158-3163.

245. Miller RE, Tadmor EB, Phillips R, Ortiz M. Quasicontinuum simulation of fracture at the atomic scale. Model Simulat Mater Sci Eng., 1998; 6(5): 607-638.

246. Miller RE, Tadmor EB. Hybrid continuum mechanics and atomistic methods for simulating materials deformation and failure. MRS Bulletin, 2007; 32(11): 920-926.

247. Liu WK, Hao W, Chen Y, Jun S, Gosz J. Multiresolution reproducing kernel particle methods. Comput Mech, 1997; 20(4): 295-309.

248. Han JG, Ren WX, Huang Y. A multivariu-ble wavelet-based finite element method and its application to thick plates. Finite Elem Anal Des, 2005; 41(9-10): 821-833.

249. He YM, Chen XF, Xiang JW, He ZJ. Adaptive multiresolution finite element method based on second generation wavelets. Finite Elem Anal Des, 2007; 43(6-7): 566-579.

250. de Borst R. Challenges in computational materials science: Multiple scales, multi-physics and evolving discontinuities. Computational Materials Science, 2008; 43(1): 1-15.

Chapter 3

A microstructure based constitutive model for modeling elastic continuum

A new micromechanical model is proposed to model the failure of elastic continuum. The continuum is assumed to have an underlying microstructure consisting of discrete particles connected by multi-dimensional internal bonds (normal and shear springs), which has been demonstrated as a useful description for fracture modeling of materials such as rock and concrete. Due to explicit considerations of the microstructure of the material, the proposed micromechanical model has the potential to give more realistic modeling of material failure behaviors than a phenomenological model does. Constitutive relationship of the model is derived from the Cauchy-Born rules and the hyperelastic theory. Relationships between the micromechanical parameters of springs and the macro material elastic constants are derived. They can be used to determine the spring stiffnesses for both discrete simulation and finite element calculation using the micro structural stress-strain relationship. The ability of the micromechanical model to reproduce the linear elastic parameters was verified through several examples. Influence of model size and microstructure are also investigated. It is found that RMIB model can provide a more general description of material than linear elasticity. Furthermore, uniaxial tensile test, hydrostatic compressive test and uniaxial compressive test are simulated by the RMIB model. Relationships between microstructure fracturing parameters and macro mechanical parameters are derived. Failure behavior of RMIB model is studied and the results show that RMIB model satisfies the Tresca criterion. It means that the RMIB model behaves more like metals. The RMIB model also provides microscopic explanation of the Tresca criterion. Due to the limitation of the assumption in RMIB model, it is still not suitable to describe the failure behavior of rock materials.

3.1 Introduction

Most materials (e.g., ceramics, cement, rock, and bone), when viewed at microscopic level, are actually discontinuous and heterogeneous with random defects. The failure of material depends sensitively on the size and spatial distributions of flaws or cracks. It is the result of the break and evolution of micro-structural components under the imposed deformation or load. It is important to consider the microstructure of a material when studying its macroscopic mechanical properties and failure behaviors. Although discrete simulation techniques such as Molecular Dynamics, Discrete Element Method, and Lattice Model can directly represent microstructures at given levels, they are computationally expensive. At present, for large scale engineering problems, conventional continuum mechanics based methods are still commonly adopted. Stress-strain relationships used in these methods have been traditionally derived following a phenomenological approach, without considering the microstructures of material. Differently, the continuum damage mechanics method (CDMM) can comprehensively account for the effect of distributed cracks by defining a damage tensor. However, it is difficult to derive a suitable damage evolution equation since an explicit representation of the microstructure is missing in the framework of CDMM. In recent years, a number of attempts have been made to develop the so-called micromechanical models by explicitly accounting for the micro-discontinuous structures and associating the microstructure properties with the micromechanical properties. The important feature of the micromechanical models is that they can yield numerically macro constitutive laws which are valid for solids with evolving discontinuities and can be directly implemented in the finite element method. The first micromechanical model in this context may be attributed to the pioneer work by Gao and Klein [1], who proposed the virtual internal bond (VIB) model to simulate the crack growth in an isotropic solid. In the VIB model, a continuum element is represented by an equivalent microstructure consisting of random distributed particles connected by atomic-like normal bonds. Based on the Cauchy-Born rules [2, 3], a macro constitutive relationship is derived by integrating the microstructure properties. At the continuous state, VIB corresponds to a linear elastic solid with a fixed Poisson ratio, namely, 0.25 for three-dimensional cases and 0.33 for two-dimensional cases. Later, the VIB was extended to the anisotropic materials by Ganesh et al. [4]. To represent the diversity of the Poisson ratio, Zhang and Ge [5, 6] developed the virtual multi-dimensional internal bond (VMIB) model, in which a shear constraint was added into the interaction between two coupled particles. An idea similar to the VIB is adopted in the Peridynamic model, which was proposed by Silling [7, 8] to solve the crack problem in solid. In the Peridynamic model, two particles are linked through real bonds and the basic equations of continuum mechanics are formulated by integration rather than differentiation. Chang et al. [9, 10] developed a micromechanical model to simulate the fracture behavior of concrete, assuming the continuum has an underlying microstructure of lattice type. Each pair of particles in the lattice network is connected by three types of spring, namely, a normal spring, a shear spring and a rotational spring. The approach used in granular mechanics was adopted to derive the stress-strain relationship. The model will be named as the Lattice Spring (LS) model.

Although different microstructures lead to different macromechanical properties, the above-mentioned models have the following characteristics in common: (i) Materials are discretized into particles which are connected through spring-type forces; (ii) The macromechanical response is derived from the microscopic interactions between particles; (iii) The material failure at the continuous level results naturally from the spring failure at the micro-discontinuous level; (iv) The macro constitutive relationship can be easily implemented into a finite element code. These characteristics make the micromechanical modeling approaches good candidates for numerical simulation of continua based on their microstructures. Nevertheless, each micromechanical model has its limitations, for example, a fixed Poisson ratio for VIB, a constant original bond length for VMIB, and a regular lattice network and a certain arrangement of springs for LS. Moreover, for VIB and VMIB, the bonds are generated randomly without spatial constraints. Therefore, these models are only conceptual rather than physical.

In this chapter, a new micromechanical model is proposed to overcome some of the limitations of the existing micromechanical models. The presented model could give a more realistic and flexible description of materials and represent the diversity of the Poisson ratio. The constitutive relationship and the relationship between micro parameters and material constants are derived and validated through numerical examples. The results show that the proposed model is more general, including VIB and VMIB as special cases. Correspondences between micromechanical strength criteria and continuum strength criteria are studied. Applications of the derived micro-macro relationship for discrete simulation are provided in Chapter 4.

3.2 Constitutive model

3.2.1 Physical microstructure

In both VIB and VMIB, materials are discretized into mass particles linked through randomly distributed bonds. The bond here is a virtual concept rather than a real existence. The springs in the LS model are closer to reality. However, the regular arrangement of particles and the same particle size make this model not suitable for most materials. In this chapter a micromechanical model which takes in advantages of both VMIB and LS model is proposed. The microstructure of the model is shown in Figure 3.1. Spherical particles are distributed randomly in space. The particles are not restricted to the same size. Whenever two particles are detected in contact, they are linked together through bonds between their center points. The multi-dimensional internal bond of VMIB is adopted, that include one normal spring and one shear spring for 3D case and 2D case. Actually polyhedron or another shape of particle is also acceptable in the model, where bond rather than particle is the main object. Although the bonded-particle network does not directly reflect the microstructure of any material, it has been demonstrated as a useful description for fracture modeling of some materials such as rock and concrete. This underlying microscopic picture can be regarded as a "real" geometry model of the material's microstructure. This is the essential difference from VIB and VMIB. Hereafter, the proposed micromechanical model will be denoted as the Real Multi-dimensional Internal Bond (RMIB) model.

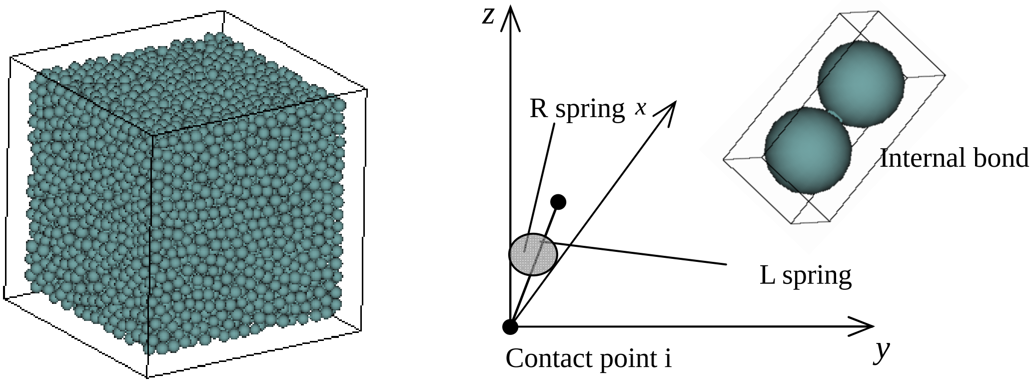

(a) Continuum element

(b) Multi-dimensional internal bond

Figure 3.1. Microstructure of the Real Multi-dimensional Internal Bond (RMIB) model.

3.2.2 Constitutive relationship

As shown in Figure 3.1, the side length of the cubic continuum element is taken as L. Here the cube could be regarded as the representative element volume (REV) [11]. Consider a deformation state ε_{ij} imposed on the cube. As the cube is represented through internal bonds, the energy stored in the continuum element is equal to the sum of energy stored in each bond. As translation operation of bonds will not influence their deformation energy, the distribution of bonds in the cube could be equivalent to a semi sphere distribution as shown in Figure 3.2. Using the spherical coordinate system as shown in Figure 3.3, the strain energy stored in each normal bond can be expressed as

$$U_L = \frac{1}{2} k_n l^2 \left(\xi_i \varepsilon_{ij} \xi_j \right)^2 \tag{3.1}$$

where k_n is the normal stiffness of the bond, l is the original length of the bond and ξ is the direction vector of the bond which is $\left(\sin\theta\cos\phi, \sin\theta\sin\phi, \cos\theta \right)$. In small deformation case strain energy stored in the shear bond can be written as:

$$U_R = \frac{1}{2} k_s u_s^{\,2} \tag{3.2}$$

where u_s is the relative shear displacement of the bond and k_s is the shear stiffness. Based on tensor and vector operation, Equation (3.2) can be further written as

$$U_R = \frac{1}{2} k_s l^2 \left(\varepsilon_{kl} \xi_l - \xi_i \varepsilon_{ij} \xi_j \xi_k \right) \left(\varepsilon_{km} \xi_m - \xi_n \varepsilon_{nm} \xi_m \xi_k \right) \tag{3.3}$$

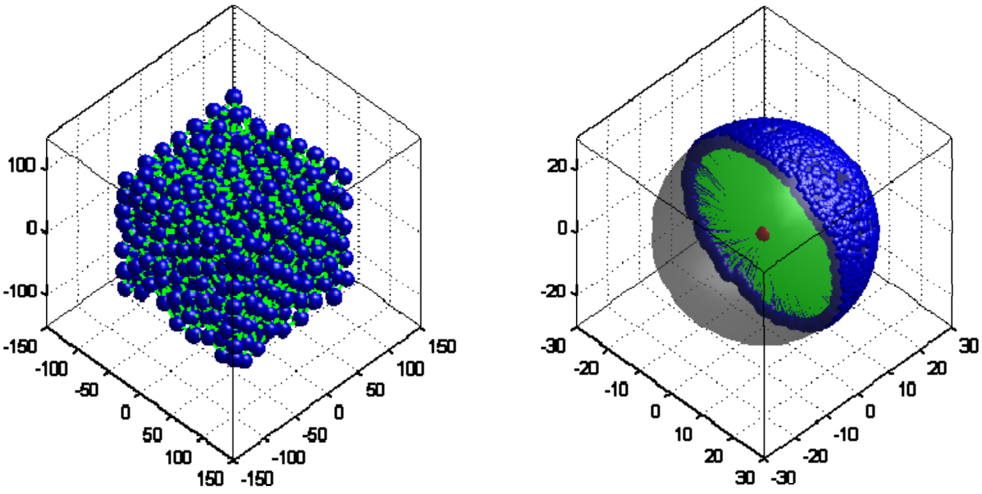

(a) RMIB model (b) Equivalent form

Figure 3.2. The RMIB model and its energy equivalent form.

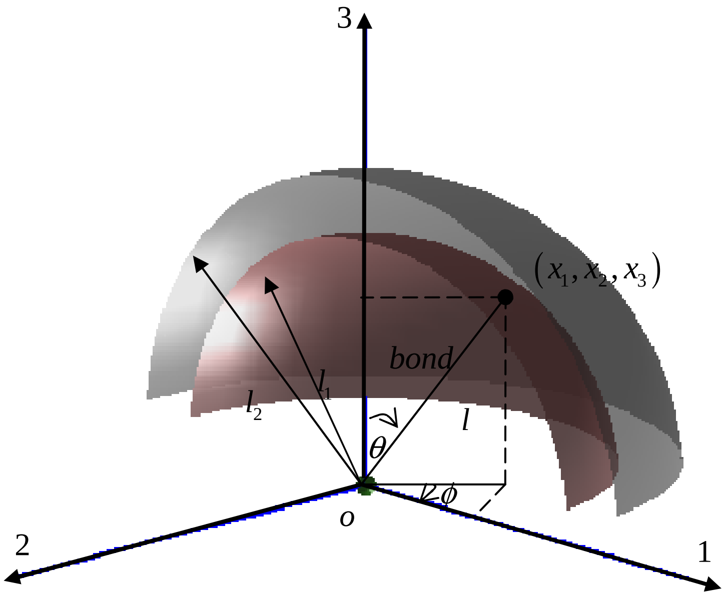

Figure 3.3. Equivalent bond distribution of the RMIB model under the spherical coordinate system.

Then the total energy stored per unit volume is expressed as

$$\Phi = \frac{\sum U_L + \sum U_R}{L^3} \tag{3.4}$$

The stress tensor of the continuum element can be obtained through the Cauchy-Born rule [2, 3] and the hyperelastic theory [12, 13] and it can be written as

$$\sigma_{ij} = \frac{\partial \Phi}{\partial \varepsilon_{ij}} = \sum \frac{l^2 \left(k_n \xi_i \xi_j \xi_n \varepsilon_{nm} \xi_m + k_s \left(\varepsilon_{ik} \xi_k \xi_j - \xi_n \varepsilon_{nm} \xi_m \xi_i \xi_j \right) \right)}{L^3} \tag{3.5}$$

The elastic modulus is expressed as

$$c_{ijnm} = \frac{\partial^2 \Pi}{\partial \varepsilon_{ij} \partial \varepsilon_{nm}} = \sum \frac{l^2 \left(k_n \xi_i \xi_j \xi_n \xi_m + k_s \left(\delta_{in} \xi_j \xi_m - \xi_i \xi_j \xi_n \xi_m \right) \right)}{L^3} \tag{3.6}$$

Equation (3.5) can be served as a numerical constitutive law which describes the macroscopic stress-strain relationship of material through its microstructure information and relatively simple microscopic constitutive law. By using Equation (3.6) the equivalent elastic modulus of the continuum element is obtained directly from its microstructure information.

3.3 Relationship between micro and macro parameters

When the number of multi-dimensional internal bonds in the cube is sufficiently large enough, Equation (3.6) can be written in the integral form as

$$c_{ijnm}=\frac{1}{L^3}\int_{l_1}^{l_2}\int_0^{2\pi}\int_0^{\pi} l^2\left(k_n\xi_i\xi_j\xi_n\xi_m+k_s\left(\delta_{in}\xi_j\xi_m-\xi_i\xi_j\xi_n\xi_m\right)\right)D(l,\theta,\phi)\sin(\theta)d\theta d\phi dl \quad (3.7)$$

where $D(l,\theta,\phi)\sin(\theta)d\theta d\phi dl$ is the number of multi-dimensional internal bonds per REV in the undeformed solid with bond length between $(l,l+dl)$ and bond orientation between $(\theta,\theta+d\theta)$ and $(\phi,\phi+d\phi)$. Different from VMIB, the bond length in RMIB varies within the range $[l_1,l_2]$ and the integration volume in equation (3.7) is a spherical shell with thickness. For the isotropic material, the bonds distribute uniformly in each direction as illustrated in Figure 3.3. The bond distribution function $D(l,\theta,\phi)$ is reduced to $N(l)/2\pi$ with $N(l)dl$ being the number of multi-dimensional internal bonds with length between $(l,l+dl)$ in the continuum element.

In numerical methods, e.g., FEM, the elastic tensor c_{ijnm} is often written in the elastic matrix form as follows:

$$\Omega=\begin{bmatrix} C_{1111} & C_{1122} & C_{1133} & \frac{1}{2}\left(C_{1112}+C_{1121}\right) & \frac{1}{2}\left(C_{1132}+C_{1123}\right) & \frac{1}{2}\left(C_{1113}+C_{1131}\right) \\ C_{2211} & C_{2222} & C_{2233} & \frac{1}{2}\left(C_{2212}+C_{2221}\right) & \frac{1}{2}\left(C_{2232}+C_{2223}\right) & \frac{1}{2}\left(C_{2213}+C_{2231}\right) \\ C_{3311} & C_{3322} & C_{3333} & \frac{1}{2}\left(C_{3312}+C_{3321}\right) & \frac{1}{2}\left(C_{3332}+C_{3323}\right) & \frac{1}{2}\left(C_{3313}+C_{3331}\right) \\ C_{1211} & C_{1222} & C_{1233} & \frac{1}{2}\left(C_{1212}+C_{1221}\right) & \frac{1}{2}\left(C_{1232}+C_{1223}\right) & \frac{1}{2}\left(C_{1213}+C_{1231}\right) \\ C_{2311} & C_{2322} & C_{2333} & \frac{1}{2}\left(C_{2312}+C_{2321}\right) & \frac{1}{2}\left(C_{2332}+C_{2323}\right) & \frac{1}{2}\left(C_{2313}+C_{2331}\right) \\ C_{1311} & C_{1322} & C_{1333} & \frac{1}{2}\left(C_{1312}+C_{1321}\right) & \frac{1}{2}\left(C_{1332}+C_{1323}\right) & \frac{1}{2}\left(C_{1313}+C_{1331}\right) \end{bmatrix} \quad (3.8)$$

For the linear elastic cases, the tangent modulus is equal to the secant modulus and Equation (3.7) can be considered as the secant modulus. So the following relationship exists:

$$\sigma=\Omega\cdot\varepsilon \quad (3.9)$$

where $\sigma=\left[\sigma_{11},\sigma_{22},\sigma_{33},\sqrt{2}\sigma_{12},\sqrt{2}\sigma_{23},\sqrt{2}\sigma_{13}\right]^{\mathrm{T}}$, $\varepsilon=\left[\varepsilon_{11},\varepsilon_{22},\varepsilon_{33},\sqrt{2}\varepsilon_{12},\sqrt{2}\varepsilon_{23},\sqrt{2}\varepsilon_{13}\right]^{\mathrm{T}}$. Here σ_{ij} and ε_{ij} are the components of stress and strain tensor, respectively. By integrating

Equation (3.7) and using Equation (3.8), the corresponding elastic matrix is obtained as:

$$\Omega = \frac{\int_{l_1}^{l_2} l^2 N(l)dl}{15L^3}\begin{bmatrix} 3k_n+2k_s & k_n-k_s & k_n-k_s & 0 & 0 & 0 \\ & 3k_n+k_s & k_n-k_s & 0 & 0 & 0 \\ & & 3k_n+2k_s & 0 & 0 & 0 \\ & & & k_n+1.5k_s & 0 & 0 \\ & \text{symmetry} & & & k_n+1.5k_s & 0 \\ & & & & & k_n+1.5k_s \end{bmatrix} \tag{3.10}$$

Let $\alpha^{3D} = \int_{l_1}^{l_2} l^2 N(l)dl \Big/ L^3$, then the relationship between the micromechanical parameters k_n, k_s and the macro material constants, i.e. the Young's modulus E and the Poisson ratio v can be obtained from Equation (3.10) as follows:

$$k_n = \frac{3E}{\alpha^{3D}(1-2v)},\ k_s = \frac{3(1-4v)E}{\alpha^{3D}(1+v)(1-2v)} \tag{3.11}$$

Here α^{3D} can be regarded as a microstructure geometry coefficient. For the two dimensional problems, Equation (3.7) reduces to

$$c_{ijnm} = \frac{1}{L^2\Delta}\int_{l_1}^{l_2}\int_0^{2\pi} l^2\left(k_n\xi_i\xi_j\xi_n\xi_m + k_s\left(\delta_{in}\xi_j\xi_m - \xi_i\xi_j\xi_n\xi_m\right)\right)D(l,\phi)d\phi dl \qquad (3.12)$$

where Δ is the unit length in the third dimension. For the isotropic material, we have $D(l,\phi) = N(l)/\pi$ and the integration of Equation (3.12) gives

$$\Omega = \frac{\int_{l_1}^{l_2} l^2 N(l)dl}{8L^2\Delta}\begin{bmatrix} 3k_n+2k_s & k_n-2k_s & 0 \\ & 3k_n+2k_s & 0 \\ \text{symmetry} & & k_n+2k_s \end{bmatrix} \tag{3.13}$$

For the plane-stress problems the micro-macro relationship is then obtained as

$$k_n = \frac{2E}{\alpha^{2D}(1-v)},\ k_s = \frac{2(1-3v)E}{\alpha^{2D}(1-v^2)} \tag{3.14}$$

where $\alpha^{2D} = \int_{l_1}^{l_2} l^2 N(l)dl \Big/ L^2\Delta$. In the plain-strain problems the micro-macro relationship is given by

$$k_n = \frac{2E}{\alpha^{2D}(1+v)(1-2v)}, \; k_s = \frac{2(1-4v)E}{\alpha^{2D}(1+v)(1-2v)} \tag{3.15}$$

Given the geometry data of the microstructure, α^{3D} and α^{2D} can be estimated through:

$$\alpha^{3D} = \frac{\sum l_i^2}{L^3} = \frac{\sum l_i^2}{V} \tag{3.16}$$

$$\alpha^{2D} = \frac{\sum l_i^2}{L^2\Delta} = \frac{\sum l_i^2}{A\Delta} \tag{3.17}$$

where l_i is the original length of the ith bond, V and A are the volume and area of the geometry model. From now on, given a microstructure, the micro elastic parameters can be obtained directly from the macro elastic parameters. Reversely, once the state of the micromechanical model is determined, the macro elastic matrix could be obtained directly from Equation (3.12) and used for finite element analysis. In this sense, the RMIB model can be regarded as a numerical constitutive model or a stress calculator, i.e., with the input of strain, stress is calculated from the strain-induced microstructure evolution with simple constitutive law and failure criterion for bonds. It is important to note that the micro-macro relationships, i.e. Equations (3.11), (3.14) and (3.15), can also be used to estimate the spring stiffness of a spring lattice model for discrete simulation. From Equation (3.11), the stiffness of shear spring becomes negative when the Poisson's ratio exceeds 0.25. Given a molecular model as shown in Figure 3.4, where $\Phi_B(u_s)$ is the potential variation at

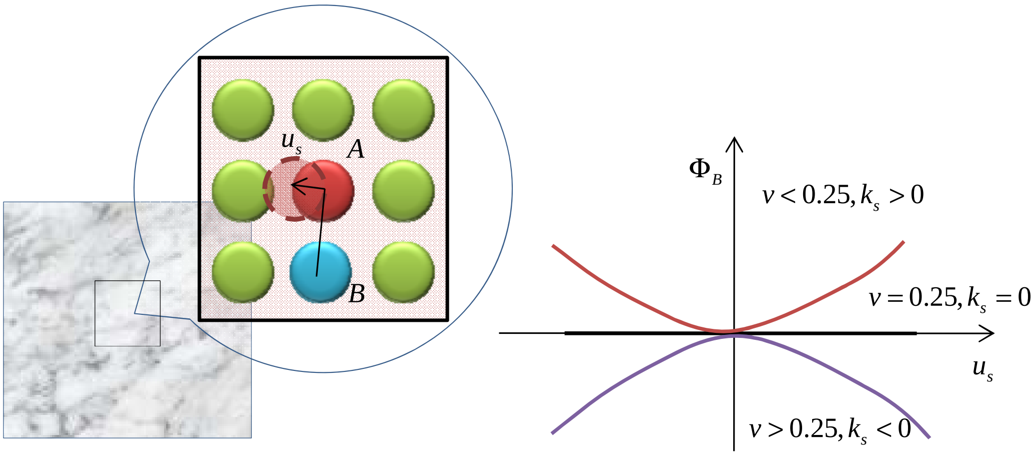

(a) Molecular model of material (b) The potential energy on molecular B *vs* u_s

Figure 3.4. Physical explanation of the shear spring in material.

molecular B versus the displacement of molecular A in the shear direction between A-B. The shape of $\Phi_B\left(u_s\right)$ determines the shear stiffness (see Figure 3.4(b)). When the potential function is a constant, the shear stiffness equals to zero as there is no work needs to do for a displacement. The shear stiffness is positive/negative when the potential function is of an upward/downward bowl shape. Therefore, the proof of negative shear spring can be based on the potential functions used in MD simulation. The proof is given in Appendix A.

3.4 Examples of validation and application

3.4.1 Representation of elastic continuum

The modeled material microstructures were built through computer simulation. Eight models as shown in Figure 3.5 will be analyzed in this section. The elastic matrix is obtained through Equation (3.6) and the micro parameters of the model are obtained through Equations (3.11) and (3.14)-(3.17). This example will show the ability of the RMIB model to represent the elastic material. The precision of RMIB is evaluated using the following indexes:

$$\mathrm{Err}_1=\frac{\left|\Omega_{11}^e-\Omega_{11}^r\right|}{\Omega_{11}^e}\quad,\quad \mathrm{Err}_2=\frac{\left|\Omega_{12}^e-\Omega_{12}^r\right|}{\Omega_{12}^e}\quad \text{and}\quad \mathrm{Err}_3=\frac{\left|\Omega_{33}^e-\Omega_{33}^r\right|}{\Omega_{33}^e} \tag{3.18}$$

where Ω_{ij}^e represent the components of the elastic matrix of classical elasticity and Ω_{ij}^r represent the components of the elastic matrix reconstructed by the RMIB model. These error indexes also measure the ability of the RMIB model to reproduce both the Young's modulus and the Poisson ratio. In this chapter, the elastic constants of RMIB model are taken as: $E=1$ and $\nu=0.2$ unless defined otherwise. The results are given in Table 3.1 for the three-dimensional case (a-d) and the two-dimensional plain-stress case (e-h), with the total number of bonds increasing from (a) to (d) and from (e) to (h). It can be seen that as the total number of bonds increases, the RMIB model gives a more precise description of the elastic properties.

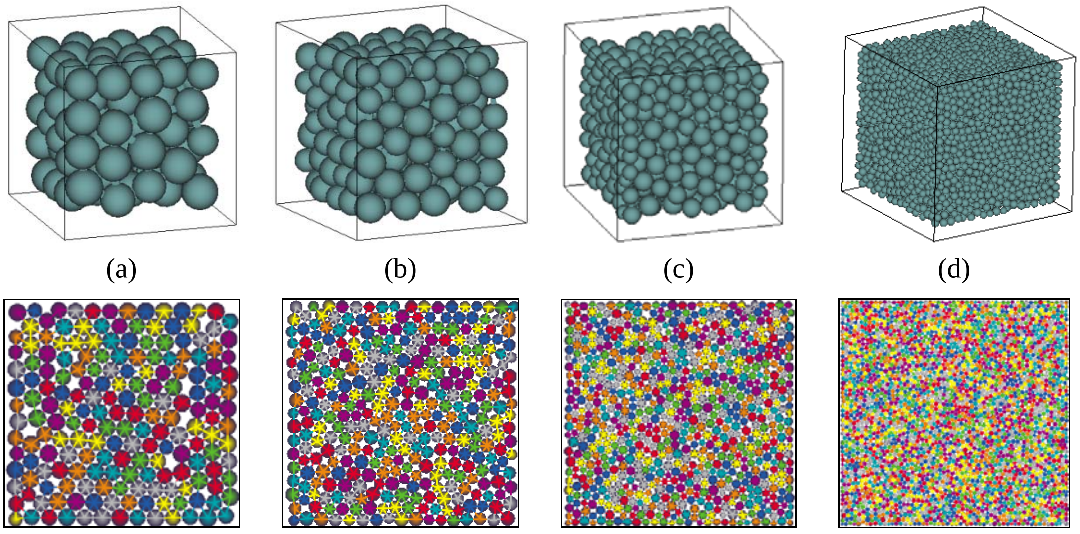
(a) (b) (c) (d)

(e) (f) (g) (h)

Figure 3.5. Different 3D (a-d) and 2D (e-h) RMIB models.

Table 3.1. The micro parameters of the RMIB model with different microstructures and the errors of the RMIB model predictions of the linear elastic properties.

Model	a^{2D}/a^{3D}	k_n	k_s	Err_1 (%)	Err_2 (%)
a	0.0957	52.2272	8.7045	5.85	15.51
b	0.1344	37.1989	6.1998	0.89	5.60
c	0.2028	24.6588	4.1098	2.73	5.66
d	0.5516	9.0647	1.5108	1.48	2.55
e	2.8007	0.8926	0.2975	3.02	5.49
f	2.8512	0.8768	0.2923	4.28	1.74
g	2.9679	0.8424	0.2808	1.56	1.93
h	3.1095	0.8040	0.2680	1.41	1.50

The ability of RMIB model with regular microstructure is further investigated. Different regular RMIB models with different model size (5×5×5, 10×10×10, 15×15×15 and 20×20×20) are analyzed (see Figure 3.6). The corresponding errors of these RMIB models on representing linear elastic material are shown in Figure 3.6. It can be seen that only CubicII RMIB model can predict the correct linear elastic properties. This also means that other microstructure models cannot be correctly described by classical linear elasticity. It is known that the microstructure of elastic material can change under mechanical or chemical reactions. So the linear elasticity may become not applicable for some conditions, while the RMIB model is still applicable. In this sense, the RMIB model also provides a more general mechanical description of material under different states.

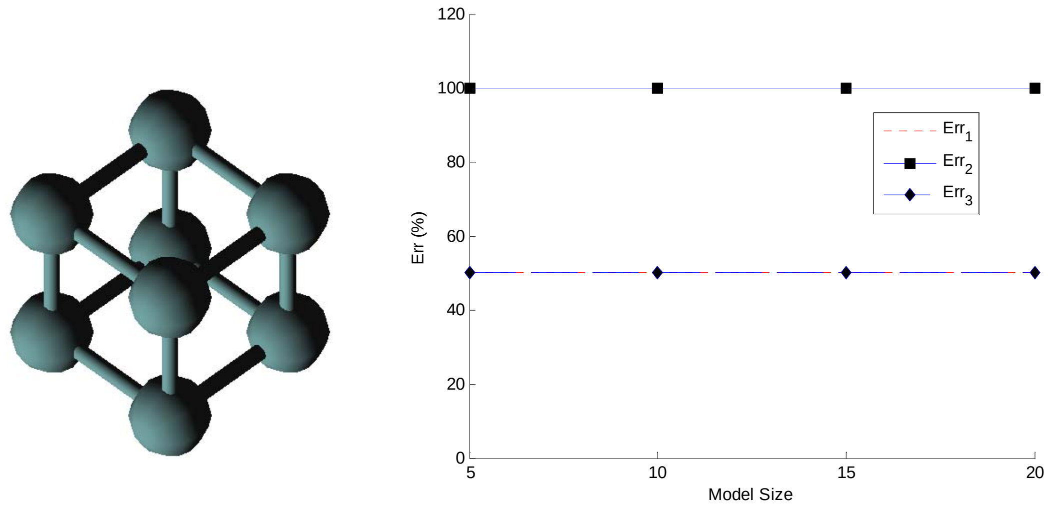

(a) Cubic I structure

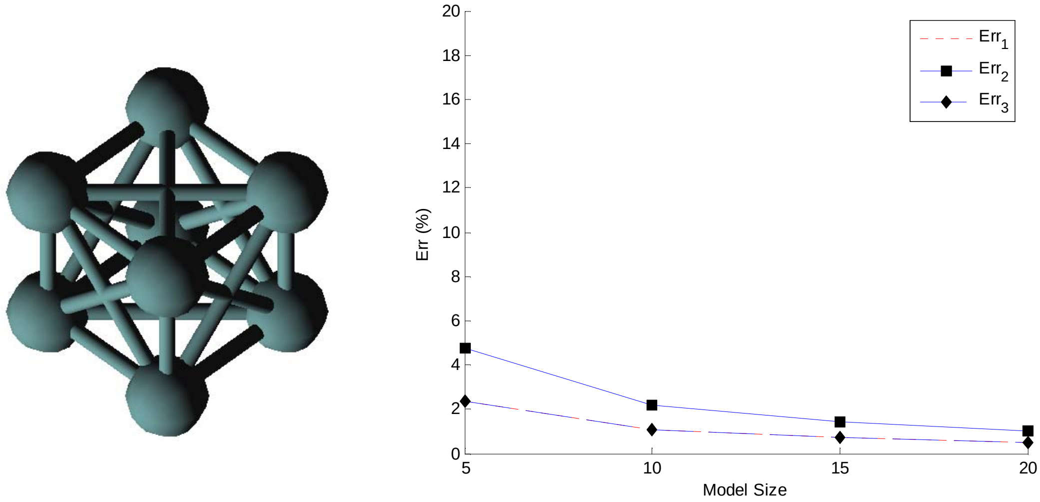

(b) Cubic II structure

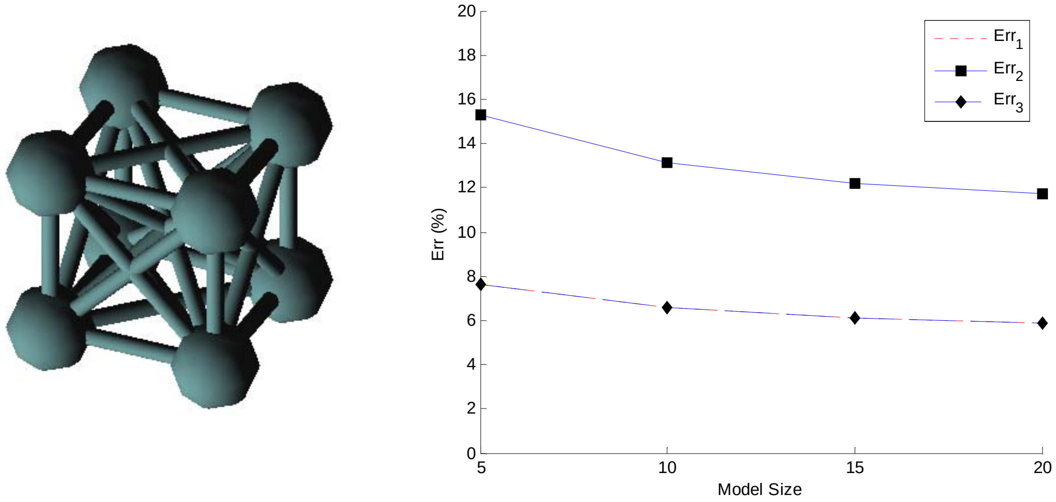

(c) Cubic III structure

Figure 3.6. Different RMIB models of regular microstructure and their errors on representing the linear elastic properties.

3.4.2 Failure behaviour of RMIB model

The failure behaviour of RMIB model is studied in this section. It is assumed that particles of RMIB model are rigid and failure can only happen at the bond between particles (see Figure 3.7(a)). The micro failure criterion of the bond is shown in Figure 3.7(b). The bond will be broken when its normal or shear deformation exceeds the corresponding ultimate value. Force based criteria are not applicable for RMIB model because the shear bond force always equals to zero when the Poisson's ratio is 0.25.

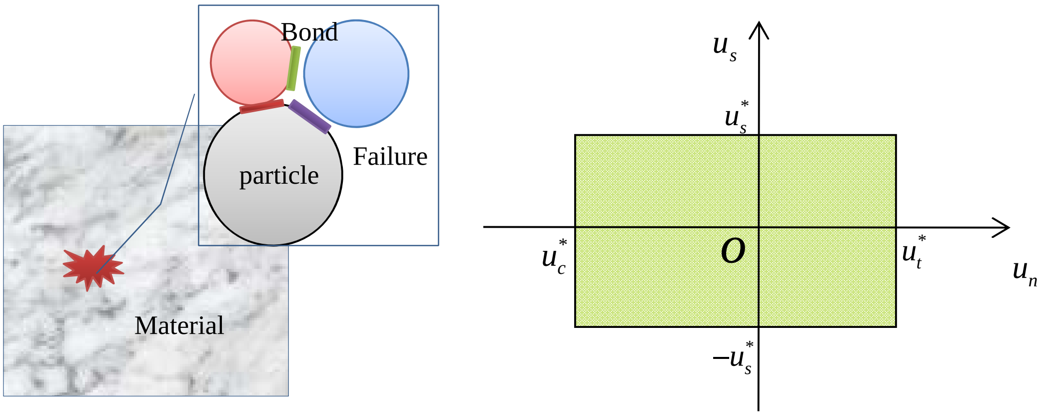

(a) Failure principle of RMIB model (b) Micro criterion

Figure 3.7. Failure principle of RMIB model and its micro failure criterion.

There are three possible failure modes. The first one is tensile failure and occurs when

$$u_n > u_n^* \tag{3.19}$$

where u_n is the normal deformation of the bond and u_n^* is the ultimate tensile deformation. The second mode is compressive failure and happens when

$$-u_n > u_c^* \tag{3.20}$$

where u_c^* is the ultimate compressive deformation of the bond. The last one is shear failure and occurs when

$$|u_s| > u_s^* \tag{3.21}$$

where u_s is the shear deformation of the bond layer and u_s^* is the ultimate shear deformation. The failure process of RMIB model can be simulated by using the following procedure. First, given the initial stress state σ_{ij}^0 and the final stress state σ_{ij}^n, the deformation state of the *i*th step is given as

$$\varepsilon_{ij}^i = \Omega^{-1}\left(\sigma_{ij}^0 + \frac{\left(\sigma_{ij}^0 - \sigma_{ij}^n\right)i}{n}\right) \tag{3.22}$$

After a deformation state ε_{ij} is imposed, the normal and shear deformation for each bond can be calculated. Then, according to Equations (3.19) to (3.21), the status of each bond (failure or not) is obtained. Whenever a bond fails, it is deleted and no longer takes part in the calculation using Equation (3.6). By this way, the elastic matrix changes accordingly as a result of the damage evolution in the microstructure and the stress state of the RMIB model can be obtained through Equation (3.9). Repeating the above calculation from step *1* to step *n*, the strain-stress curve is obtained. Figure 3.8 shows the obtained results for the uniaxial tensile test of different RMIB models. The used micro failure parameters are $u_t^* = 0.001$, $u_c^* = 1$ and $u_s^* = 1$ and control stresses are given as $\sigma_{ij}^0 = (0,0,0,0,0,0)$ and $\sigma_{ij}^n = (E/200,0,0,0,0,0)$. It can be seen that the strain-stress curve of the regular structured RMIB model has two peaks (see Figure 3.8(a)). The first one is the ultimate elastic strength and the second one is the ultimate strength of the model. This kind of strain stress curve is observed in uniaxial tensile test for some metals. It only has one peak for the random structured RMIB model (see Figure 3.8(b)). The variation of the main components of the elastic matrix and the bond broken ratio for these RMIB models during uniaxial tensile test are shown in Figure 3.9. For the regular structured RMIB model, the curves of the variations appear a staircase shape (see Figure 3.9(a)). In contrary, Smooth curves are obtained for the random structured RMIB model (see Figure 3.9(b)). From Figures 3.8 and 3.9, it can be found that the first peak happens when the bonds begin to break. This value is the ultimate elastic strength of the material. Here, it is defined as the macro tensile strength σ_t^{macro}. The strain stress relationship in elasticity is written as

$$\varepsilon_x = \frac{1}{E}\left(\sigma_x - v\left(\sigma_y + \sigma_z\right)\right) \tag{3.23}$$

Then, the relationship between the micro tensile parameter and the macro tensile strength is obtained as

$$u_n^* = \frac{\sigma_t^{macro}}{E} \bar{d} \tag{3.24}$$

where $\bar{d}$ is the mean diameter of the rigid particle in the RMIB model and the ultimate value of ε_x is estimated as $u_n^*/\bar{d}$.

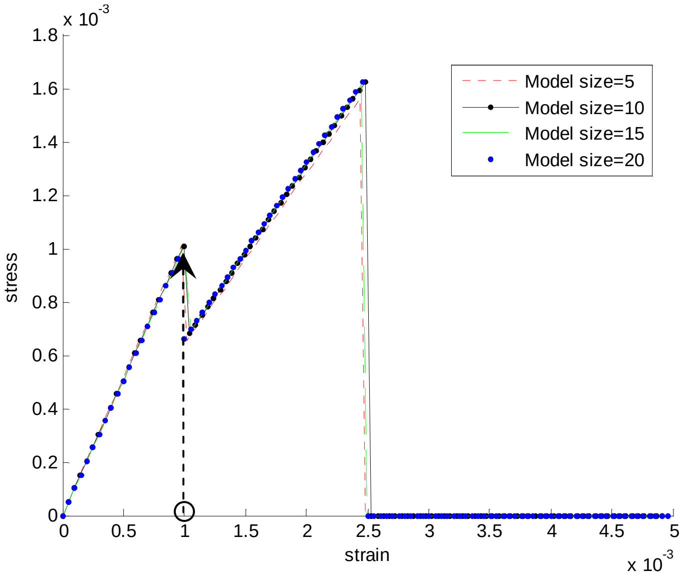

(a) Cubic II

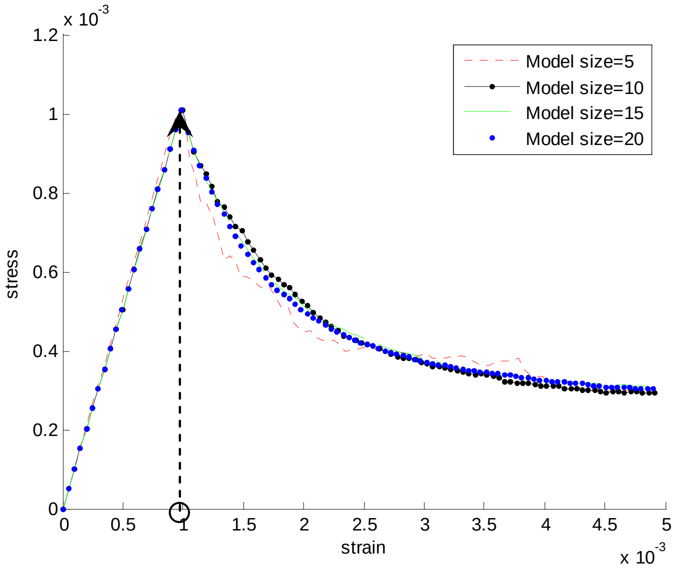

(b) Random structure

Figure 3.8. Results of uniaxial tensile test predicted by RMIB model with different microstructures.

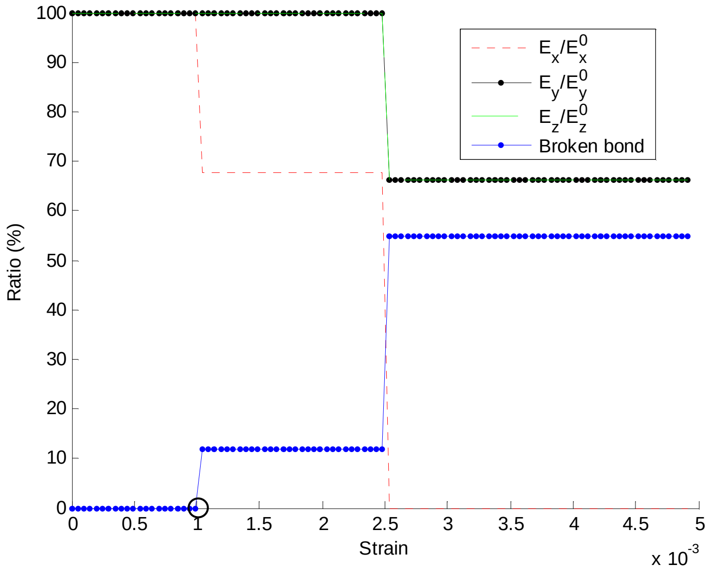

(a) Cubic II

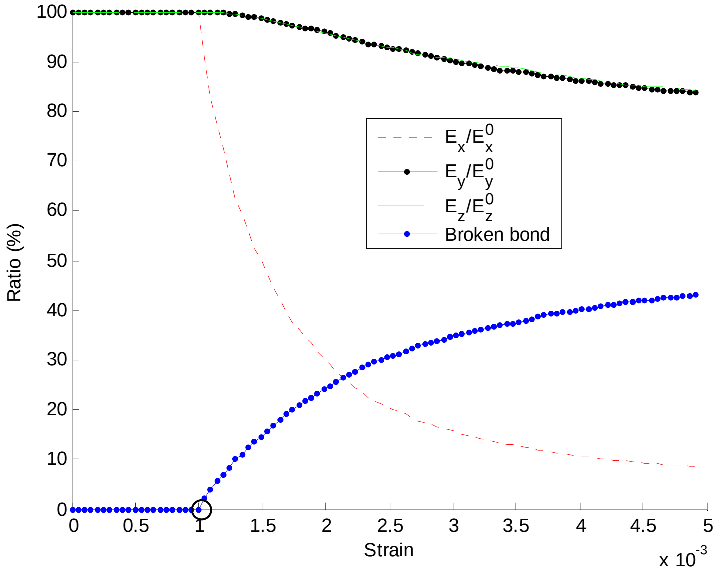

(b) Random structure

Figure 3.9. Variation of the main components of the elastic matrix and the bond broken ratio of RMIB model with different microstructures under uniaxial tensile loading.

The influence of Poisson's ratio on uniaxial tensile failure of RMIB model is given in Figure 3.10. It can be seen that the Poisson's ratio has slight influence on the macro tensile strength. While the post stage of the strain stress curves is obviously influenced by the Poisson's ratio.

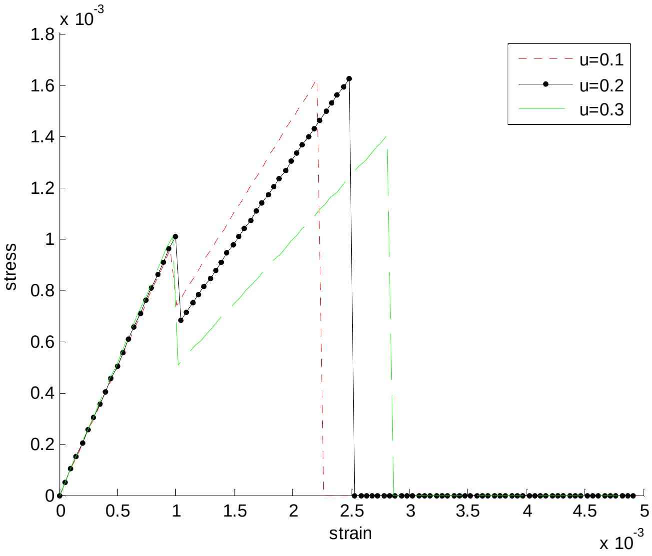

(a) Cubic II

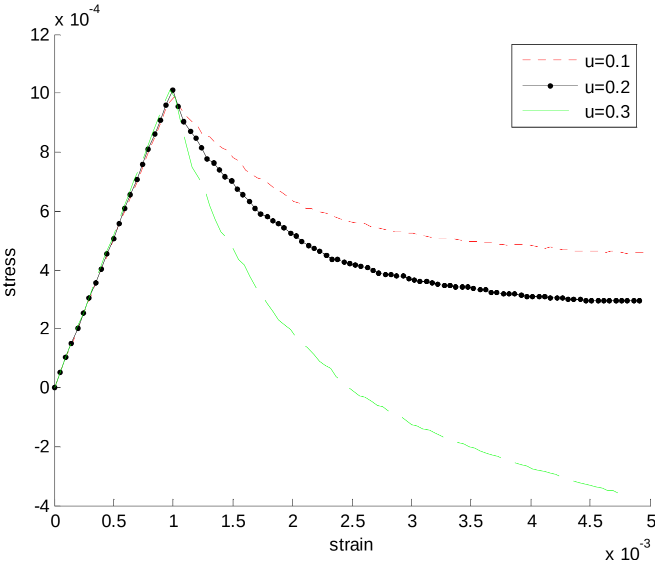

(b) Random structure

Figure 3.10. Influence of the Poisson's ratio on uniaxial tensile failure of RMIB models.

It is known that the hydrostatic compressive strength is infinite for most materials, which means the bond in RMIB model for these cases cannot be broken under compressive deformation. However, some geologic materials can yield under high hydrostatic compressive stress. For this kind of materials, the bond has a micro compressive strength. Figure 3.11 shows the hydrostatic compressive failure process predicted by the RMIB model with the failure parameters given as $u_n^* = 0.001$, $u_c^* = 0.01$ and $u_s^* = 0.001$, 0.01, 0.1 for three different tests respectively.

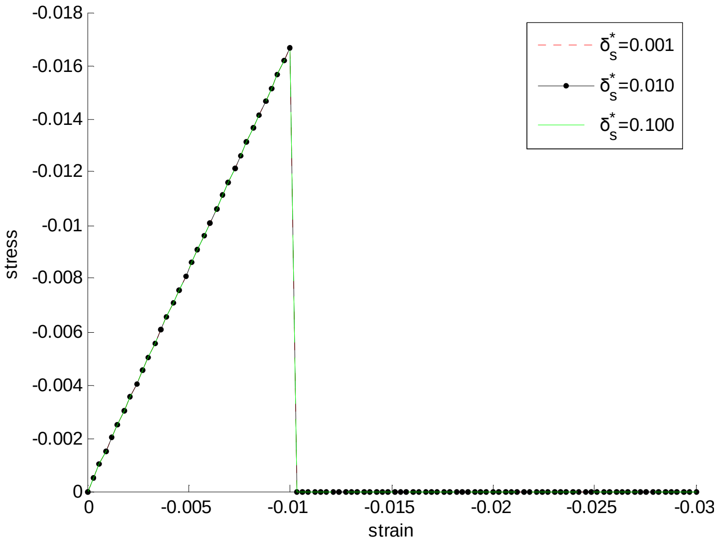

(a) Cubic II

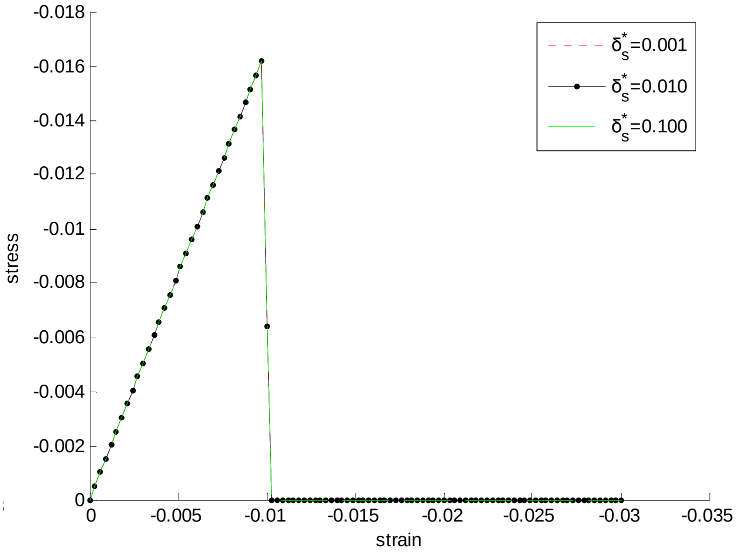

(b) Random structure

Figure 3.11. The hydrostatic compressive failure of RMIB model with different microstructures.

The micro shear failure parameter has no influence on the hydrostatic compressive strength of RMIB model (see Figure 3.11). It means that there exists a one-to-one relationship between the micro compressive failure and the macro hydrostatic compressive failure for the RMIB model. From Equation (3.23), this relationship is derived as

$$u_c^* = \frac{(1-2\nu)\sigma_{hydro}^{macro}}{E}\bar{d} \tag{3.25}$$

where σ_{hydro}^{macro} is the hydrostatic compressive strength of the material. The uniaxial compressive test for the RMIB model only considering the micro tensile failure ($u_n^* = 0.001$) is given in Figure 3.12.

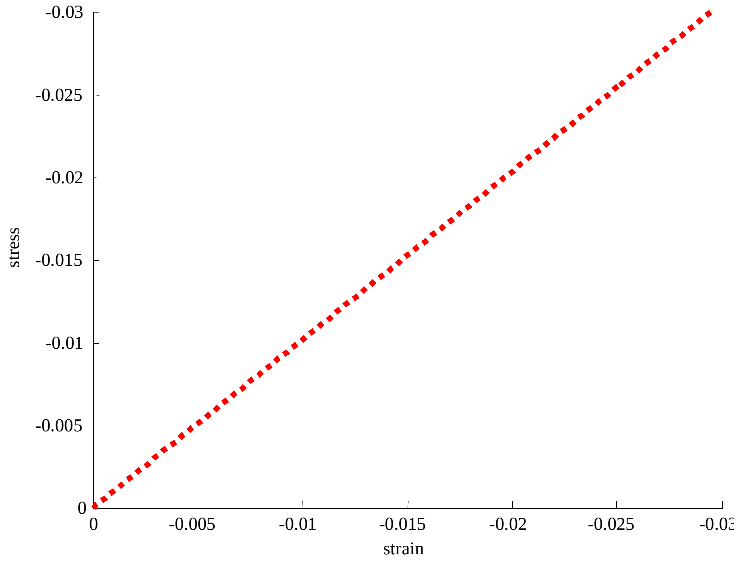

(a) Strain-stress curve

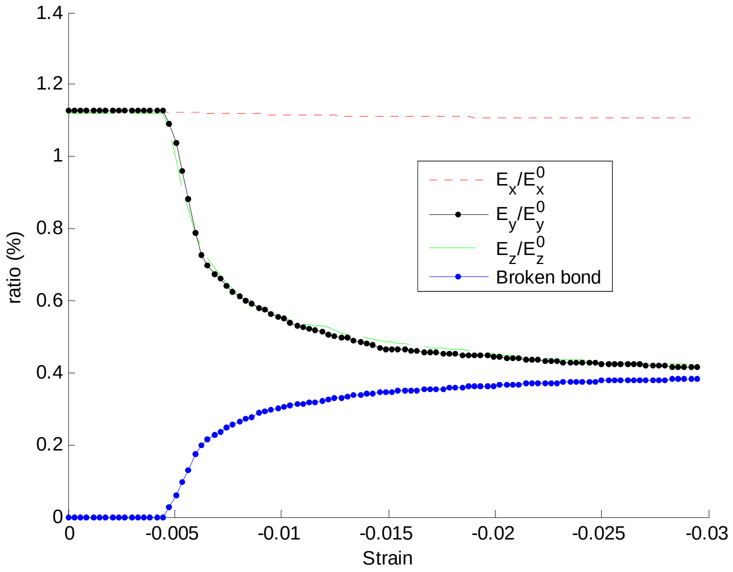

(b) Elastic matrix components and bond broken ratio

Figure 3.12. Uniaxial compressive test on RMIB model only considering the micro tensile failure.

It can be seen that the micro tensile failure cannot induce the uniaxial compressive failure in RMIB model. Due to the fact that the bond cannot be broken under compressive deformation for most materials, the micro shear failure has to be considered for the uniaxial compressive failure. Figure 3.13 shows the results when the micro shear failure of the bond ($u_s^* = 0.006$) is added.

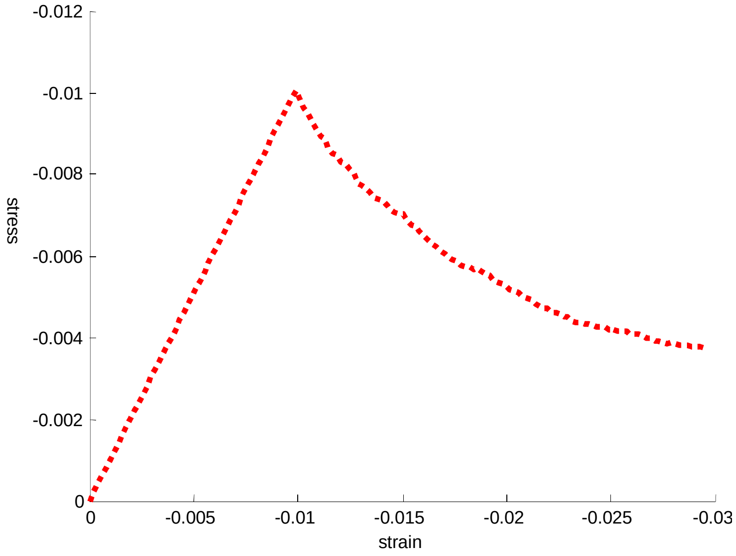

(a) Strain-stress curve

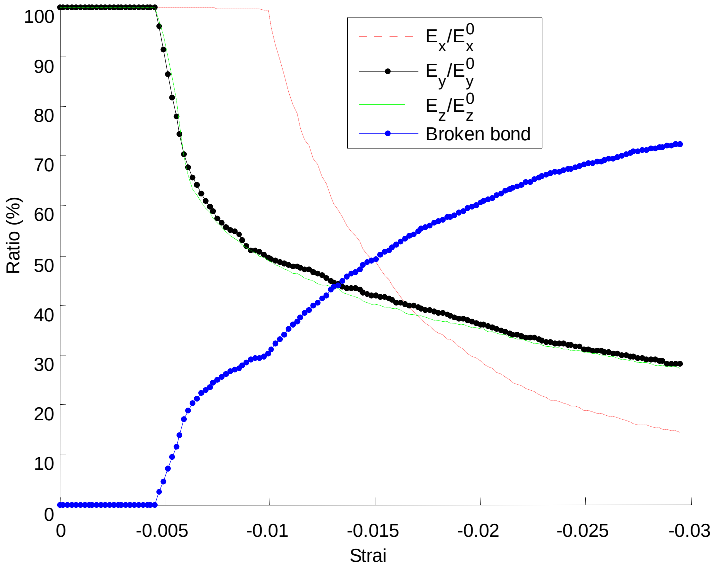

(b) Elastic matrix components and bond broken ratio

Figure 3.13. Uniaxial compressive test on RMIB model considering additionally the micro shear failure.

According to elasticity, the following relationship can be established between the ultimate shear strain and the uniaxial compressive strength as

$$\gamma_{xy}^* = \frac{1+v}{E}\tau_{\max}^{macro} = \frac{1+v}{E}\frac{\sigma_c^{macro}}{2} \tag{3.26}$$

for which $\tau_{\max} = (\sigma_1 - \sigma_3)/2$ is applied. Then, relationship between the micro shear failure parameter and the macro uniaxial compressive strength is obtained as

$$u_s^* = \frac{(1+v)\sigma_c^{macro}}{2E}\bar{d} \tag{3.27}$$

The uniaxial compressive failure can also be induced by the compressive failure of the bond for some materials. Similar to the uniaxial tensile case, we have

$$u_{c'}^* = \frac{\sigma_c^{macro}}{E}\bar{d} \tag{3.28}$$

where $u_{c'}^*$ is the micro compressive failure parameter under the assumption that the uniaxial compressive failure is only caused by the compressive failure of the bond. For the equation (3.27) to be valid, $u_{c'}^*$ must be smaller than u_c^* given by equation (3.25). Comparing the equation (3.28) and the equation (3.25), we obtain

$$\sigma_c^{macro} < (1-2v)\sigma_{hydro}^{macro} \tag{3.29}$$

as the precondition for the equation (3.27). For most materials, e.g., rock and metal, this requirement is satisfied. Acoording to [14], there exist various strength criteria for different materials. For example, the Tresca and Mises criteria are used to describe metals and the Mohr-Coulomb and Hoke-Brown criteria are developed for rock materials. In the following, the strength criteria of RMIB model with random microstructure is obtianed through numerical simulation of triaxial test. The macro tensile strength of the model is given as 0.001E and the ratio of the compressive strength to the tensile strength ranges from 1 to 12. Micro failure paramters are caculated from Equations (3.24) and (3.27). The simulation procedure is the same as that described before around the equation (3.22). The obtianed strength criteria of the RMIB model are shown in Figure 3.14(a). Here σ_3 is obtained from the simulated failure curve and σ_1 changes for different tests. The incline angles of the linear parts of these curves are listed in Table 3.2. For metals, the tensile strength is equal to the compressive strength. For this case, it is found that the reproduced criterion by the RMIB model is very close to the Tresca criterion. In this sense, RMIB provides a microscopic interpretation of the Tresca criterion.

The modeling results in this sectoin show that the RMIB model is suitable for desribing the tensile failure of rock material. However, it is not suitable to model the compressive failure of rock material as the frictional angle of the RMIB model is nearly zero. This may be due to the uniform deformation assumption in the RMIB model.

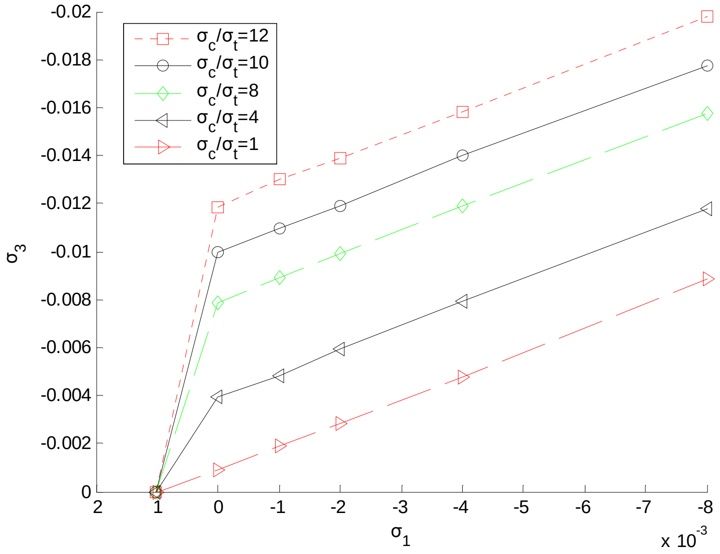

Figure 3.14. Reproduced failure criteria by RMIB models.

Table 3.2. The incline angles in failure curve of RMIB model with different Poisson's ratios.

σ_c^*/σ_t^*		12	10	8	4	1
v	0.1	45.1306	44.0454	44.9564	44.6342	44.5175
	0.2	44.8466	44.3021	44.9991	44.6342	44.5175
	0.3	41.0168	41.5483	42.3037	44.5633	44.5175

3.5 Conclusions

In this chapter, the real multi-dimensional internal bond model (RMIB) has been developed, which is more physically realistic than the existing models of the same function of microstructure-based constitutive modeling. Based on the Cauchy-Born rules, a constitutive relationship is derived, which bridges the micro mechanical parameters and the macro material constants. The RMIB model can represent the diversity of the Poisson's ratio. It can be regarded as a generalized version of the VMIB model. It is found that the linear elastic material can be well represented by RMIB. The relationship between the micro failure parameters in the RMIB model and the macro mechanical failure parameters are derived. Uniaxial tensile test, hydrostatic compressive test and uniaxial compressive test are simulated by using the model. The macro strength criterion obtained by the RMIB model is found to be similar with the Tresca criterion. It means that the RMIB model behaves like metals. It turns out that the RMIB model is not suitable for modeling rock materials due to the limitation of the basic assumption in the model. Further improvements of the model by releasing the limitation will be reported in the following chapters.

3.6 References

1. Gao HJ, Klein P.Numerical simulation of crack growth in an isotropic solid with randomized internal cohesive bond. J Mech Phys Solid, 1998; 46(2): 187–218.
2. Tadmor EB., Ortiz M, Phillips R. Quasicontinuum analysis of defects in solids. Phil Mag A., 1996; 73(6): 1529 –1593.
3. Milstein F. Review: theoretical elastic behavior at large strains. J Mater Sci, 1980; 15:1071–1084.
4. Ganesh T, Misra A. Fracture simulation for anisotropic materials using a virtual internal bond model. Int J Solid Struct, 2004; 41: 2919 –2938.
5. Zhang ZN, Ge XR. A new quasi-continuum constitutive model for crack growth in an isotropic solid. Eur J Mech A Solids, 2005; 24 (2): 243–252.
6. Zhang Z.N, Ge XR. Micromechanical consideration of tensile crack behavior based on virtual internal bond in contrast to cohesive stress. Theor Appl Fract Mech, 2005; 43(3): 342–359.
7. Silling SA. Reformulation of elasticity theory for discontinuities and long-range forces. J Mech Phys Solid, 2000; 48(1): 175-209.
8. Silling SA, Zimmermann M, Abeyaratne R. Deformation of a peridynamic bar. J Elasticity, 2003; 73(1-3): 173-190.
9. Chang CS, Wang TK, Sluys LJ, VanMier JGM. Fracture modelling using a micro-structural mechanics approach-I Theory and formulation. Eng Frac Mech, 2002; 69: 1941–1958.
10. Chang CS, Wang TK, Sluys LJ, VanMier JGM. Fracture modelling using a micro-structural mechanics approach-II. Finite element analysis. Eng Frac Mech, 2002; 69: 1959 –1976.
11. Kanit T, Forest S, Galliet I, Mounoury V, Jeulin D. Determination of the size of the representative volume element for random composites: statistical and numerical approach. Int J Solid Struct, 2003; 40(13-14): 3647-3679.
12. Marsden JE, Hughes TJR. Mathematical foundations of elasticity. Prentice-Hall: Englewood Cliffs, NJ, 1983.
13. Ogden RW. Non-linear elastic deformations. Wiley: New York, 1984.
14. Yu MH. Advances in strength theories for materials under complex stress state in the 20th century. Appl Mech Rev, 2002; 55 (3): 169-218.

Chapter 4

Distinct lattice spring model (DLSM)

A 3D distinct lattice spring model (DLSM) is proposed where an object is discretized into individual particles linked by springs. The presented model is different from the conventional lattice spring models in that a shear spring is introduced to model the multi-body force by evaluating the spring deformation from the local strain rather than the particle displacement. By doing this, the proposed model can represent the diversity of the Poisson's ratio without violating the rotational invariance. The local strain of the spring is calculated through a least square method which makes the model possessing meshless properties. Because of this and explicitly representing the microstructure, DLSM is able to model dynamic fracturing problems and can be used to study the microstructure influences. The material parameters inputted in the model is the conventional material parameters, e.g., the elastic modulus and the Poisson's ratio. Relationships between microscopic spring parameters and macroscopic material constants are derived based on the Cauchy-Born rules and the hyperelastic theory. Numerical examples are presented to show the abilities and properties of DLSM in modeling elastic and dynamic failure problems.

4.1 Introduction

The classical elasticity theory could provide an adequate description of the macroscopic mechanical response of most materials, even though they are actually heterogeneous when viewed at the microscopic level. However, dynamic fracturing of heterogeneous materials such as rock and concrete cannot be modeled realistically without appealing to their microstructures. This requires that a successful numerical method must be capable of considering not only the elastic stage, but also the formulation and evolution of micro discontinuities. Lattice models [1, 2] represent material by a system of discrete units (e.g. particles) interacting via springs, or, more generally, rheological elements. These discrete units are much coarser than the true atomic ones and may represent larger volumes of heterogeneities such as grains or clusters of grains. Lattice models are close relative to the common finite element method (FEM) when dealing with elastic problems. Yet, due to their discrete nature, lattice models are known to be more suitable for complex fracturing simulation. For example, lattice models have been successfully applied to investigate the spatial cooperative effects of crack formation and heterogeneities in elastic-plastic [3] and elastic-brittle [4] systems.

However, for lattice models composed of normal springs transmitting central forces only it is known that the modeled Poisson's ratio approaches, in the limit of an infinite number of particles, a fixed value e.g. 1/4 in three-dimensional cases. This kind of problem has been reported for example in the works of Beale and Strolovitz [5], Srolovitz and Beale [6], Nayfeh and Hefzy [7] and Donze and Magnier [8]. Such restriction is not suitable for many materials. It can be overcome by introducing non-central shear-type interactions between particles. One possible way is to add shear spring between each pair of particles. This approach was applied by Kawai [9] and Zubelewicz and Bažant [10]. It was investigated in greater detail by Griffiths and Mustoe [11] and refined by Cusatis et al. [12]. The addition of shear spring allows these lattice models to model the Poisson's ratio less than 1/4. In addition to the particle displacements, these models also introduce the particle rotations as degrees of freedom, hence can be viewed as discretizations of micropolar continua. Another approach is to replace the normal springs by beams, which yields the so-called lattice beam models (LBMs) [13-16]. LBMs consider not only rotations but also bending deformations. There are arguments on the inclusion of the latter. For example, Cusatis et al. [12] pointed out that the bending of beams is not a characteristic of the physical phenomena in the microstructure. Attempts have also been made to tackle the problem without the cost of introducing rotational degrees of freedom. The models obtained in this way are usually called as lattice spring models (LSMs). Hassold and Srolovitz [17] proposed a method to modify the Poisson's ratio by introducing a harmonic potential for rotation of bonds from their initial orientation. Here bonds denote the connecting elements between particles. A non-central two-body interaction limiting the rotational freedom of bonds is introduced in the Born spring model [18, 19] to allow a broad choice of the Poisson's ratio. Nevertheless, rotational invariance of the models can only be recovered if a three-body interaction is considered. The Kirkwood-Keating spring model [20, 21] introduces angular springs to penalize the angular variations between the contiguous bonds incident onto the same node. Modeling the multi-body interactions by angular springs is not so convenient (the angular terms are nonlinear functions of displacements) and may bring difficulties in the failure modeling. Although the aforementioned approaches relax the restriction, they cannot model Poisson’s ratios greater than 1/4.

In this chapter we propose an alternative 3D dynamic lattice spring model which overcomes the restriction on the Poisson’s ratio while preserving the rotational invariance. The model includes a normal spring and a multi-body shear-type spring for each pair of lattice points (particles). The lattice structure can be either random or regular. It shall be shown that negative shear stiffness can be adopted in the proposed model to allow the full range of the Poisson’s ratio of elastic solid to be modeled. The deformation of the shear springs is evaluated by using the local strain rather than the particle displacement. It shall be proven that this technique makes the model rotationally invariant. The local strain is calculated by a fully meshless approach which avoids meshing or re-meshing in case of fracture simulation. The method of solving system equations is the same as used in DEM developed by Cundall [22]. In view of the multi-body shear spring and the solver used in the model, we name it as Distinct Lattice Spring Model (DLSM). In DLSM, there is no need to form the global stiffness matrix and only a local interaction is considered during calculation. This is very suitable for large scale parallel computing implementation. The context of the chapter is organized as following. Firstly, the proposed model and associated numerical techniques are described. Secondly, the relationship between micro spring stiffness and macro elastic constants is derived. Then, the model is validated through numerical simulation of three elastic problems, one wave propagation problem and two dynamic failure problems. The chapter ends up with some conclusions and remarks.

4.2 Distinct Lattice Spring Model (DLSM)

This section will give the basic conception, formulations and numerical techniques used in the distinct lattice spring model. At the beginning, the physical model and equation of motion of the system and the solution method will be introduced. Then, mathematical formulation of the interactions between particles will be addressed. The multi-body shear spring is introduced in a distinct way using the local strain to evaluate the shear deformation. A least square method is used to obtain the local strain. The damping scheme and time step selection will be discussed in the last part.

4.2.1 Physical model and system equations

In DLSM, material is discretized into mass particles with different sizes. Whenever the gap between two particles is smaller than a given threshold value, the two particles are linked together through a bond between their center points (as shown in Figure 4.1(a)), which consists of normal and shear springs. The threshold value will influence the lattice structure of the model; different threshold values would produce different lattice structures. This will be discussed later. The particles and bonds form a network system representing the material. For this system, its equation of motion can be expressed as

$$[\mathbf{K}]\mathbf{u}+[\mathbf{C}]\dot{\mathbf{u}}+[\mathbf{M}]\ddot{\mathbf{u}}=\mathbf{F}(t) \tag{4.1}$$

where $\mathbf{u}$ represent the vector of particle displacement, $[\mathbf{K}]$ the stiffness matrix, $[\mathbf{M}]$ the diagonal mass matrix, $[\mathbf{C}]$ the damping matrix, $\mathbf{F}(t)$ the vector of external force. Equation (4.1) is solved by using the explicit central finite difference scheme, which was reported by Rougier et al. [23] as the most efficient and robust method among the various explicit integration schemes. The calculation cycle is illustrated in Figure 4.1(b). Given the particle displacements (either prescribed initially or obtained from the previous time step), new contacts and broken bonds are detected. The list of neighboring particles for each particle is updated. Then, contact and spring forces between particles are calculated according to the prescribed force-displacement relations. The particle velocity is advanced individually as

$$\dot{\mathbf{u}}_i^{(t+\Delta t/2)}=\dot{\mathbf{u}}_i^{(t-\Delta t/2)}+\frac{\sum \mathbf{F}_j^{(t)}}{m_p}\Delta t \tag{4.2}$$

where $\dot{\mathbf{u}}_i^{(t+\Delta t/2)}$ is the particle velocity at $t+\Delta t/2$, $\dot{\mathbf{u}}_i^{(t-\Delta t/2)}$ the particle velocity at $t-\Delta t/2$, m_p the particle mass, $\sum \mathbf{F}_j^{(t)}$ the sum of forces acting on the particle i including applied external forces, Δt the time step. Finally, the new displacement of particle is obtained as

$$\mathbf{u}_i^{(t+\Delta t)}=\mathbf{u}_i^{(t)}+\dot{\mathbf{u}}_i^{(t+\Delta t/2)}\Delta t \tag{4.3}$$

where $\mathbf{u}_i^{(t+\Delta t)}$ is the displacement at $t+\Delta t$, $\mathbf{u}_i^{(t)}$ the displacement at t. This central difference scheme is equivalent to the Newton’s second law used in DEM and MD simulations. In the next subsection, the formulation of the interaction forces between particles is described.

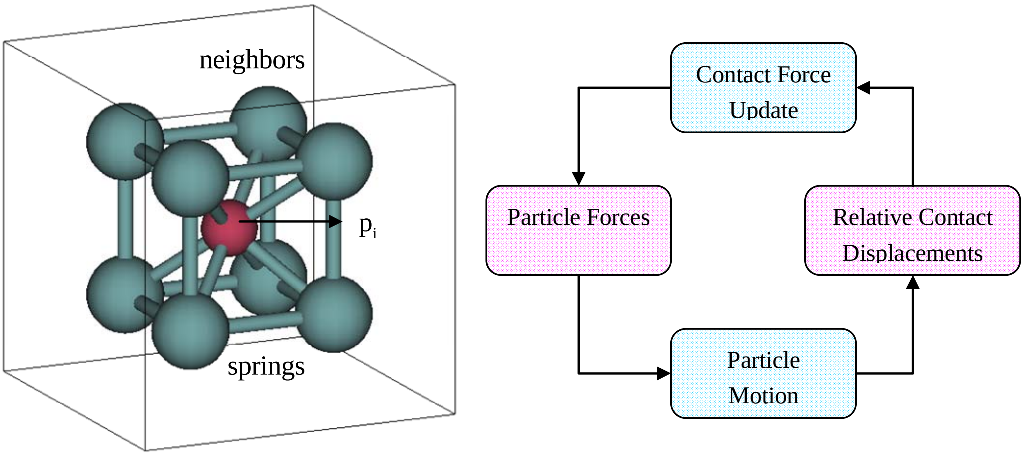

(a) The physical model of DLSM (b) Calculation cycle

Figure 4.1. The physical model and the calculation cycle of DLSM.

4.2.2 Interactions between particles

Figure 4.2(a) shows the forces exerted on one particle. These forces are made up of the external force and contact force between particles. The interaction between linked particles is represented by one normal spring and one shear spring as illustrated in Figure 4.2(b). Different from the conventional LSMs, the shear spring is introduced to model the multi-body non-central interaction and make the model capable of handling problems with a variable choice of the Poisson's ratio. The normal spring is implemented in a conventional way. For a bond connecting particle *i* and particle *j*, the normal unit vector $\mathbf{n}=\left(n_x, n_y, n_z\right)^{\mathrm{T}}$ pointing form particle *i* to particle *j* is defined (see Figure 4.2(c)). The relative displacement is calculated as

$$\mathbf{u}_{ij} = \mathbf{u}_j - \mathbf{u}_i \tag{4.4}$$

The normal force between the two particles is defined as

$$\mathbf{F}_{ij}^n = k_n \mathbf{u}_{ij}^n \tag{4.5}$$

where k_n is the stiffness of the normal spring and $\mathbf{u}_{ij}^n = \left(\mathbf{u}_{ij} \bullet \mathbf{n}\right)\mathbf{n}$ is the vector of normal displacement (see Figure 4.2(c)).

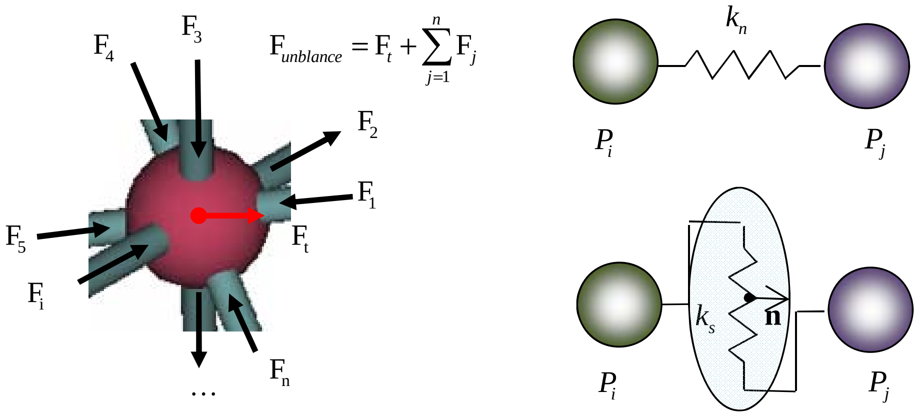

(a) The forces on one particle (b) The normal and shear springs

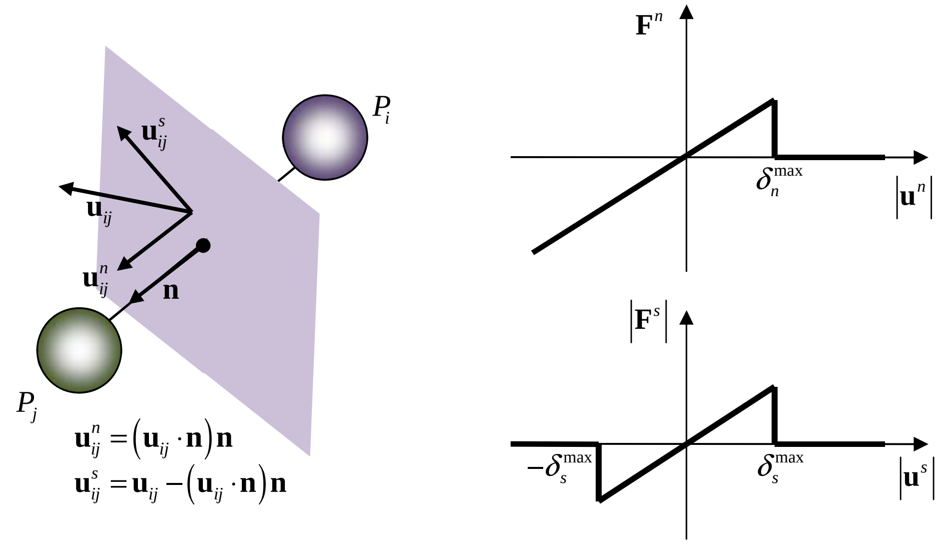

(c) The shear and normal displacement (d) Constitutive laws of lattice springs

Figure 4.2. The force and displacement relationships between two particles and the micro constitutive laws.

For the shear spring, the relative shear displacement between two particles can be obtained simply as $\mathbf{u}_{ij}^{s}=\mathbf{u}_{ij}-\mathbf{u}_{ij}^{n}$ like in some conventional lattice spring models. However, it is straightforward to show that the shearing force calculated in this way is not rotationally invariant. To overcome the problem, we propose a local strain based method. Assuming the strain at the two particles is evaluated as $[\boldsymbol{\varepsilon}]_i$ and $[\boldsymbol{\varepsilon}]_j$ respectively, the strain state of the connecting bond is given as the average of the two particle strains:

$$[\boldsymbol{\varepsilon}]_{bond} = \frac{[\boldsymbol{\varepsilon}]_i + [\boldsymbol{\varepsilon}]_j}{2} \tag{4.6}$$

where $[\boldsymbol{\varepsilon}]=\begin{bmatrix}\varepsilon_{xx} & \varepsilon_{xy} & \varepsilon_{xz}\\ \varepsilon_{yx} & \varepsilon_{yy} & \varepsilon_{yz}\\ \varepsilon_{zx} & \varepsilon_{zy} & \varepsilon_{zz}\end{bmatrix}$. The shear displacement vector is obtained as

$$\hat{\mathbf{u}}_{ij}^{s}=[\boldsymbol{\varepsilon}]_{bond}\cdot\mathbf{n}l\text{-}\Big(\big([\boldsymbol{\varepsilon}]_{bond}\cdot\mathbf{n}l\big)\cdot\mathbf{n}\Big)\mathbf{n} \qquad (4.7)$$

where l is the initial bond length, i.e. the initial distance between the pair of particles. Then the shearing force between the two particles reads

$$\mathbf{F}_{ij}^{s}=k_s\hat{\mathbf{u}}_{ij}^{s} \qquad (4.8)$$

where k_s is the stiffness of the shear spring. The proposed method here together with the strain calculation procedure described in the next subsection ensures that the model preserves the rotational invariance of LSM consisting of normal springs only. A proof of this is given in Appendix B.

Equation (4.5) and Equation (4.8) are valid for unbroken bonds. The failure criterion used in DLSM is shown in Figure 4.2(d). When the normal or shear displacement of the bond exceeds the prescribed value, the bond is broken and becomes a contact bond for which only a normal spring with zero strength is applied. At current stage, only a simple fracture criterion is adopted and more comprehensive study on the fracture criteria is needed. The proposed model has only two spring parameters and two failure parameters. Hence it is suitable for microscopic modeling as the less input parameters the easier to observe and study the microstructure influence on the mechanical response of materials.

4.2.3 Least square method for obtaining the local strain

In DLSM, the local strain of one particle is evaluated by a least square scheme which only uses the displacement of itself and other particles which have intact bonds with the particle. By doing so, discontinuities (e.g. fracture/crack) could be directly considered without using the “visibility criterion” adopted by most meshless methods. First, assume the displacement function within a small volume (cloud) around the particle can be approximated as a linear function

$$f\left(x,y,z\right)=ax+by+cz+d \qquad (4.9)$$

Given the displacement of all the particles in the cloud, the coefficients of Equation (4.9) can be estimated by using the least square method. Taking the *x*-component of ***u*** as an example, it is achieved by minimizing the quadratic equation

$$J = \sum_{j=1}^{n} \left(u_{jx} - \hat{u}_{jx} \right)^2 \tag{4.10}$$

where n is the number of particles in the cloud, u_{jx} is the *x*-component of ***u*** at particle *j* and $\hat{u}_{jx}$ is its corresponding approximated value which is given as

$$\hat{u}_{jx} = ax_j + by_j + cz_j + d \tag{4.11}$$

The coefficients are obtained as

$$\boldsymbol{\alpha} = \begin{pmatrix} a & b & c & d \end{pmatrix}^T = \left(\mathbf{A}^T \mathbf{A} \right)^{-1} \left(\mathbf{A}^T \boldsymbol{\beta} \right) \tag{4.12}$$

where

$$\mathbf{A} = \begin{bmatrix} x_1 & y_1 & z_1 & 1 \\ x_2 & y_2 & z_2 & 1 \\ \vdots & \vdots & \vdots & \vdots \\ x_n & y_n & z_n & 1 \end{bmatrix} \text{ and } \boldsymbol{\beta} = \begin{bmatrix} u_{1x} \\ u_{2x} \\ \vdots \\ u_{nx} \end{bmatrix} \tag{4.13}$$

Using this approach, the approximated displacement field in the cloud is obtained as linear functions, of which first-order derivatives yield the strain, e.g., $\varepsilon_{xx} = \frac{\partial u_x}{\partial x} = a$.

The least square method used in DLSM makes the model fully meshless and the inverse matrix of $A^T A$ (4×4) can be calculated very fast. In a practical simulation, the inverse of $A^T A$ may not exist in some conditions. In this case shear spring will not be considered anymore for the relevant particles. Since the least square approximation is first-order consistent, it can be proven that the calculated strain is independent of rotational displacement (see Appendix A).

4.2.4 Damping and time step

The solution scheme used in DLSM is conditionally stable. To keep the computation stable, the time step could be chosen according to the requirement that it is less than the time needed for elastic wave propagation through the smallest element of the model. This leads to

$$\Delta t_{\mathrm{n}} = \min\left(\frac{l_i}{C_p}\right) \tag{4.14}$$

where C_p is the P-wave velocity of the model, l_i is the ith spring length of the model. The P-wave velocity of the model can be obtained through

$$C_p = \sqrt{\frac{K + 4G/3}{\rho}} \tag{4.15}$$

where ρ is the density, K and G are the bulk and shear elastic modules of the model which have relationship with the elastic module E and the Poisson's ratio ν as following

$$K = \frac{E}{3(1-2\nu)} \tag{4.16}$$

$$G = \frac{E}{2(1+\nu)} \tag{4.17}$$

It should be mentioned that the input parameters of DLSM are macroscopic elastic parameters rather than microscopic spring parameters. This makes the DLSM modeling consistent with the conventional FEM modeling. The relationship between macroscopic elastic parameters and microscopic spring parameters will be introduced in the next section.

Mechanical damping is used in DLSM to obtain static solutions. For static analysis, the approach is conceptually similar to dynamic relaxation proposed by Otter et al. [24]. The equations of motion are damped to reach a force equilibrium state as quickly as possible under the applied initial and boundary conditions. A local damping scheme, which is used in the DEM to overcome the difficulties of the velocity-proportional damping, is adopted in DLSM. When the local damping is incorporated, the equation of motion, Equation (4.2), is replaced by the following equation:

$$\dot{\mathbf{u}}_i^{(t+\Delta t/2)} = \dot{\mathbf{u}}_i^{(t-\Delta t/2)} + \left\{\sum \mathbf{F}_i^{(t)} - \alpha \left|\sum \mathbf{F}_i^{(t)}\right| \operatorname{sgn}\left(\dot{\mathbf{u}}_i^{(t-\Delta t/2)}\right)\right\} \frac{\Delta t}{m_p} \tag{4.18}$$

where α is the damping constant (set to 0.8 in DLSM) which is dimensionless and independent of mechanical properties and boundary conditions. This type of damping is equivalent to a local form of adaptive damping. By using this damping scheme, the damping forces vanish for steady-state conditions. The local damping is reported to be under-damped in general. For the dynamic case, DLSM switches off the damping term (α=0). As a microscopic based model, it is regarded the dynamic effect of spring bond can be neglected. The inertia effect, which reported by Li et al. [25] as the main influence of experimental observation, can be automatically considered as the Newton's second law is used in DLSM.

4.3 Relationship between spring parameters and elastic constants

In DLSM model, the inputted elastic parameters are the macro material constants, i.e. the Young's modulus E and the Poisson ratio ν, in order to keep consistent with classical FEM. During calculation, the micromechanical parameters are automatically calculated based on the RMIB theory in Chapter 3. Considering the material heterogeneity, Equation (3.15) is rewritten into following form:

$$k_n = \frac{3}{2\alpha^{3D}}\left(\frac{E_i}{1-2v_i}+\frac{E_j}{1-2v_j}\right) \tag{4.19}$$

$$k_s = \frac{3}{2\alpha^{3D}}\left(\frac{(1-4v_i)E_i}{(1+v_i)(1-2v_i)}+\frac{(1-4v_j)E_j}{(1+v_j)(1-2v_j)}\right) \tag{4.20}$$

where E_i and E_j are the Young's modulus assigned to the linked particles, and ν_i and ν_j are the corresponding Poisson ratios. The α^{3D} is the microstructure geometry coefficient of the lattice model, which can be directly obtained from Equation (3.16). As the least square scheme is used in DLSM, the model can be viewed as a totally meshless method. There is not integration domain needed and the model only needs a collection of points. In this sense, the DLSM can also be regarded as a new meshless method where the PDEs are approximated through lattice model.

4.4 Numerical Examples

4.4.1 Simple cube under pure tensile loading

In this section the pure tensile loading of a cubic cell with a length of 10mm is simulated. The purpose is to study the influence of lattice structure on the mechanical response. The model setup and three different particle distributions are shown in Figure 4.3(a). The first one is the simple cubic model for which particle arrangement is shown in Figure 4.3(b). The simple cubic structure is one of the most common crystal structures. The second one is the body-centered cubic (BCC) model. The third one is the random distributed model which is generated by the PFC3D code of Itasca Consulting group and the details of this generation method were described in [26]. The lattice structure is formed according to the threshold value of particle gap. Different threshold values would lead to different lattice structures. Figure 4.4 shows the structures of the three particle models.

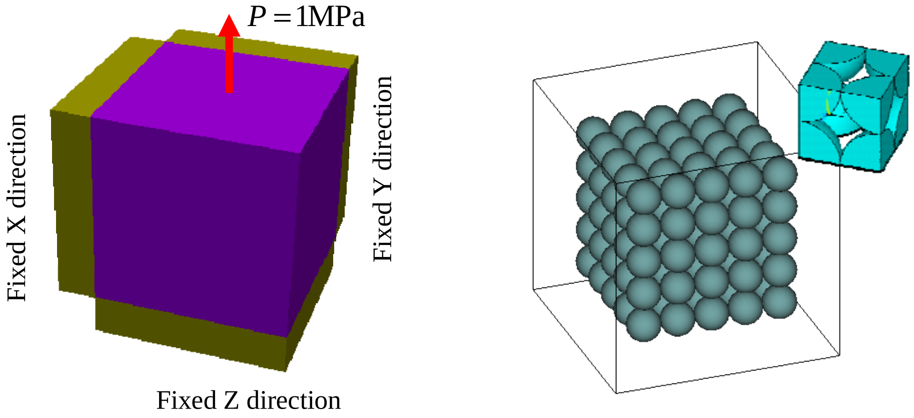

(a) 1/8 part of the specimen

(b) Simple cubic structure

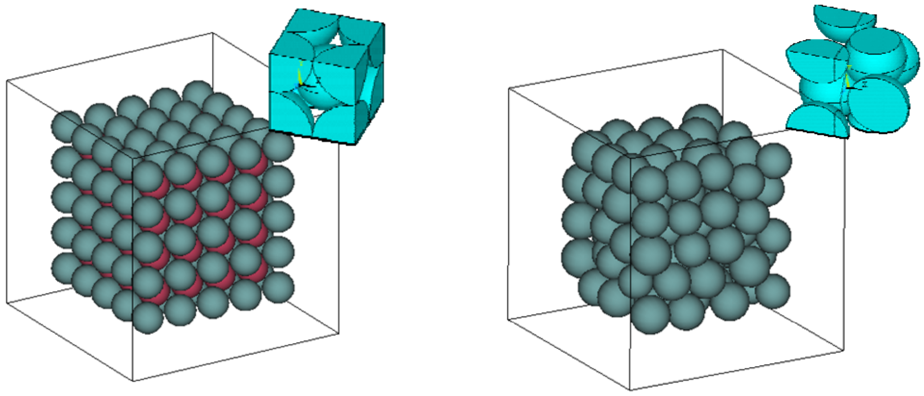

(c) Body centered structure

(d) Random structure

Figure 4.3. The 1/8 part of the cubic cell under uniaxial tensile loading and different microstructures.

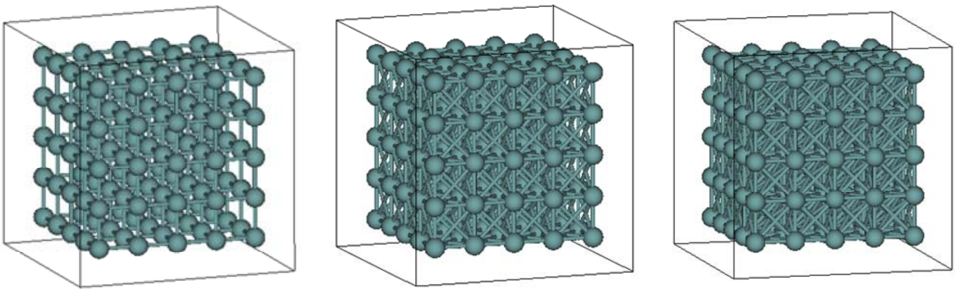

(a) Cubic I (b) Cubic II (c) Cubic III

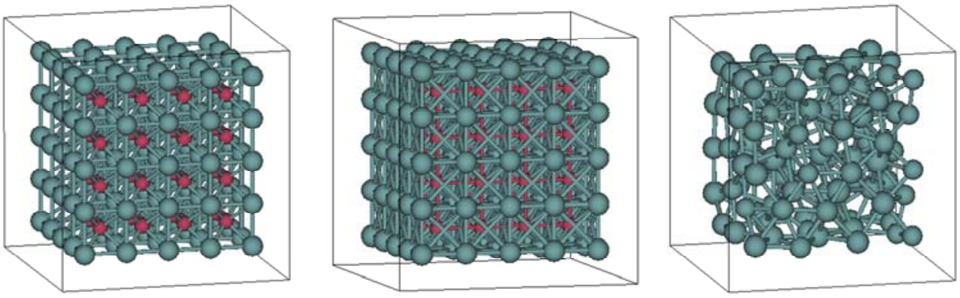

(d) BCC I (e) BCC II (f) Random structure

Figure 4.4. Different lattice structures created by using different interaction ranges.

For the simple cubic case, there are three types of structure: cubic I (shown in Figure 4.4(a)), cubic II (shown in Figure 4.4(b)) and cubic III (shown in Figure 4.4(c)). For the BCC model, two types of structure are considered, the first one is BCC I (shown in Figure 4.4(d)) and the second one is BCC II (shown in Figure 4.4(e)). For the random structure, only one case is studied (see Figure 4.4(f)). The number of particles is 125 in the simple cubic model, 189 in the BCC model and 100 in the random model. Simulations are performed to study the microstructure influence on the mechanical response of the lattice model. All the models are calculated for different Poisson's ratios ranging from 0.2 to 0.3 and a fixed elastic modulus 10GPa. The time step is selected according to Equation (4.14). The simulation results show that this time step selection criterion is correct. For obtaining a static solution, the local damping scheme is used.

The Equation (4.20) indicates that a shear spring of negative stiffness would occur when the Poisson's ratio is greater than 1/4. The negative spring seems non-physical, but for DLSM, shear spring is introduced in a way to model the multi-body interactions, so negative stiffness may result from a structural effect of the high Poisson's ratio material. In reality, materials with negative stiffness are also reported and used for extreme damping in composite materials [27]. From previous simulations, it is shown that the lattice model is convergent for most of the lattice structures except for the cubic I case. Figure 4.5 shows the kinetic energy varying with the iteration steps during the calculation using the cubic I model. For the stable case ($\nu \leq 1/4$), the model will reach a static equilibrium state and the kinetic energy of the model will be zero as shown in Figure 4.5(a). While for the unstable case the kinetic energy increases to a divergent state and the model collapses as shown in Figure 4.5(b).

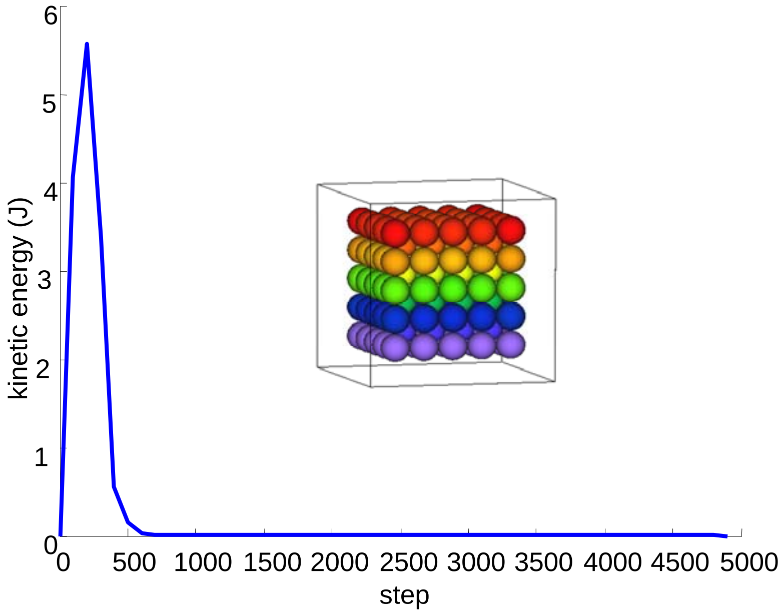

(a) The stable case

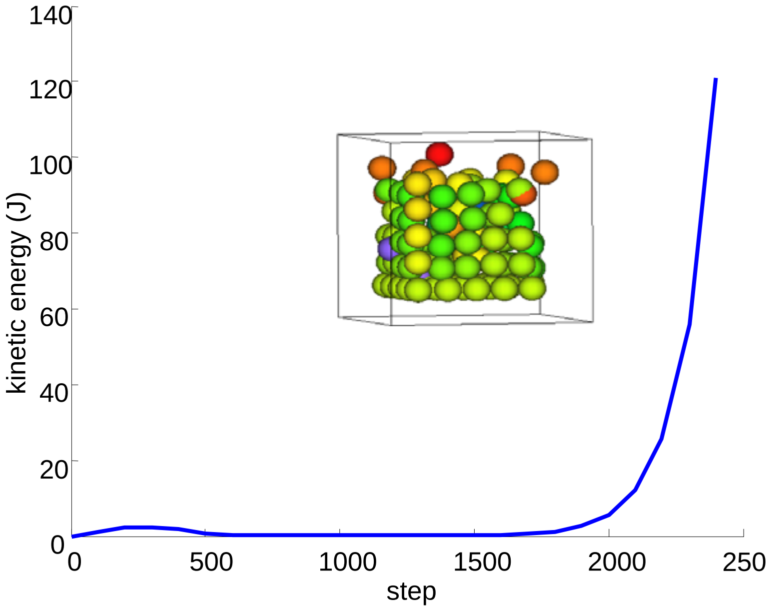

(b) The unstable case

Figure 4.5. The stable and unstable case of DLSM for simulating tensile loading of a simple cube.

Table 4.1 lists the simulation results of different models with different Poisson's ratios. Results shown are the z-direction displacement of the center particle in the top surface. Since the particle is a sphere with a radius of 1mm and the boundary force (P=1MPa) is applied on the centre of the sphere, the effective length is $H_e = 8\text{mm}$ (the sample length minus twice of the radius). So the expected value for the z-direction displacement is $H_e P/E$ =0.0008mm for all cases. From the results we can see that the cubic I and cubic III are not good for the simulation of isotropic elasticity. Because the first one is unstable for the Poisson's ratio greater than 1/4 and the second one cannot reflect well the correct Poisson's effect (the displacement is too sensitive to the change of the Poisson's ratio). We see that the predicted displacements of the measured particle have relative errors of about 20% for each case. This is due to a small number of particles being used. Our purpose in this section is not to compare the elasticity solution with the lattice model but to study the structure influence on the mechanical behavior of the proposed lattice model. In the following section a more complex problem will be simulated.

Table 4.1. The *z*-direction displacement predicted by different microstructure models with different Poisson's ratios for the simple cube problem.

	u_z (mm)	Poisson's ratio		
		0.2	0.25	0.30
Models	cubic I	0.00038	0.00032	- (unstable)
	cubic II	0.00058	0.00058	0.00057
	cubic III	0.00072	0.00086	0.00120
	BCC I	0.00057	0.00058	0.00058
	BCC II	0.00060	0.00062	0.00065
	Rand	0.00070	0.00073	0.00078

*The expected value is 0.0008mm for all the cases.

4.4.2 Beam subjected to bending

The previous example shows that the lattice structure has great influence on the simulation results. It is found that the Cubic I lattice structure is not stable and cannot be used to model the elasticity correctly. In this section, a problem with more complex loading conditions is simulated using a large number of particles to further check whether DLSM could reproduce the elasticity correctly. Another purpose of this example is to screen out the most proper lattice structures. Figure 4.6 gives the geometry information, boundary conditions and material parameters. The left end of the beam is fixed and the right end is subjected to a shearing force of 1MPa. The beam will undergo a complex stress condition, i.e. tensile, compressive and shear stress would appear. Figure 4.7(a) shows the FEM model and the DLSM model of different structures.

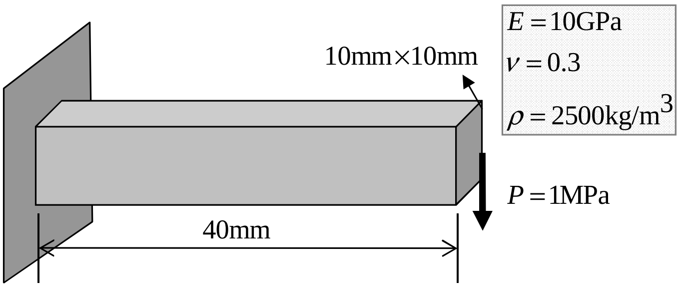

Figure 4.6. The boundary conditions and material parameters for the beam bending problem.

The resolution of the FEM model is $10\times10\times40$ using 4000 evenly distributed 8-node elements. The lattice model has 4000 particles in case of regular structure and 4965 particles in case of random structure. Figure 4.7 shows the simulation results of FEM and DLSM. It is found that the lattice model could reproduce the same displacement distribution as the FEM model. This means the lattice model can be regarded as a valid representation of isotropic elastic material. Quantitative comparison is given in Figure 4.8, where the y-direction displacements of the middle line of the beam predicted by FEM and DLSM are shown. The results of the lattice model with cubic II, BCC I, BCC II and random structure have a good agreement with the FEM solution. However, the model with cubic III structure does not yield satisfactory results. This implies that the cubic III structure does not correspond to an elastic material. Comparing with the first example, the number of particles plays a very important role in the lattice spring model for accurate modeling of the isotropic elasticity and the relative error here is reduced to 5%. It is important to point out that the simulations have been performed with Poisson’s ratio of 0.3, i.e. negative shear springs being used. All of these models are convergent and correct solutions are obtained as demonstrated by the results presented in Figure 4.8. From the above studies, it can be concluded that the Cubic II structure is the most suitable lattice structure in terms of accuracy and efficiency. This structure is much easier to be generated (compared with the random one) and contains a smaller total number of particles for the same model resolution (defined by the number of divisions in each dimension) compared with the BCC structures. As the contour map cannot give a quantitative comparison between DLSM and FEM results, two section lines, Line I

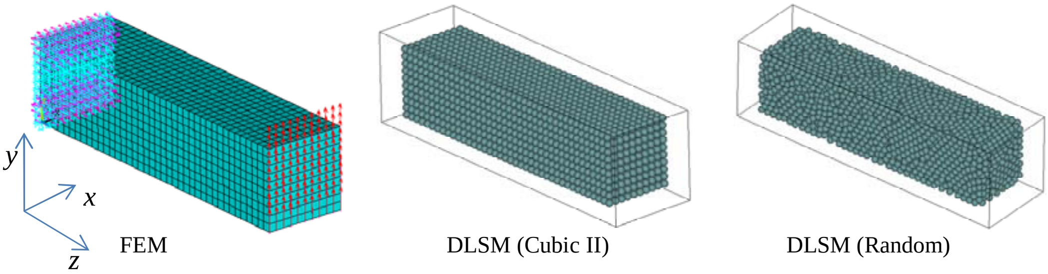

FEM DLSM (Cubic II) DLSM (Random)

(a) The numerical models

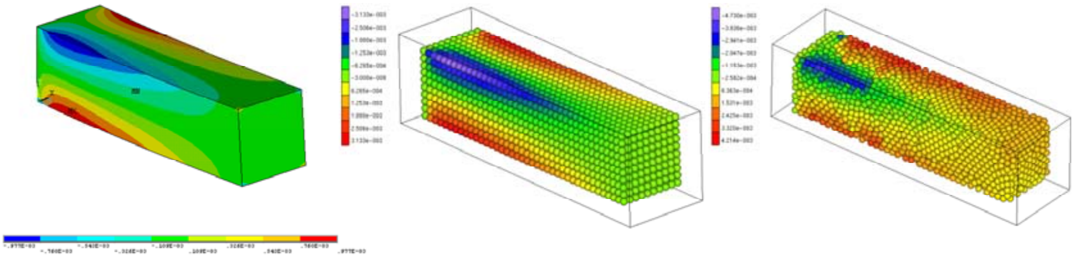

FEM DLSM (Cubic II) DLSM (Random)

(b) The z-direction displacement

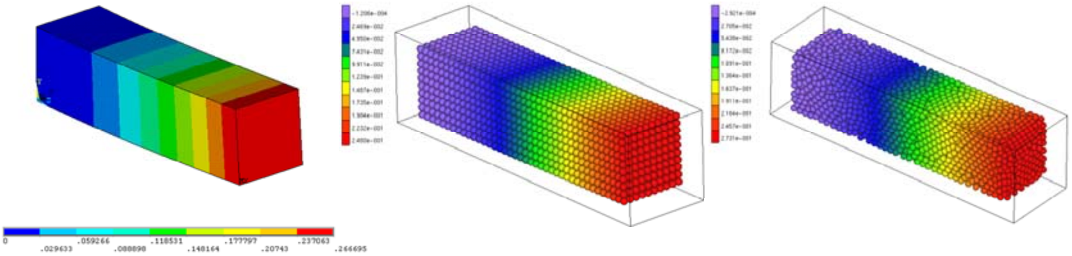

FEM DLSM (Cubic II) DLSM (Random)

(c) The y-direction displacement

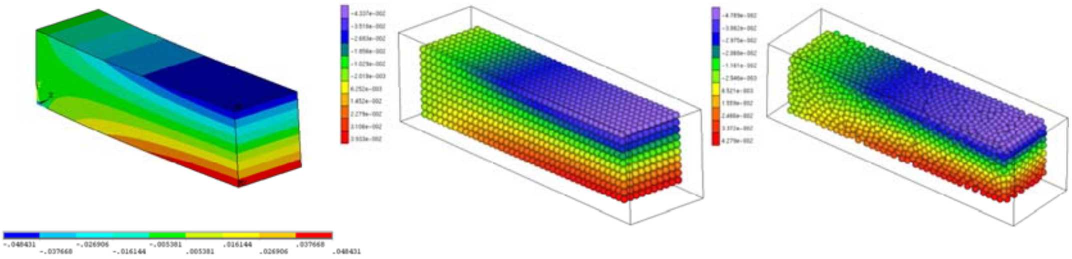

FEM DLSM (Cubic II) DLSM (Random)

(d) The x-direction displacement

Figure 4.7. Numerical models and contour plot of the displacement results predicted by FEM and DLSM for the beam bending problem with Poisson’s ratio of 0.2.

((0.125,2.125,2.125)-(39.125,2.125,2.125)) and Line II ((0.125,8.125,8.125)-(39.125,8.125,8.125)), are selected to record displacements predicted by the DLSM model using a higher resolution with particle size of 0.25 mm. A full comparison with the displacement field of FEM is given in Figure 4.9. It can be seen that the displacement field predicted by DLSM is almost identical to that of FEM model. For the y-direction displacement along these two lines, the maximum errors of the DLSM model are 1.53% and 1.13% respectively. Additionally, a slender beam problem (see Figure 4.10 (a) for detailed problem description) which was solved by using another discrete lattice model in [28] is simulated by DLSM. Particle size used is 1mm and the DLSM modeling result is shown in Figure 4.10(b). The predicted top-end displacement is 3.967mm which is 0.82% stiffer than the analytical solution, while the discrete model in [28] with similar resolution provided an error around 10% to 15%. For the two beam bending problems, the regular Cubic II structure can predict correct results. However, DLSM model based on the Cubic II structure is not strictly isotropic because of the regular arrangement of particles and hence the non-uniform distribution of bonds. The influence of this kind of anisotropy on the numerical simulation of isotropic elastic materials will be studied in the next example.

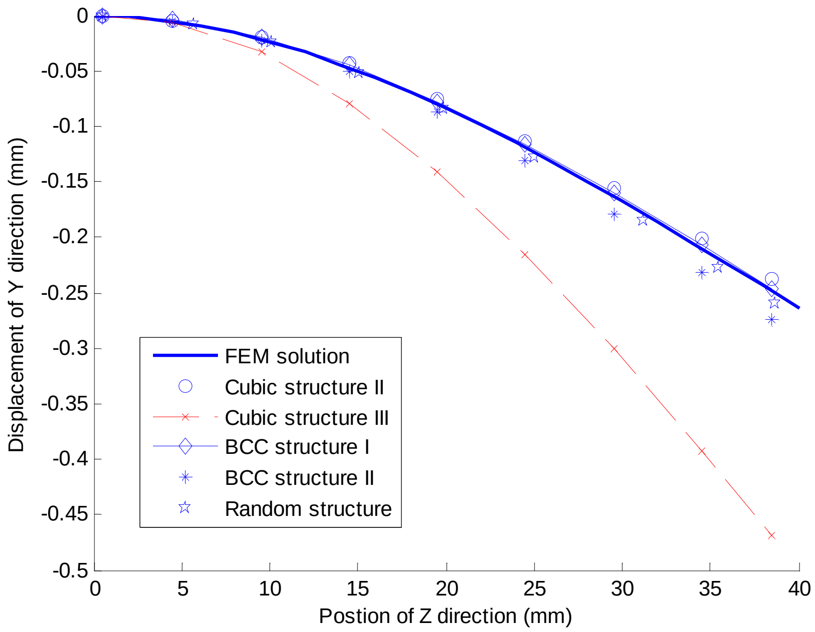

Figure 4.8. The y-direction displacement along the middle line of the beam predicted by FEM and DLSM with different lattice structures with Poisson’s ratio of 0.3.

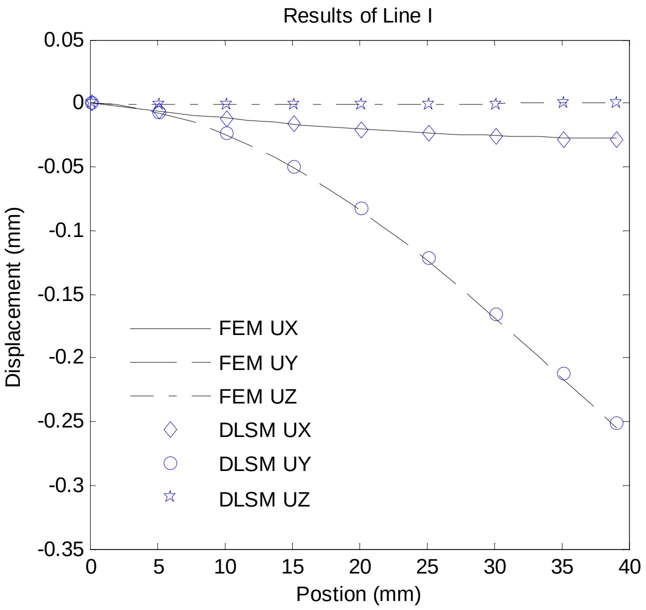

(a) Detection points of Line I

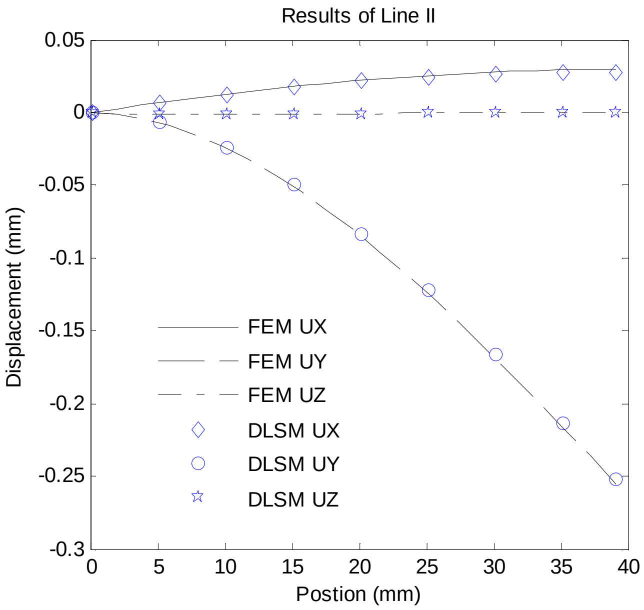

(b) Detection points of Line II

Figure 4.9. Full comparison of displacement field predicted by FEM with DLSM with Poisson’s ratio of 0.3.

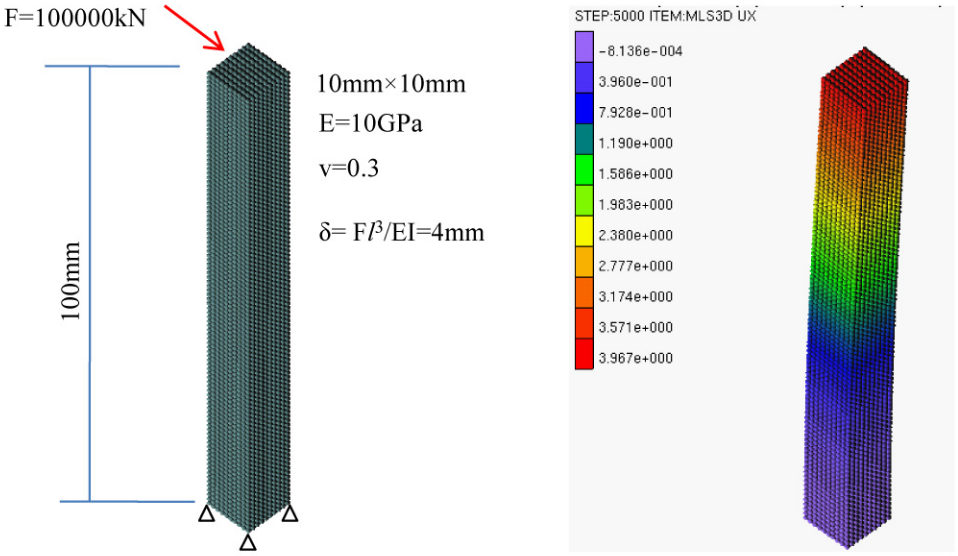

(a) The slender beam DLSM model (b) DLSM modeling result

Figure 4.10. The slender beam problem and the results of the DLSM model.

4.4.3 Brazilian test

In this section the Brazilian disc problem is selected to study the anisotropic effects of the DLSM model. As shown in Figure 4.11, two DLSM models of two different lattice structures are used for this study. The elastic properties of the modeled isotopic material are $\mathrm{E} = 10\mathrm{GPa}$ and $\nu = 0.2$. The average particle diameter of the random lattice model generated by PFC is 7.15mm and that of the Cubic II lattice is 5mm. In order to check the anisotropic behavior of the two DLSM models, the original models are rotated to different angles (10°, 30°, 45°) as shown in Figure 4.12. The strain component ε_{xx} at center of the disc is calculated by the rotated models and is compared with the value obtained by the original model. From the results given in Table 4.2, it can be seen that for the random model, the differences caused by the rotation are small (less than 2%) and for the Cubic II model the maximum difference happens at the rotation angle of 45°, which reaches 9.2% for a low space resolution. In this sense, the random model is a more realistic choice for the simulation of isotropic elastic materials. However, as we mention before, the generation of this kind of model is complex and time consuming. Regarding to the fact that the Cubic II model with a high resolution $(100\times100\times10)$ reduces the maximum difference to 5.34% (see Table 4.2), which is acceptable for practical applications, we recommend it be an alternative choice, especially when efficiency is considered to be prior. The particle size of the high resolution DLSM model is 1mm and the whole model is made up of 100000 particles. This DLSM model is then used to simulate the Brazilian disc problem for different Poisson's ratios. The results obtained by different methods

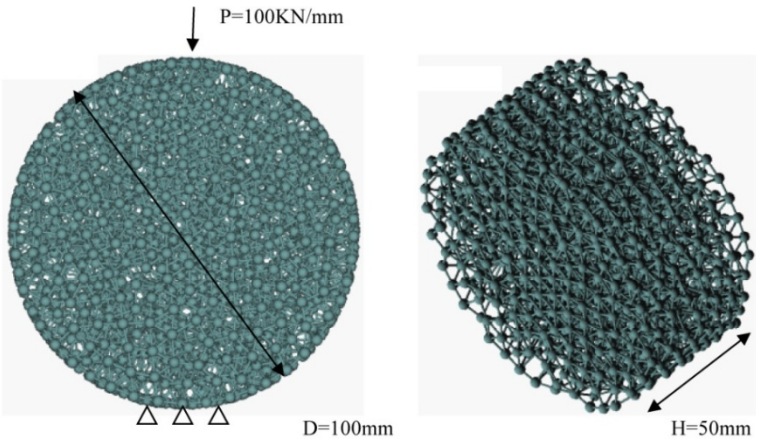

(a) The random lattice structure model (left: plane view)

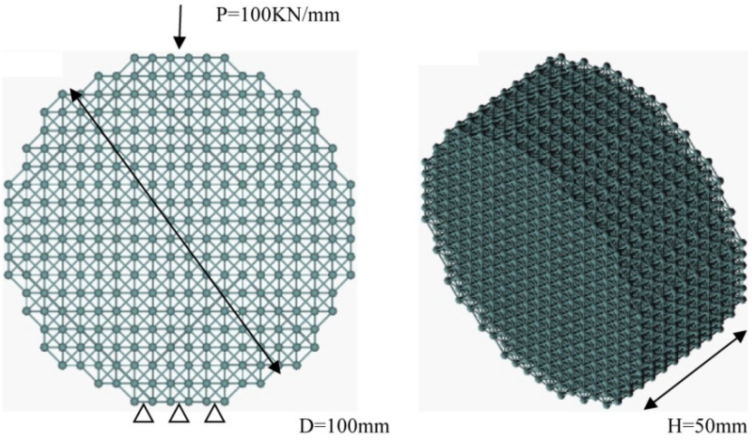

(b) The Cubic II lattice structure model (left: plane view)

Figure 4.11. Two lattice structures for the Brazilian disc problem.

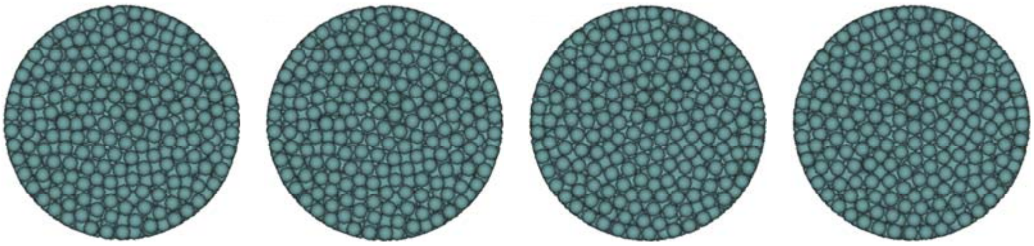

(a) Random 0° (b) Random 10° (c) Random 30° (d) Random 45°

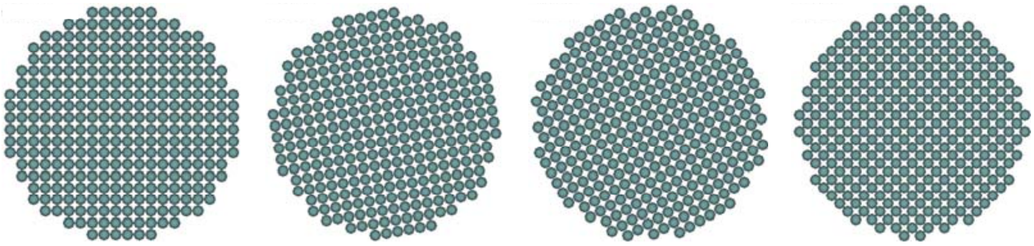

(e) Cubic II 0° (f) Cubic II 10° (g) Cubic II 30° (h) Cubic II 45°

Figure 4.12. The lattice models with different rotation angles for the Brazilian disc problem.

Table 4.2. Predicted ε_{xx} (10^{-6}) at the disc center by DLSM models with different rotated angles.

Rotation angle (^{o})	Random model $\varepsilon_{xx}^{\text{center}}$	Error (%)	Cubic II model $\varepsilon_{xx}^{\text{center}}$	Error (%)	Cubic II model (high resolution) $\varepsilon_{xx}^{\text{center}}$	Error (%)
0	0.0717	0.00	0.0674	0.00	0.0749	0.00
10	0.0718	0.11	0.0651	3.41	0.0738	1.47
30	0.0710	0.94	0.0644	4.45	0.0738	1.47
45	0.0705	1.65	0.0612	9.20	0.0709	5.34

including FEM as a reference solution are summarized in Table 4.3, where CLSM stands for the classical lattice spring model which directly calculates the deformation of shear springs using the particle displacement. Here, the particle size of DLSM and CLSM are both taken as 1mm. Cubic II is selected as the lattice type. The elastic module is taken as 10GPa and the Poisson's ratio is taken as 0.10, 0.20, 0.25 and 0.30. The spring parameters are calculated based on Equations (4.19) and (4.20) for both DLSM and CLSM. The comparison is used to illustrate the importance of keeping rotation invariance. From the results, it can be seen that the Poisson's ratio has a great influence on the results and the Poisson's ratio dependant mechanical response can be well captured by FEM and DLSM. However, CLSM could only provide reasonable results at the Poisson's ratio of 0.25 when shear spring is not present. This indicates that preserving the rotation invariance is very important for the lattice spring model.

Table 4.3. Results predicted by FEM, DLSM and CLSM for the Brazilian disc problem.

Possion's ratio	FEM ε_{xx} (10^{-6})	DLSM $\varepsilon_{xx}^{\text{center}}$ (10^{-6})	DLSM Error (%)	CLSM $\varepsilon_{xx}^{\text{center}}$ (10^{-6})	CLSM Error (%)
0.10	0.0794	0.0749	5.6	0.0207	74.0
0.20	0.0982	0.0941	4.1	0.0545	44.5
0.25	0.1076	0.1040	3.3	0.1040	3.3
0.30	0.1170	0.1144	2.3	- (unstable)	- (unstable)

4.4.4 Elastic wave propagation

Wave propagation can be viewed as the transmission of dynamic loads trough materials. It is an important research issue in dynamic failure study. For example, the prediction of wave attenuation across fractured rock masses is very important in solving problems in geophysics, seismic investigations and rock protective engineering. Numerical methods and computing techniques have been proven as a powerful and effective tool to simulate and model rock mechanical problems, for example in the work of Chen and Zhao [29], wave propagation in jointed rock masses was studied through DEM. The following example will show the ability of DLSM in modeling wave propagation in elastic materials. Wave propagation through an assembly of discrete bodies is, in general, dispersive. That is, the apparent wave velocity depends on wavelength, particularly for wavelengths that approach the average particle size. For longer wavelengths, the propagation behaviors like in a continuous elastic medium without an internal length scale. The example illustrates wave propagation through a one-dimensional bar composed of 20000 particles bonded together. The right end of the bar is free and an input pulse is applied at the left-hand boundary. In DLSM, the input parameters are the macroscopic parameter and the microscopic parameters are automatically computed from Equations (4.19) and (4.20). In the following calculations, it is assumed that the elastic modulus is 80.461GPa and the Poisson's ratio is 0.2563 and the rock density is 2600kg/m^3, which are typical parameters for the Bukit Timah granite. The theoretical wave velocity of P-wave and S-wave is calculated as:

$$C_p = \sqrt{\frac{K + 4G/3}{\rho}} = 6128.68 \text{ m/s}$$

$$C_s = \sqrt{G/\rho} = 3508.295 \text{ m/s}$$

where K and G are the bulk and shear stiffness of the material which can be obtained from Equation (4.16) and Equation (4.17) and ρ is the density. A half-cycle sinusoidal wave with 1MPa amplitude is applied at the left boundary as the incident wave, where the sinusoidal wave is 50000Hz. Three detection points A(4.5,4.5,49.5), B(4.5,4.5,99.5), C(4.5,4.5,149.5) are placed in the bar to record the wave propagation. Figure 4.13 shows the propagation of P-wave and S-wave at the three points. From these data we obtain

$$\hat{C}_p = \frac{d_{AC}}{t_{AC}^p} = \frac{100\times10^{-3}}{2.862\times10^{-5} - 1.264\times10^{-5}} = 6257.8 m/s$$

$$\hat{C}_s = \frac{d_{AC}}{t_{AC}^s} = \frac{100\times10^{-3}}{4.725\times10^{-5} - 1.890\times10^{-5}} = 3527.3 m/s$$

where $\hat{C}_p$ and $\hat{C}_s$ are the calculated P-wave speed and S-wave speed. d_{AC} is the distance from A point to C point. t_{AC}^p and t_{AC}^s are the time used for P-wave and S-wave transmitted from A point to C point. The error of the calculated speed is 2.11%

for P-wave and 0.54% for S-wave. It can be concluded that DLSM could predict correct wave propagation speed. The Poisson's ratio is greater than 0.25, so again the model here has negative shear springs involved. This means negative spring is also applicable in DLSM for dynamics problems. Figure 4.14 shows the contour map of particle velocity on P-wave propagation. From this figure, the propagation and reflection of the stress wave can be observed clearly. Overall, this example demonstrates that the dynamic behaviors of elastic material could be well predicted by DLSM and gives us confidence to use DLSM to study the dynamic failure behavior of elastic material.

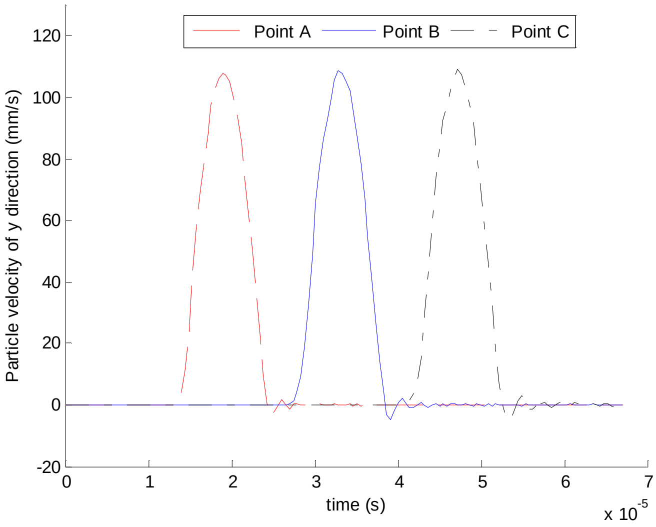

(a) P-wave

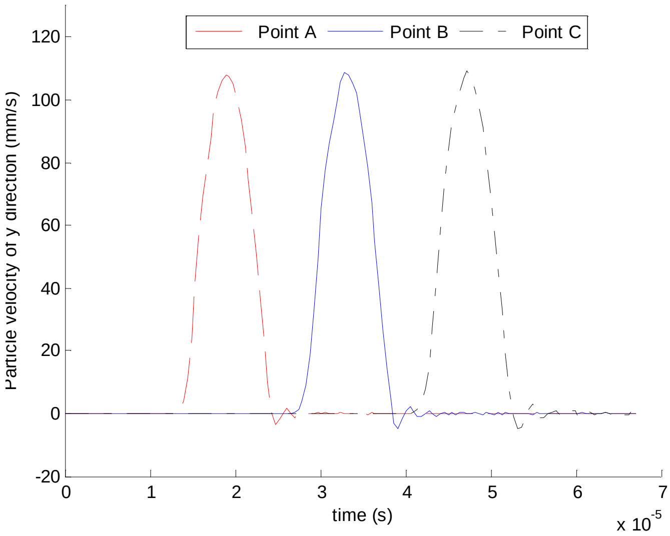

(b) S-wave

Figure 4.13. Wave propagation history at the detection points.

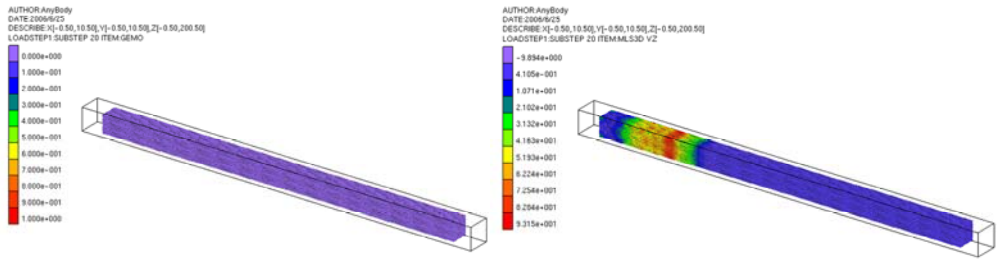

t=0us *t*=9us

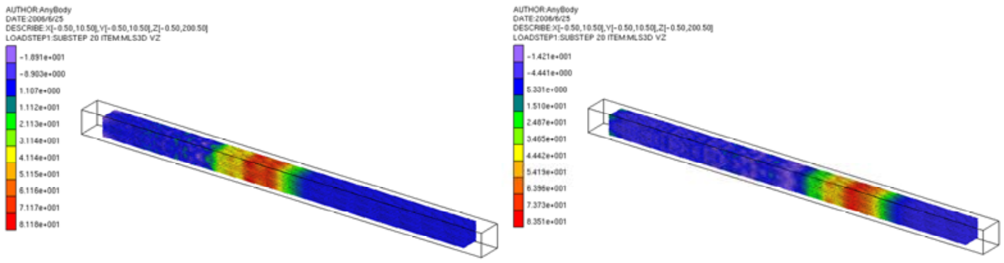

t=18us *t*=27us

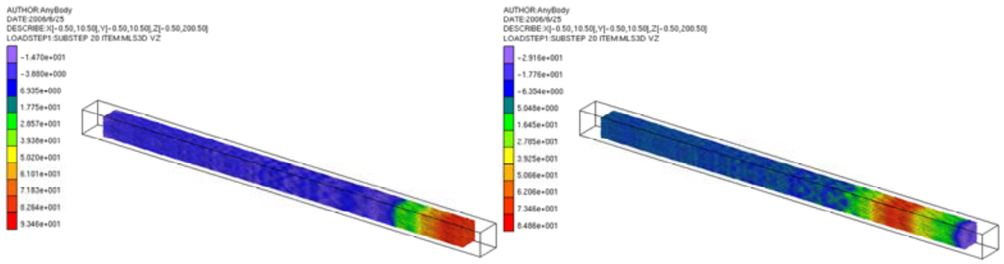

t=36us *t*=45us

Figure 4.14. The process of wave propagation through the elastic bar predicted by DLSM.

4.4.5 Dynamic spalling of 3-D bar

The dynamic spalling of quasi-brittle material occurs when an incident compressive wave is reflected by a free end and transformed into a tensile one. Spalling happens when the inputted incident compressive stress wave is lower than the material compressive strength while larger than its tensile strength. It has been successfully simulated by FEM in the work of Zhu and Tang [30]. In this subsection, the ability of DLSM on modeling dynamic fracturing process will be studied through this example. The geometries and loading conditions for the bar model are shown in Figure 4.15. The mechanical properties of the bar are as follows: the Young's modulus is 60.0 GPa, the direct tensile strength is 19.0MPa, and the Poisson's ratio is 0.20. The model is 200mm in length, 10mm in width and height, and it is discretized with $200\times10\times10$ particles. The incident compressive stress wave is applied at the left end of the bar. The right end is keeping free during calculation. Other faces are fixed in their normal directions. Two cases were simulated. Different compressive incident waves were applied on the left surface of the model (as shown in Figure 4.15) to study the stress amplitude influence on the spalling failure.

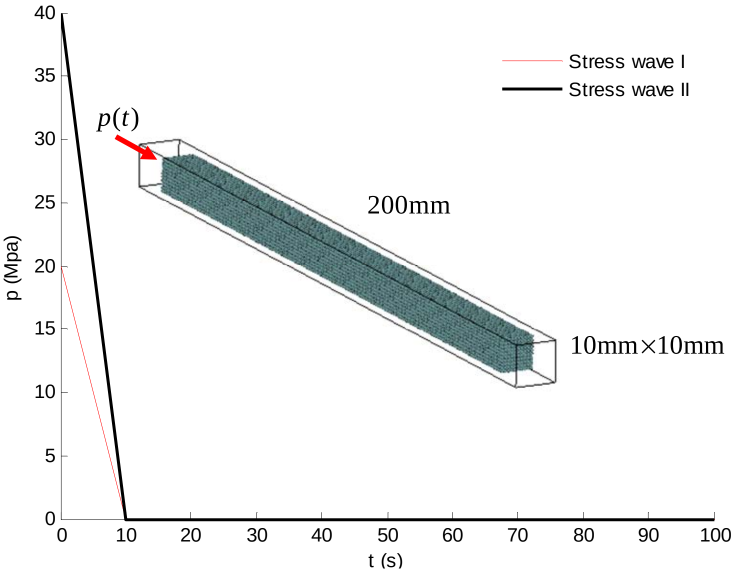

Figure 4.15. The incident compressive stress waves with different peak amplitudes applied on the left surface of the bar.

For the incident compressive stress wave I ($p_{\max} = 20MPa$), a fracture face located at 24mm from the right end of the model is detected (see Figure 4.16). The principle behind this phenomenon can be explained as follows. First, the compressive stress

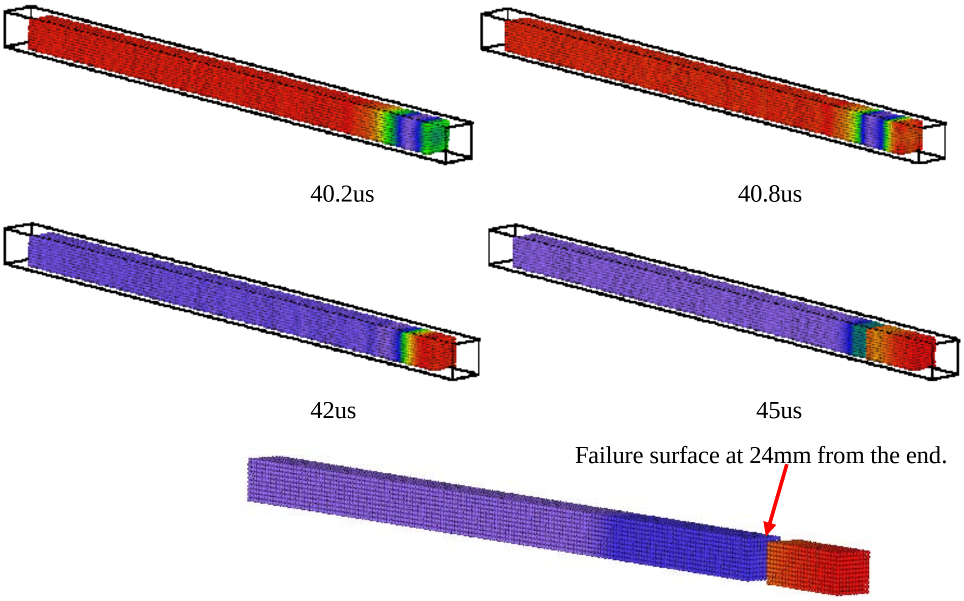

Figure 4.16. Dynamic spalling predicted by DLSM (incident compressive stress wave of 20MPa).

First, the compressive stress wave travels through the bar and reaches the right end. Because of the wave reflection, the original compressive stress wave will be transformed into a tensile stress wave which eventually induces the failure. After this, the strain energy is released and the stress amplitude of the residual wave is not large enough anymore to cause further failure. For the incident compressive stress wave II (pmax=40MPa) where the peak value of the stress is twice bigger than the tensile strength of the material, two apparent successive spalling failures occur (see Figure 4.17). The first fracture surface happens at 12mm from the right end of the model. After failure, the yielded surface reduces a portion of the original wave (see Figure 4.17). Meanwhile, the fraction of the stress wave that has passed the first failure surface continues traveling along the specimen. Because its magnitude is still larger than the tensile strength of the material, another spalling failure happens. The second failure surface occurs at 25mm from the right end of the model. After this, the residual stress wave is not strong enough to fracture the material. The simulation results of DLSM are compared with the theoretical solutions based on 1D wave propagation theory [31] and the experimental observations [32] (see Table 4.4). Based on these results, it can be concluded that DLSM is able to model the dynamic failure process of brittle materials, e.g., rock and concrete, under dynamic loading.

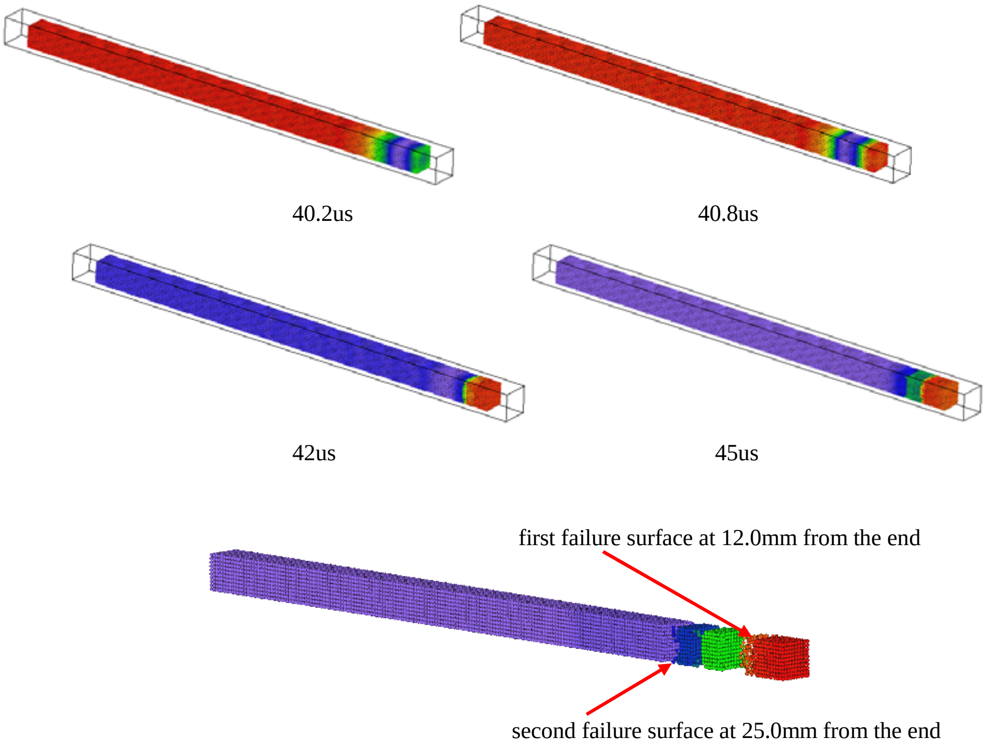
40.2us

40.8us

42us

45us

first failure surface at 12.0mm from the end

second failure surface at 25.0mm from the end

Figure 4.17. Dynamic spalling predicted by DLSM (incident compressive stress wave of 40MPa).

Table 4.4. The spalling results predicted by DLSM.

	Number of spalling		Distance from the specimen end (mm)		
	Theoretical [31]	DLSM	Theoretical [31]	DLSM	Relative Error
Stress wave I	1	1	24.5	24	2.0%
Stress wave II	2	2	12.25	12	2.0%
			24.5	25	2.0%

4.6 Collision of two bodies

The collision of two bodies made from different materials is selected as another example to illustrate the simulation of dynamic failure using DLSM. A sketch of the initial configuration for the simulation is shown in Figure 4.18. The smaller body (called intruder here) strikes the large body with a high velocity. At the beginning of the simulation, the two bodies are formed using $10\times10\times10$ and $50\times50\times5$ particles respectively. The velocity of the intruder is initially set to $\mathbf{v} = 100 mm/s$. Table 4.5 shows the parameter values for the simulation. The strength of the large body is set to different values to study the effect of the strength on the collision results. The elastic parameters are chosen in such a way that the two bodies are rather stiff.

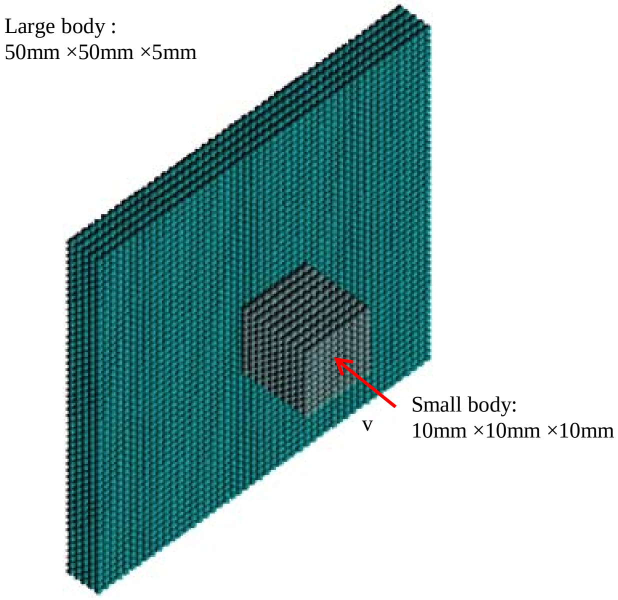

Figure 4.18. Diagram for the collision of two bodies.

Figure 4.19 shows the results of the simulation. The color of each particle represents its velocity in z-direction. It is found that immediately after impact shock waves start

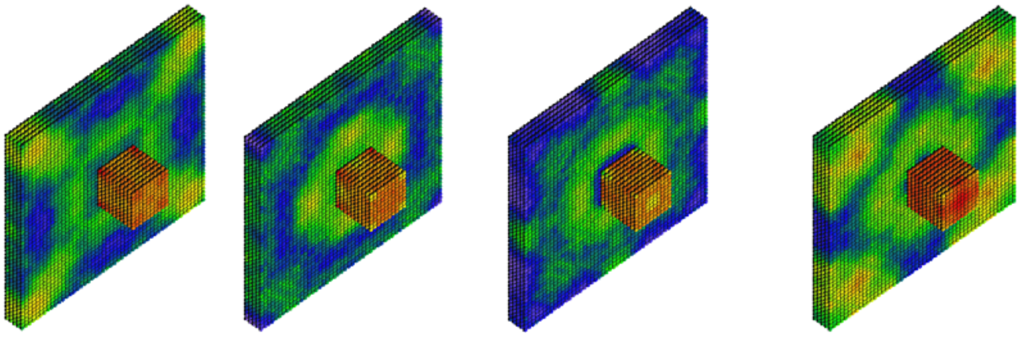

10.2ms 11.0ms 11.2ms 12.0ms

(a) Large body with strength of 16MPa.

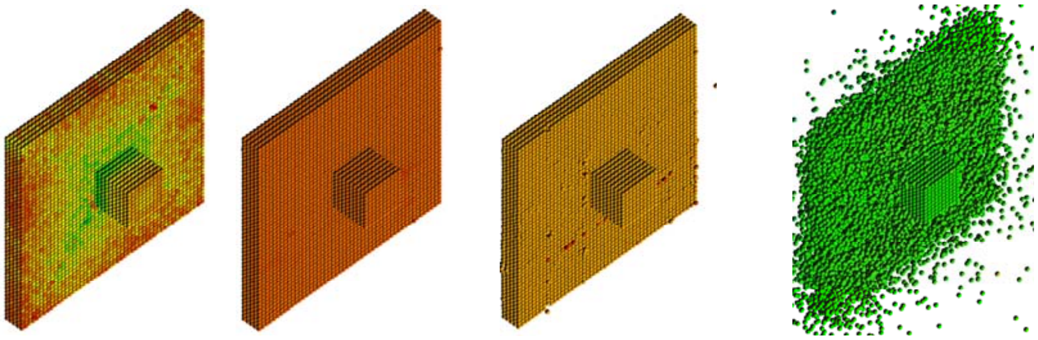

10.2ms 11.0ms 11.2ms 12.0ms

(b) Large body with strength of 0.59MPa.

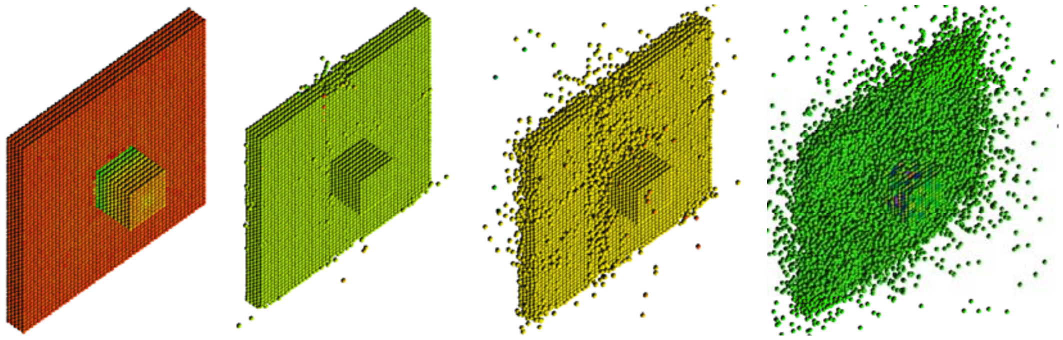

10.2ms 11.0ms 11.2ms 12.0ms

(c) Large body with strength of 0.16MPa.

Figure 4.19. DLSM simulation of the dynamic failure process of the large body impacted by the intruder.

to spread through the larger body. They first appear on the surface and then propagate into the internal part of the body. In the first case (see Figure 4.19(a)), the larger body keeps intact after collision. In the last two cases (Figure 4.19(b) and Figure 4.19(c)), the larger body is completely destroyed under the impact of the small body. Because of the simple fracture criterion used in the simulation, the results only qualitatively demonstrate the collision of solid bodies. More realistic and quantitative simulation can be accomplished if more advanced micro failure laws are implemented.

Table 4.5. Parameter values for the simulation of the collision problem.

	Elastic Modules (GPa)	Poisson’s ratio	Density (kg/m^3)	Strength (MPa)
Small body	120	0.2	7900	30000
Large body	60	0.2	2500	16/0.59/0.16

4.5 Conclusions

This chapter presents a novel 3D lattice spring model, in which the deformation of shear springs is calculated by using the local strain instead of the particle displacement. It has been proven that this novelty makes the model rotationally invariant and be capable of representing the diversity of Poisson’s ratio. Based on the Cauchy-born rules, the relationship which bridges the spring parameters and the elastic constants is derived. Several numerical examples are presented to show that the proposed model is capable of modeling elasticity, wave propagation and dynamic failure. For Poisson’s ratio greater than 1/4, the model with negative shear springs still produces reasonable results for both static and dynamic cases as demonstrated numerically. The DLSM model has advantages of directly using macroscopic parameters and allowing general lattice structures to be adopted. The disadvantage of the proposed model is that a local strain has to be calculated which costs more computing resources than the classical lattice model does. Generally speaking, like other discrete models based on the minimum potential energy principle, the model gives a stiff approximation of the corresponding elastic solution. The proposed model supplies an alternative numerical tool for studying the microstructure influences on dynamic fracturing of geo-materials such as rock and concrete. Further developments of method will be presented in following chapters.

4.6 References

1. Bažant ZP, Tabbara MR, Kazemi MT, Pijaudier-Cabot G. Random particle model for fracture of aggregate or fiber composites. J. Eng. Mech. 1990; 116(8):1686-1705.
2. Ostoja-Starzewski M. Lattice models in micromechanics. Appl. Mech. Rev. 2002; 55(1):35-59.
3. Buxton GA, Care CM, Cleaver DJ. A lattice spring model of heterogeneous materials with plasticity. Modell. Simul. Mater. Sci. Eng. 2001; 9(6):485-97.
4. Ostoja-Starzewski M, Sheng PY, Jasiuk I. Damage patterns and constitutive response of random matrix-inclusion composites. Eng. Fract. Mech. 1997; 58(5-6):581-606.
5. Beale PD, Srolovitz DJ. Elastic fracture in random materials. Phys. Rev. B 1988; 37(10):5500-7.
6. Srolovitz DJ, Beale PD. Computer simulation of failure in an elastic model with randomly distributed defects. J. Am. Ceram. Soc. 1988; 71(5):362-9.
7. Nayfeh AH, Hefzy MS. Continuum modeling of three-dimensional truss-like space structures. AIAA. J. 1978; 16(8):779-787.
8. Donze F, Magnier SA. Formulation of a 3-D numerical model of brittle behaviour. Geophys. J. Int. 1995; 122(3):790-802.
9. Kawai T. New discrete models and their application to seismic response analysis of structures. Nucl. Eng. Des. 1978; 48(1):207-229.
10. Zubelewicz A, Bažant, ZP. Interface element modeling of fracture in aggregate composites. J. Eng. Mech. 1987; 113(11):1619-1630.
11. Griffiths DV, Mustoe GGW. Modelling of elastic continua using a grillage of structural elements based on discrete element concepts. Int. J. Numer. Meth. Eng. 2001; 50(7):1759-1775.
12. Cusatis G, Bažant ZP, Cedolin L. Confinement-shear lattice model for concrete damage in tension and compression: I. Theory. J. Eng. Mech. 2003; 129(12):1439-1448.
13. Lilliu G, van Mier JGM. 3D lattice type fracture model for concrete. Eng. Fract. Mech. 2003; 70:927-941.
14. Schlangen E, Garboczi EJ. Fracture simulations of concrete using lattice models: computational aspects. Eng. Fract. Mech. 1997; 57:319-332.
15. Karihaloo BL, Shao PF, Xiao QZ. Lattice modelling of the failure of particle composites. Eng. Fract. Mech. 2003; 70(17):2385-2406.
16. Liu JX, Deng SC, Zhang J, Liang NG. Lattice type of fracture model for concrete. Theor. Appl. Fract. Mech. 2007; 48(3):269-284.
17. Hassold GN, Srolovitz DJ. Brittle fracture in materials with random defects. Phys. Rev. B 1989; 39(13):9273-81.
18. Caldarelli G, Castellano C, Petri A. Criticality in models for fracture in disordered media. Phys. Stat. Mech. Appl. 1999; 270(1):15-20.
19. Parisi A, Caldarelli G. Self-affine properties of fractures in brittle materials. Phys. Stat. Mech. Appl. 2000; 280(1):161-5.
20. Ostoja-Starzewski M, Sheng PY, Alzebdeh K. Spring network models in elasticity and fracture of composites and polycrystals. Cmp. Mat. Sci. 1996; 7(1-2):82-93.
21. Monette L, Anderson MP. Elastic and fracture properties of the two-dimensional triangular and

square lattices. Modell. Simul. Mater. Sci. Eng. 1994; 2(1):53-66.

22. Cundall PA, Strack ODL. A discrete numerical model for granular assemblies. Geotechnique 1979; 29(1):47-65.
23. Rougier E, Munjiza A, John NWM. Numerical comparison of some explicit time integration schemes used in DEM, FEM/DEM and molecular dynamics. Int. J. Numer. Meth. Engng 2004; 61:856–879.
24. Otter JRH, Cassell AC, Hobbs RE. Dynamic Relaxation (Paper No. 6986). Proc. Inst. Civil Eng. 1966; 35:633–656.
25. Li QM, Lu YB, Meng H. Further investigation on the dynamic compressive strength enhancement of concrete-like materials based on split Hopkinson pressure bar tests. Part II: Numerical simulations. Int. J. Impact Eng. 2009; (in press).
26. Potyondy DO, Cundall PA. A bonded-particle model for rock. Int. J. Rock. Mech. Min. Sci. 2004; 41:1329-1364.
27. Lakes RS, Lee T, Bersie A, Wang YC. Extreme damping in composite materials with negative-stiffness inclusions. Nat. 2001; 410:565-567.
28. Griffiths DV, Mustoe GGW, Modelling of elastic continua using a grillage of structural elements based on discrete element concepts. Int. J. Numer. Meth. Engng 2001; 50:1759-1775.
39. Chen SG, Zhao J. A study of UDEC modelling for blast wave propagation in jointed rock masses. Int. J. Rock Mech. Min. 1998; 35(1):93-99.
30. Zhu WC, Tang CA. Numerical simulation of Brazilian disk rock failure under static and dynamic loading. Int. J. Rock Mech. Min. 2006; 43(2):236-252.
31. Rinehart JS, Pearson J. Behavior of metals under impulsive loads. Dover Publications, New York, 1965.
32. Brara A, Camborde F, Klepaczko JR, Mariotti C. Experimental and numerical study of concrete at high strain rates in tension. Mech Mater 2001; 33:33-45.

Chapter 5

Multi-scale DLSM

In this chapter, a multi-scale lattice spring model is proposed to combine the DLSM described in Chapter 4 with the NMM. This model is named as multi-scale DLSM (m-DLSM) which can reduce the computational resources needed for DLSM model which totally built from particles. The proposed multi-scale model includes three-layer structures as: the NMM model, the PMM model and the DLSM model. A Particle based Manifold Method (PMM) is proposed to bridge the DLSM with NMM. PMM uses a special manifold model, where the physical domain is discretized into particles. During calculation, the PMM model can be automatically released into DLSM model. The developed model can be used to study the dynamic failure of brittle materials, e.g., rock and concrete. Finally, a few examples are provided to demonstrate the correctness and feasibility of the developed model.

5.1 Introduction

Multi-scale modeling is regarded as an exciting and promising methodology due to its ability to solve problems which cannot directly be handled by microscopic methods for the limitation of computing capacitance [1-3]. For this reason, the macro material response can be directly obtained based the micro mechanical properties through multi-scale modeling. This advantage is extremely useful and essential in the study of material properties based on their microstructure information. It is well known that classical elasticity theory can only provide an adequate description of macroscopic mechanical response for most materials. It would be an unsuitable theory when facing the micro-mechanical response of these materials which are actually heterogeneous at microscopic level, therefore, the microscopic modeling is necessary [4]. As it is mentioned above that directly building microscopic model is usually inaccessible due to the limitation of computing resources, in this case, the multi-scale modeling provides a good choice.

The most direct way to build a multi-scale numerical model is to combine two different scale methods. This methodology has widely been used in the coupling of MD with continuum mechanics model [5-8]. In order to further reducing the computing burden, these multi-scale methods also allow the macroscopic model automatically changed into microscopic model. This kind of implementation is regarded as the high level multi-scale coupling technique. This kind of multi-scale models have been developed for fracturing simulation of materials in [9, 10]. Moreover, multiscale modeling is also mathematically needed. It is attributed to the fact that the computing power is still the main limitation of numerical modeling. From pure mathematic view, the *secular behavior* [11] is the most important reason of performing multiscale analysis. The secular behavior of numerical modeling can be attributed to the accumulated error of the problem will increase with the scale decreasing or increasing for a given scale model. For example, when the scale is too small, the FEM cannot exactly provide correct description of the microscopic behavior of materials. This is also true for the microscopic model, e.g., when the scale is too large for MD model, it will produce too large accumulated error. From this point of view, the multiscale modeling is essentially needed for some problems which inhabit multiscale property, e.g., the volcanic eruptions [3] are regarded as a multiscale dynamic fracturing propagation problem. Development of multiscale model is also promising to solve dynamic fracturing problems of various materials including rock.

In this chapter, a multi-scale model is developed to couple DLSM [13, 14] and NMM [15, 16]. The reason of choosing NMM is that it is an advanced FEM and the back ground mesh used in manifold method is independent to physical model [17]. Meantime, the DLSM is close to FEM due to the DOFs for each particle are same with that of FEM node. These properties make it very suitable to couple these different methods. The context of this chapter is organized as following. Firstly, the elastic dynamic and explicit manifold method will be introduced. Secondly, the multi-scale Distinct Lattice Spring Model (m-DLSM) will be described in details including equations of PMM and how to integrate DLSM and NMM. Then, the proposed model is validated through numerical simulations of two elastic problems, one wave propagation problem and two dynamic failure problems. Finally, this chapter ends up with some remarks and conclusions.

5.2 Elastic dynamics and numerical manifold method

5.2.1The basic of elastic dynamics

In this section, the basic equations for linear elastic dynamics will be briefly introduced. Consider the elastic body Ω as shown in Figure 5.1. The boundary Γ is composed of the traction boundary Γ_t and the displacement boundary Γ_u. The governing equation of motion, or momentum conservation law, for the solid body under the Lagrangian frame of reference is

$$\nabla \bullet \boldsymbol{\sigma} + \mathbf{b} = \rho \ddot{\mathbf{u}} \tag{5.1}$$

with the boundary condition being

$$\mathbf{u} = \bar{\mathbf{u}} \quad \text{on} \ \ \Gamma_u \tag{5.2}$$

$$\boldsymbol{\sigma} \bullet \mathbf{n} = \bar{\mathbf{t}} \quad \text{on} \ \ \Gamma_t \tag{5.3}$$

where ∇ is the gradient operator with respect to the current position $\mathbf{x}$, $\mathbf{u}$ is the displacement and $\ddot{\mathbf{u}}$ is the accelerate, $\boldsymbol{\sigma}$ is the Cauchy stress, ρ is the mass density, $\mathbf{b}$ is the body force per unit mass, $\mathbf{n}$ is the outward normal vector on the boundary surface in the current configuration, and $\bar{\mathbf{t}}$ and $\bar{\mathbf{u}}$ are the prescribed traction and displacement on the corresponding boundaries, respectively.

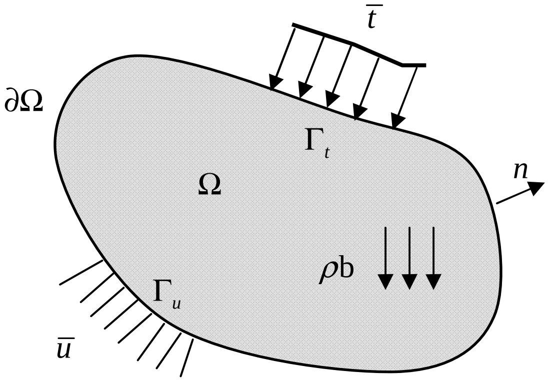

Figure 5.1. An solid elastic body under Lagrangian frame.

5.2.2 Explicit numerical manifold method

NMM is a numerical method proposed by Shi [15] to integrate FEM with DDA [17]. It can be regarded as an advanced FEM or PUM based FEM. The relationship between PUM FEM and NMM is discussed in the work of Kurumatani and Terada [18]. Basic unit used in NMM is called as manifold element which is made up from mathematic cover and physical domain (see Figure 5.2). The physical cover is the intersection of mathematic cover and physical domain. It is equivalent to FEM node used in classical FEM. Degrees of freedoms are defined in these physical covers to represent deformation state of their physical domains. The detail of how to construct these manifold elements can be found in [15]. The manifold element can also be simply regarded as a regular FEM with an irregular integration domain. This is the most distinct feature of NMM, which make the regular mesh can be used to model irregular domain. NMM has similar properties of meshless methods and meantime kept some advantages of the classical FEM. It is found that the meshless properties are extremely useful to realize coupling between the different methods.

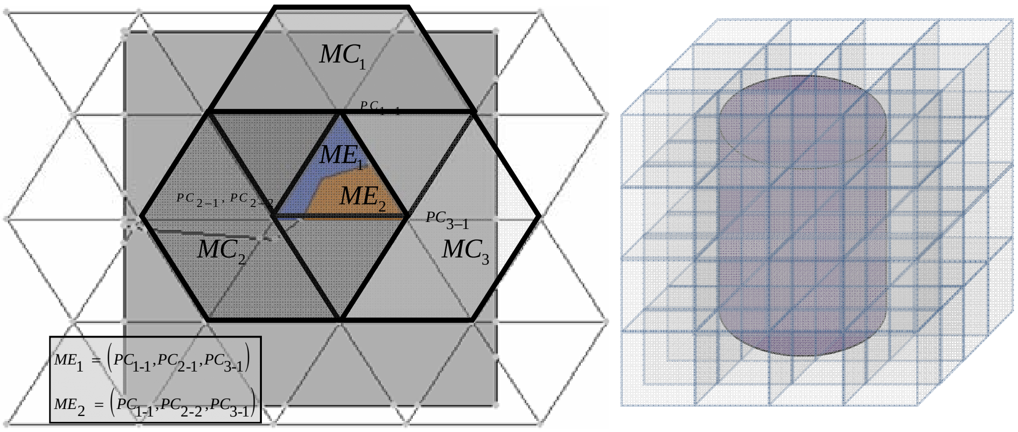

(a) Manifold model in 2D (b) Manifold model in 3D

Figure 5.2. Manifold elements in NMM.

In following sections, the basic theory of NMM and its explicit version will be explained. Compared with FEM, approximation function in NMM is given in a similar way. First, the deformation function is defined in the physical cover as

$$c_j(\mathbf{x}) = \sum_{i=1}^{n} b_{ji}(\mathbf{x}) \bullet u_{ji} \tag{5.4}$$

where $c_j(\mathbf{x})$ is the displacement function of the jth physical cover, u_{ji} is the general DOFs of the cover, $b_{ji}(\mathbf{x})$ is the basis of the displacement function and n is the number of DOFs. Finally, the approximation function of the manifold element is written as

$$u^h(\mathbf{x}) = \sum_{j=1}^{m} \phi_j(\mathbf{x}) c_j(x) = \sum_{j=1}^{m} \phi_j(\mathbf{x}) \sum_{i=1}^{n} b_{ji}(\mathbf{x}) u_{ji} \tag{5.5}$$

where ϕ_j is the weight function of the cover and m is the number of physical covers of the manifold element. The weight functions should satisfy the partition of unity, namely

$$\sum_{j=1}^{m} \phi_j(\mathbf{x}) = 1 \tag{5.6}$$

The manifold elements are called as three-cover element or eight-cover element in order to distinguish with the FEM elements. Equation (5.6) can be further written into a more familiar form as

$$u^h(\mathbf{x}) = \sum_{i=1}^{n \times m} N_i(\mathbf{x}) u_i \tag{5.7}$$

where $N_i(\mathbf{x})$ is the shape function of i-th general degree of freedoms, u_i is the degree of freedoms defined in ith cover. Now, the integration equations of NMM on elastic dynamics can be obtained through weighted residual approach or variation principle. The system equations of manifold method are obtained through imposing the boundary conditions into Equation (5.1) in a weak sense as

$$\begin{aligned} &\int_{\Omega} \rho \mathbf{u}^* \bullet \ddot{\mathbf{u}} dV + \int_{\Omega} \nabla \mathbf{u}^* : \boldsymbol{\sigma} dV + \lambda \int_{\Gamma_u} \mathbf{u}^* \bullet (\mathbf{u} - \bar{\mathbf{u}}) d\Gamma \\ &= \int_{\Omega} \mathbf{u}^* \bullet \mathbf{b} dV + \int_{\Gamma_t} \mathbf{u}^* \bullet \bar{\mathbf{t}} d\Gamma, \ \forall \mathbf{u}^* \end{aligned} \tag{5.8}$$

where $\mathbf{u}$ is the displacement field and $\mathbf{u}^*$ is its variation. The third term in the left-hand side is the penalty term involving in boundary condition (5.2). The λ is a large number called as the penalty parameter which is taken as

$$\lambda = \beta E \tag{5.9}$$

where E is the elastic modules, β is a ratio suggested to take from 40 to 100. In

NMM, the direct boundary condition can be applied directly when the manifold nodes (physical cover) are exactly placed on the boundaries. In this case, the third term in the left part of Equation (5.8) can be neglected. From Equation (5.8), we can further derive the following discretized equation of motion:

$$\mathbf{K}\mathbf{u}^{\mathbf{t}} + \mathbf{M}\ddot{\mathbf{u}}^{t} = \mathbf{F}^{t} \tag{5.10}$$

where $\mathbf{u}^{t}$ is the displacement vector, $\ddot{\mathbf{u}}^{t}$ is the accelerate vector and $\mathbf{F}^{t}$ is the external force vectors, respectively. The external force can be written as

$$\mathbf{F}^{t} = \sum_{e=1}^{N_{el}} \int_{\Omega_e} \mathbf{N}_e^T \mathbf{b} d\Omega_e + \sum_{e=1}^{N_{el}} \int_{\Gamma_t} \mathbf{N}_e^T \bar{\mathbf{t}} d\Gamma_t \tag{5.11}$$

The stiffness matrix and mass matrix are evaluated as follows:

$$\mathbf{M} = \sum_{e=1}^{N_{el}} \rho_e \int_{\Omega_e} \mathbf{N}_e^T \mathbf{N}_e d\Omega \tag{5.12}$$

$$\mathbf{K} = \sum_{e=1}^{N_{el}} \int_{\Omega_e} \mathbf{B}_e^T \mathbf{D} \mathbf{B}_e d\Omega \tag{5.13}$$

where $\mathbf{N}_e$ and $\mathbf{B}_e$ are respectively interpolation matrix of displacement and strain, $\mathbf{D}$ is elastic matrix and N_{el} is the number of manifold elements involved in the NMM model.

The integration domain involved in Equations (5.12) and (5.13) is an irregular domain. It can be integrated through simplex integration method or simplex gauss integration method. The details of these integration methods can be found in [15, 16]. In the original NMM [15], system equations are solved by using an implicit method. In this chapter, the explicit center difference method will be used to solve Equation (5.10). The integrate method for explicit NMM is written as:

$$\ddot{\mathbf{u}}^{t} = \left(\mathbf{F}^{\mathbf{t}} - \mathbf{K}\mathbf{u}^{t}\right)\mathbf{M}_{lump}^{-1} \tag{5.14}$$

$$\dot{\mathbf{u}}^{t+\Delta t/2} = \dot{\mathbf{u}}^{t-\Delta t/2} + \ddot{\mathbf{u}}^{t}\Delta t \tag{5.15}$$

$$\mathbf{u}^{t+\Delta t} = \mathbf{u}^{t} + \dot{\mathbf{u}}^{t+\Delta t/2}\Delta t \tag{5.16}$$

where Δt is the time step used in the center difference integration and the mass matrix is assembled in a lumped form. This allows the calculation can be performed through an element by element way. The main advantage of explicit method is that the global stiffness matrix does not need to be assembled explicitly during calculation. Boundary conditions can also be directly applied to the corresponding manifold nodes. However, this solution scheme is conditionally stable. To keep the computation stable, the time step have to be chosen according to the requirement, it should be less than the time needed for elastic wave to propagate through the smallest element of the model, this reads as

$$\Delta t_{\mathrm{n}} = \min\left(\frac{l_i}{C_p}\right) \tag{5.17}$$

where C_{p} is the P-wave velocity of the model, l_i is the *i*th manifold element length of the model. This requirement is the same as that used in DLSM which is the microscopic model to be coupled with NMM. In DLSM, the particles and springs make up a network system which represents the solid model. The equation of motion of DLSM is just the same as Equation (5.10), and the used integration method is also explicit center difference method (equivalent to the Newton’s second law). This means all elements in the multi-scale model, particles and manifold nodes, can be treated exactly through single set of motion equations and the force interaction between NMM and DLSM can be treated directly.

5.3 Multi-scale Distinct Lattice Spring Model (m-DLSM)

In order to integrate DLSM model with NMM, interaction between them has to be treated properly. The basic element of DLSM is particle and that of NMM model is polyhedral manifold element. Contact detection between these two 3D objects is difficult to be implemented. Moreover, directly coupling these two models will cause sudden vibration at their interface and further leads to some unstable solutions. In order to solve these problems, a method for mixing the NMM with DLSM is proposed. The method is named as Particle based Manifold Method (PMM), where the physical domain of manifold element is replaced by the particle based DLSM model and DOFs of the model are defined in the physical covers as in standard NMM. The PMM element is a mixture of DLSM and manifold element. By using this element, there is only sphere to sphere contact detection is required. It is much easy to be implemented. The PMM model also provides a cushion layer in the multi-scale model, which naturally bridge the DLSM model with the NMM model. Following, the PMM element and the solving procedure used in the proposed multi-scale model (m-DLSM) will be presented.

5.3.1 Particle based Manifold Method (PMM) element

In this section, the basic idea of PMM element will be introduced. PMM element is realized by replacing the physical domain of manifold element by the particle based DLSM model (see Figure 5.3). The 3D PMM element used in m-DLSM is illustrated in Figure 5.3. The eight-node FEM element is used as the mathematic element and DLSM model is used as the physical domain.

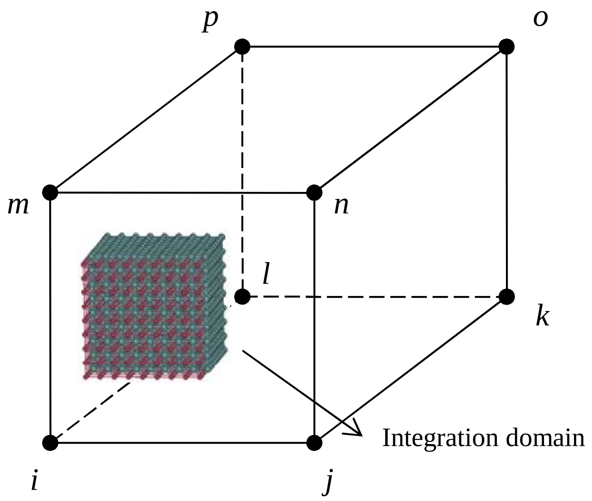

Figure 5.3. PMM element in m-DLSM.

As the explicit integration method and lumped mass matrix are used in m-DLSM, the mass matrix of PMM element is taken as the 1/8 of the DLSM model included in the element:

$$\mathbf{M}_i^{\mathbf{PME}} = \frac{1}{8}\sum_{j=1}^{m_i} m_{ij}^p \tag{5.18}$$

where $\mathbf{M}_i^{\mathbf{PME}}$ is the mass matrix of PMM element, m_i is the number of particles included in the PMM element and m_{ij}^p is the mass of the particle. The stiffness matrix of the PMM element has to be obtained from a distinct way. As the deformation energy of DLSM model is stored on the network of bonds between particles. The integration domain of PMM element is neither 2D nor 3D. Actually, as the discrete natural property of the lattice network, the integration is realized through a summarizing operation as

$$\mathbf{K}_i^{\mathbf{PME}} = \sum_{j=1}^{n_i} \mathbf{K}_{ij}^{\mathbf{b}} \tag{5.19}$$

where $\mathbf{K}_i^{\mathbf{PME}}$ is the stiffness matrix of PMM element, n_i is the number of bonds included in the PMM element and $\mathbf{K}_{ij}^{\mathbf{b}}$ is the stiffness matrix contributed by each lattice bond (a pair of normal and shear springs).

First, the stiffness of the bond in local coordinate as follows:

$$\mathbf{K}_{ij}^{\text{bond}} = \begin{pmatrix} k_n & 0 & 0 & 0 \\ 0 & k_s & 0 & 0 \\ 0 & 0 & k_s & 0 \\ 0 & 0 & 0 & k_s \end{pmatrix} \tag{5.20}$$

And the bond deformation is represented as

$$\mathbf{u}^{bond} = \left(u^n, u_x^s, u_y^s, u_z^s\right) \tag{5.21}$$

It should be mention that the shear spring in DLSM model is a vector spring whose deformation is represented by a vector with three variables. The strain state of the PMM element is given as

$$\boldsymbol{\varepsilon} = \left(\varepsilon_{xx} \quad \varepsilon_{yy} \quad \varepsilon_{zz} \quad \varepsilon_{xy} \quad \varepsilon_{yz} \quad \varepsilon_{xz}\right)^T = \mathbf{B}^* \mathbf{u}^{\text{ME}} \tag{5.22}$$

where u^{ME} is the node displacement of PMM element, $\mathbf{B}^*=[\mathbf{B}_\mathrm{i}]$ is the strain interpolation matrix of the mathematic element, which can be obtained as

$$\mathbf{B}_i = \begin{pmatrix} N_{i,x} & 0 & 0 \\ 0 & N_{i,y} & 0 \\ 0 & 0 & N_{i,z} \\ \frac{1}{2}N_{i,y} & \frac{1}{2}N_{i,x} & 0 \\ 0 & \frac{1}{2}N_{i,z} & \frac{1}{2}N_{i,y} \\ \frac{1}{2}N_{i,z} & 0 & \frac{1}{2}N_{i,x} \end{pmatrix} \tag{5.23}$$

where $N_{i,x}$, $N_{i,y}$ and $N_{i,z}$ are derivatives of the shape functions. The shape functions N_i and their corresponding derivatives are provided in Appendix C.

Then, the bond deformation vector can be represented by

$$\mathbf{u}^{bond} = \mathbf{L}_{4\times6}\boldsymbol{\varepsilon} \tag{5.24}$$

where $\mathbf{L}_{4\times6}$ is a transformation matrix. Based on Equation (B.13) in Appendix B, $\mathbf{L}_{4\times6}$ is obtained as

$$\mathbf{L}_{4\times6} = \mathbf{T}_{4\times3}\mathbf{Q}_{3\times6} = l_{ij}\begin{pmatrix} n_x & n_y & n_z \\ 1-n_x{}^2 & -n_x n_y & -n_x n_z \\ -n_y n_x & 1-n_y{}^2 & -n_y n_z \\ -n_z n_x & n_z n_y & 1-n_z{}^2 \end{pmatrix}\begin{pmatrix} n_x & 0 & 0 & n_y & 0 & n_z \\ 0 & n_y & 0 & n_x & n_z & 0 \\ 0 & 0 & n_z & 0 & n_y & n_x \end{pmatrix} \tag{5.25}$$

where l_{ij} is the length of the bond and (n_x,n_y,n_z) is the normal vector of the bond, it is define as

$$\mathbf{n} = \left(n_x, n_y, n_z\right) = \left(\frac{x_2 - x_1}{l}, \frac{y_2 - y_1}{l}, \frac{z_2 - z_1}{l}\right) \tag{5.26}$$

where $\left(x_1, y_1, z_1\right)$ and $\left(x_2, y_2, z_2\right)$ are the coordinates for two particles.

Now, the strain energy of the bond can be written as

$$\Pi_{\mathrm{b}} = \frac{1}{2}\left(\mathbf{K}_{ij}^{\mathrm{bond}}\left(\mathbf{LB}^{*}\mathbf{u}^{\mathrm{ME}}\right)\right)^{T}\left(\mathbf{LB}^{*}\mathbf{u}^{\mathrm{ME}}\right) \tag{5.27}$$

Finally, the contribution of each bond to the stiffness matrix is obtained from the energy minimization principle as

$$\mathbf{K}_{ij}^{\mathrm{b}} = \left[\frac{\partial^2 \Pi_{\mathrm{b}}}{\partial u_i \partial u_j}\right] = \left(\mathbf{LB}^{*}\right)^{T}\mathbf{K}_{ij}^{\mathrm{bond}}\mathbf{LB}^{*} \tag{5.28}$$

5.3.2 Coupling scheme

Figure 5.4 shows the work flow of the coupled calculation cycle in m-DLSM. The DLSM and NMM computations are performed in parallel. Interactions between them are finished by the PMM model. Information exchange only happen at the begin and the end of each cycle. The mapping of unbalance force from particles to PMM element computation is realized by using following equation

$$\mathbf{F}_i^{\mathrm{ME}} = \mathbf{N}_{ij}\mathbf{F}_{ij}^{\mathrm{LS}} \tag{5.29}$$

where $\mathbf{F}_i^{ME}$ is the transferred force to the i-th PMM element, $\mathbf{N}_{ij}$ is the interpolation matrix of displacement at the linked particle and $\mathbf{F}_{ij}^{\mathrm{LS}}$ is the calculated unbalance force on the particle. After obtaining the unbalance force on particles and manifold nodes, new positions of these particles and manifold nodes can be obtained by using the Newton’s second law. Then, the displacement of NMM model is mapped to the particles which fall in the PMM model. The mapping operation is given as

$$\mathbf{u}_{ij}^{\mathrm{LS}} = \left[\mathbf{N}_{ij}\right]^T \mathbf{u}_i^{\mathrm{ME}} \tag{5.30}$$

where $\mathbf{u}_{ij}^{\mathrm{LS}}$ is the mapped displacement from PMM model to the linked particle and $\mathbf{u}_i^{\mathrm{ME}}$ is displacement vector of the PMM element. The interaction between PMM with DLSM is realized through the interaction of the DLSM particle with the PMM particle. The interaction between PMM and NMM is realized by sharing common manifold nodes. The PMM model is used as the midst scale layer of the m-DLSM to realize coupling of the DLSM and the NMM.

The used time step is selected as the minimal value of the time step used for NMM model and DLSM model. In practical, the time step of DLSM model is always selected due to the size of DLSM particle is surely smaller than the NMM element size. In order to obtain static solutions, a local damping scheme [18] is used. It can overcome the difficulties of the velocity-proportional damping. The local damping is simply written as

$$\sum \mathbf{F}_i^{(t)} = \sum \mathbf{F}_i^{(t)} - \alpha \left| \sum \mathbf{F}_i^{(t)} \right| \mathrm{sgn}\left(\dot{\mathbf{u}}_i^{(t-\Delta t/2)}\right) \tag{5.31}$$

where α is the damping constant which is dimensionless and independent of mechanical properties and boundary conditions. For the dynamic case, the damping term will be switched off (α =0).

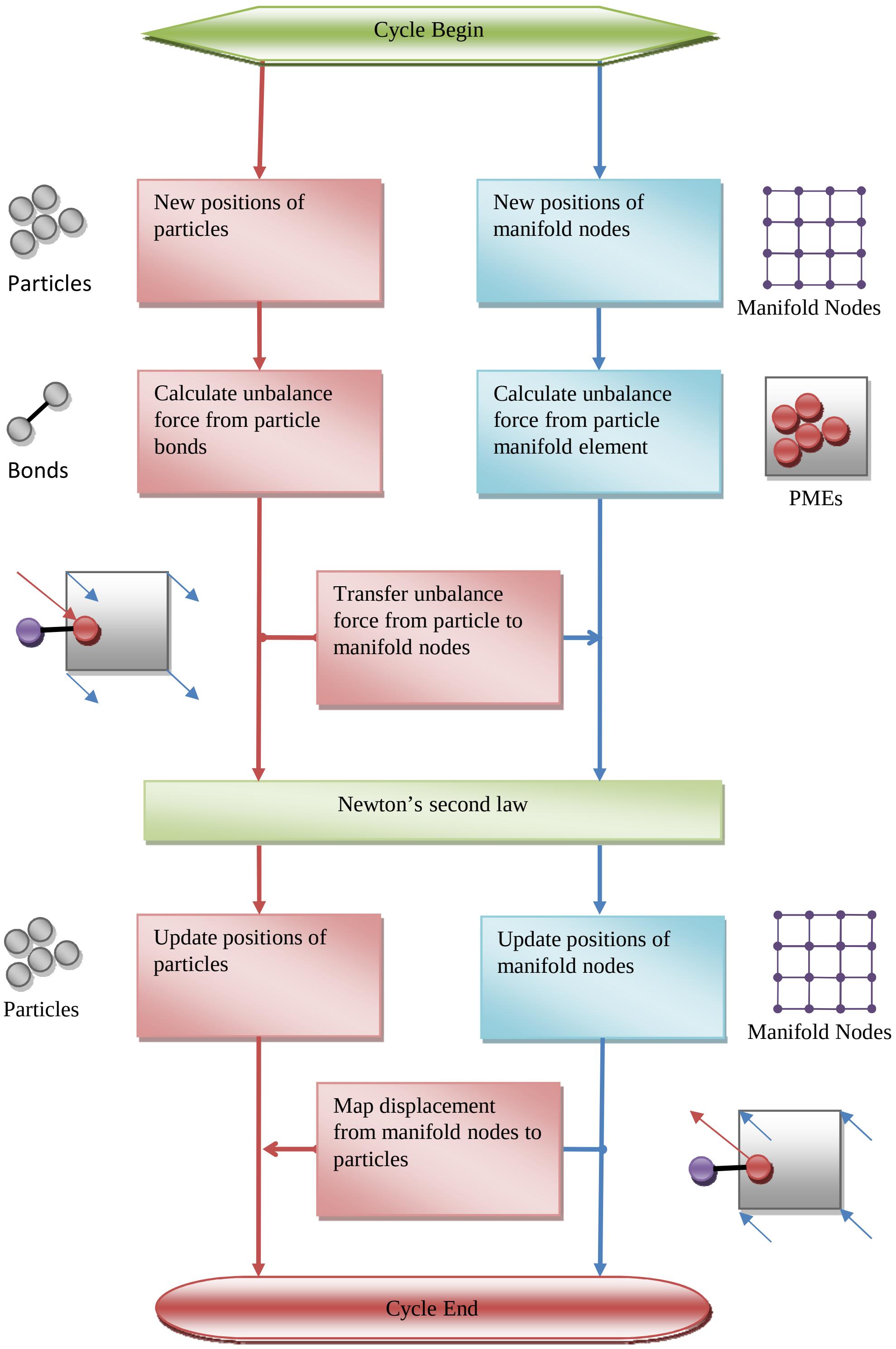

Figure 5.4. Coupled calculation cycle in m-DLSM.

5.3.3 Releasing PMM element into DLSM

In this section, we will discuss the technique of automatic releasing of PMM element into DLSM during calculation. Releasing of particles is treated as a pre-failure process in m-DLSM. A reduced macroscopic strength criterion is used as the releasing criteria. When the state of the PMM element satisfies this criteria, the PMM element is released into DLSM model. In this chapter, a simple maximum strain based criteria is preliminarily used as the releasing rule. PMM element will be released into DLSM model when strain state of the PMM element satisfies:

$$\varepsilon_1 > \gamma\varepsilon_t^* \tag{5.32}$$

where ε_1 is the maximum main strain of the PMM element, ε_t^* is the ultimate strain of the model and γ is a reduction factor which is taken 0.8. When the PMM element is released, it will be removed from the calculation cycle and new released particles will take part in the calculation cycle of DLSM model.

5.4 Examples

5.4.1 Simple tensional test

In this section, a pure tensile loading of a bar of $10\text{mm}\times 10\text{mm}\times 20\text{mm}$ is simulated. The purpose is to test the influence of different coupled models on the simulation results and to validate the correctness of the proposed method. Four m-DLSM models are shown in Figure 5.5. The applied boundary force is 1MPa and the material properties of the model are selected as: the elastic modulus is 12.5GPa and the Poisson’s ratio is 0.3. The first model is a full DLSM model (see Figure 5.5(a)) which is made up from particles with diameter of 1mm. The second one is made up from DLSM model and PMM model with element length of 5mm (see Figure 5.5(b)). The third one is a model only made up from NMM and DLSM (see Figure 5.5(c)). The last one is a three layer model includes NMM model, PMM model and DLSM model (see Figure 5.5(d)). The simulation results of contour map of the displacement in z direction (loaded direction) are shown in Figure 5.6 separately.

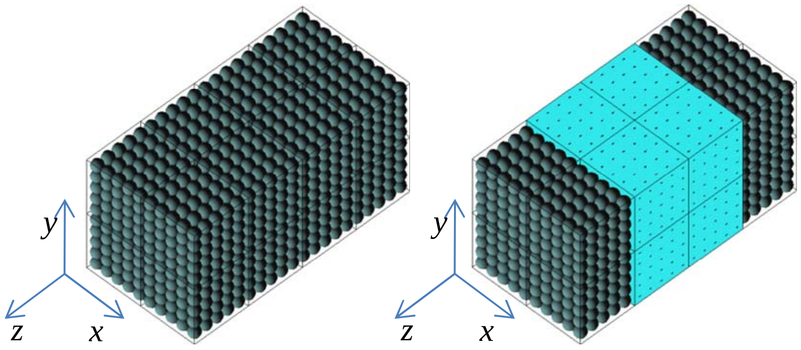

(a) Full DLSM model (b) DLSM & PMM model

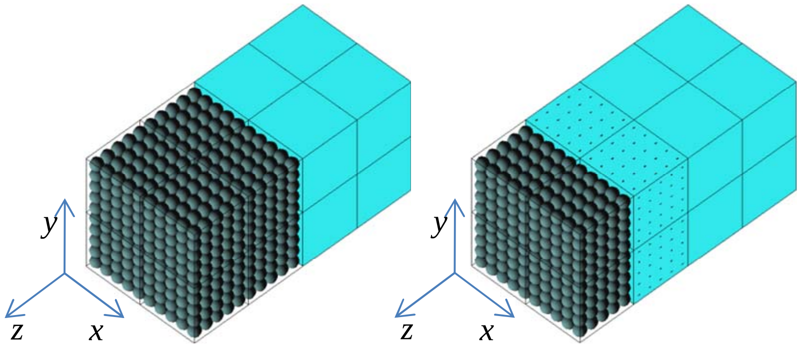

(c) DLSM & NMM model (d) DLSM & PMM & NMM model

Figure 5.5. Different m-DLSM models for the bar under tensile loading problem.

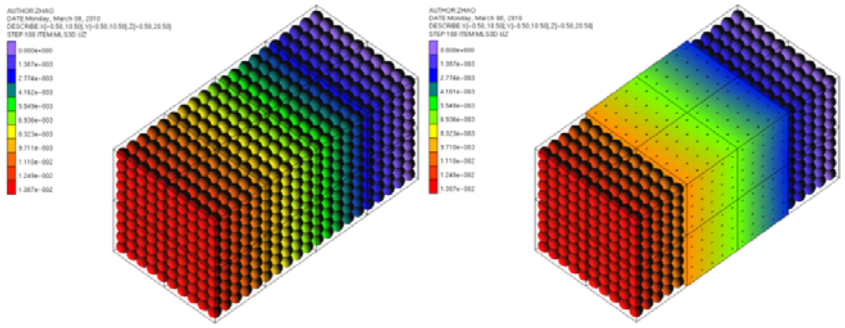

(a) Full DLSM model (b) DLSM & PMM model

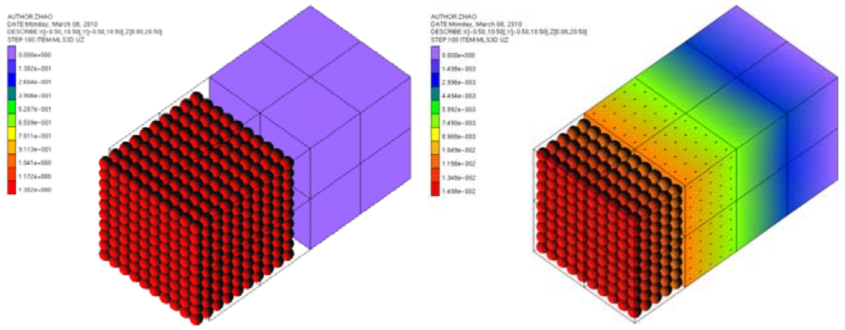

(c) DLSM &NMM model (d) DLSM & PMM & NMM model

Figure 5.6. Contour map of the displacement in z direction for different coupled models.

It can be seen that the DLSM and NMM cannot work together without using the PMM element, the DLSM & NMM model cannot predict the correct displacement distribution (see Figure 5.6(c)). In order to further verify the implementation of the proposed multi-scale method, displacement in z direction of the top surface are recorded and compared with analytical solution. The expected displacement in the z direction of the top surface is given as

$$u^* = \frac{\left(1-\nu^2\right) PL^*}{E} \tag{5.33}$$

where u^* is the expected displacement and L^* is the effective length of the model. The effective length and the predicted displacement in z direction of different m-DLSM models are listed in Table 5.1. It shows that the proposed coupling procedure and its implementation are correct.

Table 5.1. The predicted z direction displacement by different m-DLSM models.

	Full DLSM	DLSM & PMM	DLSM & NMM	DLSM & PMM & NMM
L^* (mm)	18.00	18.00	19.00	19.00
Predicted (mm)	1.36e-2	1.36e-2	1.32	1.47e-2
Excepted (mm)	1.44e-2	1.44e-2	1.52e-2	1.52e-2
Err (%)	5.87	5.87	-	3.28

5.4.2 Uniaxial loading of a plate with a circular hole

A square plate containing a central circular hole is selected another example to further check the ability of m-DLSM on modeling static elastic problems. The dimension of the plate is 100mm×200mm×10mm and a circle hole with radius of 20mm is placed in the center of the plane. The used multi-scale DLSM models are shown in Figure 5.7. Two coupled models are used (DLSM & PMM & NMM model (see Figure 5.7(a)) and PMM & NMM model (see Figure 5.7(b))). The applied boundary force at the top of the plane is 1MPa and the bottom boundary is fixed during calculation. Material properties of the model are taken as: the elastic modulus is 12.5GPa and the Poisson’s ratio is 0.30.

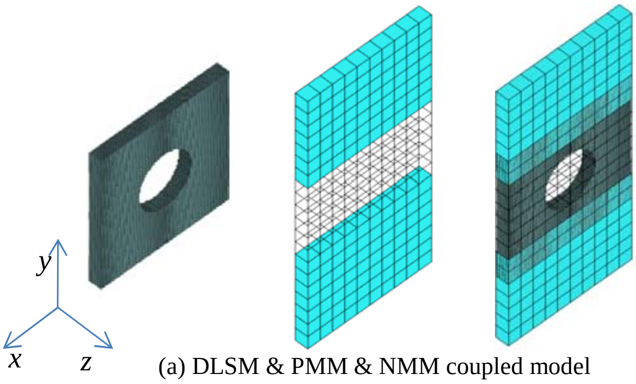

(a) DLSM & PMM & NMM coupled model

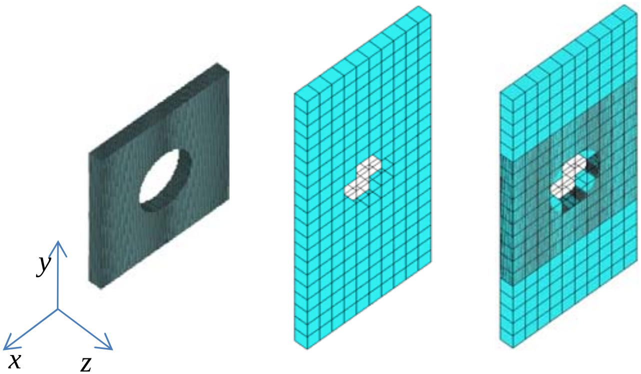

(b) PMM & NMM coupled model

Figure 5.7. Two m-DLSM models for the uniaxial tensile loading of a plate with a circular hole.

The modeling results of contour map of y direction displacement for these two models are shown in Figure 5.8. The same distribution is obtained for different coupled models. It reveals that the PMM model can give a good estimation of the DLSM model for static elastic problems. The displacements in y direction at detection points, A(0.5,100.5,5.5), B(10.5,100.5,5.5), C(20.5,100.5,5.5), D(79.5,100.5,5.5), E(89.5,100.5,5.5) and F(99.5,100.5,5.5), are record and listed in Table 5.2. Similar results are produced by different models.

5.4.3 Wave propagation through elastic bar

This example is used to show the ability of the m-DLSM modeling of wave propagation through elastic bar. The m-DLSM models are shown in Figure 5.9. The model dimension is 20mm×20mm×200mm. The material parameters are taken as: the elastic modulus is 12.5GPa, the Poisson’s ratio is 0.3 and the density is 2650kg/m^3. A half-cycle sinusoidal velocity wave with 100mm/s amplitude and frequency of 50000Hz is applied at the left boundary. Right boundary of the bar is set to be free and other four side boundaries are all fixed in their normal direction.

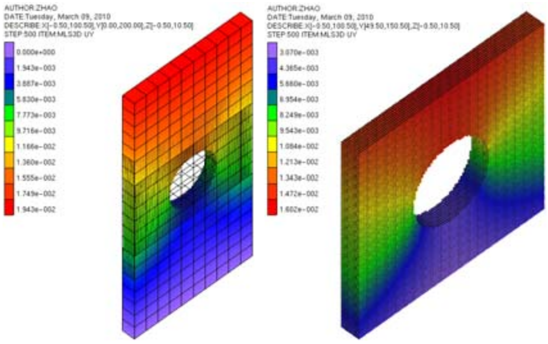

(a) DLSM & PMM & NMM model

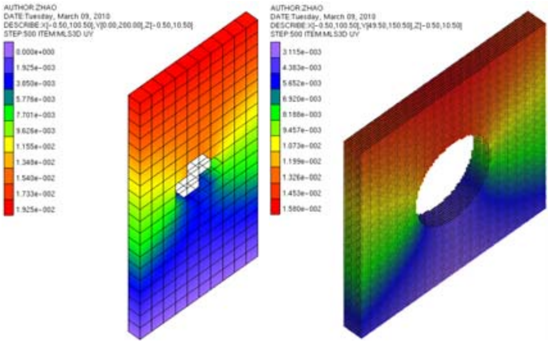

(b) PMM & NMM model

Figure 5.8. The simulation results of the multi-scale DLSM.

Table 5.2. Displacements in y direction of the plane predicted by different models.

	Point A	Point B	Point C	Point D	Point E	Point F
DLSM & PMM & NMM (mm)	9.58e-4	9.60e-4	9.62e-4	9.60e-4	9.60e-4	9.58e-4
PMM & NMM (mm)	9.50e-4	9.52e-4	9.53e-4	9.53e-4	9.52e-4	9.50e-4
Percentage difference (%)	0.84	0.83	0.94	0.73	0.83	0.84

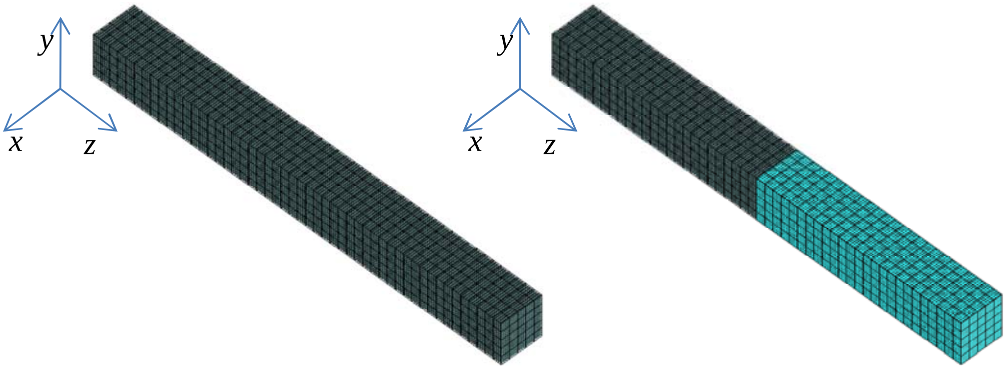

(a) full DLSM model

(b) DLSM & PMM model

Figure 5.9. Used m-DLSM models for the wave propagation through elastic bar problem.

Figure 5.10 and Figure 5.11 show the contour map of the particle velocity in z direction for the full DLSM model and DLSM & PMM coupled model. The propagation and reflection of the wave can be observed clearly for these two models.

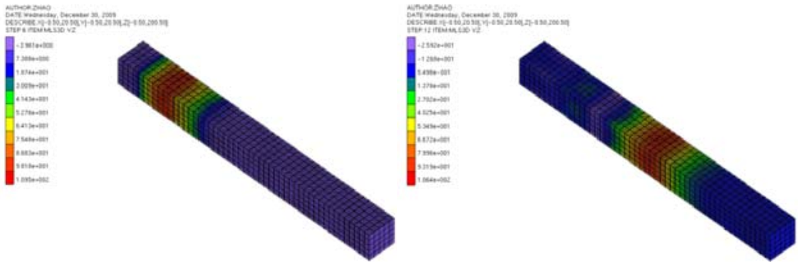

(a) t=5μs (b) t=12μs

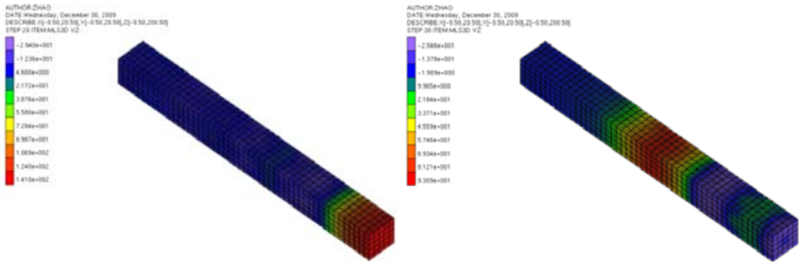

(c) t=20μs (d) t=30μs

Figure 5.10. The process of wave propagation through elastic bar predicted by full DLSM model.

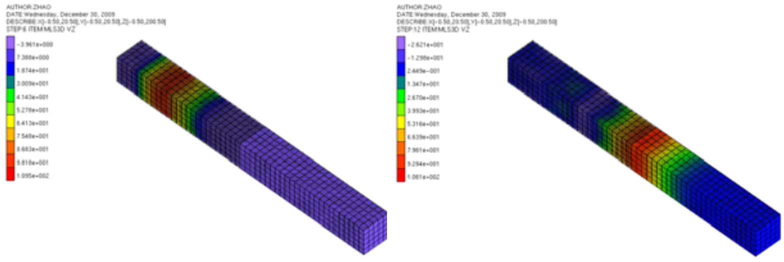

(a) t=5μs (b) t=12μs

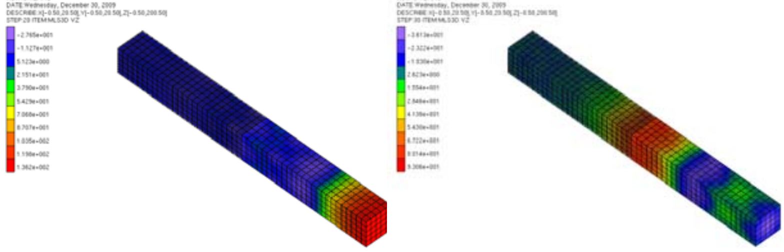

(c) t=20μs (d) t=30μs

Figure 5.11. The process of wave propagation through elastic bar predicted by DLSM & PMM model.

Four detection points, A(5.5,5.5,0.5), B(5.5,5.5,50.5), C(5.5,5.5,150.5) and D(5.5,5.5,199.5), are placed in the bar to record the wave propagated through the model. The recorded waves at these points for different models are shown in Figure 5.12. The DLSM & PMM model produces slightly different wave forms at some detection points. The reason is that the PMM element size is larger than the particle size of DLSM. This will cause some high frequency parts of the wave to be filtered out in the DLSM & PMM model. Even so, both the wave form and the amplitude are in good agreement between two models. This example shows that m-DLSM can well predict the process of dynamic loads transmitted through elastic body.

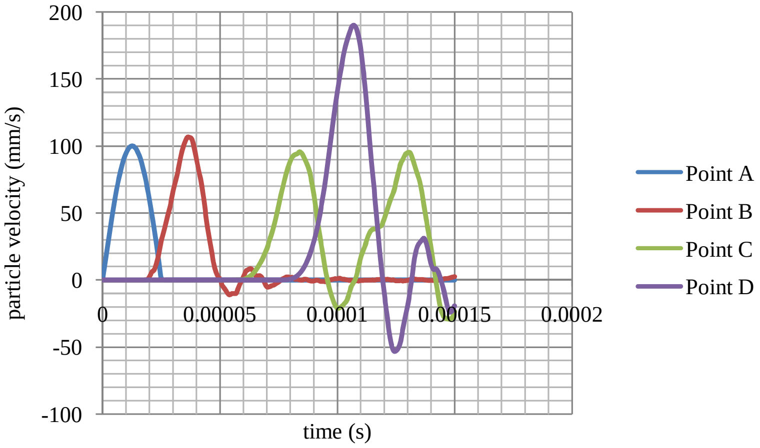

(a) Full DLSM model

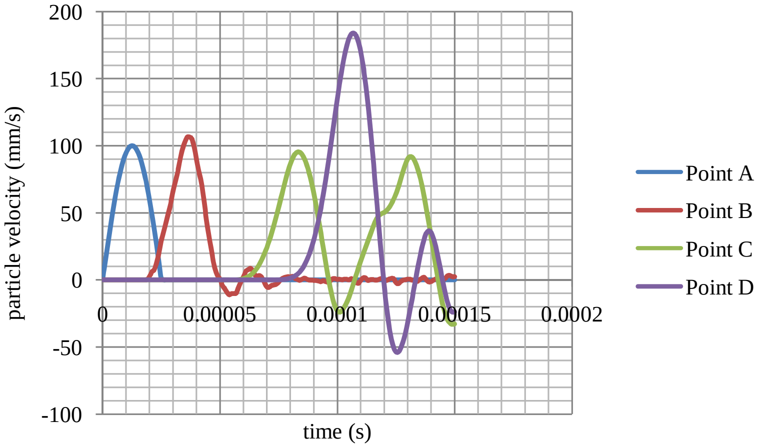

(b) DLSM & PMM model

Figure 5.12. Simulation results of the wave propagation by m-DLSM.

5.4.4 Progressive failure of a solid specimen with a side notch

A solid specimen with a side notch as shown in Figure 5.13 is simulated by the m-DLSM. The mechanical constants of the material are elastic modulus 12.5GPa, Poisson's ratio 0.3 and density 2650kg/m^3. The particle size of the DLSM model is taken as 1mm and the manifold element length is taken as 5mm. The dimension of the solid specimen is 100mm×200mm×5mm and the dimension of the notch is 20mm×5mm×5mm. The ultimate strain for the PMM element is taken as 4×10^{-4} and the reduction factor for the releasing criteria is taken 0.8. The ultimate deformation of the lattice bond in DLSM is given as 5×10^{-4}mm. The applied force on the top boundary is taken as 1MPa and the bottom boundary is fixed.

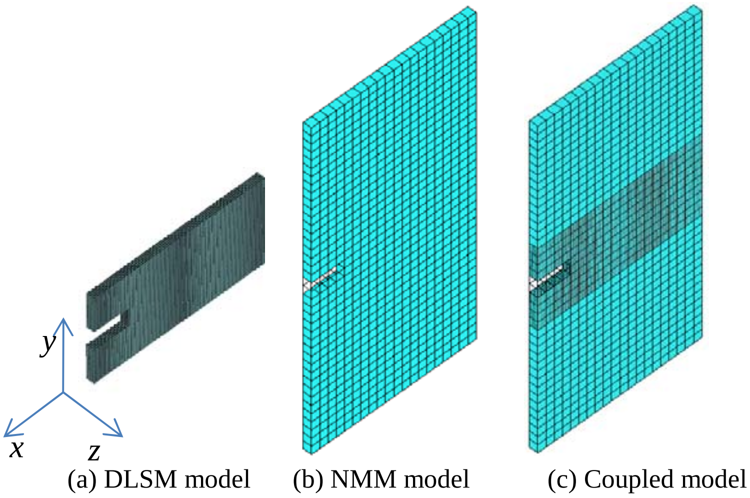

(a) DLSM model (b) NMM model (c) Coupled model

Figure 5.13. The multi-scale model for a solid specimen with a side notch under tensile loading problem.

During computation, the PMM elements near the notch will be firstly transformed into DLSM model. Then, the DLSM will be further broken and finally to form a fracture. Figure 5.14 shows the process of the PMM elements releasing into DLSM particles. The contour maps of y displacement for six stages are also presented in Figure 5.15. With regard to the failure patterns obtained, the simulation gives a realistic description of the fracture process of the notched solid specimen under tensile loading. This example shows the ability of m-DLSM on automatically releasing the macroscopic model (PMM elements) to microscopic model (DLSM particles). This is only a simple example to show the ability of the proposed method on modeling crack propagation problem. In following, the m-DLSM will be used to one example related to rock dynamics engineering application.

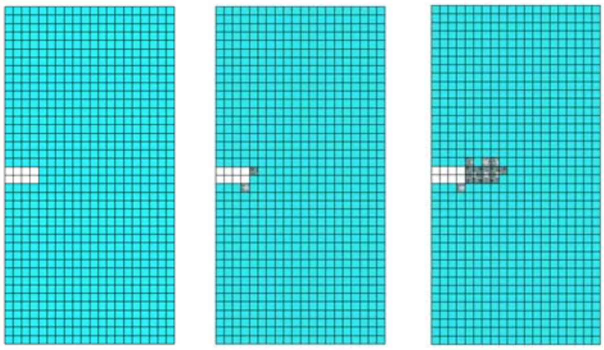

(a) step=10 (b) step=20 (c) step=30

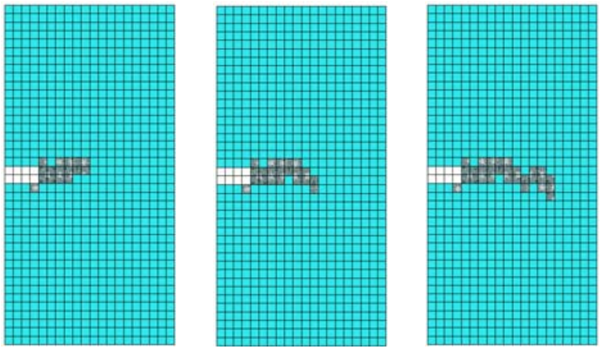

(d) step=40 (e) step=50 (f) step=60

Figure 5.14. Releasing process of PMM elements of the m-DLSM during calculation.

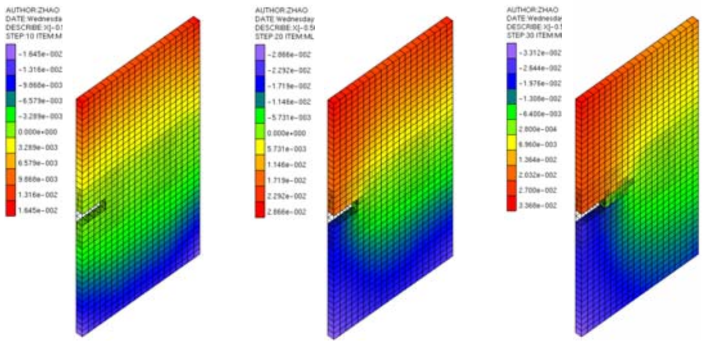

(a) step=10 (b) step=20 (c) step=30

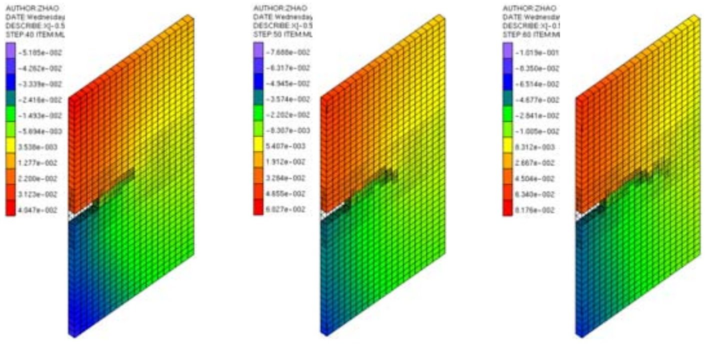

(d) step=40 (e) step=50 (f) step=60

Figure 5.15. Contour map of the y direction displacement at different steps.

5.45 Dynamic failure of tunnel under blasting loading

As multi-scale model can largely reduce computing time required by micro numerical model, it is possible to deal some engineering problems which cannot be handled by the micro model. Following, the blasting wave propagation through rock mass and the influence of discontinuous on the failure pattern of tunnel under blasting wave will be simulated by the m-DLSM.

The dynamic failure of tunnel under blasting loading is an important issue for rock engineering, e.g., the safety of the existing tunnel must be well estimated when a new adjacent tunnel is under blasting. Field tests are performed to study this kind problems and reported in [20, 21]. In this section, one example on blasting wave propagation through tunnel will be modeled by the m-DLSM code. Figure 5.16 shows the computational model and boundary conditions for the problem. The dimension of the model is 50m×50m×2m and particle size is 0.0125m. For DLSM model, more than two million particles are needed to build this computational model. It means more than ten millions of bonds information need to be stored, which is surely an inaccessible problem for the normal PC. However, only about half million particles are used for the m-DLSM model (see Figure 5.17). Blasting load is applied at the left

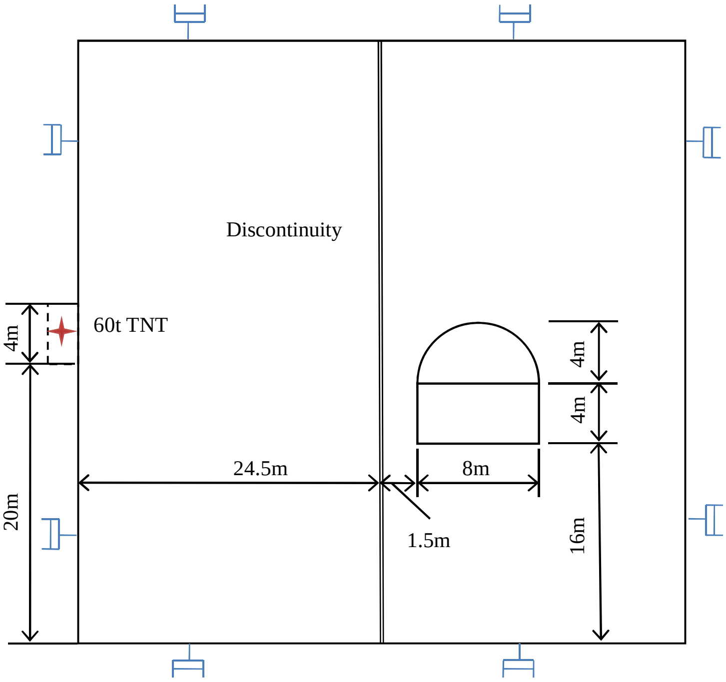

Fiugre 5.16. Computational model of the tunnel under blasting loading problem.

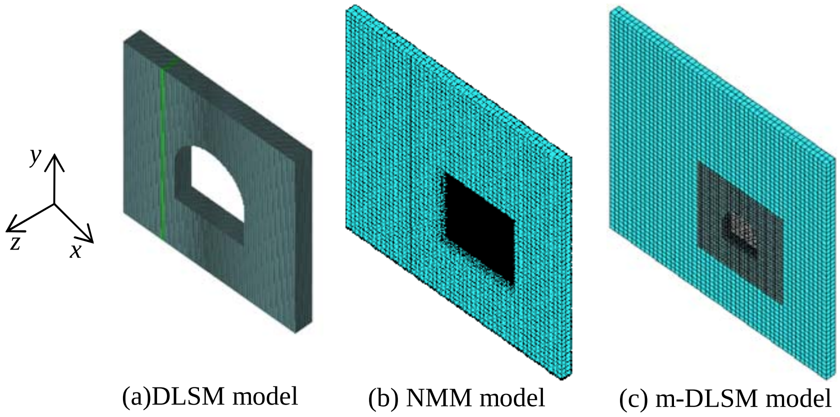

(a)DLSM model (b) NMM model (c) m-DLSM model

Figure 5.17. The multi-scale model for the tunnel under blasting loading problem.

of the boundary from 20m to 24m in vertical to simulate an explosion chamber of $4\text{m}\times2\text{m}$. The blasting wave is simplified as a triangular over-pressure history with two phases. The maximum over-pressure $P_{\max}$ is equal to 30.23MPa, and the duration of rise phase t_1 and the total duration t_2 are 0.5 and 2.5 ms, respectively. The material properties of the rock are taken as: the elastic modulus is 74GPa, the Poisson’s ratio is 0.2 and the density is 2650 kg/m^3. The ultimate bond deformation is taken as 2.5e-5m, which is calculated based on the tensile strength of Bukit Timah granite. Discontinuity is represented by setting a material layer with weaker elastic modulus, where the weakness ratio are taken as 1.0 (Model I), 0.5 (Model II), 0.1(Model III) and 0.01 (Model IV). The modeling results of Model III are shown in Figure 5.18, in which the left side of the tunnel is broken under blast loading (see Figure 5.18).

The failure patterns of m-DLSM models with different stiffness of discontinuity are shown in Figure 5.19. The failure pattern of the tunnel is influenced by the stiffness of the discontinuity. When the stiffness is decreasing, the damage degree will first increase and then decrease. This is an interesting result and reveals that the damage of tunnel under dynamic loading can be released through pre-setting some weak discontinuity/cavern. Due to the weak enough discontinuity leads the spalling be happen far away from the tunnel (see Figure 8.19 (d)).

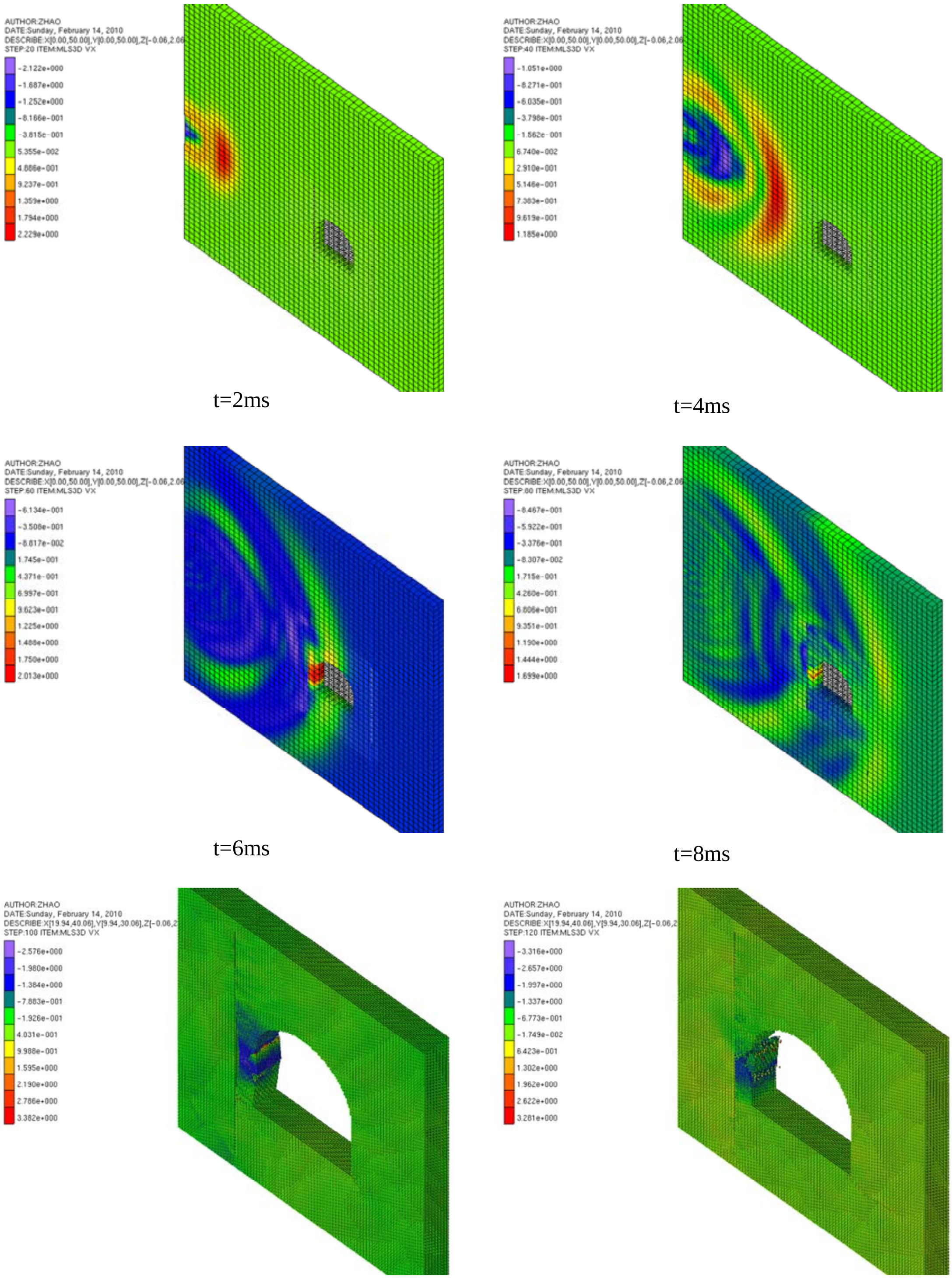

t=2ms t=4ms

t=6ms t=8ms

t=10ms t=12ms

Figure 5.18. Failure process of the tunnel surface under blasting loading (Model III).

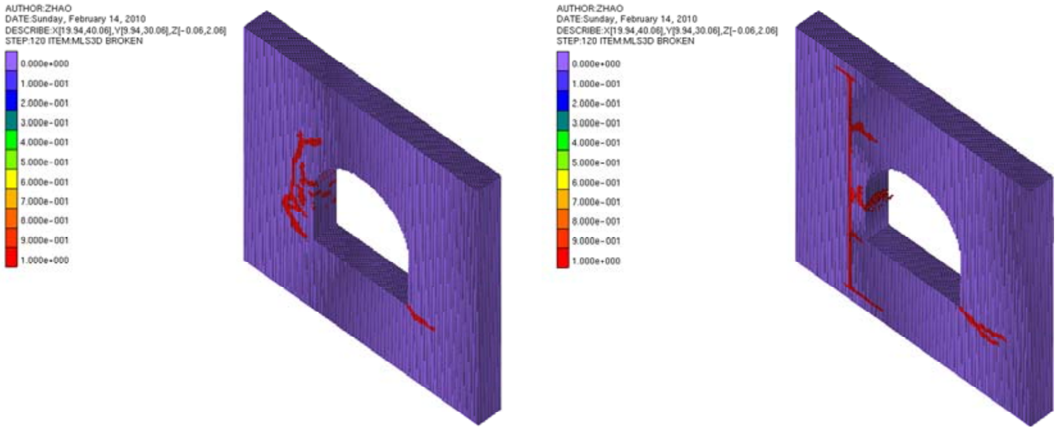

(a) Model I

(b) Model II

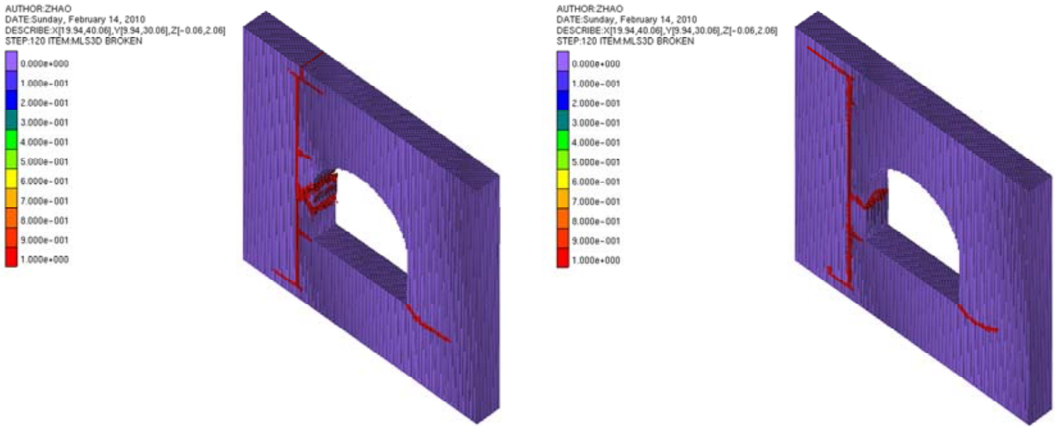

(c) Model III

(d) Model IV

Figure 5.19. Failure modes of different models under blasting loading.

This example proves that the m-DLSM can be used to solve previously inaccessible problem for DLSM in a normal PC. However, more complex constitutive model for bond springs in DLSM and more advanced representation techniques of discontinuities are needed for further applying m-DLSM on real engineering problems.

5.5 Conclusions

This chapter presents a multi-scale lattice spring model, in which DLSM is coupled with NMM. A three layer structure is used to combine DLSM and NMM. The PMM is proposed to bridge between DLSM and NMM. PMM element simplify the contact detection between the particle in DLSM model and NMM model and also serves as the cushion layer. The proposed multi-scale model can be used to model dynamic fracturing problems and wave propagation problems. A few examples are provided to validate the correctness of the proposed coupling procedure. One memory demanding problem for DLSM is solved by the m-DLSM on a normal PC. Results show that the proposed coupling method and implementation are correct.

5.6 Reference

1. Guidault PA, Allix O, Champaney L, Navarro JP. A two-scale approach with homogenization for the computation of cracked structures. Comput Struct, 2007; 85: 1360-1371.

2. Hettich T, Hund A, Ramm E. Modeling of failure in composites by X-FEM and level sets within a multiscale framework. Comput Meth Appl Mech Eng, 2008; 197: 414-424.

3. Xiao SP, Belytschko T. A bridging domain method for coupling continua with molecular dynamics. Comput Meth Appl Mech Eng, 193: 1645-1669.

4. Darve F, Nicot F. On incremental non-linearity in granular media: phenomenological and multi-scale views (Part I), Int. J. Numer. Anal. Meth. Geomech., 2005; 29:1387–1409

5. Mullins M., Dokainish MA. Simulation of the (001) Plane crack in alpha-iron employing a new boundary scheme. Philos Mag A., 1982; 46: 771-787.

6. Tadmor EB, Ortiz M, Phillips R. Quasicontinuum analysis of defects in solids. Philos Mag A., 1996; 73: 1529-1563.

7. Hasnaoui A, Van Swygenhoven H, Derlet PM. Dimples on nanocrystalline fracture surfaces as evidence for shear plane formation. Sci., 2003; 300: 1550-1552.

8. Ma J, Lu H, Wang B, Hornung R, Wissink A, Komanduri R. Multiscale simulation using generalized interpolation material point (GIMP) method and molecular dynamics (MD). Comput Model Eng Sci., 2006;14: 101-117.

9. Haidar K, Dube JF, Pijaudier-Cabot G. Modelling crack propagation in concrete structures with a two scale approach. Int J Numer Anal Meth Geomech., 2003; 27: 1187-1205.

10. Belytschko T, Loehnert S, Song JH. Multiscale aggregating discontinuities: A method for circumventing loss of material stability. Int. J. Numer. Meth. Engng, 2007; 73(6): 869-894

11. Wilcox DC. Perturbation methods in the computer age. Wood & Jones, 1995.

12. Kilburn CRJ. Multiscale fracturing as a key to forecasting volcanic eruptions. J Volcanol Geoth Res, 2003; 125: 271-289.

13. Zhao GF, Zhao J. Microscopic numerical modelling of the dynamic strength of brittle rock. Proc. ICADD9 Analysis of Discontinuous Deformation: New Developments and Applications, 2009; 633-640.

14. Zhao GF, Fang J, Zhao J. A 3D distinct lattice spring model for elasticity and dynamic failure, Int J Numer Anal Meth Geomech, 2010 ; DOI: 10.1002/nag.930.

15. Shi GH. Manifold method of material analysis, Transactions of the 9th Army 11 Conference on Applied Mathematics and Computing, U.S. Army Research Office, Minneapolis, MN, 1991; 57–76.

16. Zhao GF, Ma GW, Zhang HH, Zhao J. A numerical manifold method for plane micropolar elasticity. Int J Comp Meth., 2010; 7:151–166..

17. Shi GH. Discontinuous deformation analysis- a new numerical model for the static and dynamics of

block systems. Civil Engineering. Berkeley, University of California. Ph. D Thesis 1988.

18. Kurumatani M, Terada K. Finite cover method with mortar elements for elastoplasticity problems. Comput Mech., 2005;36:45-61.
19. Cundall PA, Strack ODL. A discrete numerical model for granular assemblies. Geotech., 1979; 29:47-65.
20. Zhou Y, Zhao J, Chong K., Seah CC. Dynamic response and tunnel damage from explosion loading. Proc. International Symposium on Defence Construction 2002; Singapore.
21. Zhou YX, Arnfinn J. Internal separation distances for underground explosives storage in hard rock. Tunnel Under Space Tech 2009; 24:119-125.

Chapter 6

DLSM modeling dynamic failure of rock material

In this chapter, capability of DLSM on modeling dynamic failure of rock material is enhanced and verified. Firstly, advanced micro constitutive laws of bond springs are developed and implemented into DLSM to consider the complex mechanical behavior of rock material. Then, influence of the new implemented micro constitutive law on macro mechanical behavior of DLSM model is preliminarily studied through uniaxial tensile and compressive tests. Empirical equations of the relationship between parameters of the micro constitutive law and macro failure parameters of the material, e.g., uniaxial tensile strength and fracture energy, are derived. These equations can be used to determine the micro parameters under given macro failure parameters or predict the macro mechanical behavior when input micro parameters are known. One problem of dynamic crack propagation through PMMA plate is modeled by DLSM with the new developed micro constitutive law. The results are compared with Cohesive FEM solution. When considering crack bifurcation, the results of DLSM model using a rate independent micro constitutive law produce similar results as that of using a rate-dependent constitutive law. Following this, the dynamic fracture toughness test on the Laurentian granite is modeled, where only rate independent constitutive law is adopted. The modeling results are comparable with the experimental data. It should be mention that all input micro parameters are directly computed from the developed empirical equations based on the static macro failure parameters, i.e., tensile strength and fracture energy, provided in literature. Finally, conclusions on DLSM modeling of dynamic failure of rock are presented.

6.1 Advanced micro constitutive law for DLSM

Micro constitutive law for bond spring used in Chapter 4 is the simplest brittle linear one, which is not enough to describe the complex mechanical behavior of rock material. An advanced micro constitutive law will be developed in this section. The non-linear cohesive laws used in FEM [1, 2] and the constitutive law used for contact joints in DEM [3, 4] can be used as reference in the development of new micro constitutive laws. However, these constitutive laws used in both FEM and DEM are not suitable to be implemented directly into DLSM because the stiffness of shear spring is the Poisson's ratio dependent and can be negative or zero. That is the reason of why damage based constitutive laws are used instead. Here, two micro failure modes, tensile failure of the normal spring and shear failure of the shear spring, are considered. Firstly, consider the force-deformation relationship of the normal spring satisfying the curve as shown in Figure 6.1(a), where u_n represents the normal deformation of the bond spring, and u_n^* is the ultimate deformation, δ_1 is the ratio of the deformation at hardening point to the ultimate deformation, and δ_2 is the ratio of the deformation at softening point to the ultimate deformation. It can be seen that the curve can fully represent the linear stage, the hardening stage and the softening stage of the micro normal bond spring. Instead of directly providing the force displacement relationship, a damage variable function is defined as:

$$D(u_n) = 1 - \frac{\bar{k}(u_n)}{k_0} \tag{6.1}$$

where k_0 is the initial stiffness and $\bar{k}(u_n)$ is the secant modulus when the bond deformation is u_n. The damage variable is initially equal to zero when the spring is intact and finally turn into one when the spring is totally broken. The damage variable function corresponding to Figure 6.1(a) is shown in Figure 6.1(b). Given a damage variable function, the force-displacement relationship can easily be obtained as

$$f(u_n) = \left(1 - D(u_n)\right) k_0 u_n \tag{6.2}$$

where $f(u_n)$ is the spring interaction force when the spring deformation is u_n. Different micro constitutive laws can be realized by developing different damage variable functions. In this section, displacement is used as the synonyms of deformation. Micro parameters $u_n^*, \delta_1, \delta_2, K^{red}$ are selected to identify the damage variable function for the normal spring. The K^{red} is the ratio of secant modulus at softening point to the initial stiffness. Damage variable functions are constructed based on these parameters. For example, a tri-linear micro constitutive law for the normal spring is given as

$$D(u_n) = D'\left(\frac{u_n^*}{u_n}\right) = D'(\alpha) = \begin{cases} 0 & 0 \le \alpha \le \delta_1 \\ 1 - \alpha\delta_1 - \left(K^{red}\delta_2 - \delta_1\right)\left(1 - \alpha\delta_1\right) \big/ \left(\delta_2 - \delta_1\right) & \delta_1 < \alpha \le \delta_2 \\ 1 - K^{red}\delta_2\left(\alpha - 1\right) \big/ \left(1 - \delta_2\right) & \delta_2 < \alpha \le 1 \end{cases}$$

(6.3)

where α is introduced to simplify the formulation of the equation. Equation (6.3) can be rewritten into the force-displacement form as

$$f=\begin{cases} k_0u_n & u_n\le\delta_1u_n^* \\ k_0u_n^*\delta_1+\dfrac{\left(k_{red}u_n^*\delta_2-k_0u_n^*\delta_1\right)\left(u_n-u_n^*\delta_1\right)}{u_n^*\delta_2-u_n^*\delta_1} & \delta_1u_n^*<u_n\le\delta_2u_n^*a \\ k_{red}u_n^*\delta_2\dfrac{u_n^*-u_n}{u_n^*-u_n^*\delta_2} & \delta_2u_n^*<u_n\le u_n^* \end{cases} \tag{6.4}$$

where $k_{\mathrm{red}}=k_0K^{red}$. Assume $k_0=1$, the force-displacement relationship given by equation (6.4) is plotted in Figure 6.2. Different constitutive models can be obtained by setting K^{red} to different values (see Figure 6.2). K^{red} is a dimensionless parameter, which can be regarded as the secant stiffness at the softening point when $k_0=1$. The brittle linear constitutive law is the special case of the tri-linear constitutive law when $\delta_1=\delta_2=1.0$ and $K^{red}=0$. The widely used bi-linear constitutive law is obtained when $\delta_2=1.0$ and $K^{red}=0$. Using the damage variable function, nonlinear micro constitutive law has also been developed. An example is given as follows:

$$D\left(u_n\right)=D'\left(\frac{u_n}{u_n^*}\right)=D'\left(\alpha\right)=\begin{cases} 0 & 0\le\alpha\le\delta_1 \\ 1-\alpha\delta_1-\beta\alpha\left(K^{red}\delta_2-\delta_1\right)de^{1+d} & \delta_1<\alpha\le\delta_2 \\ 1-\left(1-\beta\right)\alpha\delta_1-\beta\delta_2K^{red}\left(\alpha-1\right)/\left(1-\delta_2\right) & \delta_2<\alpha\le1 \end{cases}$$

(6.5)

where $\beta=0.3$ and $d=\left(\alpha-\delta_1\right)/\left(\delta_2-\delta_1\right)$. The corresponding force-displacement relationship for $k_0=1$ is shown in Figure 6.3.

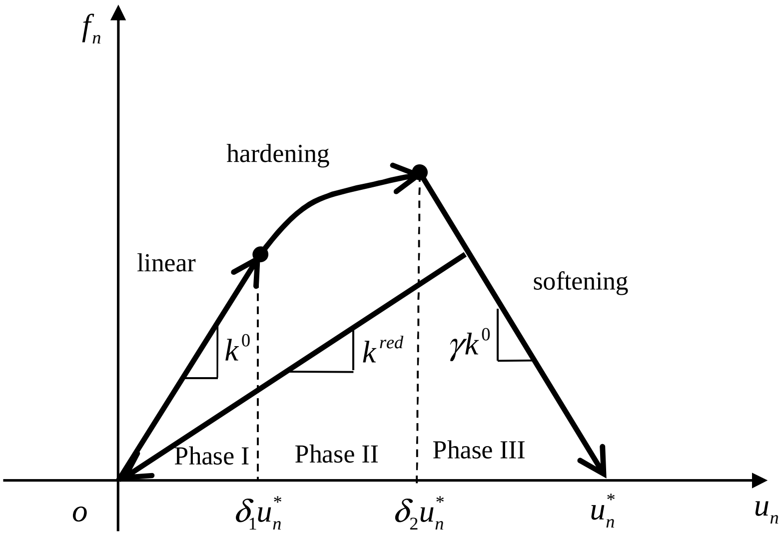

(a) Force-deformation curve of normal spring

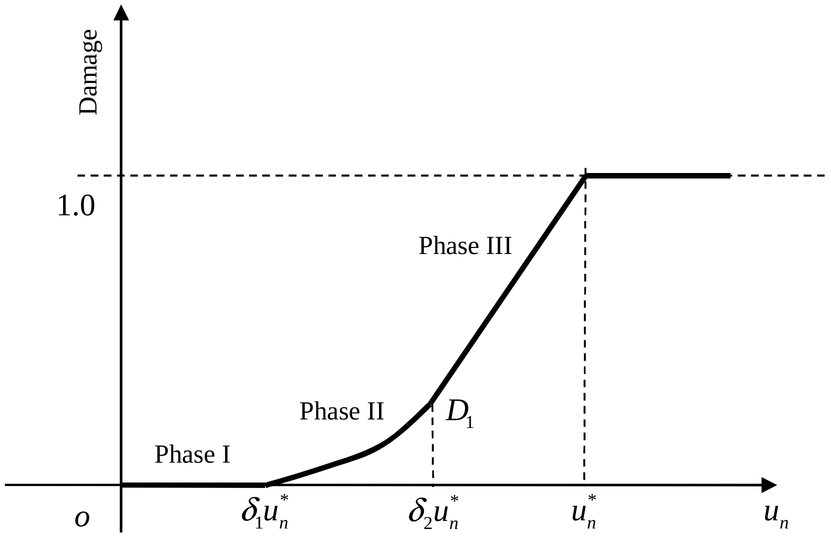

(b) Damage variable function

Figure 6.1. The force-deformation relationship and the damage variable function for the normal spring.

As it is mentioned before, the shear spring is a dilemma for directly implementing force based constitutive law into DLSM. Fortunately, this problem no longer exists when the damage variable function is used. Because shear deformation of the bond can always be computed and the damage variable still has physical meaning even the stiffness of shear spring is negative or zero. The used damage variable function and the corresponding non-dimensional parameters for shear spring are taken from those for normal spring, but with u_n^* replaced by u_s^* which is the ultimate shear deformation. The damage variable function for shear spring is shown in Figure 6.4, which is formally the same as that for normal spring but in a symmetrized form.

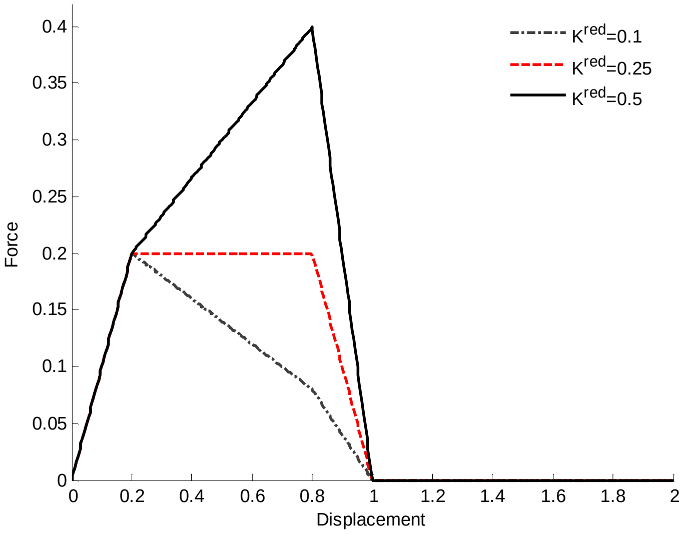

Figure 6.2. Force-displacement curve of the tri-linear constitutive law under different values of K^{red}.

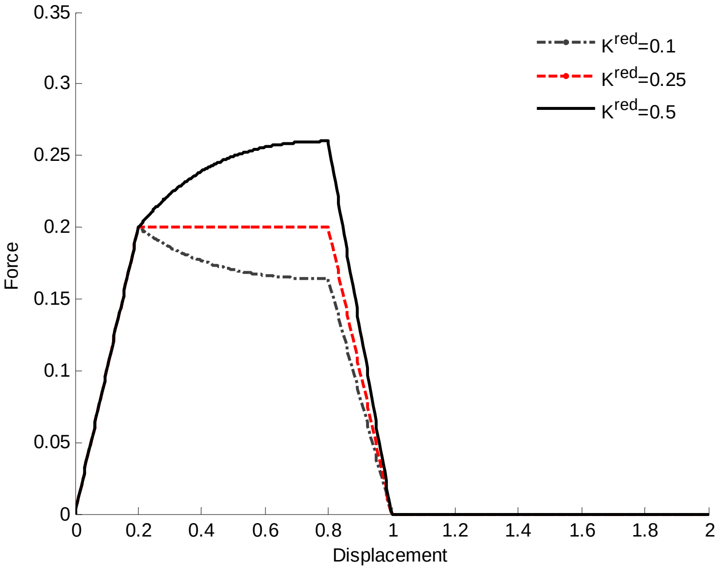

Figure 6.3. Force-displacement curves of the nonlinear constitutive law under different values of K^{red}.

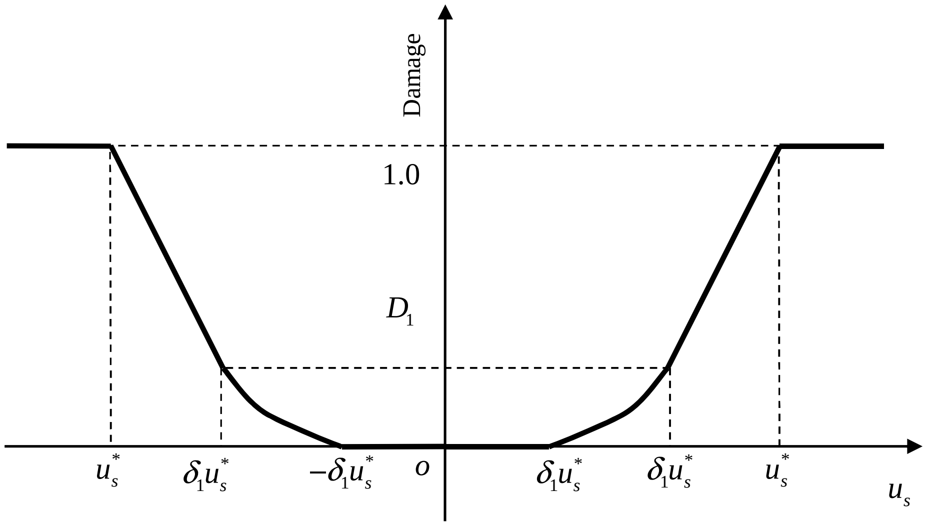

Figure 6.4. Damage evolution function of the shear spring.

Finally, there are five parameters, $u_n^*, u_s^*, \delta_1, \delta_2, K^{red}$, for these new developed micro constitutive laws for DLSM. The actual damage of bond can be caused by the shear failure or the tensile failure or the interaction between the two. Therefore, a damage variable of bond is defined as:

$$D^{bond} = \max\left(D^n, D^s\right) \tag{6.6}$$

where D^n and D^s are the damage variables for normal spring and shear spring, respectively. The force displacement-relationship for bond spring is modified accordingly as

$$f(u) = \left(1 - D^{bond}\right) ku \tag{6.7}$$

where *k* represents either the stiffness of normal spring or the stiffness of shear spring. The proposed constitutive laws can fully consider the non-linear response of bond in DLSM. The influence of the five parameters of the micro constitutive model on the final macro mechanical behavior of the DLSM model will be studied in following sections.

6.2 Uniaxial tensile and compressive failure of DLSM model

In this section, a preliminary study on failure behavior of DLSM model is performed. Figure 6.5 shows computational models used for the uniaxial tensile and compressive tests. Unlike in experiments, cubic specimen rather than cylindrical one is used. The reason is that cube is the most ideal basic unit for stress analysis. Moreover, boundary conditions can easily be applied in numerical modeling for specimen of any shape. Therefore the cubic specimen is adopted for the study here. The dimension of the computational model is 20mm×20mm×20mm (see Figure 6.5). The mechanical properties of the modeled material are as follows: the elastic modulus is 36GPa, the Poisson’s ratio is 0.25 and the density is 2450kg/m^3. A velocity of ±1mm/s is applied on the top and bottom surface to produce a piston-like uniaxial tensile/compressive loading.

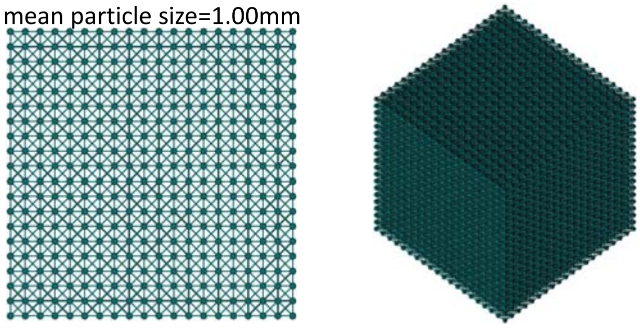

(a) The cubic lattice structure (the left is plane view)

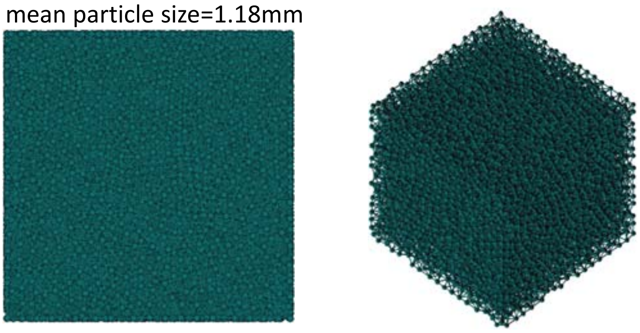

(b) The random lattice structure (the left is plane view)

Figure 6.5. Computational models to study failure behavior of DLSM under uniaxial tensile/compressive loading.

In the following, failure behavior of DLSM is studied. Influences of lattice structure type, the Poisson’s ratio, micro failure mode and micro constitutive law are investigated. Details of these considered factors are given below.

- *The lattice type*

Two lattice structures, regular lattice and random lattice, are considered (seen in Figure 6.5).

- *The Poisson's ratio*

The Poisson's ratio influences stiffness of shear spring, thus may influence the macro tensile behavior of the DLSM model. Here, three representative values, 0.20, 0.25 and 0.30 are considered for the uniaxial tensile test.

- *Micro failure mode*

Two micro failure modes of bond, tensile failure and shear failure, are investigated for the uniaxial tensile test.

- *Micro constitutive law*

It is interesting to see whether macro loading curve of DLSM will have the same shape as the input micro constitutive law. Some parameters of the used tri-linear and nonlinear constitutive law are listed in Table 6.1. The other two parameters are set to $u_n^* = 1e-4\text{mm}$ and $u_s^* = 2\text{mm}$ respectively for model which only consider micro tensile failure and $u_n^* = 2\text{mm}$ and $u_s^* = 1e-4\text{mm}$ for these only considering micro shear failure.

Table 6.1. Parameters of the used micro constitutive laws.

Index	Micro constitutive law	Non-dimensional parameters		
		δ_1	δ_2	K^{red}
C1	Brittle linear	-	-	-
C2	Tri-linear	0.20	0.80	0.10
C3	Tri-linear	0.20	0.80	0.25
C4	Tri-linear	0.20	0.80	0.50
C5	Nonlinear	0.20	0.80	0.10
C6	Nonlinear	0.20	0.80	0.25
C7	Nonlinear	0.20	0.80	0.50

6.2.1 Uniaxial tensile test of DLSM model

Lattice type

Strain stress curves of DLSM with different lattice structures using the brittle linear constitutive law (C1) are shown in Figure 6.6. It is found that the regular lattice model results in an irregular strain stress curve, whereas smooth curve is obtained for the random lattice model.

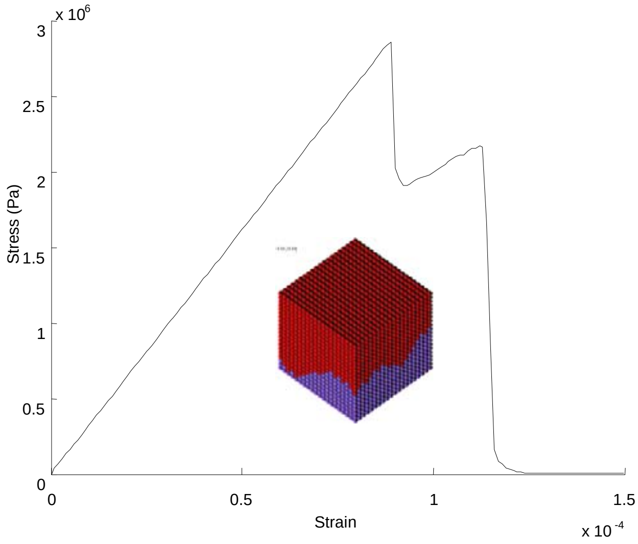

(a) Regular lattice

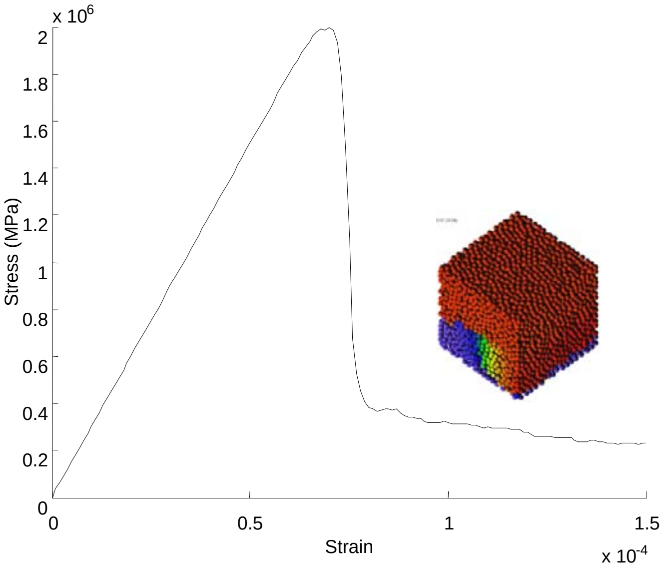

(b) Random lattice

Figure 6.6. Strain stress curves of DLSM models under uniaxial tensile loading.

The Poisson's ratio

Figure 6.7 shows influence of the Poisson's ratio on the DLSM results for the uniaxial tensile test. Different strain stress curves are produced. Difference in tensile strength caused by the Poisson's ratio is negligible for the regular lattice model, while apparent for the random lattice model.

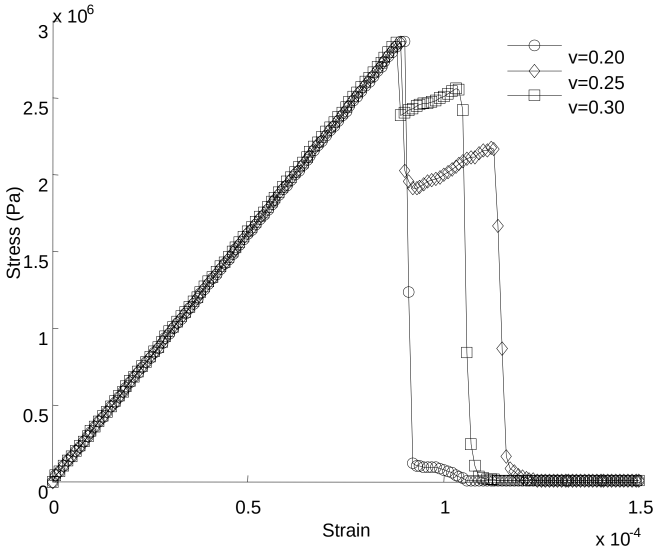

(a) Regular lattice

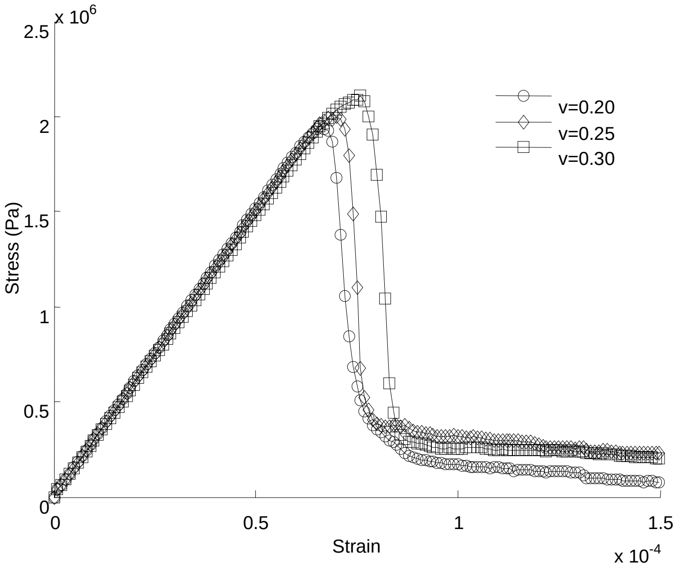

(b) Random lattice

Figure 6.7. Influence of Poisson's ratio on the uniaxial tensile failure of DLSM.

Micro failure mode

The strain stress curve of DLSM considering only the micro shear failure is given in Figure 6.8. It can be seen that the whole model is not collapse under shear micro failure, which means the main micro failure mechanism for uniaxial tensile loading should be the micro tensile failure rather than the micro shear failure. Hence, hereafter, only the micro tensile failure will be considered.

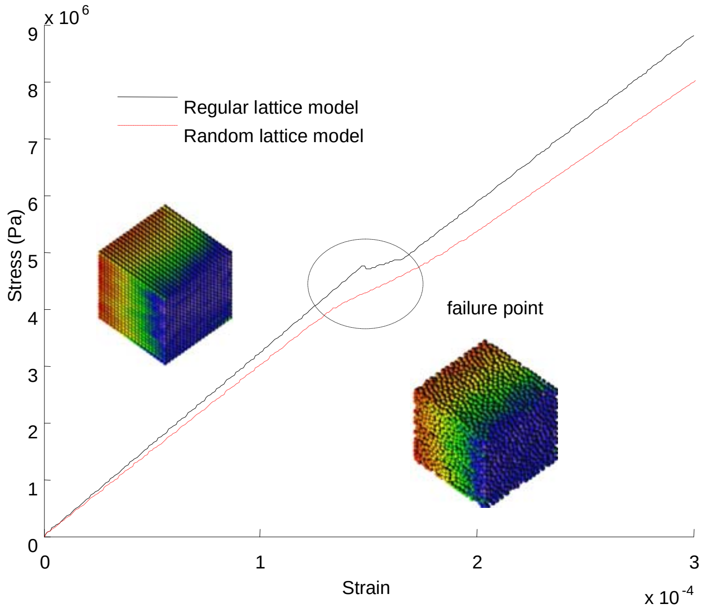

Figure 6.8. Uniaxial tensile failure of DLSM when only considering the shear failure of bond.

Micro constitutive law

Strain stress curves of DLSM models with the new developed micro constitutive laws are shown in Figure 6.9. Curves of the corresponding micro constitutive laws can be seen in Figure 6.2 and Figure 6.3. It can be observed that the obtained strain stress curves are not the same as these of the micro constitutive laws. Overall speaking, both regular and random lattice model produce smooth strain stress curves when the new developed micro constitutive models are used.

6.2.2 Uniaxial compressive test of DLSM model

The mechanism of compressive failure of rock material is much complex than that of tensile failure, which involves not only detachment between grains but also sliding of contact and generation of new contacts. In this section, the uniaxial compressive test is performed to show the compressive failure behavior of DLSM. Influence of lattice type and micro constitutive law on the strain stress curve of DLSM is investigated. Results show that the current DLSM is not suitable for modeling compressive failure of rock material.

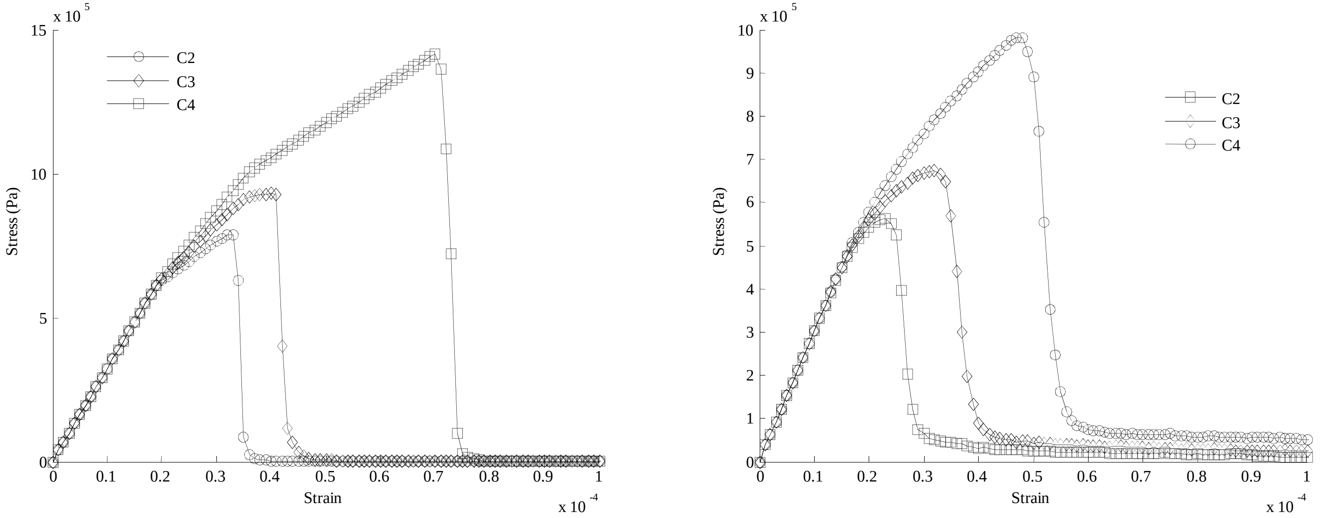

(a) Regular lattice with tri-linear law

(b)Random lattice with tri-linear law

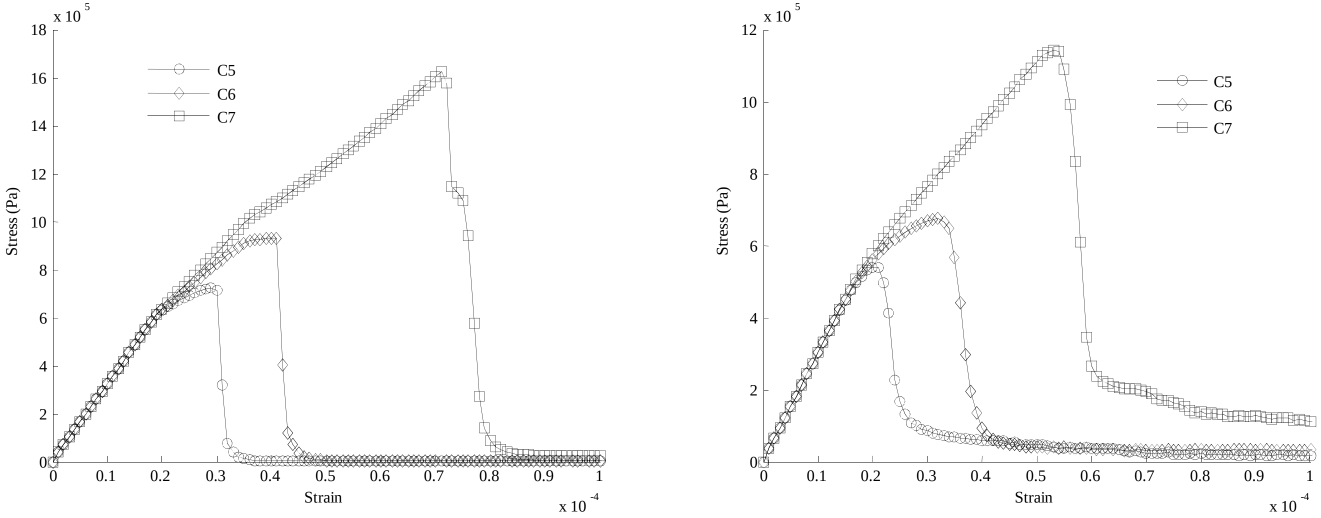

(c) Regular lattice with nonlinear law

(d)Random lattice with nonlinear law

Figure 6.9. Strain stress curves of DLSM with different micro constitutive laws for the uniaxial tensile loading test.

Lattice type

The strain stress curves for the uniaxial compressive test on DLSM with different lattice structures are shown in Figure 6.10. It can be seen that irregular strain stress curve is obtained for the regular lattice model, whereas smooth curve is obtained for the random lattice model.

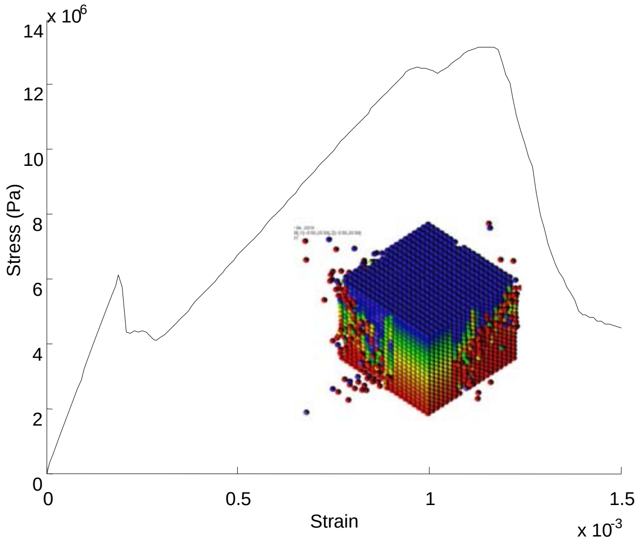

(a) Regular lattice

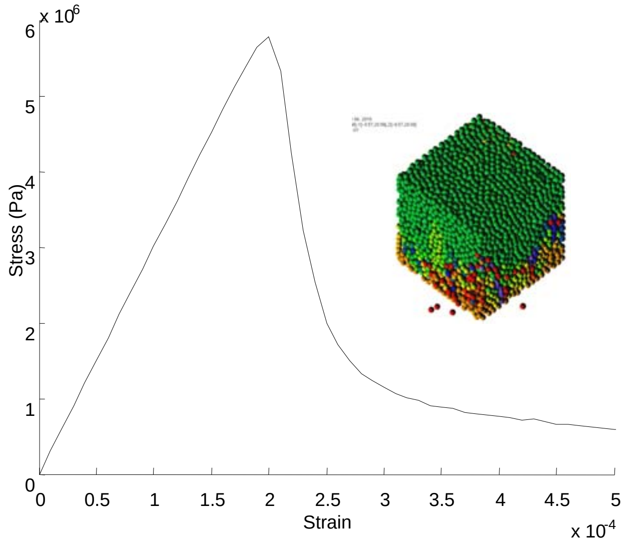

(b) Random lattice

Figure 6.10. Strain stress curves for the uniaxial compressive test of DLSM with different lattice structures.

Micro constitutive law

Influence of micro constitutive law on compressive failure of DLSM is not as apparent as that in the uniaxial tensile test in the previous section. Figure 6.11 shows the strain stress curves of the uniaxial compressive test on DLSM models with different micro constitutive laws. For the regular lattice model, there are two peaks in the strain stress curve, whereas the curve is much smooth and only has one peak for the random lattice model. There is no apparent hardening stage in the strain stress curve of DLSM under the uniaxial compressive test. This is different from the uniaxial tensile test.

As a summary, the uniaxial tensile strength and compressive strength of different DLSM models are listed in Table 6.2. As mentioned before, all models only consider the micro tensile failure of bond. However, DLSM model can have a compressive strength, which is different from the RMIB model in Chapter 3. The reason is that the uniform deformation assumption in RMIB is released in DLSM. Unfortunately, the ratio of compressive strength to tensile strength for DLSM is much lower than that for rock materials (typically around 10-12), e.g., it is around seven for the regular lattice model and three for the random lattice model. For this reason, it can be concluded that DLSM is only applicable to study the tensile failure of rock material, and further improvement of DLSM for modeling compressive failure is needed.

Table 6.2. Results of uniaxial tensile and compressive test of DLSM models.

Index	$\sigma_t^{macro}\left(MPa\right)$		$\sigma_c^{macro}\left(MPa\right)$		$\sigma_c^{macro}/\sigma_t^{macro}$	
	Regular	Random	Regular	Random	Regular	Random
C1	2.86	1.99	13.179	5.79	4.61	2.90
C2	0.79	0.56	6.56	1.69	8.35	3.01
C3	0.93	0.67	8.19	2.11	8.82	3.13
C4	1.41	0.98	8.81	2.93	6.24	2.99
C5	0.72	0.54	6.94	1.49	9.59	2.77
C6	0.93	0.67	7.26	2.11	7.81	3.13
C7	1.62	1.14	10.66	3.42	6.56	3.00

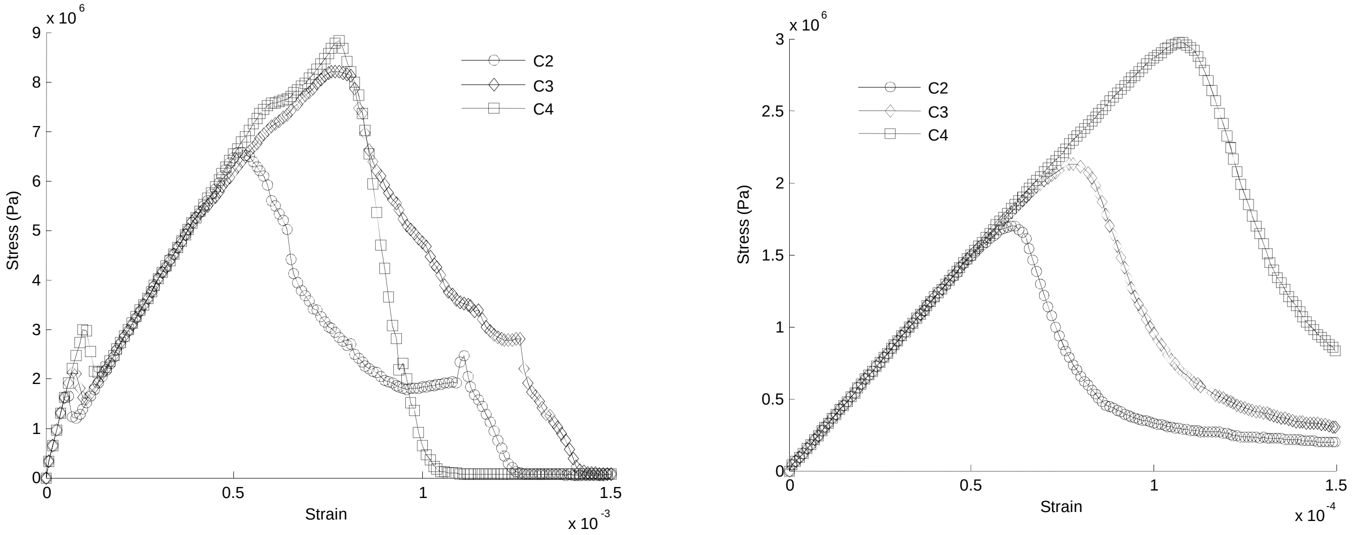

(a) Regular lattice with tri-linear law

(b) Random lattice with tri-linear law

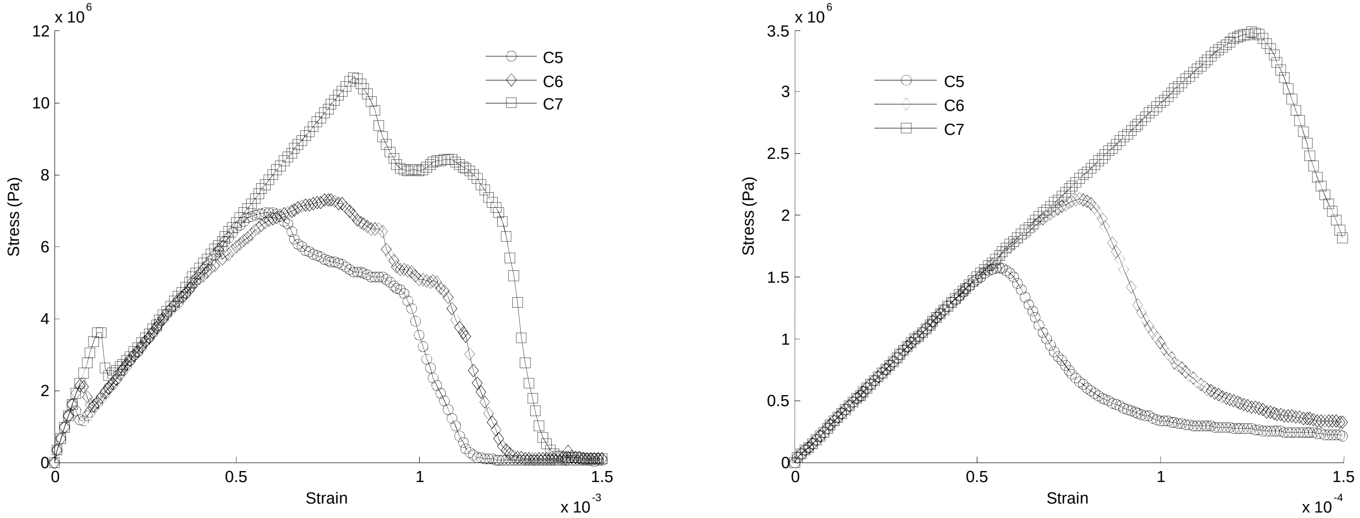

(c) Regular lattice with nonlinear law

(d) Random lattice with nonlinear law

Figure 6.11. Strain stress curves of DLSM models with different micro constitutive laws under uniaxial compressive loading.

6.2.3 Relationship between micro and macro failure parameters

Two issues will be discussed in this section. The first one is how to predict the macro strength of DLSM model when its micro constitutive model parameters are known. The second is how to determine the parameters in the micro constitutive model when macro material parameters are given. In order to solve these two problems, the relationship between micro and macro parameters need to be established. In Chapter 3, Equation (3.24) provides the relationship between the micro tensile parameter u_n^* and macro tensile strength σ_t^{macro}. However, it is not applicable for DLSM as the new developed micro constitutive laws involved non-linear terms. A simplified concept is used to derive empirical relationships between microscopic constitutive parameters and macroscopic failure parameters (see Figure 6.12). Assuming the representative spring length is l^* (equal to the mean particle size) and the representative volume is a cubic box with length of l^*. In this case, the cubic box behaves like the micro spring. Relationship between the bond strength f^* and the macroscopic tensile strength σ_t^{macro} can be given as

$$\sigma_t^{marco} = \frac{f^*}{l^{*2}} \tag{6.8}$$

Then, bond deformation at failure point can be obtained as

$$\hat{u}_n^* = \frac{f^*}{\hat{k}^*} = \frac{\sigma_t^{marco} l^{*2}}{\hat{k}^*} \tag{6.9}$$

where $\hat{k}^*$ is the secant modulus at failure point (see Figure 6.12). The initial stiffness of the representative spring is obtained as El^*. For the brittle linear micro constitutive law used in Chapter 4, from Equation (6.9) we have (see Figure 6.12)

$$u_n^* = \frac{f^*}{\hat{k}^*} = \frac{\sigma_t^{marco} l^*}{E} \tag{6.10}$$

Now, all parameters of the brittle linear micro constitutive law for normal spring can be directly obtained from Equation (6.10). However, for these new developed constitutive laws, there are two possible peak points, i.e., the hardening point and the softening point. For the hardening point, we have

$$u_n^* \delta_1 = \frac{f^*}{\hat{k}^*} = \frac{\sigma_t^{marco} l^*}{E} \tag{6.11}$$

For the softening point, we obtain

$$u_n^* \delta_2 = \frac{f^*}{\hat{k}^*} = \frac{\sigma_t^{marco} l^*}{K^{red} E} \tag{6.12}$$

It can be seen that the micro parameters of these new developed constitutive laws cannot be determined only based on the macroscopic tensile strength. However, Equations (6.11) and (6.12) can still be used to predict the macro tensile strength of DLSM model when the micro parameters are known. Figure 6.13 shows the results of the macro tensile strength obtained by DLSM simulation and these predicted by the empirical equations. It can be seen that Equations (6.11) and (6.12) provide a reasonable estimation of the macro tensile strength. Overall speaking, empirical equations work better for the new developed constitutive laws with random lattice structure, for which only about 3% percent difference between the simulated result and the predicted one is observed for C2 and C5.

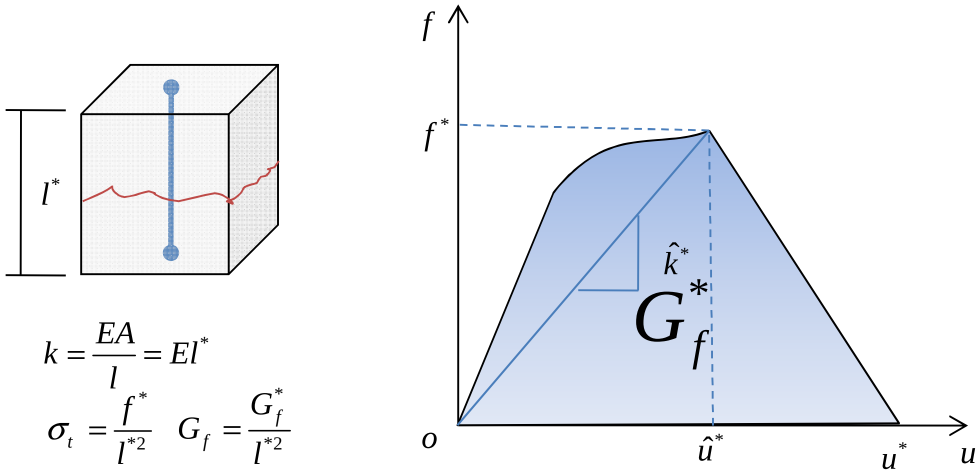

Figure 6.12. Scheme of the relationship between the micro parameters with macro tensile strength and macro fracture energy.

The fracture energy G_f is another macro failure parameter related to tensile failure. Relationship between the micro constitutive parameters and the fracture energy G_f is derived in the following. As shown in Figure 6.12, the relationship between the fracture energy of the representative spring G_f^* and the macro fracture energy G_f can be written as

$$G_f = \frac{G_f^*}{l^{*2}} \tag{6.13}$$

where G_f^* is the energy needed to break the spring, which equals the area under the constitutive curve. For the tri-linear constitutive law, it can be obtained as

$$G_f^* = \frac{1}{2} E l^* u_n^{*2} \left(\delta_1^2 + \left(\delta_2 - \delta_1\right)\left(\delta_1 + K^{red}\delta_2\right) + K^{red}\left(1-\delta_2\right)\delta_2 \right) \tag{6.14}$$

The fracture energy G_f of DLSM with the tri-linear micro constitutive law can be obtained from Equations (6.13) and (6.14) as

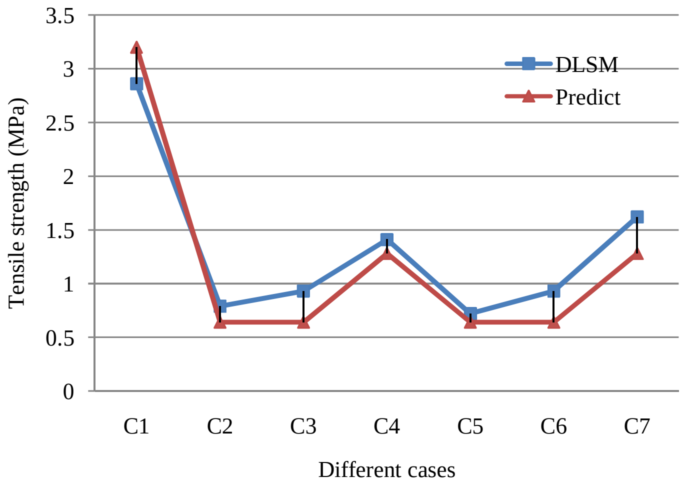

(a) Regular lattice

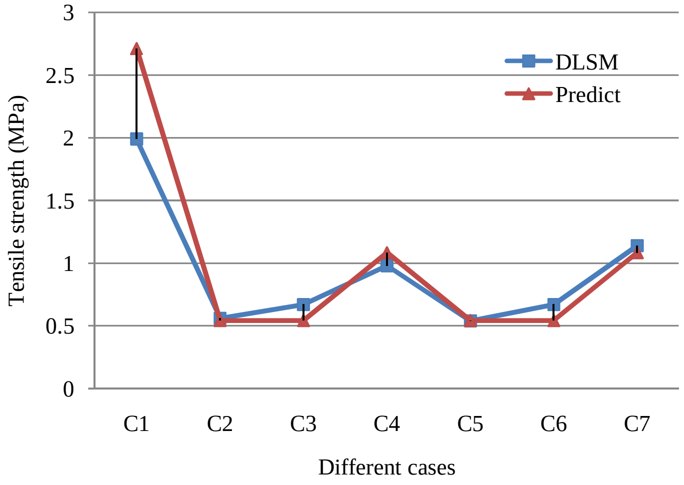

(b) Random lattice

Figure 6.13. Tensile strength predicted from empirical equations and DLSM modeling.

$$G_f = \frac{1}{2}\bar{\lambda}E\left(\frac{u_n^*}{l^*}\right)^2 l^* \tag{6.15}$$

where $\bar{\lambda}$ is a dimensionless coefficient which reads

$$\bar{\lambda} = \delta_1^2 + \left(\delta_2 - \delta_1\right)\left(\delta_1 + K^{red}\delta_2\right) + K^{red}\left(1 - \delta_2\right)\delta_2 \tag{6.16}$$

With only two empirical equations, it is still not possible to determine all the involved micro parameters for the tri-linear constitutive law. However, the micro parameters for the bi-linear case of the tri-linear constitutive law can be determined. In this case ($K^{red} = 0$ and $\delta_2 = 1$), Equation (6.14) becomes

$$G_f^* = \frac{1}{2}El^*\left(u_n^*\delta_1\right)u_n^* \tag{6.17}$$

Now, together with Equation (6.11), all micro constitutive parameters, u_n^* and δ_1, can be determined uniquely from the macro tensile strength σ_t^{marco} and fracture energy G_f. In the following simulations, the tri-linear constitutive law will be used and its parameters will be determined based on these empirical equations.

6.3 Dynamic crack propagation of PMMA plate

6.3.1 The experimental work

In this section, the experimental work done by Shioya and Zhou [5] on dynamic crack propagation of pre-strained PMMA strips is modeled by DLSM. The PMMA rectangular plate was under tension by a universal test machine before crack start to propagate (see Figure 6.14(a)). A small straight crack is cut by a razor when the specimen reaching a given load level. Then, the small crack will propagate dynamically across the specimen along a straight line. Details on the test setup and the experimental results and the numerical simulation through cohesive FEM are presented in [6]. In this section, the test is simulated through DLSM with the tri-linear micro constitutive law.

6.3.2 DLSM modeling

The used DLSM model is shown in Figure 6.14, where length l = 32 mm, height h = 16 mm, and thickness t = 1 mm, and a 4 mm long edge crack is set along the centerline. The model is made of 512000 rigid spherical particles with diameter of 0.1mm. Before crack propagates, the plate is preloaded by a prescribed tensile displacement along its upper and lower boundaries.

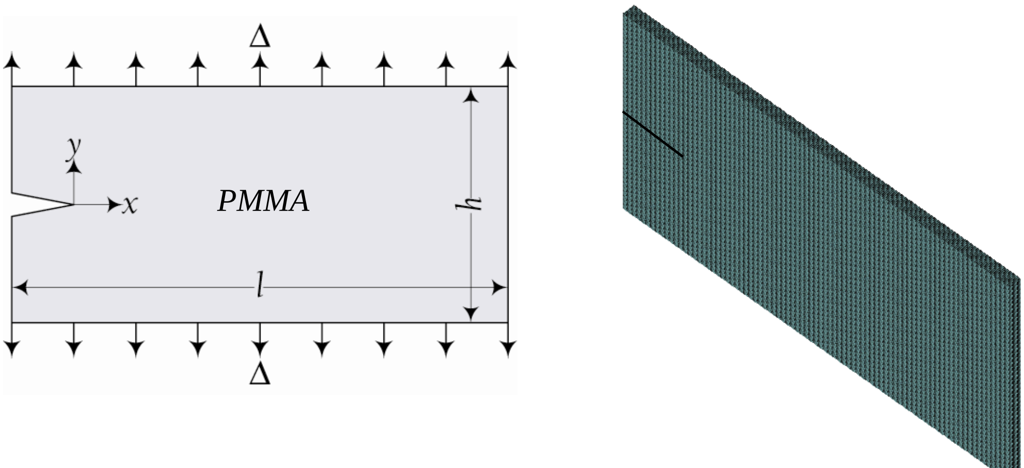

(a) Geometry model and boundary condition (b) DLSM model

Figure 6.14. DLSM model of the dynamic cracking test on PMMA plate.

The strain energy (per unit area) stored in the pre-strained plate W is calculated as:

$$W = \frac{1}{2}\frac{E(2\ )^2}{h} = \frac{2E\ ^2}{h} \tag{6.18}$$

where E is the elastic modulus of the PMM plate, Δ is the prescribed displacement load and h is the height of the plate. Crack propagation under six different loadings is simulated. The prescribed boundary displacement Δ is chosen to be 0.06 mm (case A), 0.08 mm (case B), 0.10 mm (case C), 0.12 mm (case D), 0.14 mm (case E), and 0.16 mm (case F). According to Equation (6.18), the stored energy W will be 1391 N/m, 2472 N/m, 3863 N/m, 5562 N/m, 7571 N/m, and 9888 N/m, respectively. The initial strain and stress state of the plate under prescribed tensile displacement is obtained through a static analysis. Then, the explicit dynamic calculation is performed without changing the boundary conditions.

The time step in the numerical modeling is selected as 0.01µ*s*. This value is very small and guarantees numerical stability. The PMMA material parameters are considered as: density = 1180 kg/m^3, Young's modulus E = 3090 *MPa*, and Poisson's ratio= 0.35. According to elastic wave equations [7], longitudinal, shear and Rayleigh surface wave speed are obtained as C_P = 1618 *m/s*, C_S = 985 *m/s*, and C_R = 906 *m/s*, respectively. The experimentally obtained limiting velocity, V_L, is about 70% of C_R. The tensile strength σ_t^{macro} and the material fracture energy G_f are taken to be 75.0 MPa and 300 N/m, respectively. The special bi-linear case of the tri-linear micro constitutive law is used (see Figure 6.15).

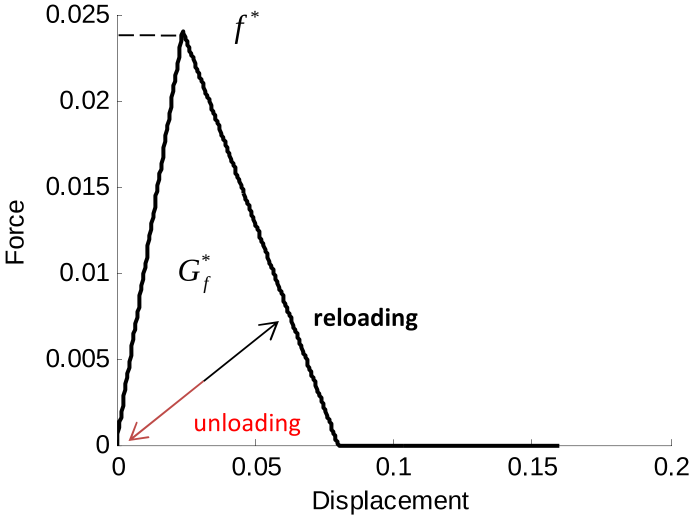

Figure 6.15. The used micro constitutive law in DLSM.

Micro parameters are determined by using Equations (6.11) and (6.17) as $u_t^* = 0.08\text{mm}$, $\delta_1 = 0.3$, $\delta_2 = 1.0$ and $K^{red} = 0$. DLSM modeling results are presented in Figure 6.16 in terms of the crack tip position versus time. Crack speed of each case is evaluated by the average slope of the corresponding curve and is shown in Figure 6.17.

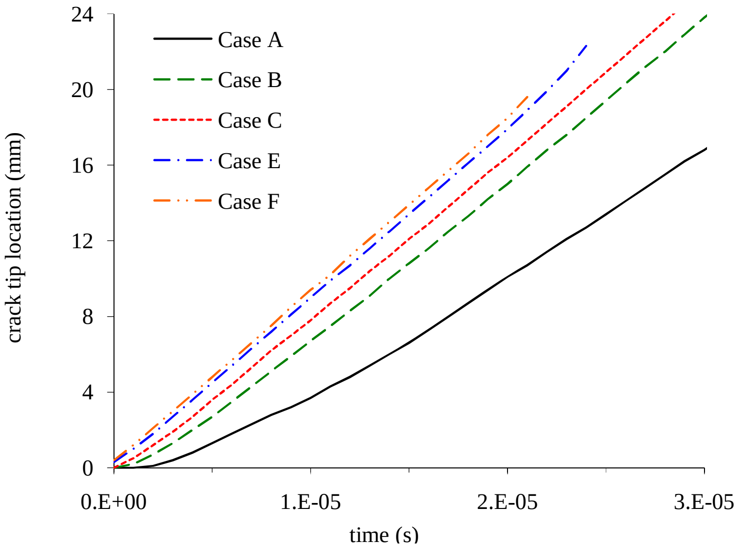

Figure. 6.16. The crack tip location versus time under different pre-loading cases.

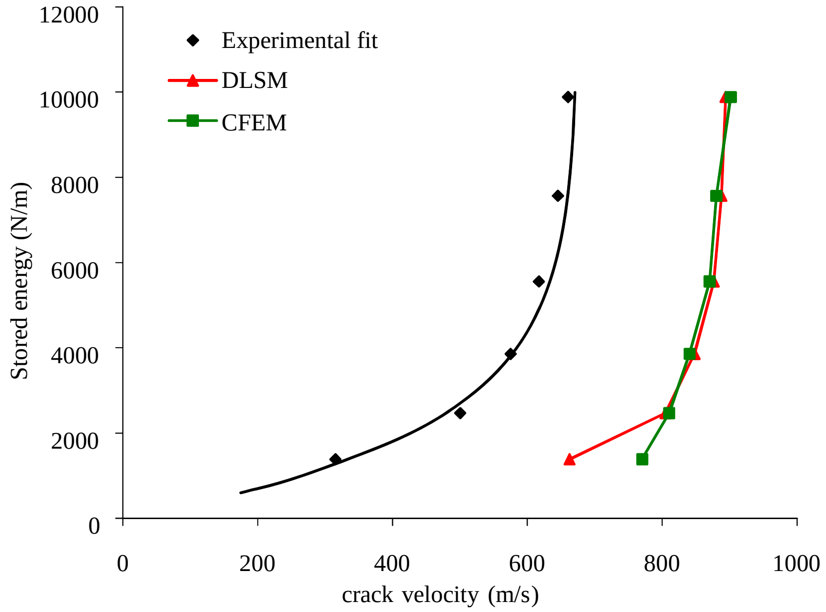

Figure 6.17. The results of crack velocity predicted by DLSM and cohesive FEM in [6].

It is shown that DLSM produces similar results as these obtained by cohesive FEM [6]. Both cohesive FEM and DLSM fails to predict the correct experimental observation when rate independent constitutive law is used. In order to obtain the correct dynamic crack propagation velocity, a full rate-dependent constitutive law developed by Kazerani and Zhao [8] is implemented into DLSM, where both the spring ultimate deformation and the spring strength are dependent on the spring deformation rate. Figure 6.18 shows the results of DLSM with the rate-dependent cohesive law. The RD-P means partial rate-dependent constitutive law and RD-F stands for full rate-dependent constitutive law. It turns out that crack velocity predicted by DLSM with RD-F agree with the experimental data. Details of the implemented rate-dependent model and DLSM modeling results are given in [9].

No crack branching is permitted in the previous model, the crack only propagates in a straight path. In experiments, the crack is allowed to propagate arbitrarily through the plate and experimental results show that branching fracture is produced for the case of the highest value of prescribed loading (Δ= 0.16 mm). DLSM modelling which allow crack to arbitrarily propagate through the PMMA plate are modeled for Case F by using the tri-linear micro constitutive law. The used micro parameters are listed in Table 6.3. The corresponding curves of the used micro constitutive law are plotted in Figure 6.19 for four different cases, and the areas of these curves are the same which represent the facture energy of 300N/m. Simulation results are shown in Figure 6.20, where crack bifurcation is observed like in the experiment.

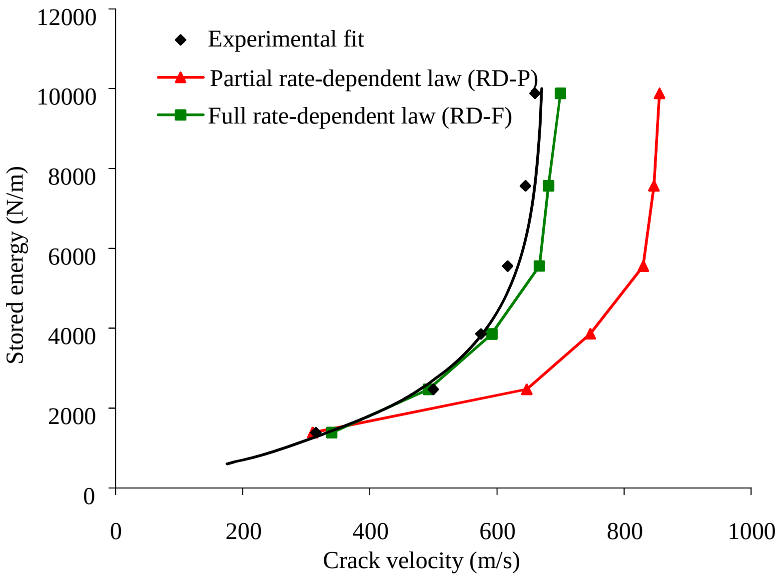

Figure 6.18. Results of dynamic crack velocity predicted by DLSM with rate-dependent constitutive law.

Table 6.3. Parameters of the tri-linear micro constitutive law for DLSM modeling of dynamic crack bifurcation in PMMA plate.

	$u_n^*\left(\mathrm{mm}\right)$	δ_1	δ_2	K^{red}
C1	8.00e-2	0.30	0.5	0.43
C2	6.79e-2	0.36	0.54	0.67
C3	6.18e-2	0.39	0.69	0.57
C4	5.57e-2	0.44	0.87	0.5

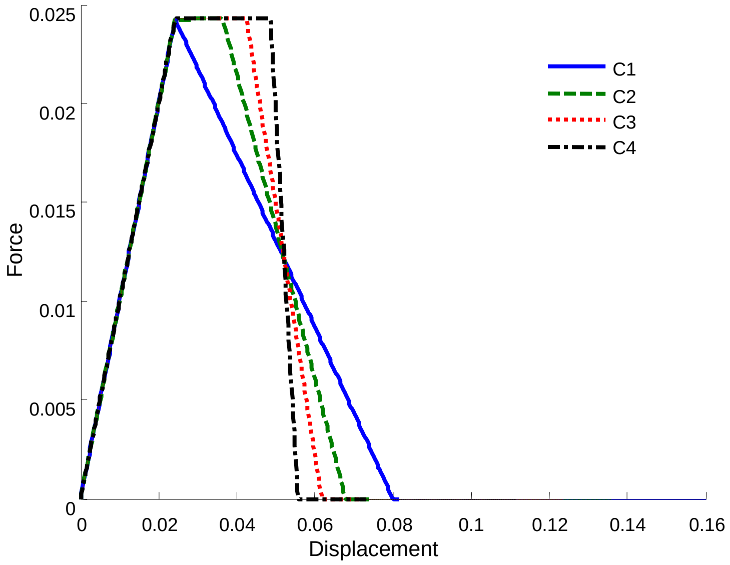

Figure 6.19. Force displacement curves of the tri-linear micro constitutive law with different parameter sets.

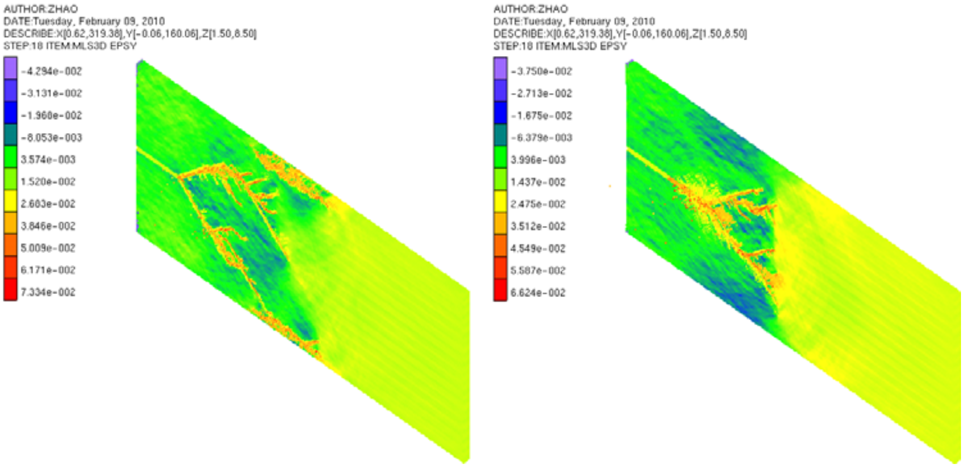

(a) C1 (b) C2

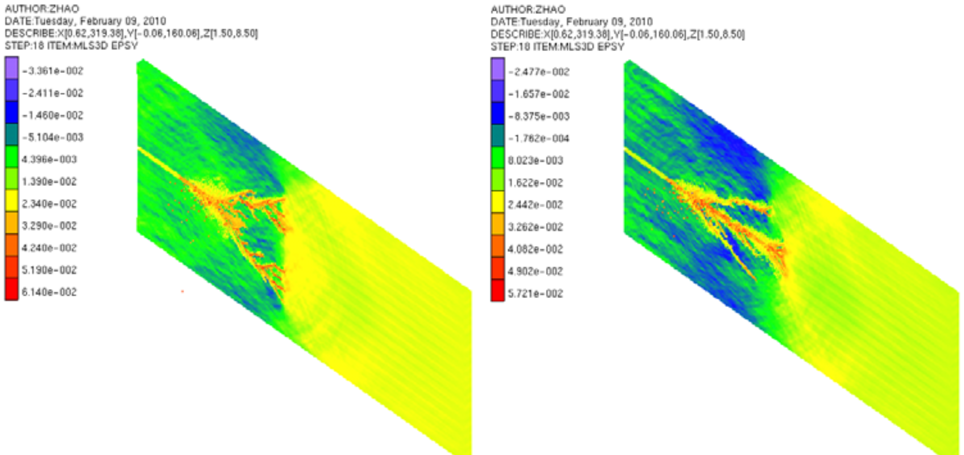

(c) C3 (d)C4

Figure 6.20. Fracture pattern of DLSM models under Case F with different micro constitutive parameters when cracking bifurcation is allowed.

Fracture patterns of these models are different (see Figure 6.20), although these models have the same fracture energy and tensile strength. The modeling results also show that crack speed decreases when considering crack branching. Figure 6.21 shows the results of DLSM modeling under different pre-loading cases with the tri-linear micro constitutive law (C2 in Table 6.3). Compared with the DLSM modeling without crack branching, a closer fit with the experimental results is obtained with crack branching but still using the rate independent micro constitutive law. In following, the dynamic effect of fracture toughness of the Laurentian granite will be modeled through DLSM with rate independent tri-linear micro constitutive law.

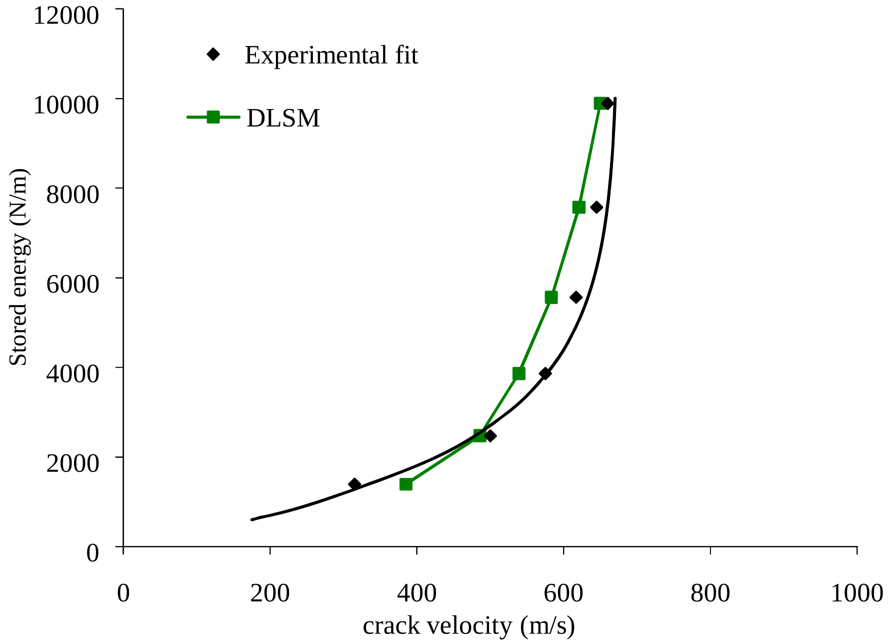

Figure 6.21. Crack velocity of DLSM models with rate independent micro constitutive law when considering crack branching.

6.4 Dynamic fracture toughness test of granite

6.4.1 The experiment

The fracture toughness of rock material is reported that the static fracture toughness is nearly a constant under low loading rate. However, when the loading rate larger than 104MPa $m^{(1/2)}s^{-1}$, the fracture toughness increases with the loading ratio [10]. Similar results are obtained from different experimental tests on rock materials [11, 12]. In this section, the dynamic fracture toughness test of rock material in [12] is modeled by DLSM. Figure 6.22 shows the experiment setup and the used specimen. Dynamic fracture toughness of the Laurentian granite under different loading rates is obtained through a semi-circular bend (SCB) specimen under the split Hopkinson pressure bar (SHPB) system. The mechanical properties and microstructure information of Laurentian granite can be found in [13, 14].

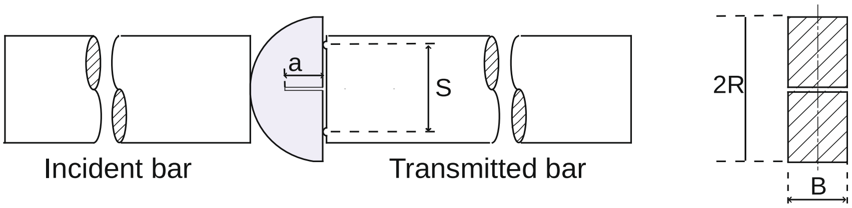

Figure 6.22. Scheme of experimental setup of dynamic fracture toughness test through semi-circular bend (SCB) sample under the split Hopkinson pressure bar (SHPB) system.

6.4.2 DLSM modeling

The geometry model, boundary conditions and the used DLSM model of the SCB dynamic fracture toughness test are shown in Figure 6.23. Dimension of the model is exactly the same as that of the specimen used in the experiment, i.e., 2R = 40 mm, B = 16 mm, S = 20.1 mm and a = 4 mm. The particle size is taken as 0.5mm, which is the mean grain size of Laurentian granite. The whole 3D model is built from 79,872 particles.

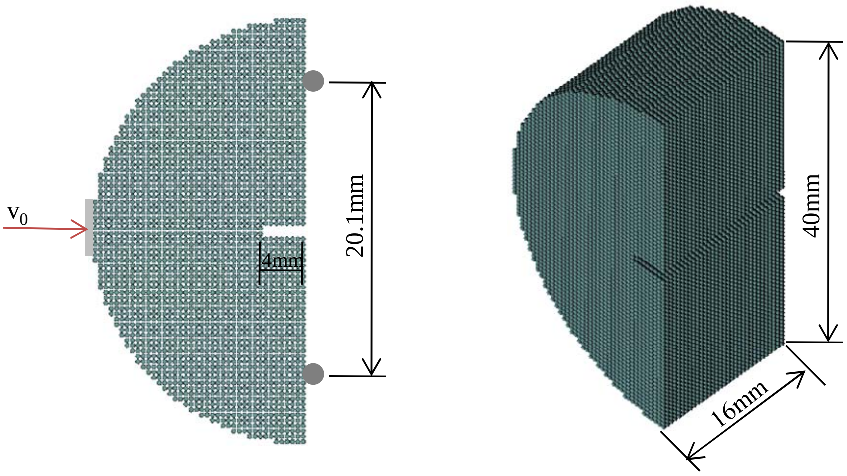

Figure 6.23. DLSM model of the SCB dynamic fracture toughness test.

A velocity is applied at the left surface to simulate the load of SHPB test [15], which is written as

$$v(t)=\begin{cases} v_d t/t_0 & t\le t_0 \\ v_d & t>t_0 \end{cases} \tag{6.19}$$

where v_d is the applied dynamic velocity (mm/s), t_0 is the arise time for reaching the applied velocity which is taken as 20μs for all simulations. At the beginning, the applied velocity is slowly increased to the given level, which helps the specimen to get stress equilibrium. This time is taken to be five or more times of that needed for wave transmission through the given specimen. The material parameters of Laurentian granite are density = 2630 *kg/m*^{3}, the Young's modulus E = 92GPa, and the Poisson ratio= 0.21. The static tensile strength and mode-I fracture toughness are taken to be 13.2MPa and 1.52MPa×m$^{1/2}$, respectively. The fracture energy is calculated from the equation provided in [16], which is

$$G_f = \frac{K_{IC}^2}{E} = 25.113 \text{ N/m} \tag{6.20}$$

Three groups of DLSM model are used to model the SCB dynamic fracture toughness test. Each group includes five models with different loading velocities.

- Group A, named as DLSM_I. The used micro constitutive law is the brittle elastic one. From Equation (6.11), the failure parameter u_n^* is calculated as 7.174e-5 mm.

- Group B, DLSM_II. The used micro constitutive law is the special case of the tri-linear constitutive law. Used parameters are calculated as $u_t^* = 0.0038\text{mm}$, $\delta_1 = 0.0189$, $\delta_2 = 1.0$ and $K^{red} = 0$.

- Group C, DLSM_III. It uses the same micro constitutive law as Group B, and additionally considers dynamic frictional force from the loading surfaces.

The frictional boundary condition is simply considered as

$$\mathbf{f}_s = -\frac{\mathbf{v}_s}{|\mathbf{v}_s|}(u_d f_n) \tag{6.21}$$

where $\mathbf{f}_s$ is the dynamic frication force applied on the boundary particle, $\mathbf{v}_s$ is the velocity in direction parallel to the loading surface and u_d is the dynamic frication ratio between rock and steel (it is taken as 0.168, which is the value reported in [17] as the mean dynamic fraction ratio between concrete and steel), and f_n is the normal component of the force acting on the particle. The data of force at loading surface are recorded during computing. The stress intensive factor is obtained as [12]:

$$K_{Id}(t) = \frac{P(t)S}{BR^{3/2}} \cdot Y\left(\frac{a}{R}\right) \tag{6.22}$$

where *P(t)* is the time-varying loading force. *B* (m), *R* (m), *S*(m) and *a* (m) are the height of the specimen, width of the specimen and depth of the crack. *Y*(*a/R*) is a dimensionless geometry factor which is taken 0.086 in [12] for the used specimen. The loading time curve and fracture pattern of the DLSM model in Group C with the loading velocity of 200mm/s are shown in Figure 6.24. It can be seen that the fracture begins at the crack tip, then propagates straightly and finally the specimen is broken into two pieces as observed in experiment. The dynamic fracture toughness K_{Id}^{c} can be obtained as the peak value of the loading curve. The average loading rate is determined as

$$\dot{K}_{Id} = \frac{K_{Id}^{c}}{t_d} \tag{6.23}$$

where t_d is the time at which $K_{Id}(t) = K_{Id}^{c}$. The simulation results of different DLSM groups are listed in Tables 6.4 - 6.6.

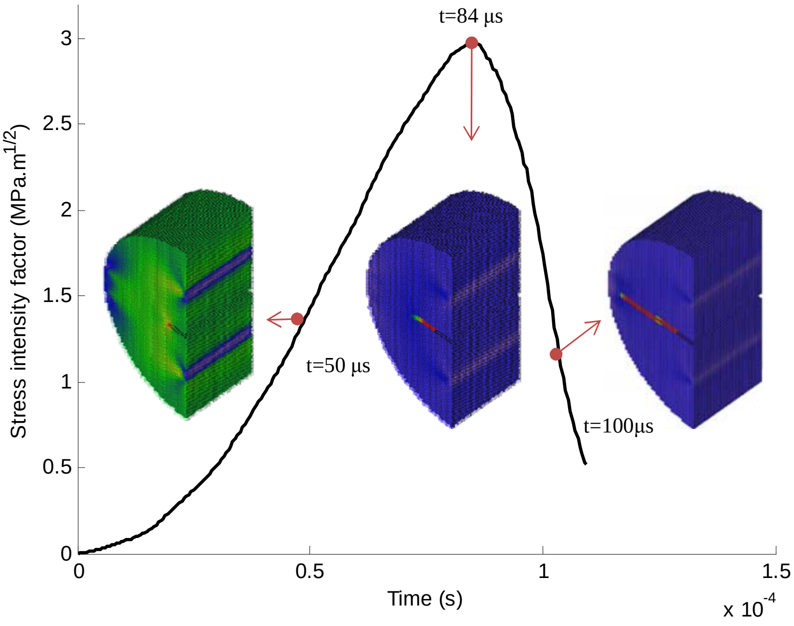

Figure 6.24. Loading curve of DLSM model for the SCB dynamic fracture toughness test.

Table 6.4. Dynamic fracture toughness of DLSM_I.

v_d (mm/s)	t_d (us)	$\dot{K}_{Id}$ (GPa.m$^{1/2}$ /s)	K_{Id}^{c} (MPa.m$^{1/2}$)
200	36.00	18.05	0.65
300	40.50	31.02	1.26
400	35.50	41.23	1.46
800	31.00	51.62	1.60
1000	27.00	63.83	1.72

Table 6.5. Dynamic fracture toughness of DLSM_II.

v_d (mm/s)	t_d (us)	$\dot{K}_{Id}$ (GPa.m$^{1/2}$ /s)	K_{Id}^{c} (MPa.m$^{1/2}$)
200	67.00	28.36	1.90
300	52.00	43.95	2.28
400	45.50	55.01	2.50
800	40.00	68.68	2.75
1000	38.50	76.92	2.96

Table 6.6. Dynamic fracture toughness of DLSM_III.

v_d (mm/s)	t_d (us)	$\dot{K}_{Id}$ (GPa.m$^{1/2}$ /s)	K_{Id}^{c} (MPa.m$^{1/2}$)
200	84.50	35.18	2.97
300	62.50	55.67	3.48
400	53.50	74.08	3.96
800	52.00	82.78	4.30
1000	50.00	92.02	4.60

Figure 6.25 summarizes the DLSM modeling results of different conditions and the experimental data reported in [12]. DLSM modeling results are in agreement with the experimental data. It should be mention that no rate dependent constitutive law is used. All used parameters are obtained directly from the static failure parameters of the Laurentian granite [13, 14]. The modeling results also show that the friction force between specimen and loading surface is an important factor and should be considered carefully in the SCB dynamic fracture toughness test.

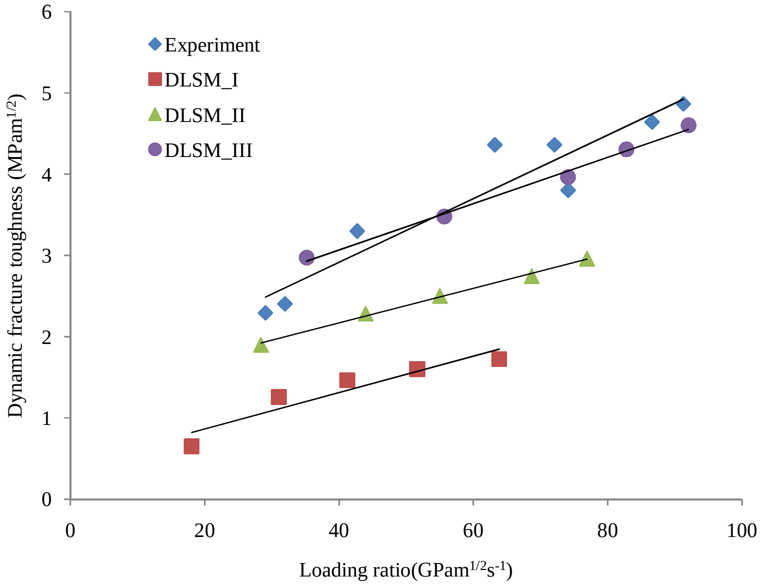

Figure 6.25. DLSM modeling results of the SCB dynamic fracture toughness test and the corresponding experimental results in [12].

6.5 Conclusions

In this chapter, the ability of DLSM on modeling dynamic fracturing of rock material is enhanced and validated. New micro constitutive laws, which include linear, hardening and softening stage, are developed and implemented into DLSM. The macro failure behavior of DLSM model is studied through the uniaxial tensile and compressive test. Empirical equations are derived to link the micro constitutive parameters with the macro failure constants of material, i.e., tensile strength and fracture energy. Dynamic crack propagation of PMMA plate is modeled by DLSM. The results are compared with cohesive FEM results and experimental data. Crack branching observed in experiment is reproduced by DLSM. The crack velocity is reproduced by using a rate independent model and considering crack branching. Then, the dynamic effect of fracture toughness of Laurentian granite is simulated through DLSM. Modeling results are in agreement with the experimental results. All used micro constitutive parameters are obtained based on the proposed empirical equations and the macro static parameters reported in literatures. Overall speaking, the ability of DLSM on modeling dynamic failure problems is enhanced through the developed micro constitutive law in this chapter. Another important issue in rock dynamics, wave propagation, will be investigated by DLSM in the next chapter.

6.6 References

1. Potyondy DO. Simulating stress corrosion with a bonded-particle model for rock. Int. J. Rock Mech. & Min. Sci., 2007; 44(5):677-691.

2. Cundall PA, Strack ODL. A discrete numerical model for granular assemblies. Geotech, 1979; 29(1):47-65.

3. Xu XP, Needleman A. Numerical simulations of fast crack growth in brittle solids. J Mech Phys Solid, 1994; 42(9): 1397-1434.

4. Yang QD, Thouless MD. Mixed-mode fracture analyses of plastically-deforming adhesive joints. Int. J. Fract. 2001;110:175-187.

5. Shioya T, Zhou F. Dynamic fracture toughness and crack propagation in brittle material. In: Constitutive relation in high/very high strain rates, 1995;105–112.

6. Zhou F, Molinari J-F, Shioya T. A rate-dependent cohesive model for simulating dynamic crack propagation in brittle materials. Eng Fract Mech, 2005; 72(9):1383–1410.

7. Bedford A, Drumheller DS. Introduction to Elastic Wave Propagation, John Wiley & Sons, 1996.

8. Kazerani T, Zhao J. Simulation of dynamic fracturing in brittle materials using discrete element method and a full rate-dependent logic for cohesive contact, Eng Frac Mech, 2009 (Submitted).

9. Kazerani T, Zhao GF, Zhao J. Dynamic fracturing simulation of brittle material using the Distinct Lattice Spring Model (DLSM) with a full rate-dependent cohesive law, Rock Mech Rock Eng., 2010, 10.1007/s00603-010-0099-0.

10. Zhang ZX, Kou SQ, Yu J, Yu, Y, Jiang LG, Lindqvist PA. Effects of loading rate on rock fracture. Int. J. Rock Mech. & Min. Sci., 1999;36(5):597-611.

11. Li HB. Experimental and theoretical studies on mechanical properties of granite under dynamic compressive loads. PhD thesis, 1999, I RSM Chinese Academy of Sciences.

12. Dai F, Chen R, Xia K. A Semi-Circular Bend Technique for Determining Dynamic Fracture Toughness, Exp Mech, 2009; 1-9 .

13. Dai F, Xia KW, Tang LZ. Rate dependence of the flexural tensile strength of Laurentian granite, Int. J. Rock Mech. & Min. Sci., 2010 (in press).

14. Nasseri MHB, Mohanty B. Fracture toughness anisotropy in granitic rocks, Int. J. Rock Mech. & Min. Sci., 2008; 45: 167-193.

15. Ma GW, Wang XJ, Li QM. Modeling Strain Rate Effect of Heterogeneous Materials Using SPH. Rock Mech Rock Eng, 2010;10.1007/s00603-010-0089-2.

16. Zdenek PB, Jaime P. Fracture and size effect in concrete and other quasibrittle materials, CRC Press LLC, 1998 ; 41-42.

17. Li QM, Lu YB, Meng H. Further investigation on the dynamic compressive strength enhancement of concrete-like materials based on split Hopkinson pressure bar tests. Part II: Numerical simulations. Int. J. Impact Eng. 2009; 36: 1327-1334.

Chapter 7

DLSM modeling of wave propagation through rock mass

Extensions and verifications on DLSM modeling of wave propagation problems are presented in this chapter. A non-reflection boundary condition based viscous element method is implemented into DLSM. The non-reflection boudary condtion is verfied through 1D and 2D wave propagation problems and the results indicate that waves can pass through the boundary without reflections. The influence of particle size on wave propagation is investaged by comparing results of DLSM models with different mesh ratio (*lr*) and these obtained from corresponding analytical solutions. Suggested *lr* are provided for modeling P-wave and S-wave propagation in DLSM. Weak material layer method and virtual joint plane method are developed to model discontinuity in DLSM. Incident P-wave and S-wave propagation through single discontinuty are modeled by these two methods and the results are compared with the analytical solutions. It shows that the virtual joint plane method is better than the weak material layer method. Finally, some remarks on DLSM modeling wave propagation problems are given in the conclusoin part.

7.1 Non-reflection boundary condition in DLSM

7.1.1 Implementation

The finite boundary of computational model causes elastic wave to be reflected and mixed with the original wave. This leads analysis of the numerical modeling results much difficult. Moreover, many wave propagation problems are treated in infinite domain. It is impossible to build an infinite model in most numerical methods. In order to solve these problems, an artificial boundary condition which can simulate a computational model without any finite boundary is needed. This kind of boundary condition is called as non-reflection boundary condition. It can eliminate the spurious reflections induced by the finite boundary. Numbers of non-reflection boundary conditions had been developed in the past years. For example, vicous boundary element [1], strip element [2] and infinite element [3] are implemented into FEM to realize the function of non-reflection boundary. These techniques used in FEM can also be implemented into other numerical methods, e.g., DEM and DDA [4,5]. The viscous element method proposed by Lysmer and Kuhlemeyer [1] is the oldest and simplest non-reflection boundary condition and has been implemented into different numerical methods, e.g., DDA and DEM. In this section, the viscous element method will be implemented into DLSM. Figure 7.1 illustrates the imposing of viscous element based non-reflection boundary condition into DLSM. Three dashpots are placed at particles on the artificial boundary plane. Reflected wave is minimized by imposing these damping dashpots. The mechanical properties of these dashpots can be determined through the material properties of the linked particle.

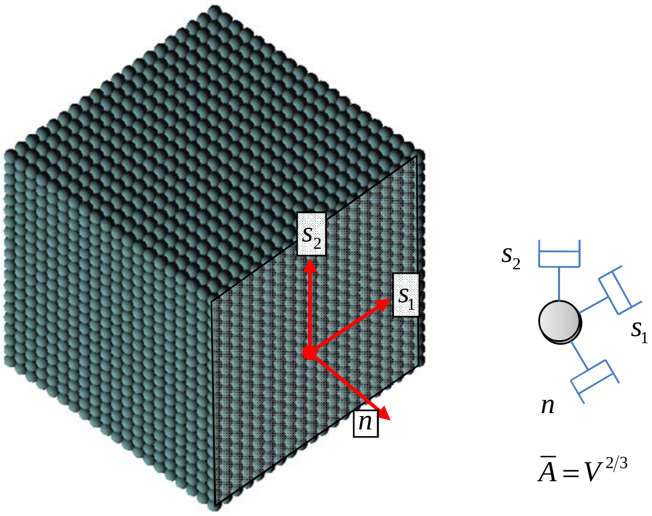

Figure 7.1. Implementation of non-reflection boundary condition in DLSM.

The normal and shear viscous tractions are given as

$$t_n = -\rho \bar{A} C_p v_n \tag{7.1}$$

$$t_{s1} = -\rho \bar{A} C_s v_{s1},\ t_{s2} = -\rho \bar{A} C_s v_{s2} \tag{7.2}$$

where ρ is the material density of the linked particle, $\bar{A}$ is the equivalent area (given as $V^{2/3}$ and V is the volume of the particle), v_n is the normal components of the velocity of the particle, v_{s1} and v_{s2} are the shear components of the velocity, C_p and C_s are the P-wave and S-wave velocities, which are given by

$$C_p = \sqrt{\frac{K + 4G/3}{\rho}}, C_s = \sqrt{\frac{G}{\rho}} \tag{7.3}$$

where K and G are the bulk and shear elastic modulus of the linked particle. This viscous element based non-reflection boundary condition is implemented into DLSM by adding Equations (7.1) and (7.2) into the force calculation procedure of DLSM (see Figure 4.1(b)). The viscous element based non-reflection boundary condition (VBC) has been widely used in many engineering applications due to its convenience of implementation and employ [5, 6], although it has been reported not effective for dispersive lamb waves. In following, the implemented viscous non-reflection boundary condition of DLSM is verified through both 1D and 2D wave propagation problems.

7.1.2 Verifications

Example A

The DLSM model used in this section is shown in Figure 7.2. A three dimensional model of 70mm×140mm×5mm is built, the diameter of spherical particles is 0.5mm. The used material parameters are elastic modulus 27.878GPa, Poisson’s ratio 0.298 and the density 2120kg/m^3, which are typical parameters for mortar. A half sinusoidal velocity wave is applied at the top surface of the model. Two lines of detection points are placed on the specimen to record the velocity waves propagated through the model (see Figure 7.2(a)).

Different types of boundary conditions are applied on the DLSM model to study influence of viscous non-reflection boundary condition on the wave propagation. The first one is only to apply velocity wave on the top surface and let all left surface be free. It is named as full free boundary condition. The modeling results are shown in Figure 7.3, where reflected wave can be clearly observed but wave forms of same detection line are different. This means 1D wave propagation theory is not strictly applicable for wave propagation through 3D plate problem under such kind of boundary condition. Figure 7.4 shows the results when non-reflection boundary condition is additionally applied on the bottom surface (named as VBC boundary condition). It can be seen that the reflected wave is largely reduced. However, fluctuations among different points of same detection line are still exist (Figure 7.4). Modeling results will exactly satisfy the 1D wave propagation theory when the side surfaces are fixed in their normal direction (named as fixed VBC condition). The DLSM modeling results under fixed VBC condition is shown in Figure 7.5.

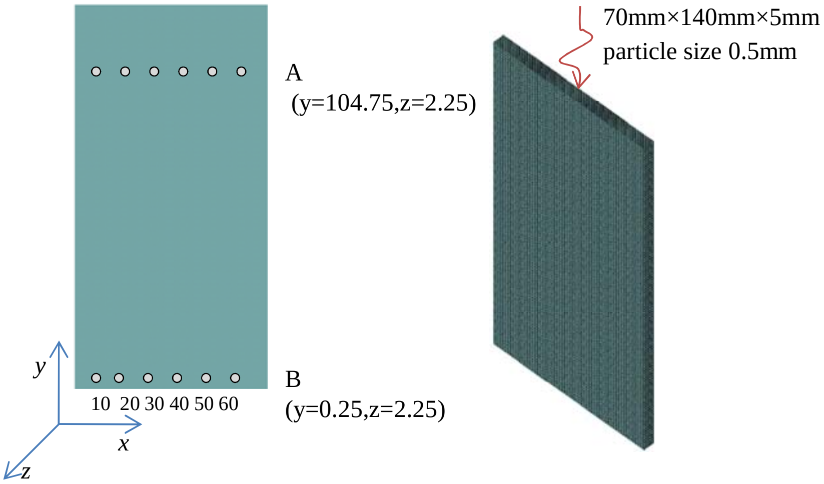

(a) Plane view (b) DLSM model

Figure 7.2. Computational model of modeling wave propagation through 3D plate.

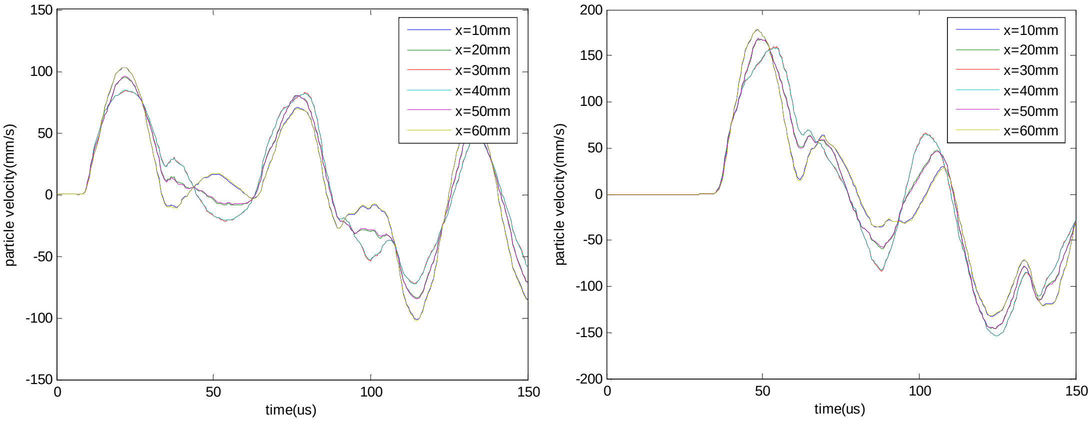

(a) Detection points of line A (b) Detection points of line B

Figure 7.3. Waves predicted by DLSM under full free boundary condition.

This example indicates that the proposed non-reflection boundary condition in DLSM is successful for one dimensional wave propagation. Modeling results also reveal that the fixing of the normal direction of side surfaces is necessary to reproduce one dimensional wave propagation in 3D model (see Figure 7.6). It means that the influence of side surface boundary condition must be considered carefully for experimental facilities which based on 1-D wave propagation theory, e.g., the split Hopkinson pressure bar (SHPB) [7].

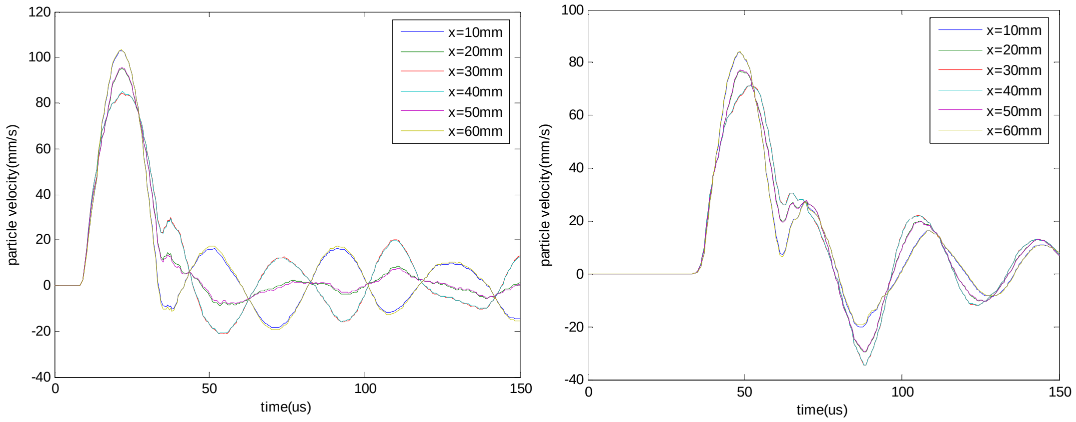

(a) Detection points of line A (b) Detection points of line B

Figure 7.4. Waves predicted by DLSM under free side VBC boundary condition.

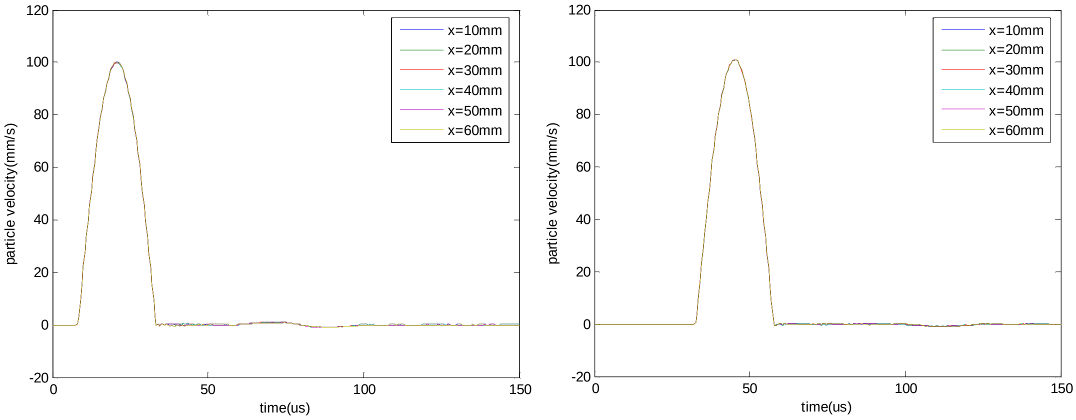

(a) Detection points of line A (b) Detection points of line B

Figure 7.5. Waves predicted by DLSM under fixed VBC boundary condition.

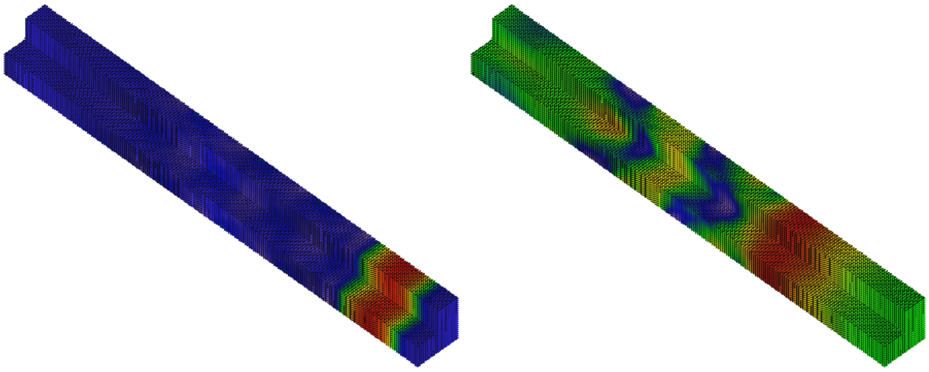

(a) Fixed side boundary condition (b) Free side boundary condition

Figure 7.6. Results of shock wave propagation through rectangle bar under different side surface boundary conditions.

Example B

Blasting wave propagation through rock is modeled by DLSM to test the ability of implemented viscous non-reflection boundary on modeling 2D wave propagation problems. This example tries to model the blasting wave propagation through rock cavern. The corresponding field test of an underground explosion is reported in [8]. The computational model with dimension of 80m×60m×5m is constructed, where an explosion chamber of 4m×2m is excavated (seen in Figure 7.7). The used particle size is 0.5m and a total of 191,680 particles are used to build the model. In order to simulate a plane strain boundary condition, two z-direction surfaces are fixed in their normal direction. The mechanical properties of rock material are the elastic modulus 74.0GPa, the Poisson's ratio 0.25 and the density 2650kg/m^3, which are typical mechanical parameters of Bukit Timah granite in the field test. A triangular over-pressure history with two phases (see Figure 7.8) is used to represent the blasting wave of effective TNT charge weight of 606kg with a loading density of 10kg/m^3. The maximum over-pressure $P_{\max}$ is equal to 30.23MPa, the duration of rise phase t_1 and the total duration t_2 are 0.5 and 2.5 ms, respectively. These parameters of triangular over-pressure history are calculated by empirical equations provided in [6]. DLSM modeling results of the blasting wave propagation through rock problem are given in Figure 7.9. The blast wave can propagate through the boundary without reflections. This implies the implemented non-reflection boundary condition is effective for 2-D case.

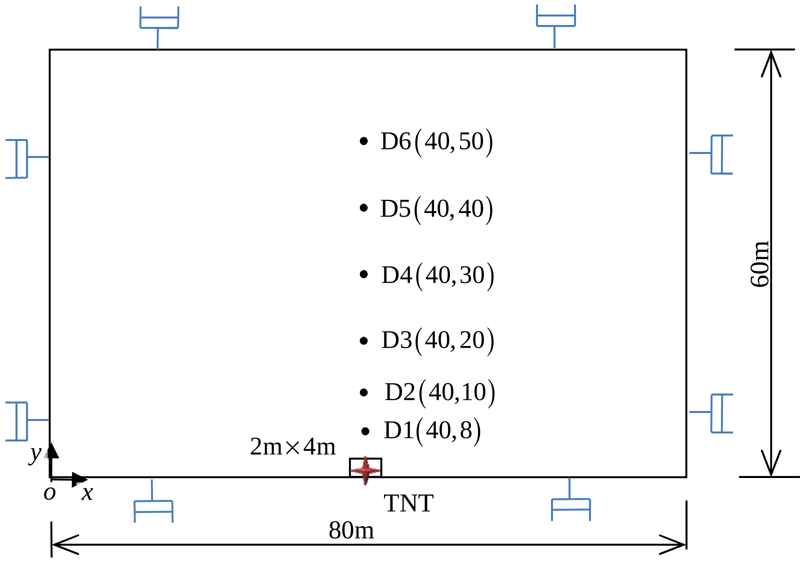

Figure 7.7. Computational model of blasting wave propagation through rock cavern.

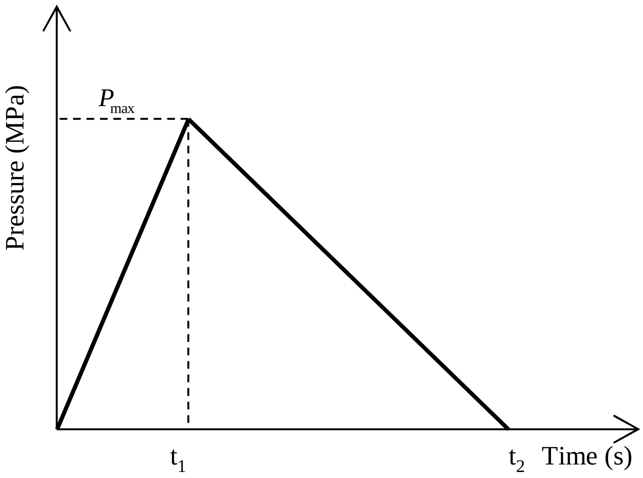

Figure 7.8. Triangle pressure wave to represent blasting loading.

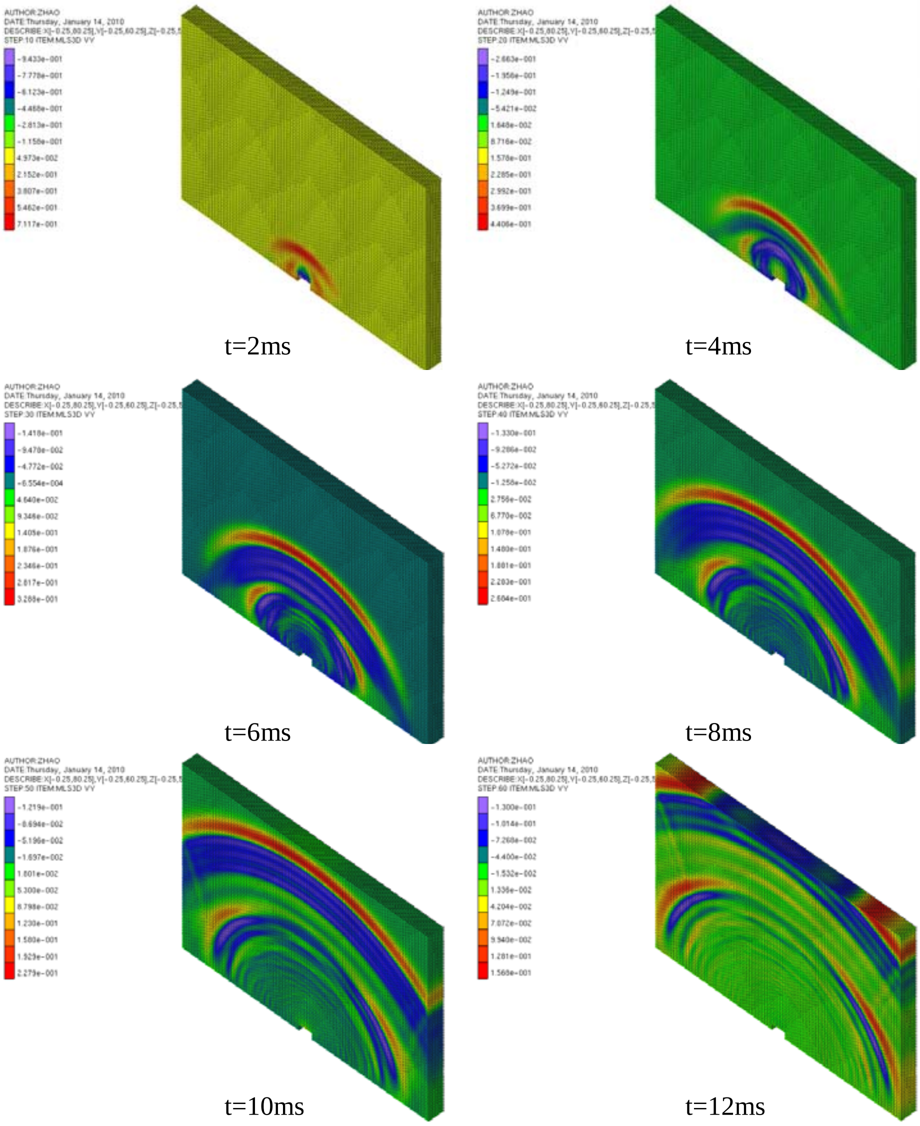

t=2ms

t=4ms

t=6ms

t=8ms

t=10ms

t=12ms

Figure 7.9. The process of blasting wave propagation through rock cavern predicted by DLSM.

The blasting waves at different record points are shown in Figure 7.10 (a). It can be seen that only slight reflection waves are observed. The velocity history predicted by DLSM model is compared with the test data at 8m above the detonation (see Figure 7.10(b)). The agreement of DLSM modeling and field test is similar with the results of FEM reported in [6]. This proves again the implemented non-reflection boundary condition in DLSM is successful. In following, the implemented non-reflection boundary condition is used for all the examples.

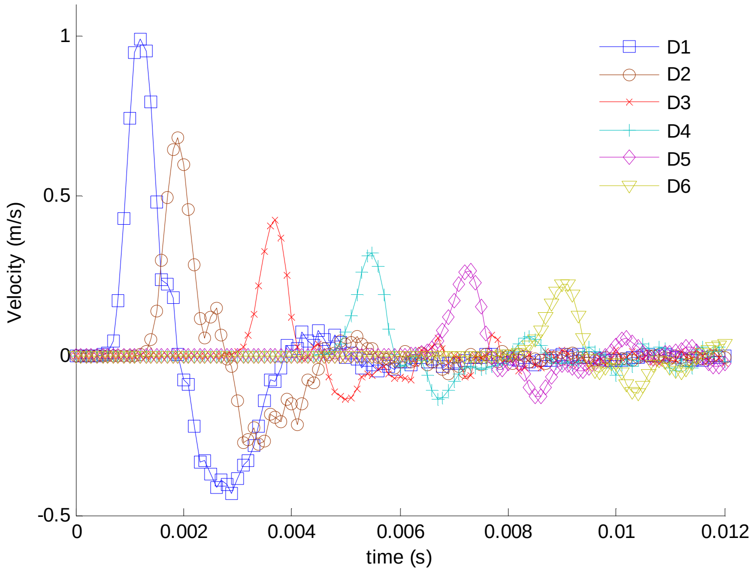

(a) Different detection points

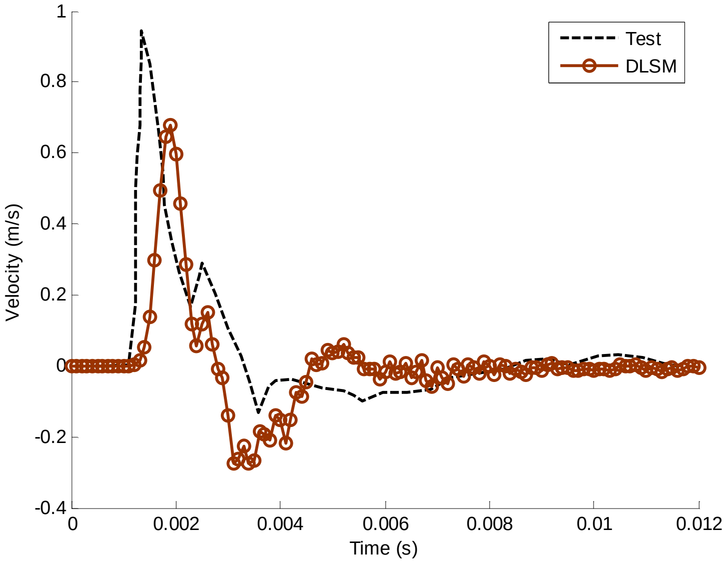

(b) Field test data and modeling result

Figure 7.10. The velocity histories predicted by DLSM and field test.

7.2 Influence of particle size on wave propagation

Influence of particle size on the numerical accuarcy of DLSM modeling of wave propagation problems is studied in this section. Similar works have been performed for some mesh based methods, e.g., the mesh size influence of UDEC on wave propagatoin is studied in [9,10]. A term called mesh ratio (*lr*) (ratio of the mesh size to the wavelength of input wave) is used as the control paramter. In order to keep consistent with previous studies same term is used, instead of the ratio of the particle size to the wave length. In this section, influence of the *lr* on DLSM modeling of 1D and 2D wave propagation problems are investaged. The main objective is to provide suggested *lr* for further study on P-wave and S-wave propagation through jointed rock mass.

7.2.1 Influence of mesh ratio on 1D wave propagation

A planer elastic wave propagates through a continuous, homogeneous, isotropic and perfectly elastic medium can be taken as an ideal example for verifying the the numerical accuracy of wave representation in DLSM. In this section, modelling of one-dimensional P-wave and S-wave propagation in a half-space with continuous, homogeneous, isotropic and linear elastic material are carried out by DLSM. The purpose is to select approximate particle size for DLSM modeling of one dimensional P-wave/S-wave propagation problems. The used DLSM models are shown in Figure 7.11. The dimension of the used model is the same with that of in Figure 7.2.

The basic properties of the material are follows: density 2120kg/m^3, elastic modulus 27.878GPa, Poisson's ratio 0.298, shear wave propagation veloicty C_s 2250m/s, and compressional wave propagation velocity C_p 4200m/s. A one-cycle sinusoidal wave with a amplitude of 100mm/s is normally or tangentially applied to the top boundary and propagates along the *y*-direction through the model. Seven measurement points are positioned in the specimen to record time histories of the particle velocities (see Figure 7.11). For P-wave, the left and right side boundaries are fixed in their *x*-direction. The wave frequencies of the P-wave are taken different values as 0.1MHz, 0.2MHz, 0.5MHz, 1.0MHz and 2.0MHz to produce different *lr* as 1/82, 1/42, 1/17, 1/8 and 1/4. The percentage error of DLSM on modeling the amplitude of P-wave is compared with the input amplitude and used as the index to represent the accuracy of the numerical results. The results of 1D P-wave propagatoin are shown in Figure 7.12.

It shows that the percentage error decrease with particle size and increase with the distance from wave source. The relationship between *lr* and the average percentage error of modeling P-wave propagation is shown in Figure 7.13. It can be seen that the percentage error will be less than 5% when the *lr* is small than 1/41. In order to

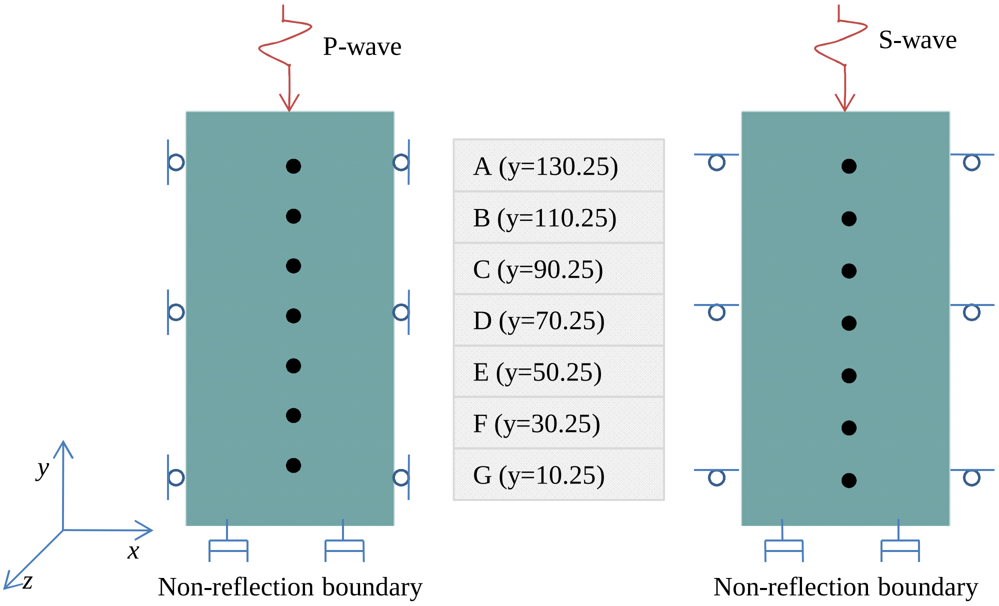

Figure 7.11. DLSM models for one-dimensional P-wave and S-wave propagation.

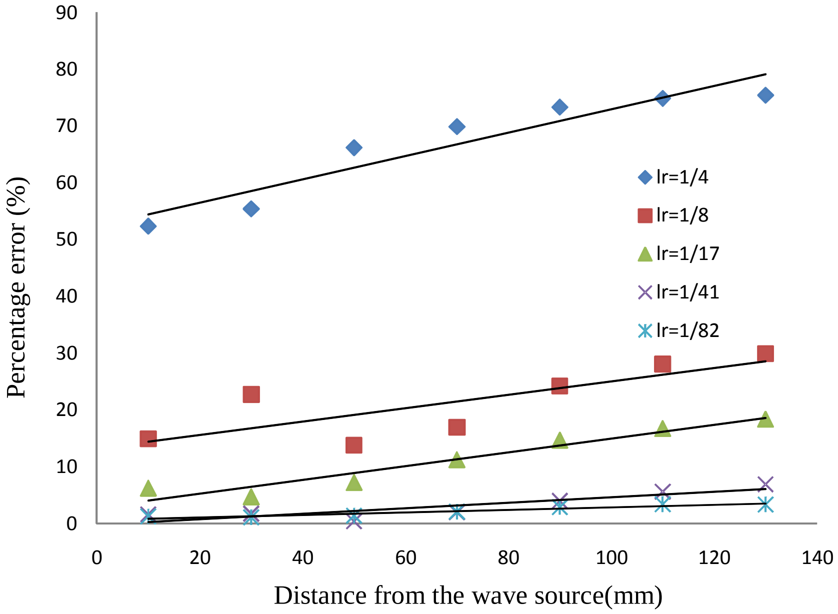

Figure 7.12. Percentage error of wave amplitudes of DLSM modeling of P-wave propagation with different *lr* models.

consider the influence of the distance and the wave frequency, normalized distance (ratio of the distance from wave source to the wave length) is used as the space control paramter. Relationship between percentage error and normalized distance under *lr* of 1/17, 1/41 and 1/82 are shown in Figures 7.14, Figure 7.15 and Figure 7.16. It can be seen that the increment percentage error of the wave propagate through one wave length distance for DLSM model with lr=1/17 is 1.24% and these of *lr*=1/41 and lr=1/82 are 0.99% and 0.90%, respectively. Therefore, the suggested *lr* for DLSM modeling of 1D P-wave is given as 1/41.

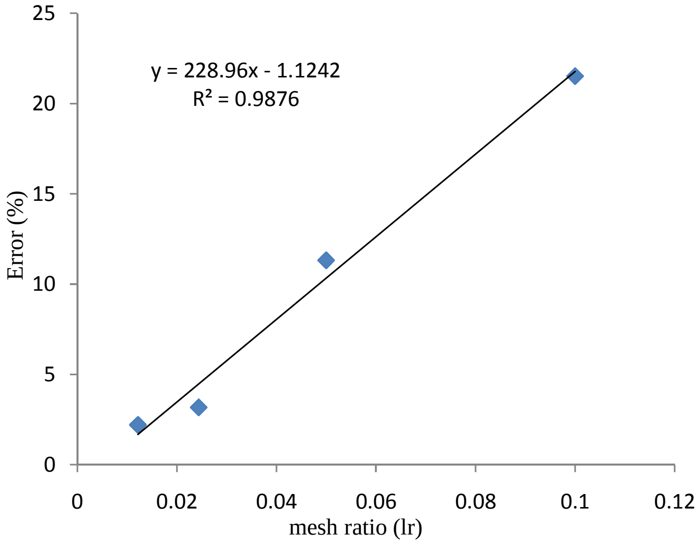

Figure 7.13. The relationship bewteen average percentage error and *lr* of DLSM modeling P-wave propagation problem.

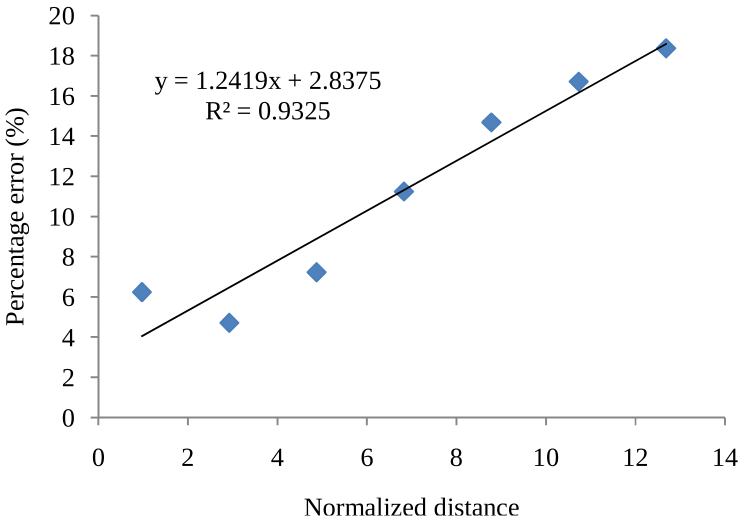

Figure 7.14. The relationship bewteen average percentage error and normalized distance of DLSM modeling P-wave propagation problem with *lr* of 1/17.

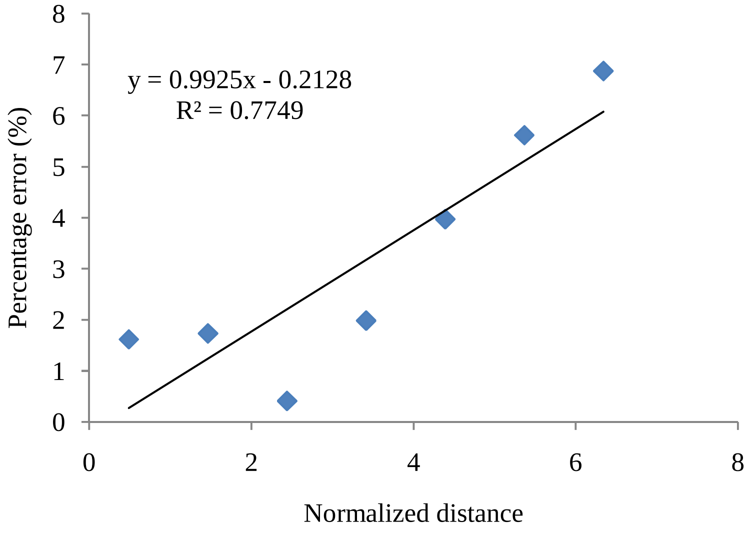

Figure 7.15. The relationship bewteen average percentage error and normalized distance of DLSM modeling of P-wave propagation problem with *lr* of 1/41.

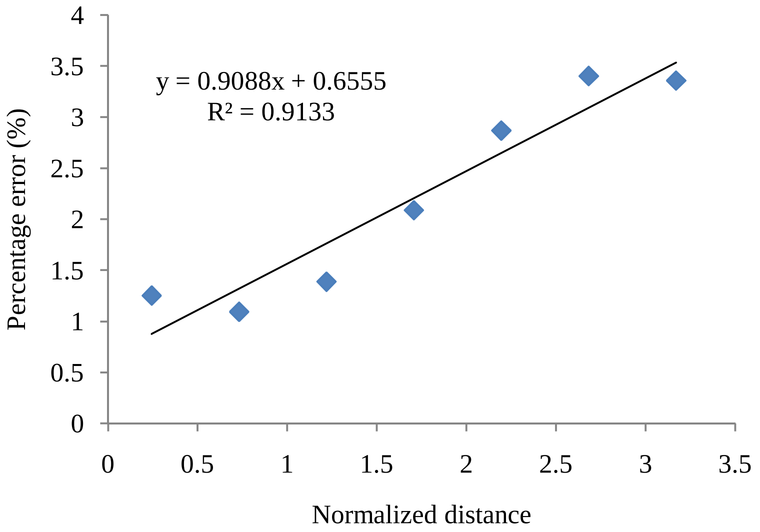

Figure 7.16. The relationship bewteen average percentage error and normalized distance of DLSM modeling of P-wave propagation problem with *lr* of 1/82.

For S-wave, the wave frequency are selected as 0.2MHz, 0.1 MHz, 0.05MHz and 0.025MHz. The crrosponding *lr* are 1/22, 1/45, 1/90 and 1/180. The DLSM modeling results are shown in Figure 7.17. Here, the same trendency as that of DLSM modeling of P-wave propagaton is obtained. The relationship between *lr* and the average percentage error of DLSM modeling of S-wave is given in Figure 7.18. Moreover, relationships between percentage error and normalized distance under *lr* of 1/45, 1/90 and 1/180 are provided in Figure 7.19, Figure 7.20 and Figure 7.21. From these results, the suggested *lr* of DLSM modeling of S-wave pragation is given as 1/90. The recorded waves at points A and G in the DLSM model with *lr*=1/90 and *lr*=1/180 are shown in Figure 7.22, it can be seen that the transmitted wave still has some difference with the orignal input wave. To obtian a precise wave form, a *lr* of 1/180 is suggested.

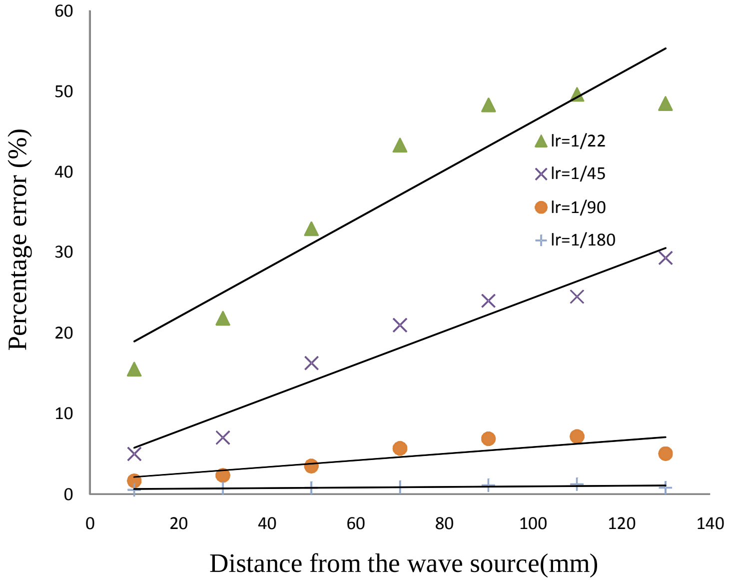

Figure 7.17. Percentage error of wave amplitudes of DLSM modeling S-wave propagation using different *lr* models.

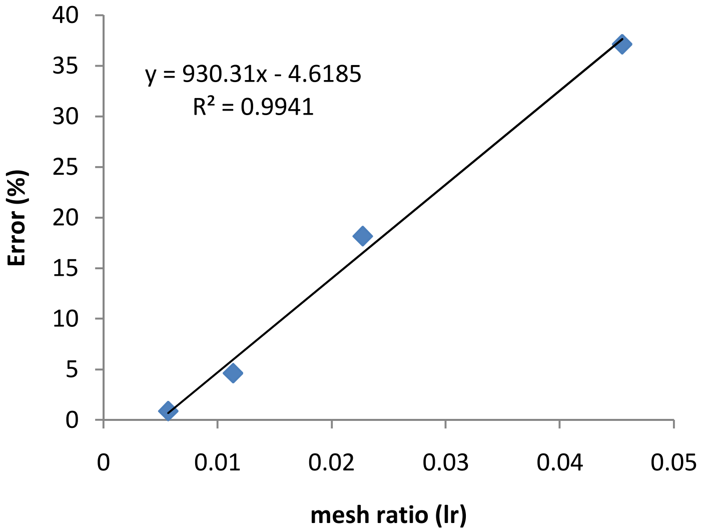

Figure 7.18. The relationship bewteen average percentage error and *lr* of DLSM modeling S-wave propagation problem.

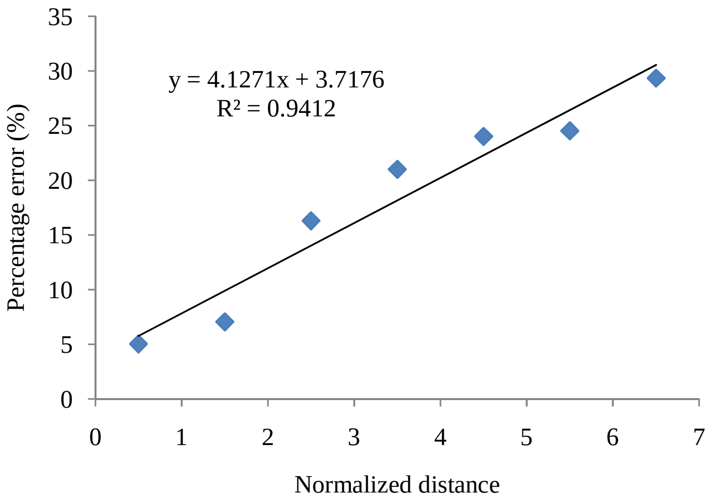

Figure 7.19. The relationship bewteen average percentage error and normalized distance of DLSM modeling of S-wave propagation with *lr* of 1/45.

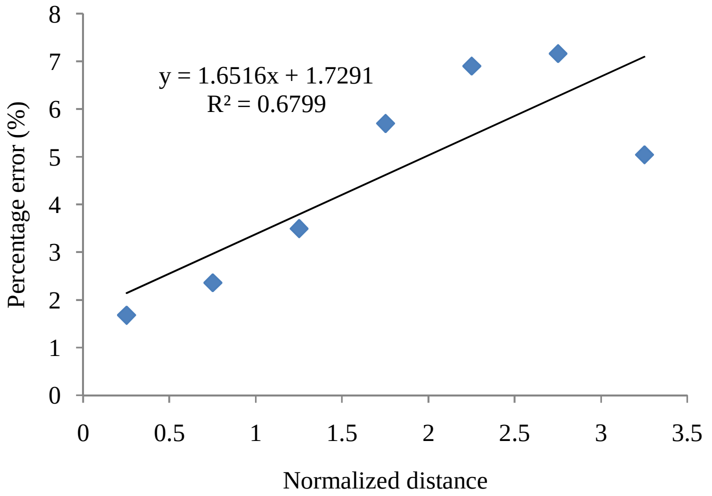

Figure 7.20. The relationship bewteen average percentage error and normalized distance of DLSM modeling of S-wave propagation with *lr* of 1/90.

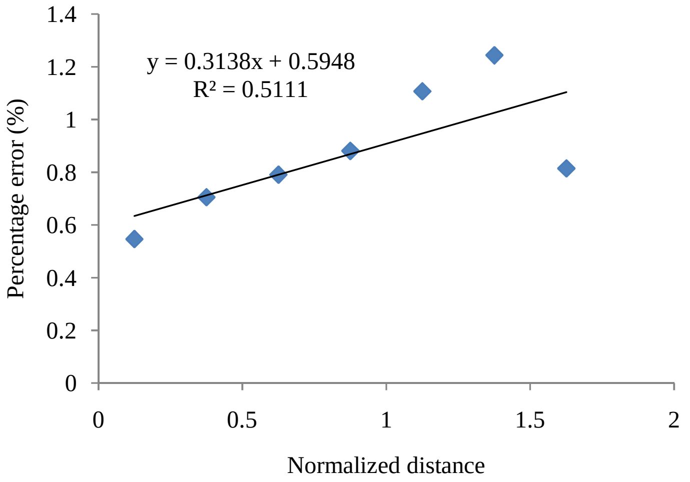

Figure 7.21. The relationship bewteen average percentage error and normalized distance of DLSM modeling of S-wave propagation problem with *lr* of 1/180.

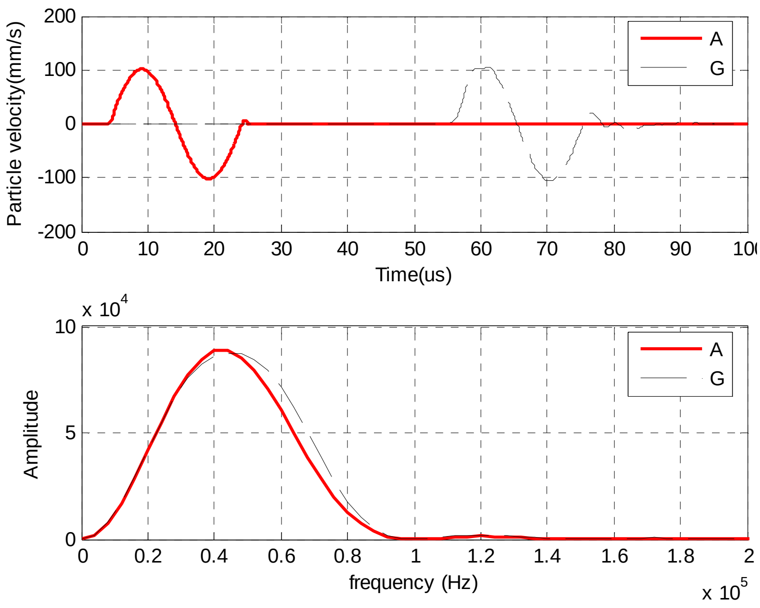

(a) *lr* =1/90

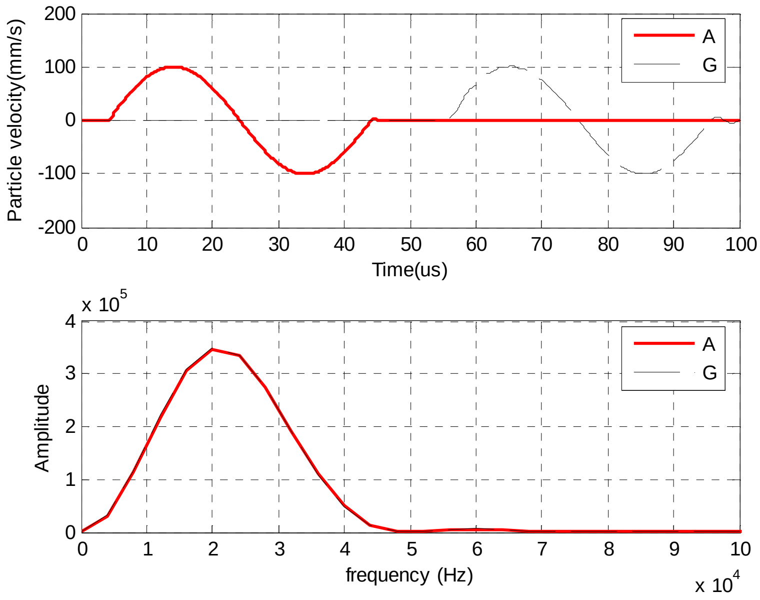

(b) *lr*=1/180

Figure 7.22. Recorded waves at detection points A and G and corresponding amplitude spectra of DLSM models with *lr* of 1/90 and 1/180.

7.2.2 Influence of mesh ratio on 2D wave propagation

In this section, influence of *lr* on 2D wave propagation is studied. The DLSM modeling results are compared with the analytical solution of stress wave propagation through a cylindrical cavity (see Figure 7.23). A uniform harmonic loading,

$\sigma_{rr}(r=a)=-p_0 e^{-i\omega t}$, is applied on the cylindrical surface. The governing equations of this problem is written as

$$\nabla^2\Phi=\frac{1}{C_p^2}\frac{\partial^2\Phi}{\partial t^2} \tag{7.4}$$

where Φ is the potential function, C_p is the p-wave velocity, t is time.

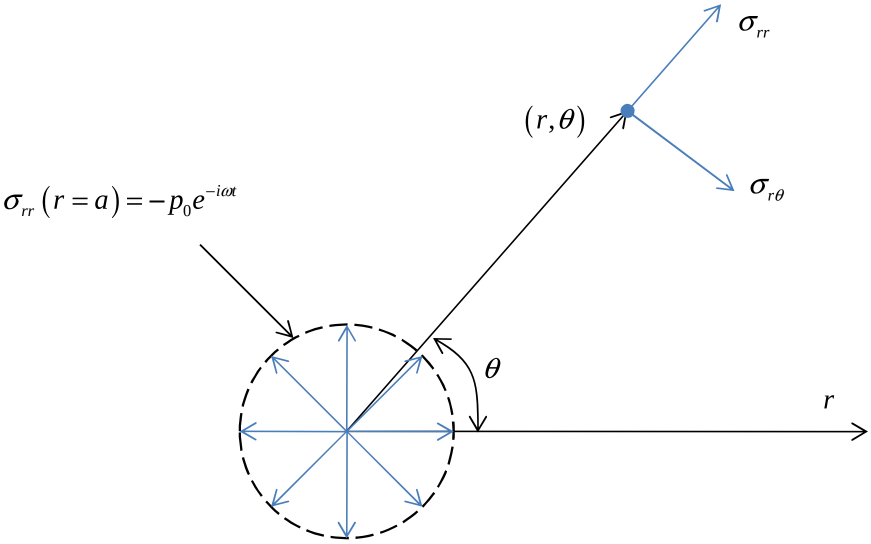

Figure 7.23. The problem of stress wave propagation from a cylindrical cavity.

The analytical solution of the radial displacement, velocity and stress in the medium are given as [11, 12]

$$\sigma_{rr}=-\mu\left(k^2\beta^2\Phi+\frac{2}{r}\frac{d\Phi}{dr}\right) \tag{7.5}$$

$$u=\frac{d\Phi}{dr}=\frac{\beta}{\mu N(\beta a)}p_0 e^{-i\omega t}\left[-H_1^{(1)}(\beta r)\right] \tag{7.6}$$

$$v=\frac{du}{dt}=\frac{i\omega\beta}{\mu N(\beta a)}p_0 e^{-i\omega t}\left[H_1^{(1)}(\beta r)\right] \tag{7.7}$$

where a is the radius of the cavity, k^2 and β^2 are deduced parameters which are written as

$$\beta^2=\frac{\omega^2}{C_p^2}, k^2=\frac{\lambda+2\mu}{\mu} \tag{7.8}$$

where $\lambda=\dfrac{E\nu}{(1+\nu)(1-2\nu)}$ and $\mu=\dfrac{E}{2(1+\nu)}$.

The potential function and its derivative of this problem are given as

$$\Phi(r,t)=\frac{p_0}{uN(\beta a)}H_0^{(1)}(\beta r)e^{-i\varpi t} \tag{7.9}$$

$$\frac{\Phi(r,t)}{dt}=\frac{\beta}{uN(\beta a)}p_0e^{-i\varpi t}\left[-H_0^{(1)}(\beta r)\right] \tag{7.10}$$

$N(\beta a)$ is given as

$$N(\beta a)=k^2\beta^2H_0^{(1)}(\beta a)-\frac{2\beta}{a}H_1^{(1)}(\beta a) \tag{7.11}$$

where $H_m^{(n)}(x)$ is Hankel function and its explicit expression can be found in [13]. The wave velocity attenuation ratio along the radial direction is obtained as

$$A(r)=\frac{H_1^{(1)}(\beta r)}{H_1^{(1)}(\beta a)} \tag{7.12}$$

Here, the wave attenuation ratio is used as the index to compare DLSM modeling results and the analytical ones. Figure 7.24 shows the DLSM used to model the stress wave propagation through cylindrical cavity problem. A cavity with a radius of 10mm exists in an infinite domain. A quarter symmetrical model with a dimension of 100mm×100mm×5mm is used. The particle size is 0.5mm and a total of 396,840 particles are used to build the model. The top and right boundaries are non-reflection boundaries, while the left and the lower boundaries are symmetrical boundaries. A compressional harmonic velocity wave with amplitude of 100mm/s is applied at the boundary of the cavity. The wave frequencies are taken as 0.1MHz and 0.2 MHz to represent *lr* of 1/41 and 1/17, respectively. The mechanical parameters are taken as: elastic modulus is 27.878GPa, Poisson's ratio is 0.298 and the density is 2120kg/m^3.

In order to quantify the DLSM results, the error for detection point is given as

$$\left|Err_i\right|=\left|\frac{A_{i(DLSM)}-A_{i(analytical)}}{A_{i(analytical)}}\right|\times 100\% \tag{7.13}$$

where $A_{i(DLSM)}$ is the attenuation value of the wave at *ith* monitoring point predicted by DLSM and $A_{i(analytical)}$ is the corresponding value of the analytical solution. The results of DLSM modeling and analytical solution are shown in Figure 7.25 and Figure 7.26.

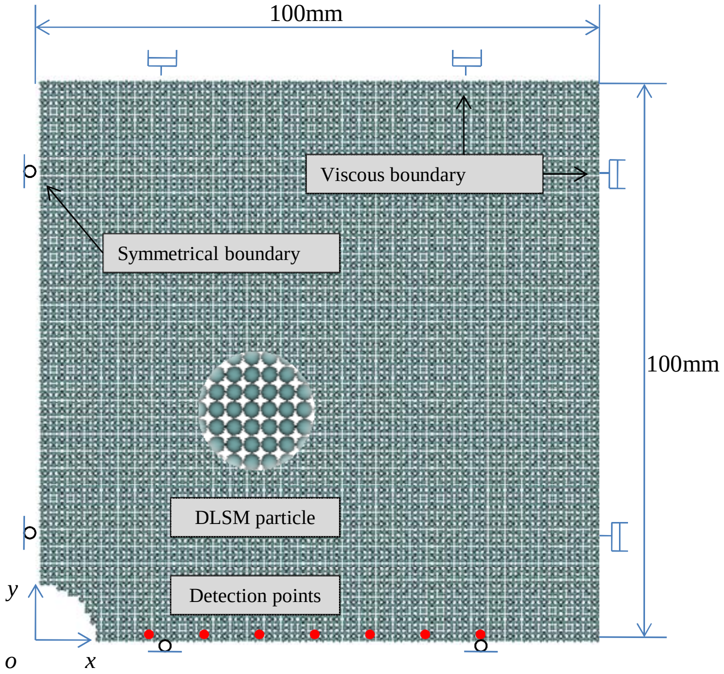

Figure 7.24. The used DLSM computational model of the stress wave propagation through cylindrical cavity problem.

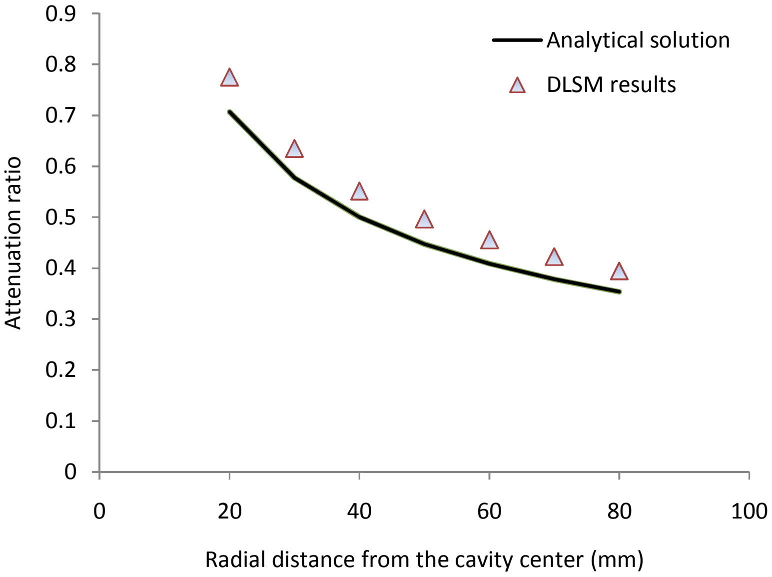

Figure 7.25. The DLSM modeling results under *lr* of 1/17 and analytical solution of the wave propagation through cylindrical cavity problem.

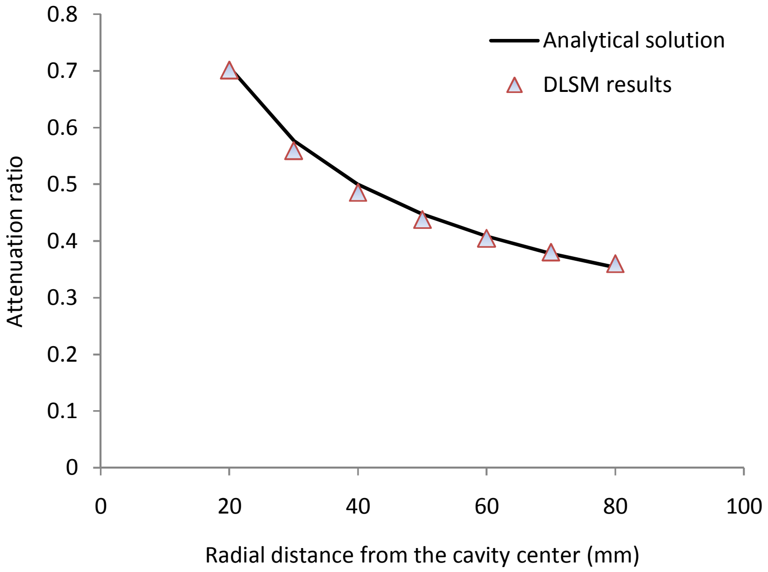

Figure 7.26. The DLSM modeling results under *lr* of 1/41 and analytical solution of the wave propagation through cylindrical cavity problem.

The average error is 10.86% for the DLSM model with *lr* of 1/17 and 1.02% for the *lr* of 1/41. In this sense, the suggested *lr* can also be taken 1/41 for 2D P-wave propagation problems. The suggested *lr* in DLSM is smaller than that in UDEC, e.g., the *lr* of 1/12 is suggested for UDEC modeling of P-wave propagation in [14]. One of the reasons is that the definination of mesh size and particle size in UDEC and DLSM (see Figure 7.27) are different. One single element in UDEC includes four sub-triangle elements. In this sense, the requirment in UDEC is actually *lr*=1/24. For S-wave propagation problem, a strict requirment is required in DLSM (*lr*=1/90), while UDEC can still use *lr*=/24 (the actual ratio). It can be concluded that a more strict requirement on particle size is needed for DLSM to model wave propagation than mesh based code UDEC.

7.3 Wave propagation through discontinuity in DLSM

It is well known that rock mass should be treated as discontinuous when joints existed. And some studies show that existing discontinuities in rock masses may play a dominant role in stress wave attenuation. There are three methodologies, analytical solutions, laboratory/field experiments and numerical modeling, for the study of stress wave propagation in discontinuous medium. The analytical solution is economic, precise and fast on computing. However, the analytical solution of wave propagation

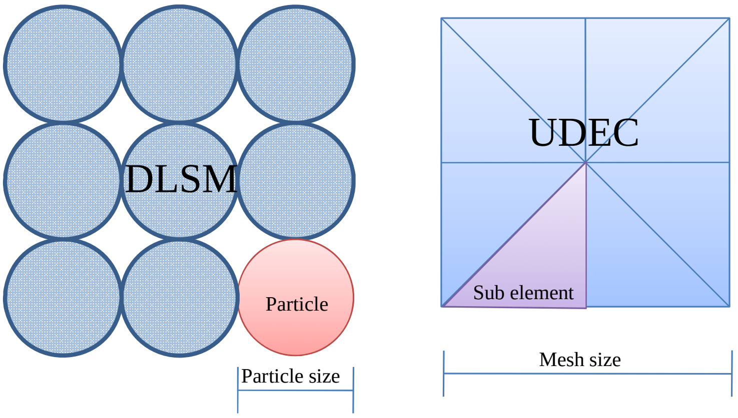

Figure 7.27. Difference between definations of the meshsize in UDEC and the particle size in DLSM.

is only available for discontinuous media under simple geometry, e.g., the analytical solution of incident wave propagates in direction parallel to fractures without considering multiple reflections were studied by Nihei et al. [15] and Nakagawa et al. [16] and considering multiple reflections in [10]. Experiments and field tests are the physical results and can be used to validate the analytical solution. For example, laboratory experiments conducted by Hopkins et al [17] and Zhao et al. [18] verified that the simplified analytical model of wave propagation. However, performing experimental/field tests are very expensive and the medium condition is uncontrollable. Fortunately, numerical modeling provides useful alterative tool. For example, the DEM code UDEC was used to simulate shock wave propagation in across discontinuous media [4, 6, 14]. As a new developed numerical code for rock dynamics, DLSM should have the ability to model discontinuity. In this section, two methods are proposed to enhance this ability of DLSM. These two methods are both implemented into DLSM code and verfied by comparing DLSM modeling restuls of P-wave and S-wave propagation through single discontinuity with analytical solutions.

7.3.1 Represent discontinuity in DLSM

Weak material layer method

The most simple way to represent a discontinuty is to treat it as a thin layer of material with weak mechanical properties as shown in Figure 7.28. This method is easy to be implemented into the DLSM code. Different joint pattern models can also easy to be generated (seen Figure 7.28). There is no need to change the orignal DLSM code but only a few modifications on the pre-processor. The stiffness paramters of the discontinuty represented through this method are given as

$$k_n = \frac{C_{11}}{d} = \frac{E(1-\nu)}{(1+\nu)(1-2\nu)d} \tag{7.14}$$

$$k_s = \frac{C_{44}}{d} = \frac{E}{2(1+\nu)d} \tag{7.15}$$

where *d* is the thickness of the weak material layer.

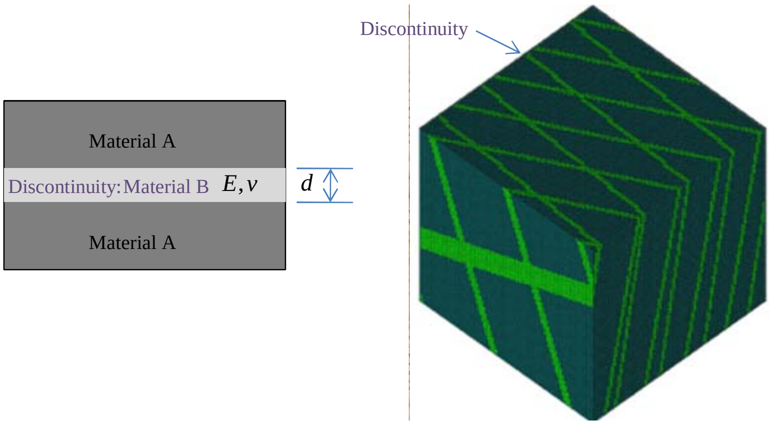

Figure 7.28. The weak material layer method used in DLSM to represent discontinuity.

Virtual joint plane method

The idea of virtual joint plane method is original from the idea of smooth-joint contact model [19]. The work principle of smooth-joint contact model is shown in Figure 7.29. The relative displacement increment between the two particles is decomposed into components normal and tangential to the smooth joint surface and the force-displacement law is operated under the smooth joint coordinate.

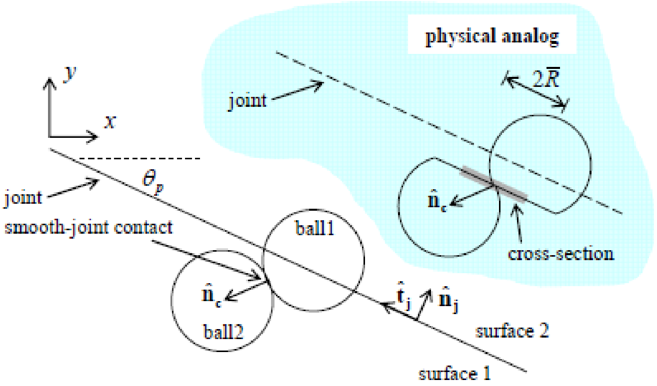

Figure 7.29. The smooth joint contact model [19].

A similar idea is proposed in DLSM to represent discontinuty. The principle is shown in Figure 7.30. A virtual joint plane is inserted into the DLSM model. When a spring is cut by the virtual joint plane, its paramters will be modified accroding the following rules:

a) Change the direction of the original spring into the normal vector of the virtual joint plane.

b) Replace stiffnesses of the bond spring as:

$$k_n^{bond} = \frac{k_n^j A l^*}{n^{cut}} \tag{7.16}$$

$$k_s^{bond} = \frac{k_s^j A l^*}{2n^{cut}} \tag{7.17}$$

where k_n^{bond} and k_s^{bond} are the normal and shear stiffness of the bond, k_n^j and k_s^j are the inputted joint stiffness parameters for the discontinuity, A is the area of the joint plane and l^* is the mapped bond length on the joint plane normal direction, n^{cut} is the number of bonds cut by the plane. Implementation of virtual joint plane is more complex than that of the weak material layer method as modifications of the caculation procedure of DLSM are needed. These two methods are implemented into the DLSM code and will be verfied in following section.

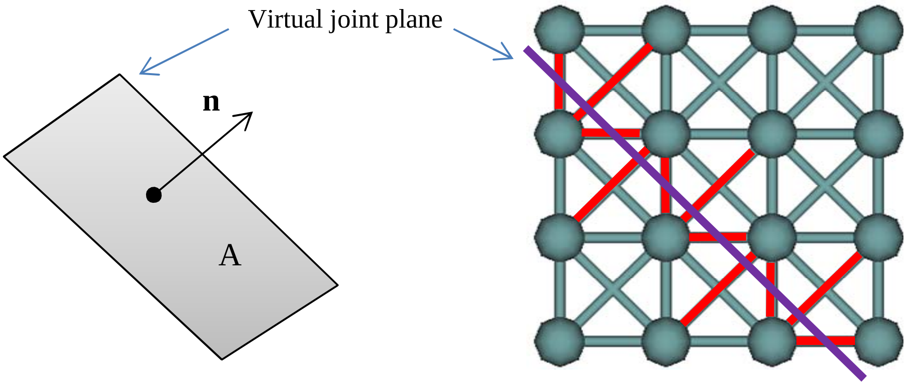

Figure 7.30. The virtual joint plane method used in DLSM to represent discontinuty.

7.3.2 Verifications

Analytical solution

The theoretical expression of transmission coefficient for normally incident harmonic P-wave/S-wave across a single linearly deformable fracture in an identical rock material is given as [15,16]:

$$|T_1| = \sqrt{\frac{4(k/z\omega)^2}{1+4(k/z\omega)^2}} \tag{7.18}$$

where $|T_1|$ is the transmission coefficient across a single fracture, *k* is the normal/shear fracture stiffness, ω is the angular frequency of the harmonic wave, and z is the P-wave/S-wave impedance, which is equal to product of P-wave/S-wave velocity and rock density. In order to obtain the analytical solution of half-cycle sinusoidal wave across a single fracture, the incident wave is first transformed into a sum of series of harmonic waves in frequency domain by Fast Fourier Transform (FFT). Transmitted waves of all harmonic components across single discontinuity are obtained from Equation (7.18). Then, the final transmitted wave can be reproduced through an Inverse Fast Fourier Transform (IFFT) of these transmitted harmonic waves.

DLSM modeling

The used DLSM model is shown in Figure 7.31. The dimension of the model is 70mm×140mm×5mm and the used particle size is 0.5mm. The material parameters are elastic modulus 27.878GPa, Poisson's ratio 0.298 and the density 2120kg/m^3. A half sinusoidal velocity P-wave/S-wave with frequency of 20 kHz is applied at the top boundary of the model. The *lr* is 1/420 for P-wave propagation problem and 1/220 for S-wave case. From the results obtained from the last section, it can be concluded that the particle size will only induce very little numerical error in the following simulations.

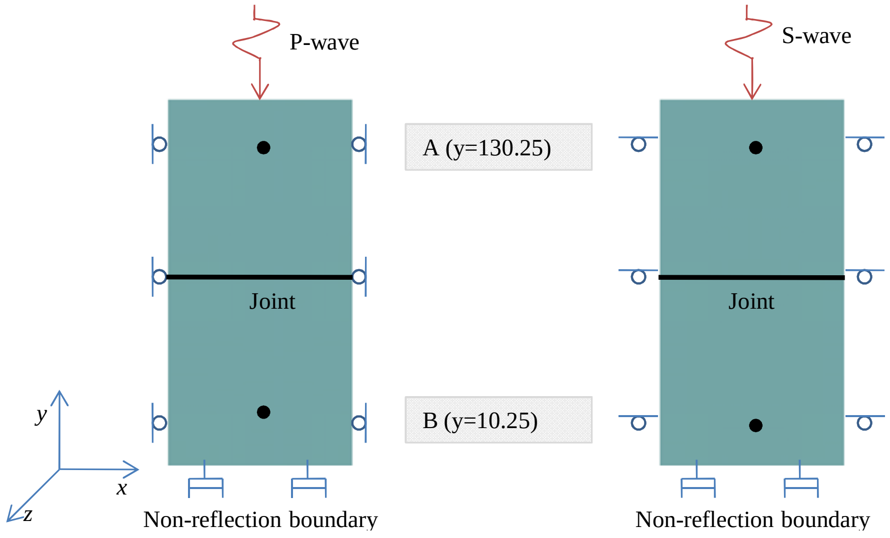

Figure 7.31. The specification of the DLSM model for P-wave/S-wave incidence.

Firstly, the weak material layer method is used to represent the discontinuity. The material properties of the weak material layer are taken as a small ratio of the original inputted parameters. Here, this ratio is taken as 0.005, 0.01, 0.02, 0.05, 0.08, 0.1, 0.3, and 0.5 to produce different normal and shear stiffness. The modeling results of the weak material layer method are shown in Figure 7.32. It points out that the difference between analytical solution and DLSM modeling is apparent. In order to provide quantity comparison, the percentage errors between numerical and analytical solutions are listed in Table 7.1. It can be seen that the error decreases with increasing of the joint stiffness. The maximum error of weak material layer method is about 9% on modeling P-wave and 18% for S-wave. So this method is not a good solution for quantitative analysis of wave propagation through discontinuities.

Figure 7.33 shows the results of virtual joint plane method. It can be seen that better agreements are obtained. The percentage errors of the virtual joint plane method based DLSM on modeling P-wave and S-wave propagation are given in Table 7.2. The maximum error for P-wave is 0.59% and 2.52% for S-wave. This means the virtual joint plane method is better than the weak material layer method on modeling discontinuity. Overall, the implementation of discontinuity in DLSM is successful. Further extensions and applications of DLSM to more complex conditions, e.g., multiple joints, crossed joints and non-linear joints, can be performed based on the work of this chapter.

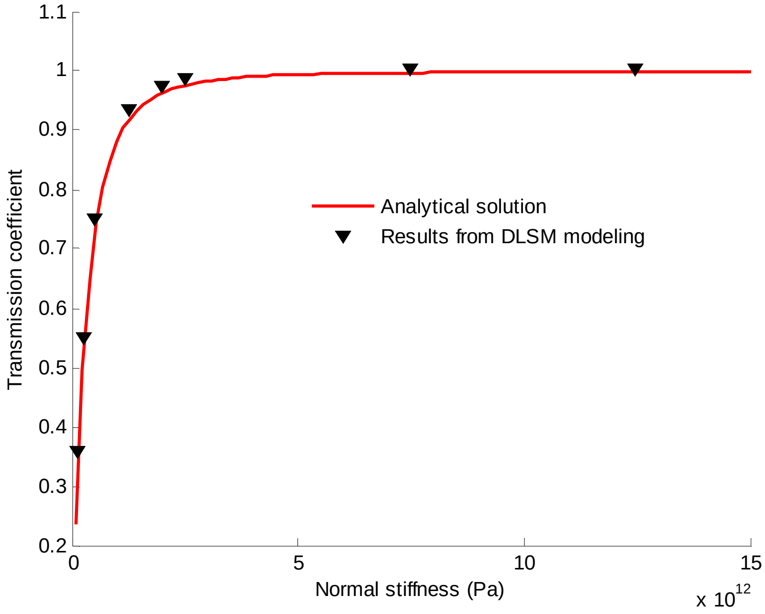

(a) P-wave

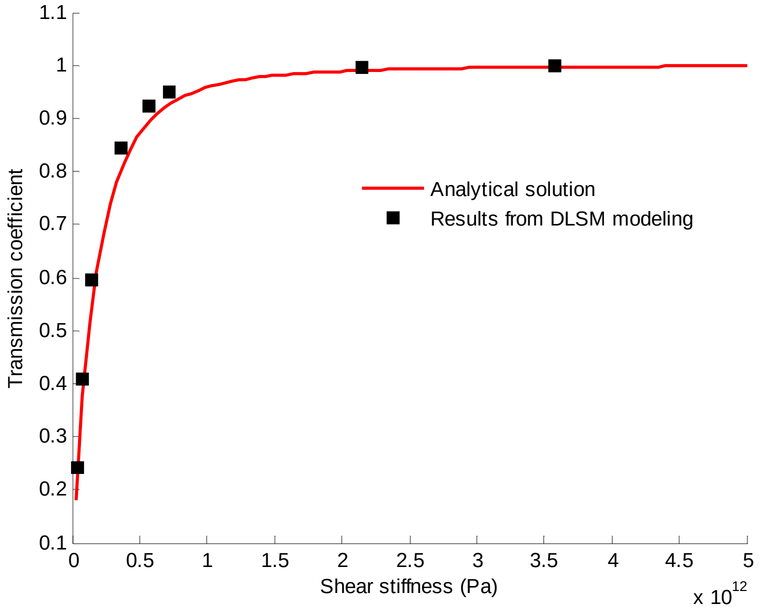

(b) S-wave

Figure 7.32. The modeling results of the weak material layer method and analytical solution of P-wave/S-wave propagation through single discontinuity.

Table 7.1 Errors of the weak material layer method on modeling P-wave/S-wave propagation through single discontinuity.

k_n(GPa)	124.64	249.28	498.56	1246.4	1994.3	2492.8	7478.5	12464.0
Error (%)	8.92	6.02	3.57	1.98	1.33	1.19	0.66	0.57
k_s (GPa)	35.8	71.5	143.1	357.8	572.4	715.5	2146.6	3577.7
Error(%)	17.94	17.98	10.11	5.70	3.15	2.50	0.57	0.27

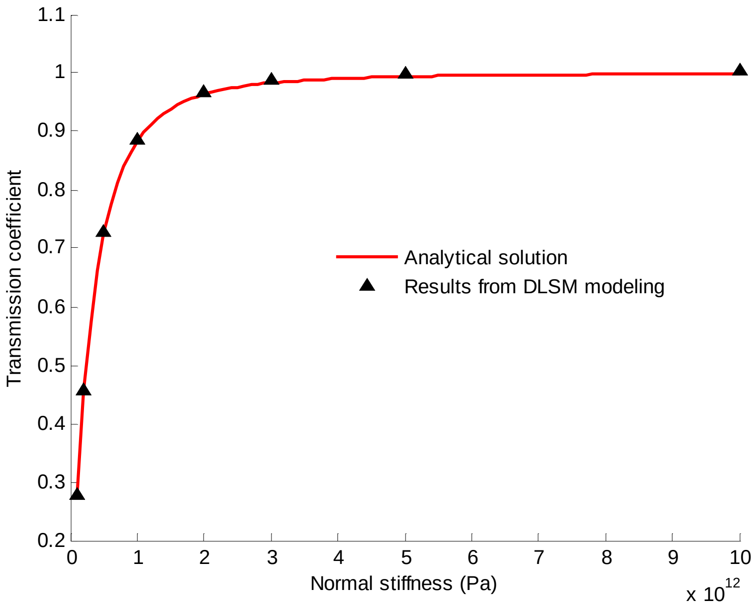

(a) P-wave

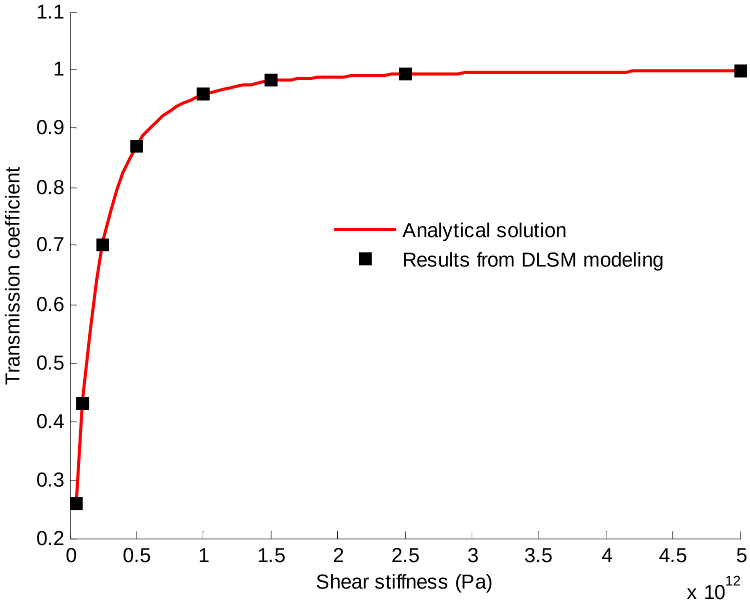

(b) S-wave

Figure 7.33. The modeling results of the virtual joint plane and analytical solution of P-wave/S-wave propagation through single discontinuity.

Table 7.2 Errors of the virtual joint plane method on modeling P-wave/S-wave propagation through single discontinuity.

k_n(GPa)	100	200	500	1000	2000	3000	5000	10000
Error (%)	0.43	0.04	0.26	0.42	0.52	0.53	0.59	0.53
k_s (GPa)	50	100	250	500	1000	1500	2500	5000
Error(%)	2.52	1.50	0.70	0.16	0.02	0.13	0.18	0.09

7.4 Conclusions

Abilities of DLSM on modeling wave propagation are extended and verified in this chapter. A non-reflection boundary condition based on visco element method was implemented into DLSM and verified through 1D and 2D wave propagation problems. The influence of particle size on the numerical error of DLSM modeling of P-wave and S-wave propagation was also investaged. The suggested mesh ratio (*lr*) for different conditions are provided. For DLSM modeling of wave problems, the suggested *lr* for P-wave is 1/41 and 1/90 for shear wave. In order to model discontinuity in DLSM, weak material layer method and virtual joint plane method are proposed. These two methods are used to model P-wave and S-wave propagation through single discontintuty and compared with the analytical solution well.

Compared with traditional numerical methods, the DLSM has the following advantages on modeling wave propagtoin problems

1. Discontinuities are easy to be implemented for both the weak material layer and virtual joint plane method.
2. Computational model is easy to be generated as the meshless properties of DLSM.
3. DLSM has the potential on modeling continuum-discontinuum wave propagation problems, e.g., wave induced damage and influence of material fracturing on the wave propagation.

The major shortcoming of DLSM on modeling wave propagation is that a strict requirment on particle size is needed. It leads the computational requirement of DLSM model is higher than the conventional methods, e.g., FEM and DEM. However, this problem can be overcame through parallel implementation of the DLSM code, which will be presented in next Chapter.

7.5 References

1. Lysmer J, Kuhlemeyer RL. Finite dynamic model for infinite media. J. Eng. Mech. Div. ASCE 1969; 95: 859–877.
2. Liu GR, Achenbach JD. A strip element method for stress analysis of anisotropic linearly elastic solids. J. Appl. Mech. 1994;61: 270–277.
3. Gratkowski S, Pichon L, Razek A. Infinite elements for 2D unbounded wave problems. Int. J. Comput & Math. Ele. Eng. 1995; 14: 65-69.
4. Chen SG, Cai JG, Zhao J, Zhou YX. Discrete element modelling of underground explosions in jointed rock mass. Geological and Geotechnical Engineering, 2000;18: 59-78.
5. Jiao YY, Zhang XL, Zhao J, Liu QS. Viscous boundary of DDA for modeling stress wave propagation in jointed rock. Int J Rock Mech Miner Sci 2007; 44:1070–1076.
6. Fan SC, Jiao YY, Zhao J. On modeling of incident boundary for wave propagation in jointed rock masses using discrete element method. Compu Geotech. 2004;31:57–66.
7. Zhao H, Gary G. On the use of SHPB techniques to determine the dynamic behavior of materials in the range of small strains. Int J Solid Struct. 1996; 33: 3363-3375.
8. Ma GW, Hao H, Zhou YX. Modeling of wave propagation induced by underground explosion. Comput Geotech. 1998;22(3–4): 283–303.
9. Chen SG. Discrete element modelling of jointed rock mass under dynamic loading, Ph.D. Thesis, Nanyang Technological University, Singapore, 1999.
10. Cai JG, Zhao J. Effects of multiple parallel fractures on apparent wave attenuation in rock masses. Int J Rock Mech Miner Sci 2000;37(4):661–82.
11. Graff KF. Wave motion in elastic solids, Ohio state university press, 1979.
12. Lei WD. Numerical studies on 2-D compressional wave propagation in jointed rock masses, Ph.D. Thesis, Nanyang Technological University, Singapore, 1999.
13. Arfken G. Hankel Functions, Mathematical Methods for Physicists, 3rd ed. Orlando, Academic Press. 1985: 604-610.
14. Zhao XB, Zhao J, Cai JG, Hefny AM. UDEC modelling on wave propagation across fractured rock masses, Computers and Geotechnics 2008;35: 97–104.
15. Nihei KT, Yi W, Myer LR, Cook NGW. Fracture channel waves. J Geophys Res 1999;104(b3): 4769-81.
16. Nakagawa S, Nihei KT, Myer LR. Shear-induced conversion of seismic waves across single fractures. Int J Rock Mech Miner Sci 2000;37: 203-18.
17. Hopkins DL, Myer LR, Cook NGW. Seismic wave attenuation across parallel fractures as a function of fracture stiffness and spacing. EOS Trans AGU 1988;68(44): 1427-35.
18. Zhao J, Cai JG, Zhao XB. Dynamic model of fracture normal behaviour and application to prediction of stress wave attenuation across fractures. Rock Mech Rock Eng. 2008;41(5): 671-693.
19. Ivars DM, Potyondy DO, Pierce M, Cundall P.A. The smooth-joint contact model, 8th. World Congress on Computational Mechanics (WCCM8) 5th. European Congress on Computational Methods in Applied Sciences and Engineering, 2008.

Chapter 8

Parallelization of DLSM

In this chapter, parallelization of the DLSM will be presented. The motivation of parallelization is to reduce computational time and memory requirements by serial computing. With the development of parallel computing technologies in both hardware and software, parallelization of a code is becoming easier than before. There are many available choices now. In this chapter, OpenMP with multi-core PC and MPI with cluster are selected as the parallelization environments to parallelize the DLSM code. Performances of these parallel DLSM codes are tested on different computers. It is found that the parallel DLSM code with OpenMP can reach a maximum speedup of 4.68× on a quad-core PC. The parallel DLSM code with MPI can achieve a speedup of 40.886× when 256 CPUs are used on a cluster. At the end of this chapter, a high resolution model with four million particles, which is too big to handle by the serial code, is simulated by using the parallel DLSM code on a cluster. It can be concluded that the parallelization of DLSM is successful.

8.1 Introduction

The basic idea of parallelization is to distribute computations to several processors and to execute the distributed works simultaneously. The implementation of a parallel code is much different from that of a serial code. Fortunately, with the development of technologies in computer science, this is becoming easier and easier. So far, there exist three popular choices for parallel computing. The first choice is the multi-core PC. Quad-core CPU is very common now and even the 80-core CPU prototype has already been developed [1]. So performing parallel computation in PC is not a dream now. The GPU computing [2] is the second choice. It has been reported that more than 100× speedup is achieved by using GPU for some applications [3]. The last choice is the computer cluster which is available for many universities and research institutes. Cluster is a high level parallelization system [4] which is made of many computer nodes (each node could be a multi-core or GPU computer). In this chapter, instead of giving a verbose review on the parallel computer history like the classification made by Flynn in 1966 [5], a review on the three parallel computer systems mentioned above and the corresponding software development environments will be presented. The reason is that these three choices are the currently available and popular solutions for parallelization implementation.

Personal computer (PC) refers to general purpose computer whose size and capabilities are small and the price is low enough to make it acceptable to individuals. PC is also called as micro computer which means its computing power is much less than super computer. However, with the development of computer hardware and software, nowadays PC becomes the dominant tool in performing scientific computing and numerical modeling. The main reason is that application software and operation system in PC are much friendly to users. Another reason is that with the improvement of CPU and memory used in PC some engineering problems can also be solved on a normal PC. For example, laptop equipped with a 2GHz CPU and 2GB of memory is enough for running the DLSM model with a half million particles. Recently, a new term called as Personal High Performance Computing (PHPC) [6] is proposed. PHPC aims to run problems previously could only be handled on a supercomputer in a normal PC. This may become true in the near future, if the 50-core CPU and the 64-bit operation system are mature enough. The future PC equipped with advanced multi-core processor will surely provide adequate computing power and memory space for scientific computing. The multi-core processor targets at providing better performance. It includes multiple execution units and the instructions per cycle can be executed separately in different cores. The typical structure of a quad-core processor is shown in Figure 8.1. The advantage of the multi-core PC is that it can handle multiple tasks at the same time. The amount of gained performance by using the multi-core processor is strongly dependent on the code implementation. Many typical applications, however, do not consider parallelization on multi-core PC, which remains an important on-going topic of research. Fortunately, parallel programming environments such as OpenMP [7], pThreads [8] and TBB [9] can be used to implement the multi-core version of an existing code. Normally, the parallelization of a code on multi-core PC is relatively simple as it only needs to deal with the shared memory environment. It does not need to consider the task distribution and communication between different processors. However, there also exist some disadvantages of multi-core processor [10, 11]. Firstly, adjustments of the existing code are required to allow maximum utilization of the computing resources. Secondly, it is more difficult to manage the thermal problem than single-chip design. Thirdly, multithread code often requires complex co-ordination of threads and is difficult to find bugs. Moreover, the interaction between different threads can also cause safety problems. Even so, our experience tells that parallel computing using multi-core processor is stable and promising at least for research purpose. In this chapter, the multi-core implementation of the Distinct Lattice Spring Model (DLSM) will be presented and its performance will be tested in multi-core PCs.

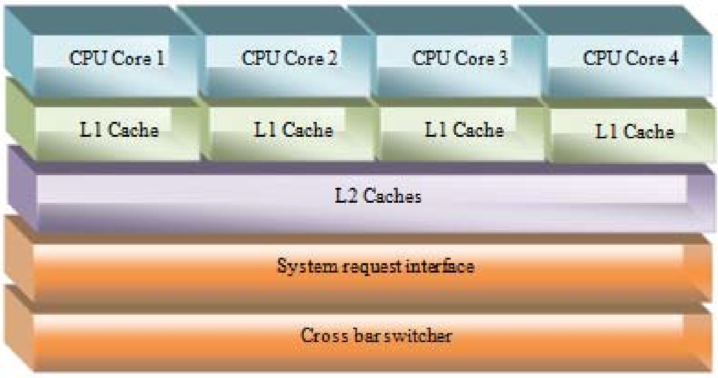

Figure 8.1. The diagram of a generic quad-core processor.

Recently, GPU (Graphics Processing Unit) computing [2] is becoming a interesting topic in high performance computing. The most attractive aspects of this new technology are the extremely high speedup for some scientific computing problems and the price of a GPU computer system is much cheaper than that of a super computer. GPU was originally used as specialized processor to deal with 3D graphics rendering. Very recently, a new concept, General Purpose GPUs, is proposed to allow the GPU to perform massive floating-point computing [3]. The basic idea of GPU is to put a large number of specified computing units on a single board and interpret hundreds of thousands of threads. These threads can deal with the calculation simultaneously. The architecture of a typical GPU computing card is shown in Figure 8.2. It has 128 thread processors and each thread processor has a single-precision FPU and 1,024 registers. These thread processors could process different data at the same time. The framework of memory communication is also different from the conventional parallel computer and could largely increase the parallel efficiency, e.g., 100× speedup is achieved when the shared memory scheme is used [13]. There are three available ways for developing a GPU based code. They are OpenGL[14], OpenCL [15] and CUDA [3]. Normally, implementation of a GPU code will require certain knowledge of the operation of GPU at hardware layer. Overall, GPU computing is a sheared memory system and it is a promising solution for PHPC. It also provides a solution for real time numerical simulation. However, the hardware and software platforms of GPU computing are still under development. For example, the double precision GPU card will be available in a few months and CUDA will support C++ in future. Taking into account of this delay, waiting for the technique to become mature is a good choice.

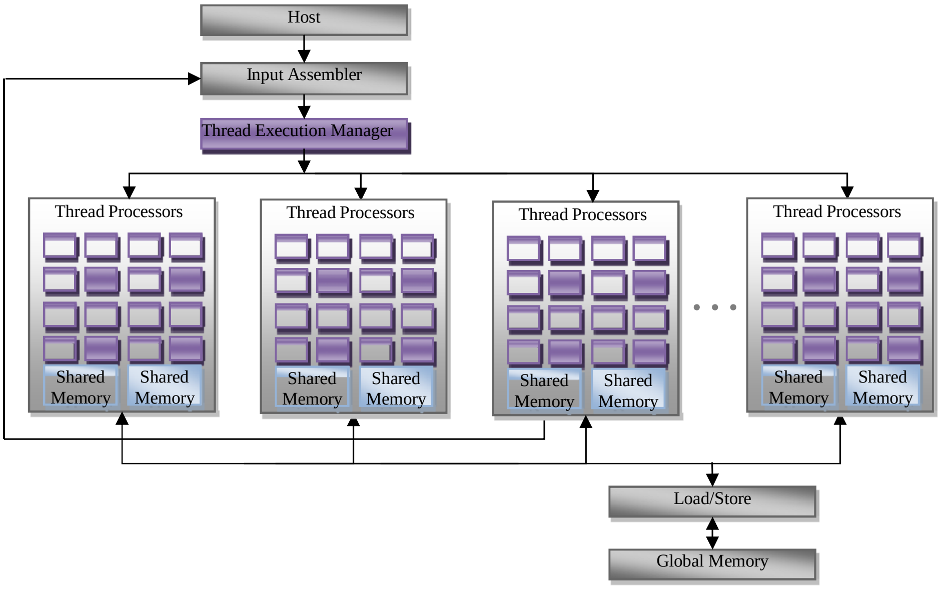

Figure 8.2. The Nvidia GeForce 8 graphics-processor architecture (redraw based [12]).

Modern supercomputer often refers to computer cluster which is a collection of computers highly connected through a high-speed network. Cluster computer is a high level parallelization system and the most powerful computers in the world are always clusters [17]. New developed technologies on high performance computing (e.g., multi-core CPU and GPU) can always be merged into a cluster system. For example, the top 5th Tianhe-1 supercomputer has integrated multi-core CPUs with GPUs [17]. The architecture of clusters is normally based on a modular concept which can be simply regarded as a group of specific computers connected through internet for working together. For example, the cluster used in this work, Pleiades2 at EPFL, is built on a Gigabit Ethernet Network as shown in Figure 8.3. MPI (Message Passing Interface) [18] and PVM (parallel virtual machine) [19] are programming tools for parallelization implementation under cluster environment. In this thesis, the free MPI library MPICH (developed at Argonne National Lab) [20] will be used. A certain amount of modifications of the original DLSM code are required. As cluster is a distributed memory system, the model decomposition and communications between different processors (computer nodes) should be handled explicitly.

Moreover, the operation system used in cluster is different from PC. For example, a standard SUSE Linux is used as the operation system in Pleiades2 cluster. How to integrate different operation systems on PC and that on the cluster is also a problem facing in the parallelization of DLSM. In this chapter, the Distinct Lattice Spring Model (DLSM) [21, 22] will be parallelized both for multi-core PC based on OpenMP and for cluster based on MPI. Firstly, the implementations of the parallel DLSM under different platforms will be presented. Then, the performance of the parallel DLSM codes will be tested on different computers. Finally, some conclusions on the parallelization of DLSM will be derived.

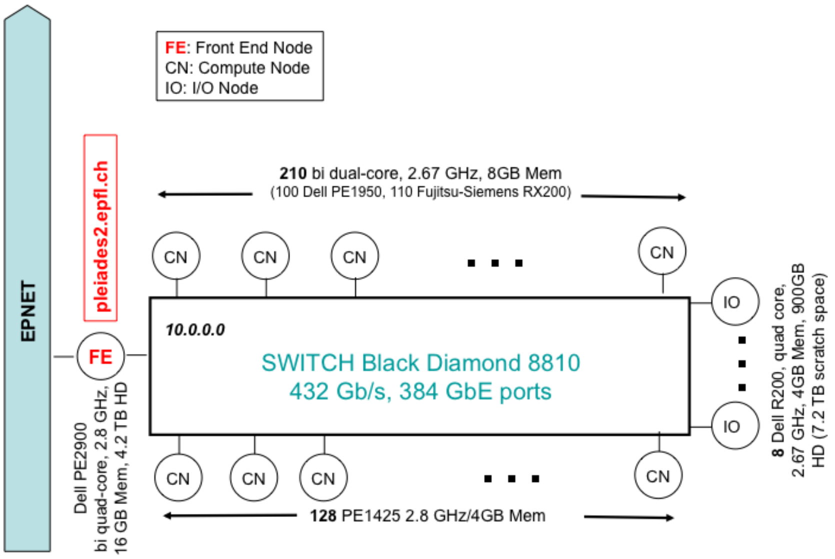

Figure 8.3. Current configuration of Pleiades2 Cluster of EPFL [16].

8.2 Parallelization of DLSM on multi-core PC

This section will present the parallel implementation of DLSM code based on OpenMP. The motivation is to reduce computational time on multi-core PC. As DLSM is an explicit method in time, only minor changes are needed to parallelize the code. Quad-core PC is quite common now, but serial code cannot well utilize its computing resources. OpenMP provides a useful tool to parallelize software for multi-core environment. It is an application program interface which comprises compiler directives, runtime library routines and environment variables. It can work under the compiler environments of FORTRAN, C and C++. Fork-joint model is used in OpenMP to parallelize a task. Hereafter, the parallel DLSM code based on OpenMP is named as the multi-core DLSM.

The work scheme of the serial and multi-core DLSM are shown in Figure 8.4. It can be seen that the serial DLSM code has only one main thread and the force and displacement of particles are calculated sequentially (as shown in Figure 8.4(a)). The multi-core DLSM uses the fork-joint model to let one cycle being calculated by more than one processor (see Figure 8.4(b)). The parallel DLSM works as follows. Firstly, the master thread is activated when DLSM begins execution. Then, when the master thread executes the points where parallel operations are required, the master thread forks and additional threads are used to realize parallel computing.

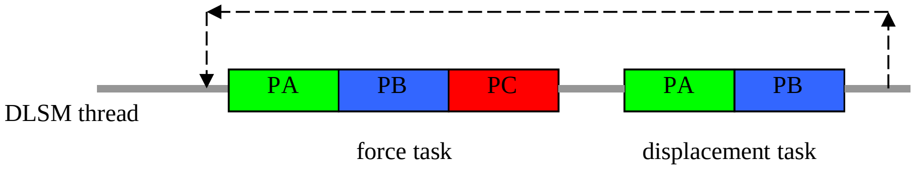

(a) serial DLSM

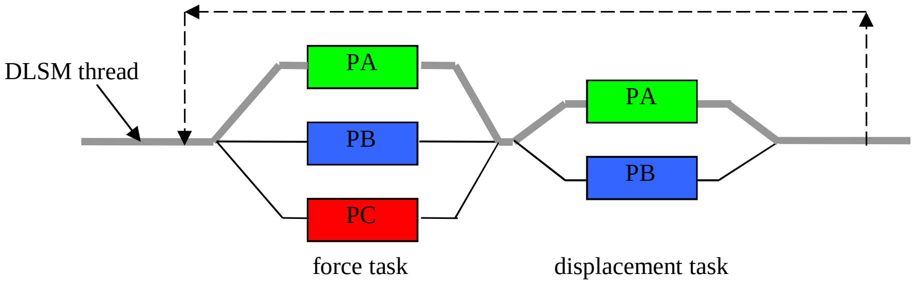

(b) parallel DLSM

Figure 8.4. Scheme of serial and parallel implementation of DLSM.

In multi-core DLSM, the force calculation and the displacement update are the only procedures needed to be parallelized. Only a few macros are added to produce fork for a single loop. A code segment of OpenMP implemented DLSM is shown in Figure 8.5. The most attractive point of OpenMP implementation is that it can increase the computational performance of the code automatically with only a few modifications and no change of code structure. In section 8.4, examples will be presented to show the efficiency of the multi-core DLSM code tested on quad-core PCs.

```
int i=0;
#pragma omp parallel for
for(i=0;i<N;i++)
{
        pList[i].x[0]+=pList[i].v[0]*dt;
         pList[i].x[1]+=pList[i].v[1]*dt;
         pList[i].x[2]+=pList[i].v[2]*dt;
}
```

Figure 8.5. The code segment of the multi-core DLSM.

8.3 Parallelization of DLSM on cluster

The multi-core DLSM targets at full utilization of the computing resources on multi-core PC. Although the 50-core CPU exists in prototype and may be available for practical usage in the near future, the limitation on available cores and memory in a normal PC cannot be removed completely. Speedup of the multi-core DLSM shall be limited eventually. Moreover, the shared memory strategy also limits the modeling capability of the multi-core DLSM. In this section, the MPI based parallelization of DLSM on cluster will be presented to solve these problems. It is named as the cluster DLSM in order to distinguish with the previous one for multi-core PC.

8.3.1Parallelization strategy

The domain decomposition is used as the parallelization strategy for the cluster DLSM. Firstly, the simulation domain is divided into many small cubic cells. Each cell contains a list of particles fallen in it. Secondly, the simulation domain is divided into a number of subdomains (larger cubes) based on these small cubes. Each subdomain contains a number of small cubes. Particles in each subdomain are distributed to a processor to be calculated separately from the others. This scheme is called as the linked cell method in Molecular Dynamic (MD) parallelization [24, 25]. The number of subdomains is equal to the number of processors used in the simulation. We have the following relation

$$np = np_x \times np_y \times np_z \qquad (8.1)$$

where np is the number of total processors (subdomains), np_x, np_y, np_z are the number of dividing in each direction of the model. A decomposition code (Domain Cutter) is designed to produce, for each subdomain, the data files, the information of corresponding neighbors and the index of particles needed to be communicated. The decomposition can be finished automatically after np_x, np_y, np_z are given.

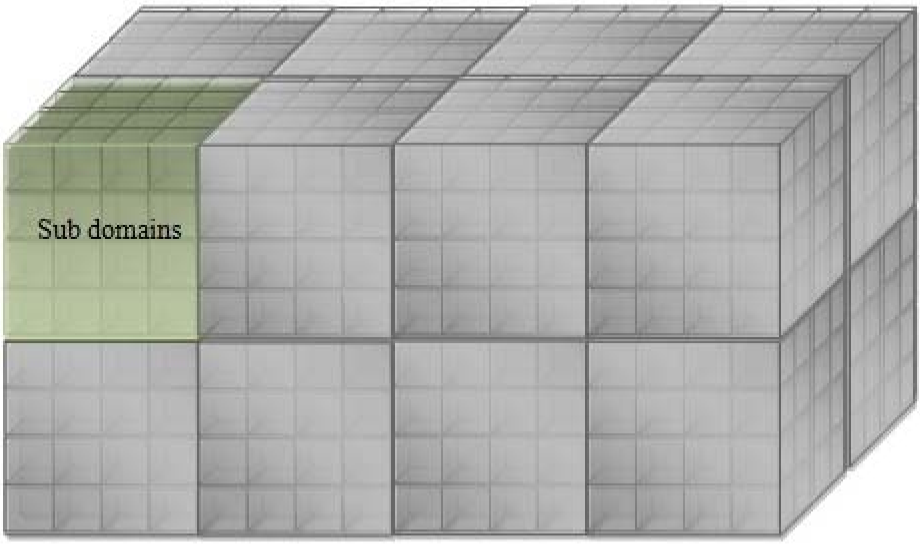

Figure 8.6. Decomposition of the simulation domain Ω into sixteen subdomains.

In the cluster DLSM, the force calculation procedure has to use the information of particles which do not belong to the current processor. Communication is needed to exchange the necessary information between different processors. In three-dimensional case, a typical subdomain has 26 neighbors. This will cause a large number of communication operations to be performed. By using a proper communication methodology [25], this number can be reduced to 6. The communication strategy is shown in Figure 8.7. First, the data are exchanged in x3 direction (left), then, data are exchanged in x2 direction (middle), and finally the data are exchanged in x1 direction (right). In Figure 8.7, green cells always send data to the yellow cells and the yellow cells always receive data from the green cells. Data are exchanged mutually between two neighboring face-to-face subdomains. The range of exchanging cells in each direction is different so that the communications between the corner-to-corner neighbors are avoided. It can be seen that only six sending and receiving operations need to be performed. The exchanged data include position, velocity, displacement, and strain state of the neighbor particles.

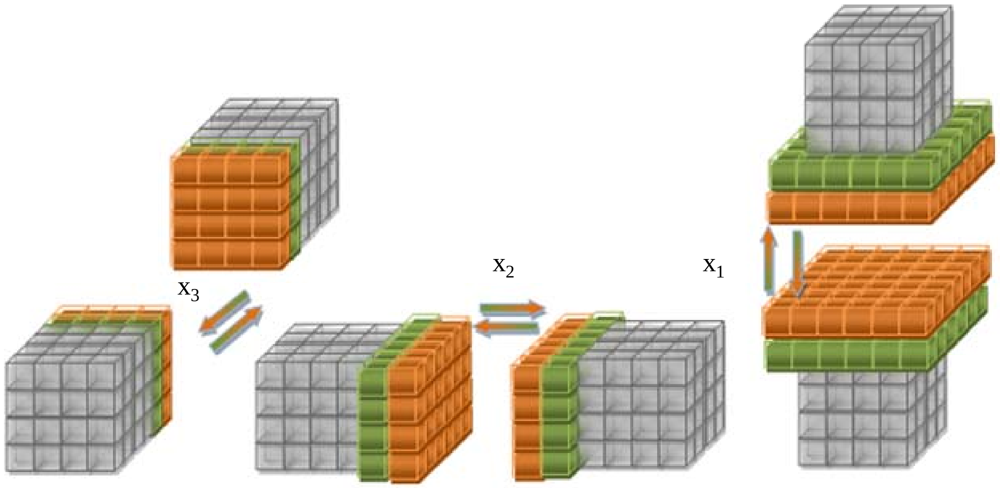

Figure 8.7. Communication scheme used in the cluster DLSM.

8.3.2 Implementation

In this section the MPI implementation of DLSM on cluster will be presented. The parallel implementation includes not only the MPI communication part but also the model pre-processing, solving and post-processing. Figure 8.8 shows the work flow of the cluster DLSM. Since PC is friendly to be used and cluster is much powerful in computing, the basic idea of this design is to let PC deal with the pre-processing and post-processing parts and cluster deal with the solving part. At the hardware layer, a server/client mode is used. PC is used as the client and cluster is used as the server for parallel computing (see Figure 8.8(a)). At the software layer, computing task is done through the cooperation between different codes running at Windows and Linux OS respectively (see Figure 8.8(b)). Firstly, the input data files are prepared by using a GUI program (RockBox DLSM3D) developed for Windows. When these data files are ready, they are sent to the cluster through network. Then, the parallel DLSM solver at cluster reads these files, solves the problem and produces the corresponding result files. Finally, the result files are copied to PC through network and transformed by a post-processing code (DLSM3D Collector) into the format which can be processed on PC by RockBox DLSM3D. This design makes the whole parallelization work only focusing on the MPI implementation of the solver. Pre-processor and post-processor still use the serial version developed for PC. By doing so, the respective advantages of different machines (cluster and PC) and different operation systems (Windows and Linux) are fully utilized.

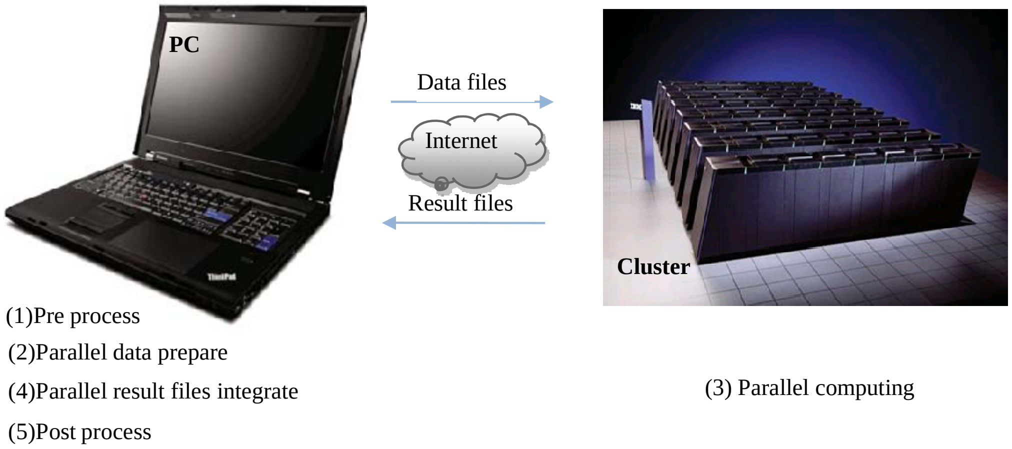

(a) work flow at hardware layer

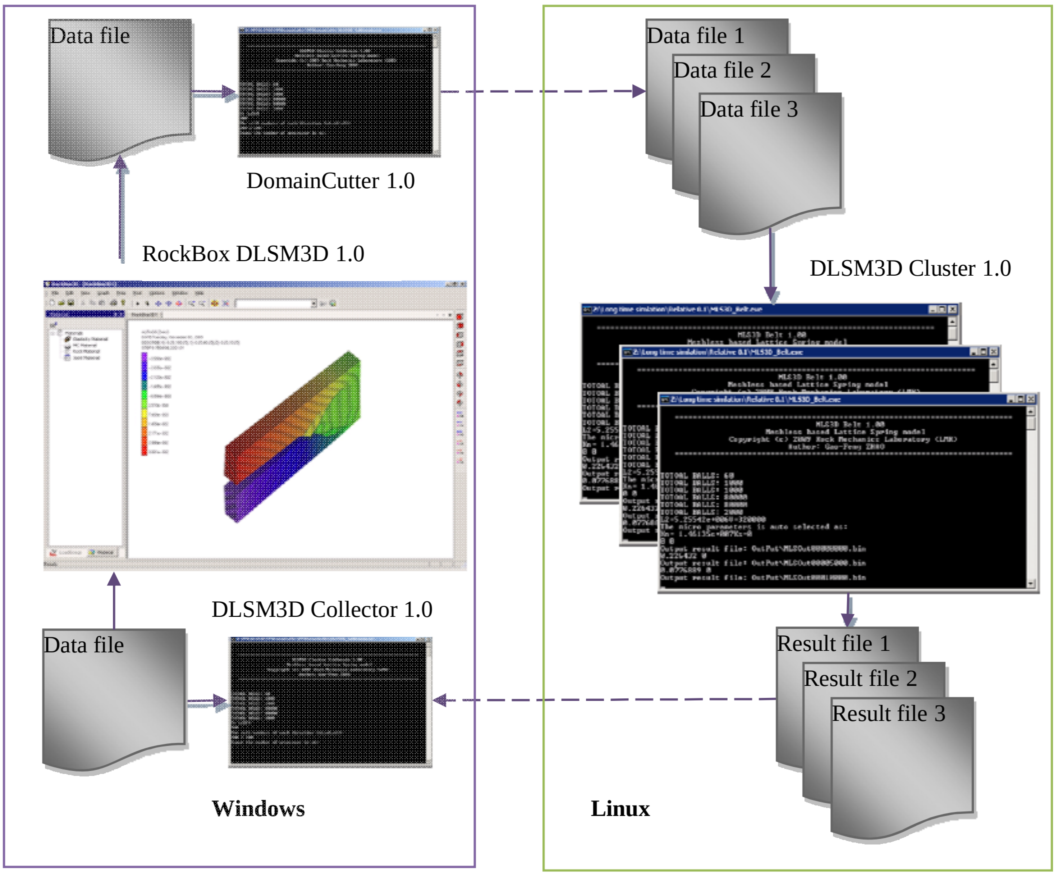

(b) work flow at software layer

Figure 8.8. Work flow of the parallel DLSM under cluster enviroment.

In the following, the MPI implementation of DLSM will be presented. The goal is to run DLSM model on a number of allocated processors in cluster through the domain decomposition approach. Data communication between different processors is realized through the MPI programming environment [18]. MPI provides a library that allows starting a given number of processes simultaneously and assigning a unique identity number for each process. It also provides communication functions which can be called to exchange the data between different processes. There are more than one hundred functions provided in the MPI library. Fortunately, the parallelization of the DLSM only uses seven of them. They are MPI_Init, MPI_Comm_size, MPI_Comm_rank, MPI_Barrier, MPI_Isend, MPI_Recv and MPI_Finalize. A few modifications are needed for the parallelization of DLSM based on these MPI functions. As a demonstration, the main function of the cluster DLSM code is shown in Figure 8.9.

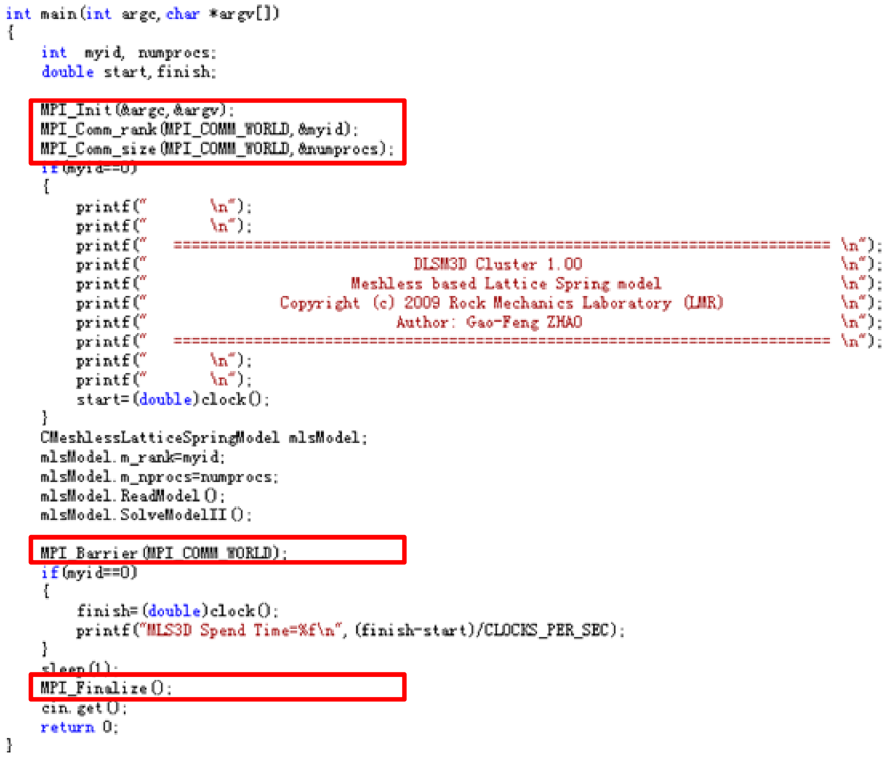

```
int main(int argc, char *argv[])
{
    int  myid, numprocs;
    double start,finish;

    MPI_Init(&argc,&argv);
    MPI_Comm_rank(MPI_COMM_WORLD,&myid);
    MPI_Comm_size(MPI_COMM_WORLD,&numprocs);
    if(myid==0)
    {
        printf("        \n");
        printf("        \n");
        printf("    ==========================================================================  \n");
        printf("                               DLSM3D Cluster 1.00                              \n");
        printf("                        Meshless based Lattice Spring model                     \n");
        printf("                Copyright (c) 2009 Rock Mechanics Laboratory (LMR)              \n");
        printf("                             Author: Gao-Feng ZHAO                              \n");
        printf("    ==========================================================================  \n");
        printf("        \n");
        printf("        \n");
        start=(double)clock();
    }
    CMeshlessLatticeSpringModel mlsModel;
    mlsModel.m_rank=myid;
    mlsModel.m_nprocs=numprocs;
    mlsModel.ReadModel();
    mlsModel.SolveModelII();

    MPI_Barrier(MPI_COMM_WORLD);
    if(myid==0)
    {
        finish=(double)clock();
        printf("MLS3D Spend Time=%f\n",(finish-start)/CLOCKS_PER_SEC);
    }
    sleep(1);
    MPI_Finalize();
    cin.get();
    return 0;
}
```

Figure 8.9. Code segment of the cluster DLSM.

In the cluster DLSM, contact detection and particle position update, failure treatment and results output will be processed separately for different processors. During the calculation, each process outputs its own results to a separate file which is identified by the process number. These files can be combined into a single file and be post-processed on PC. When the force calculation procedure is executed in the cluster DLSM, particle information will be exchanged between processors by using the communication scheme shown in Figure 8.7. Currently, the case of particle moving out of the present processor and entering into another processor is not considered because the communication of bond information between different processors is difficult. Problems involving dynamic contact detection can also be solved if the relative deformation between any two neighboring subdomains is not too large compared to the size of cell, so that it would be sufficient to use only the neighboring particles as the cushion layer between the two subdomains.

8.4 Performance Evaluation

In this section the different parallel DLSM codes are tested on different parallel computers. There are a large number of commonly used performance measures for evaluating a parallel code. In this thesis, the speedup S is adopted. It is defined as the ratio between the parallel runtime for a given number of CPUs and the serial runtime [26], i.e.,

$$S = \frac{t_p}{t_s} \tag{8.2}$$

where t_s is the runtime of the serial code using the best optimization and t_p is the runtime of the parallel code for the same problem. Another important index is the efficiency, E^{cpu}, which is the ratio between the speedup and the number of used CPUs, i.e.,

$$E^{cpu} = \frac{S}{n} \tag{8.3}$$

It is helpful in determining the proper n to be used. The speedup S can never exceed the number of used CPUs. Thus the efficiency E^{cpu} should satisfy

$$0 \le E^{cpu} \le 1 \tag{8.4}$$

8.4.1 The multi-core DLSM

A Brazilian disc model with 157,200 particles is calculated on two types of quad-core PCs. The parameters of the two used multi-core PCs are listed in Table 8.1. Figure 8.10 shows the simulation results obtained by the serial and multi-core DLSM codes.

It can be seen that the results obtained by the two codes are identical. This indicates that the parallel implementation is correct. The CPU utilization is shown in Figure 8.11 for the serial and multi-core DLSM codes. It can be seen that the serial code cannot take full advantage of the multi-core PC. Only 8% computing resource is used for the serial DLSM code, but this number increases to 88% for the multi-core DLSM code. This means the OpenMP implementation is effective and the computing resources can be fully utilized. The speedup of the multi-core DLSM has been tested on the first quad-core PC. The second one is only used to obtain the maximal speedup of the multi-core DLSM using the available PCs in LMR. Because the super thread technology is used in the second PC, the operation system will display eight CPUs instead of four (as shown in Figure 8.11). When the multi-core DLSM code is running on this computer, it is hard to control and display the type of used computing unit (super thread or CPU core). Thus, results from the second PC are not suitable for speedup analysis.

Table 8.1. Parameters of the used quad-core PCs.

CPU Name	Cores	Super thread	Speed	Memory
Intel Xeon	4	No	2.40 GHz	3GB
Intel Core i7 950	4	Yes	3.07 GHz	6GB

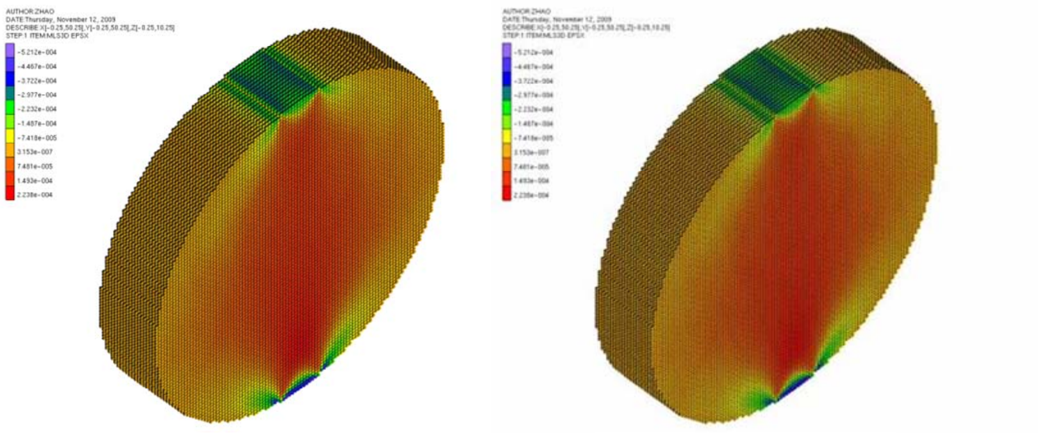
(a) Serial code (b) Parallel code (4 CPUs)

Figure 8.10. Simulation results obtained from the serial and parallel DLSM codes.

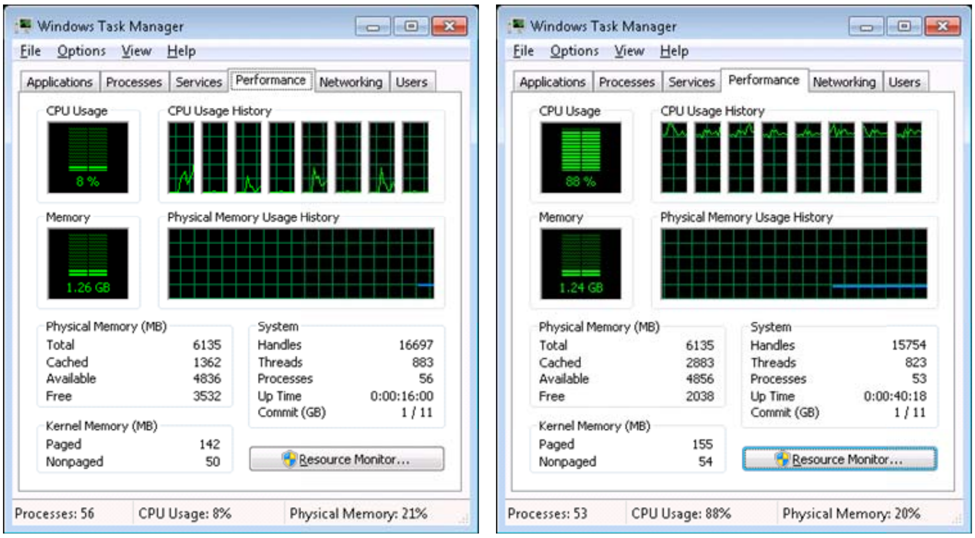

Physical Memory (MB)
Total 6135
Cached 1362
Available 4836
Free 3532

Kernel Memory (MB)
Paged 142
Nonpaged 50

System
Handles 16697
Threads 883
Processes 56
Up Time 0:00:16:00
Commit (GB) 1 / 11

Processes: 56 CPU Usage: 8% Physical Memory: 21%

Physical Memory (MB)
Total 6135
Cached 2883
Available 4856
Free 2038

Kernel Memory (MB)
Paged 155
Nonpaged 54

System
Handles 15754
Threads 823
Processes 53
Up Time 0:00:40:18
Commit (GB) 1 / 11

Processes: 53 CPU Usage: 88% Physical Memory: 20%

(a) Serial DLSM (b) Multi-core DLSM

Figure 8.11. CPU utilization of the serial and multi-core DLSM codes.

The brazilian disc model is simulated on the first quad-core PC. The computing time of the multi-core DLSM is compared with that of the serial DLSM and the results are given in Figure 8.12. It can be seen that the serial code is a little faster than the multi-core one when only one CPU is used. This is because the parallel code inserts some instructions to the original code, which cost some additional computing time. However, when two cores are used, the speed of the multi-core DLSM is obviously faster.

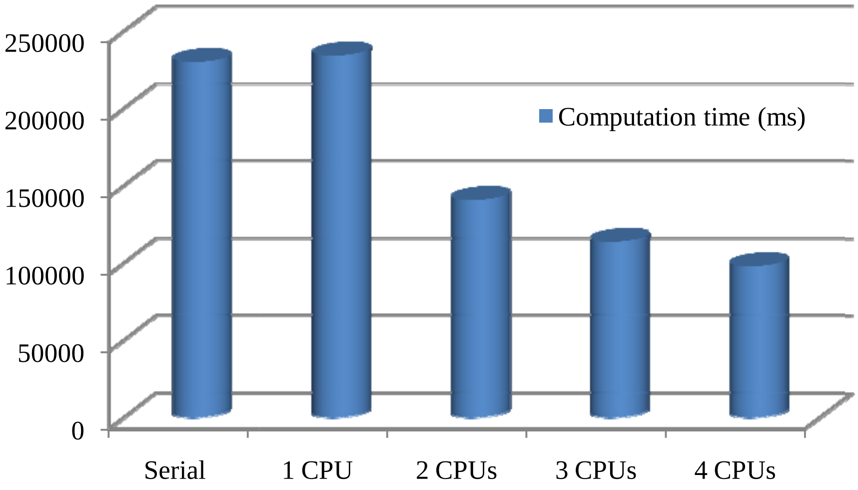

Figure 8.12. Computational time of the multi-core DLSM with different CPUs.

In order to study the influence of model size on speedup, three models, Model A (2,445 particles), Model B (19,760 particles) and Model C (157,200 particles), are computed by using both the serial DLSM code and the parallel DLSM code on the first PC. The speedup of the parallel code is shown in Figure 8.13. Results show that the speedup of the multi-core DLSM varies with the size of the simulated model non-monotonically. Overall, the trend is the same for different model sizes and a speedup around two could be achieved using the first PC.

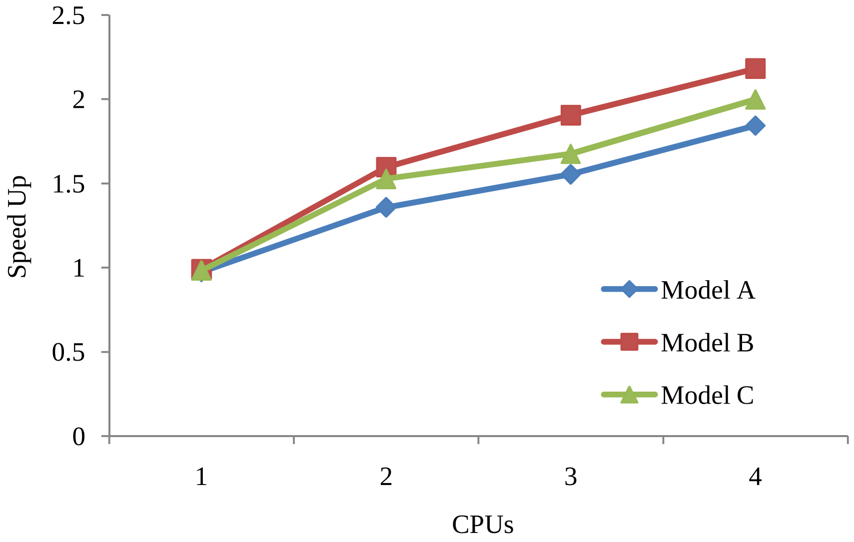

Figure 8.13. Speed up of the multi-core DLSM code.

In order to know the maximal speedup of the multi-core DLSM code, a Brazilian disc model with 78,500 particles is calculated on the second PC. It is a static simulation and in order to obtain the equilibrium state 20,000 cycles are calculated. The computing time is 86.16 minutes for the serial code, while it reduces to 18.43 minutes for the parallel code. A speedup of 4.68× is achieved. It is much higher than that obtained in the first PC. This is due to the fact that CPU equipped in the second PC is more advanced than that in the first one, e.g., larger cache and the super thread technique. A 4.68× speedup is desirable for practical application, e.g., a simulation previously taking four days could be finished now in one day. Now, it can be concluded that the implementation of the multi-core DLSM is successful.

8.4.2 The cluster DLSM

In this section, the performance of the cluster DLSM code is tested. The test problem is shown in Figure 8.14. The DLSM model is used to simulate the fragmentation process of a rock specimen under one TBM cutter. The particle size is 1mm and the model dimension is 400mm×5mm×200mm. The model is composed of 400,000 particles. The decomposition of the DLSM model for different cases is shown in Figure 8.15. Due to the limitation of available CPUs in the cluster, the maximum number of CPUs used to evaluate the speedup of the cluster DLSM is 256.

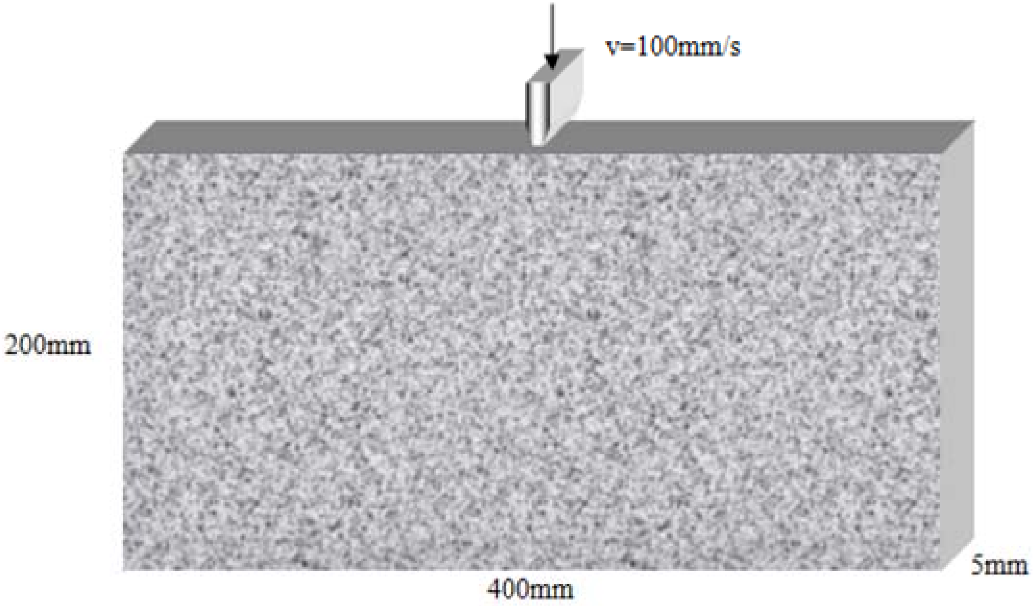

Figure 8.14. Scheme of single TBM cutter induced fragmentation problem.

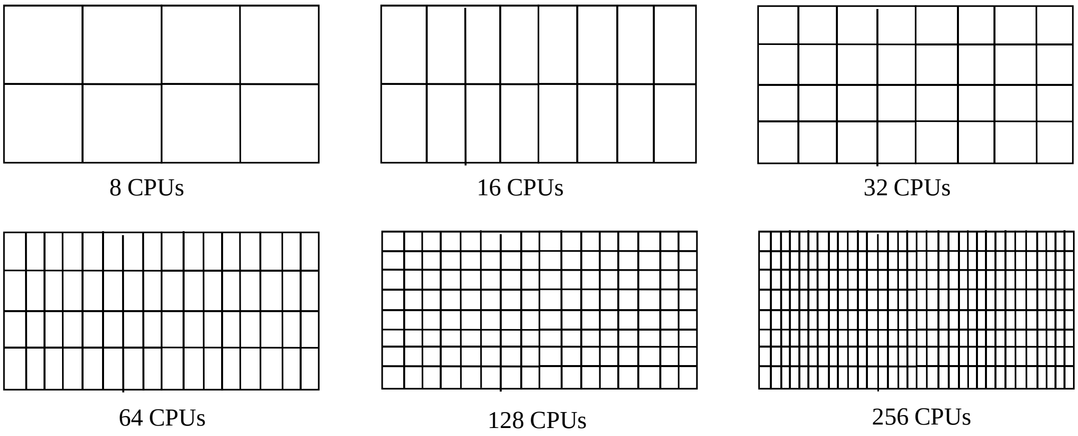
8 CPUs
16 CPUs
32 CPUs
64 CPUs
128 CPUs
256 CPUs

Figure 8.15. Domain decompostion for the TBM induced fragmentation problem.

Figure 8.16 shows the simulation results of the cluster DLSM. It turns out that the cluster DLSM can work correctly with a large number of CPUs involved in the computing simultaneously.

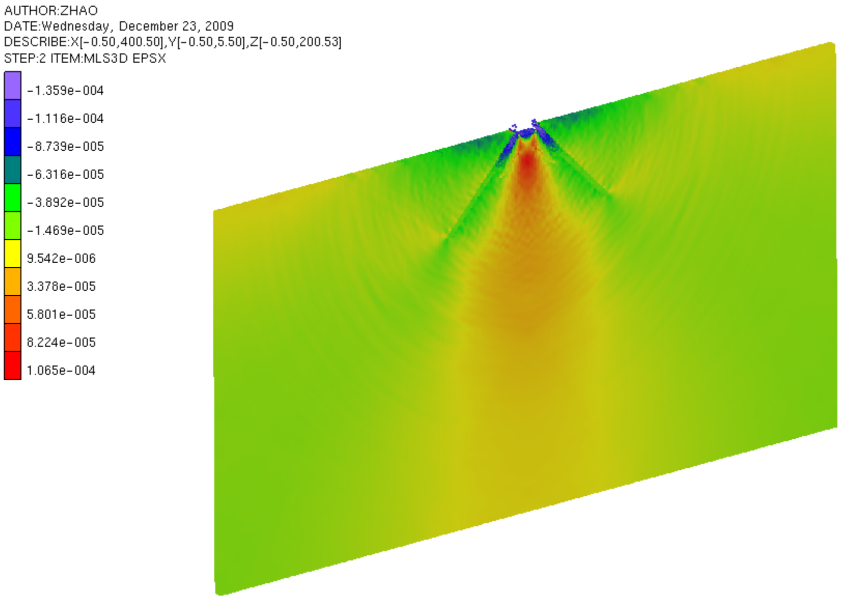

(a) Contour map of ε_{xx}

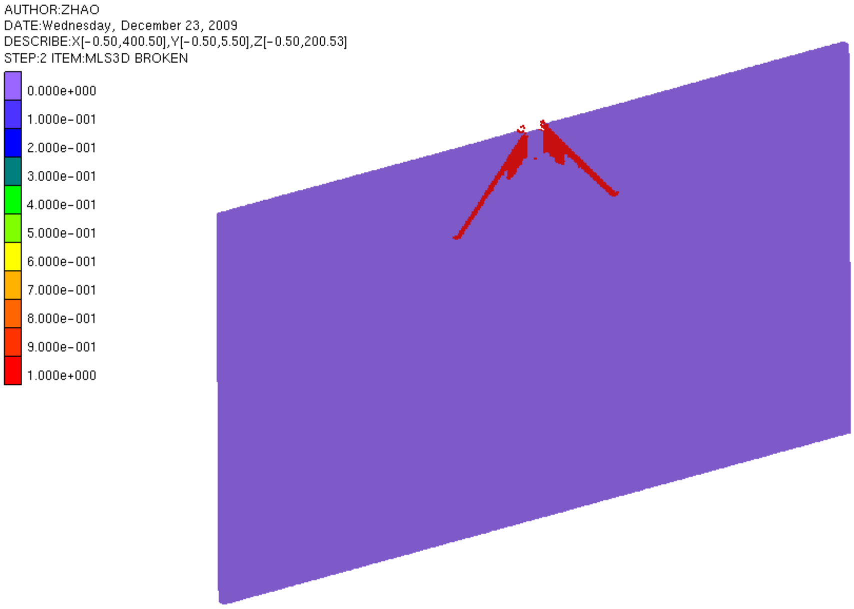

(b) Crack pattern

Figure 8.16. Simulation results of the cluster DLSM using 256 CPUs.

When a parallel job is finished, a record file will be produced (as shown in Figure 8.17). Information of computing time can be found in this file, such as the total CPU time (the summed machine time of the allocated nodes) and the wall time (the actual time used in the cluster). The code itself also prints the computing time of the processor whose rank number equals to zero, which is called the code time. These data for different cases are listed in Table 8.2. It is found that, only considering the code time, a perfect linear speedup is obtained. However, after careful investigation, it is found that it is not scientific to calculate the speedup through the code time, because it omits the I/O operation and the communication time. For this reason, the speedup is calculated based on the wall time spent for each case. It can be seen that a maximal speedup of 40.88× is achieved for the cluster DLSM code.

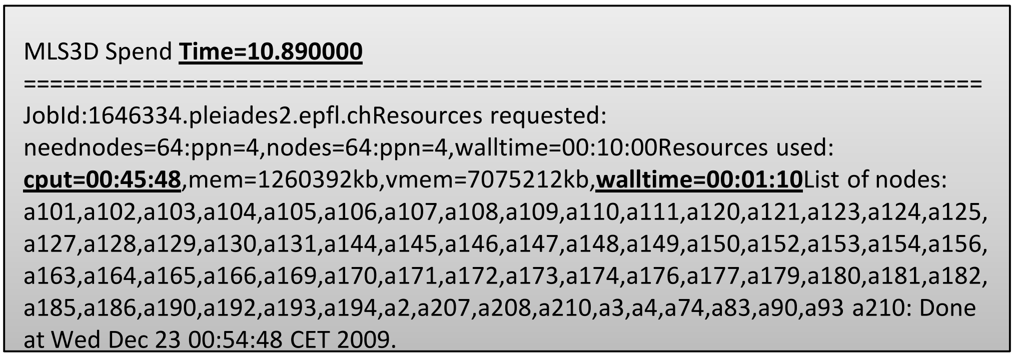

```
MLS3D Spend Time=10.890000
==================================================================================
JobId:1646334.pleiades2.epfl.chResources requested:
neednodes=64:ppn=4,nodes=64:ppn=4,walltime=00:10:00Resources used:
cput=00:45:48,mem=1260392kb,vmem=7075212kb,walltime=00:01:10List of nodes:
a101,a102,a103,a104,a105,a106,a107,a108,a109,a110,a111,a120,a121,a123,a124,a125,
a127,a128,a129,a130,a131,a144,a145,a146,a147,a148,a149,a150,a152,a153,a154,a156,
a163,a164,a165,a166,a169,a170,a171,a172,a173,a174,a176,a177,a179,a180,a181,a182,
a185,a186,a190,a192,a193,a194,a2,a207,a208,a210,a3,a4,a74,a83,a90,a93 a210: Done
at Wed Dec 23 00:54:48 CET 2009.
```

Figure 8.17. Fragement of the output file in *pleiades2*.

Table 8.2. Performance analysis results of the cluster DLSM.

CPUs	total cpu time (s)	code time (s)	wall time (s)	S	E^{cpu} (%)
1	2858	2859.61	2862	1	100
4	3557	893.25	901	3.1765	79
8	3508	435.01	488	5.8648	73
16	3308	199.04	426	6.7183	42
32	2990	89.96	196	14.602	46
64	2866	40.49	144	19.875	31
128	2705	18.87	88	32.523	25
256	2748	10.89	70	40.886	16

As mentioned before, the advantage of the cluster DLSM code is not only making the computing time shorter but also making it possile to solve problems which are beyond the capacity of a normal PC. It has been found that when the number of particles in the DLSM model exceeds one million (more than ten million bonds), it will become unsolvable for a normal PC because of the limitation of its memory space. As distributed memory is used in the cluster DLSM, this problem can be easily solved by using an adequate number of processors in the cluster. In the following, the three dimensional case of the TBM cutter problem (as shown in Figure 8.18) is chosen as an exmaple of demonstration. For this problem at a medium discretization level, even one quarter of the model needs four million particles. It exceeds the memory limit of a normal PC. Now, the problem is solved by the cluster DLSM code using 128 CPUs on Pleiades2. The simulation results are shown in Figure 8.19.

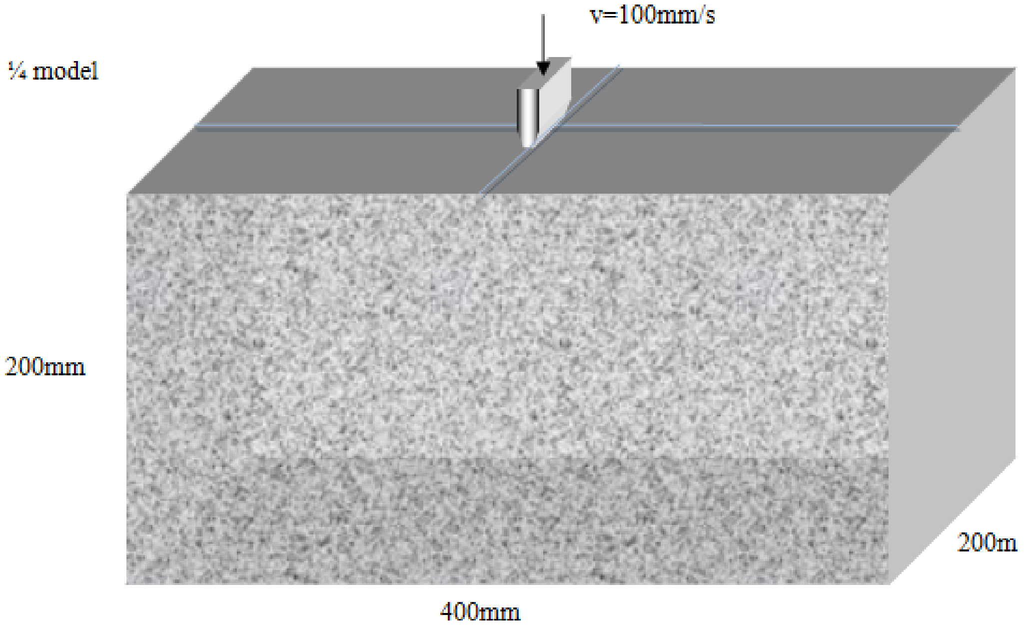

Figure 8.18. The 3D model of single TBM cutter induced fragmentation problem.

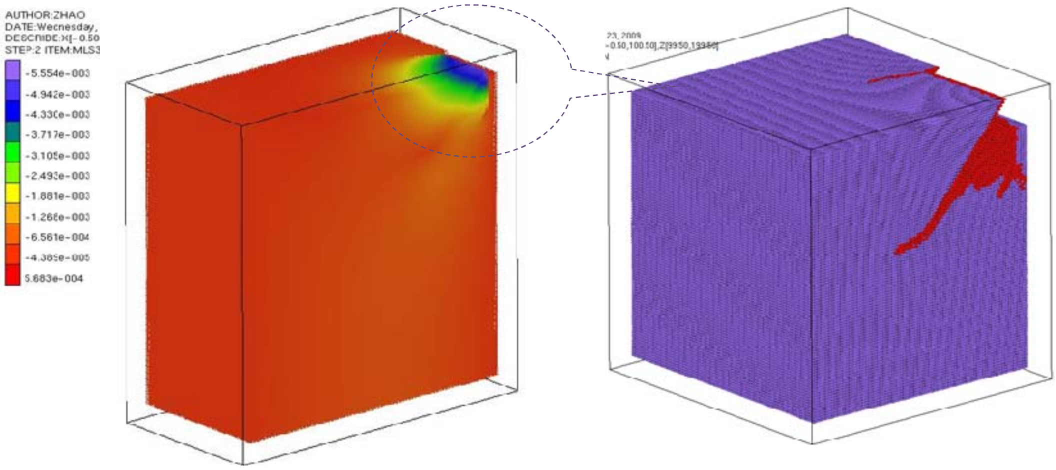

controur map of ε_{xx} crack pattern

Figure 8.19. The 3D simulation results of the TBM cutter induced fragmentation.

8.5 Conclusions

In this chapter, the parallelization of the Distinct Lattice Spring Model (DLSM) is presented. The available parallel environments are briefly introduced. Then, the parallelization of DLSM on multi-core PC and cluster are presented. The OpenMP is used to parallelize the DLSM code and make it working effectively on multi-core PC. The OpenMP implementation only needs a few modifications of the original code. Examples are given to show the performance of the parallel DLSM code on multi-core PC. It is found that the implementation is effective and successful. Another version of the code, the cluster DLSM, has been developed for massive parallel computing using clusters. The parallel DLSM solver on cluster is implemented by using MPI. The whole software package is finished through the cooperation between PC and cluster. The performance of the cluster DLSM is tested and a speedup of 40.88 is achieved for the case of using 256 CPUs in the Pleiades2 cluster. Finally, a problem with four million particles, which is previously impossible to handle by a normal PC, is successfully solved by using the developed cluster DLSM code.

8.6 Reference

1. http://techfreep.com/intel-80-cores-by-2011.htm, 2010.

2. Owens JD, Houston M, Luebke D, Green S, Stone JE, Phillips JC. GPU computing. Proc. of the IEEE, 2008; 96 (5):879-899.

3. http://www.nvidia.com/cuda_home.html, 2010.

4. Mark Baker, et al., Cluster computing white paper, 2001.

5. Flynn M. Very high-speed computing systems, Proc. IEEE, 1966; 54:1901–1909.

6. Chang V. Experiments and investigations for the personal high performance computing (PHPC) built on top of the 64-bit processing and clustering systems. In: 13th Annual IEEE International Symposium, Germany, 2006; 27-30.

7. http://www.openmp.org, 2010.

8. Dick B. Jacqueline F., Bradford N., pThreads programming, O'Reilly Media, 1996.

9. http://www.threadingbuildingblocks.org/, 2010.

10. Rick M. CPU designers debate multi-core future, EE Times, 2008.

11. http://en.wikipedia.org/wiki/Multi-core_processor#cite_note-1., 2010.

12. Wasson S. NVIDIA's GeForce 8800 graphics processor, Tech Report, 2007.

13. Maciej M. GPGPU programming on example of CUDA, Institute of Theoretical Physics, University of Wrocław, 2009.

14. http://www.opengl.org/, 2010.

15. http://www.khronos.org/opencl/,2010.

16. http://pleiades.epfl.ch/, 2010.

17. http://www.top500.org/, 2010.

18. http://www.mpi-forum.org, 2010.

19. http://www.csm.ornl.gov/pvm/,2010.

20. http://www-unix.mcs.anl.gov/mpi/mpich.,2010.

21. Zhao GF, Zhao J. Microscopic numerical modelling of the dynamic strength of brittle rock. Proc. ICADD9 Analysis of Discontinuous Deformation: New Developments and Applications 2009; 633-640.

22. Zhao GF, Fang J, Zhao J. A 3D distinct lattice spring model for elasticity and dynamic failure, Int J Numer Anal Meth Geomech, 2010 ; DOI: 10.1002/nag.930.

23. Rougier E, Munjiza A, John NWM. Numerical comparison of some explicit time integration schemes used in DEM, FEM/DEM and molecular dynamics. Int. J. Numer. Meth. Engng 2004; 61:856–879.

24. Kadau K, Germann TC, Lomdahl PS. Large-scale molecular dynamics simulations of 19 Billion Particles, Int J Modern Phys C, 2004; 15(1):193-201.

25. Michael G, Stephan K, Gerhard Z. Numerical simulation in molecular dynamics, Springer, 2007.

26. Kumar V, Grama A, Gupta A, Karypis G. Introduction to parallel computing: design and analysis of Algorithms, Benjamin/Cummings, 1994.

Chapter 9

Implicit DLSM

The DLSM model in Chapter 4 is based on explicit solution method in which a very small time step has to be chosen for numerical stability. This will lead a very long computing time for static simulation. In order to solve this problem, a preliminary study on the implicit solution on DLSM is performed. By directly solving the system equation, static problem can be solved through one step [1]. In this section, the 2D implicit DLSM is introduced for static problems.

9.1 The model

The proposed lattice spring model is illustrated in Figure 9.1 in which the material is represented by a distribution of particles linked through bonds. Each bond includes one normal spring and one shear spring.

The bond stiffness matrix is of the form

$$\mathbf{K}^{\mathrm{bond}} = \begin{bmatrix} k_{\mathrm{n}} & 0 \\ 0 & k_{\mathrm{s}} \end{bmatrix} \tag{9.1}$$

where k_{n} is the normal stiffness and k_{s} is the shear stiffness. Assume the strain in the local coordinate system is $\left(\varepsilon_{nn}, \varepsilon_{ss}, \varepsilon_{ns}\right)$, and then the normal and shear deformation of the bond can be expressed as

$$\hat{\mathbf{u}} = \left\{l\varepsilon_{nn}, l\varepsilon_{ns}\right\} \tag{9.2}$$

where l is the original length of the bond. Note that in the Born spring model, $\hat{\mathbf{u}}$ is given directly by the displacement differences of the two end particles of the bond along the normal and shear directions, i.e. $(\Delta u_n, \Delta u_s)$. The normal strain ε_{nn} in Equation (9.2) can be written as

$$\varepsilon_{nn} = \xi_i \varepsilon_{ij} \xi_j \tag{9.3}$$

where ε_{ij} is the strain in the global coordinate system and $\boldsymbol{\xi}$ is the direction vector of the bond which is $(\cos\beta, \sin\beta)$. The shear strain ε_{ns} in Equation (9.2) is given by

$$\varepsilon_{ns} = \xi_i \varepsilon_{ij} \eta_j \tag{9.4}$$

where $\boldsymbol{\eta}$ is the unit vector perpendicular to $\boldsymbol{\xi}$ which is $(-\sin\beta, \cos\beta)$. After some matrix operations, we obtain

$$\hat{\mathbf{u}} = \mathbf{T}\mathbf{s} \tag{9.5}$$

where

$$\mathbf{T} = l\begin{bmatrix} \cos^2\beta & \sin^2\beta & 2\cos\beta\sin\beta \\ -\cos\beta\sin\beta & \cos\beta\sin\beta & \cos^2\beta - \sin^2\beta \end{bmatrix} \tag{9.6}$$

$$\mathbf{s} = \left[\varepsilon_{xx}, \varepsilon_{yy}, \varepsilon_{xy}\right]^{\mathrm{T}} \tag{9.7}$$

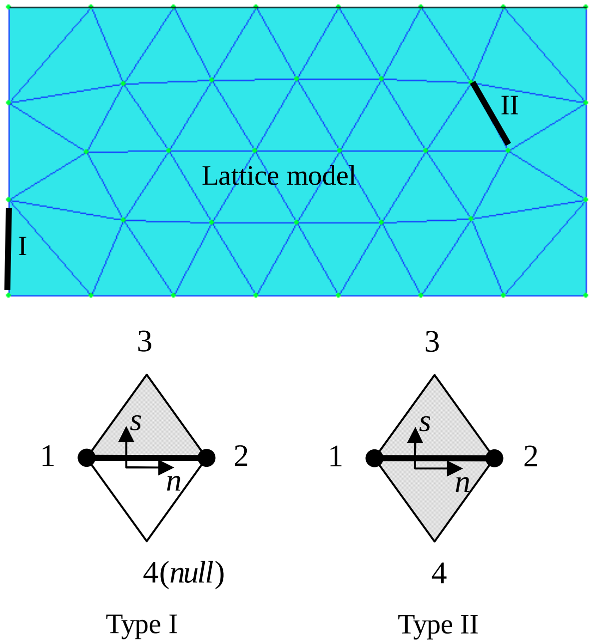

Type I Type II

Figure 9.1. The 2D lattice spring model and the two types of bond.

Here $\mathbf{s}$ is the vector composed of the three strain components. It can be calculated according to

$$\mathbf{s} = \mathbf{B}\mathbf{u} \tag{9.8}$$

where $\mathbf{B}$ is the interpolation matrix and $\mathbf{u}$ is the displacement vector. For the type-I bond (see Figure. 9.1) which only belongs to one triangular element, we use the common finite element interpolation which gives

$$\mathbf{B} = \begin{bmatrix} N_{1,x}^{\mathrm{e}} & 0 & N_{2,x}^{\mathrm{e}} & 0 & N_{3,x}^{\mathrm{e}} & 0 \\ 0 & N_{1,y}^{\mathrm{e}} & 0 & N_{2,y}^{\mathrm{e}} & 0 & N_{3,y}^{\mathrm{e}} \\ \frac{1}{2}N_{1,y}^{\mathrm{e}} & \frac{1}{2}N_{1,x}^{\mathrm{e}} & \frac{1}{2}N_{2,y}^{\mathrm{e}} & \frac{1}{2}N_{2,x}^{\mathrm{e}} & \frac{1}{2}N_{3,y}^{\mathrm{e}} & \frac{1}{2}N_{3,x}^{\mathrm{e}} \end{bmatrix} \tag{9.9}$$

$$\mathbf{u} = \left[u_1, v_1, u_2, v_2, u_3, v_3\right]^{\mathrm{T}} \tag{9.10}$$

where N_i^{e} is the element shape function associated with the node i. For the type-II bond (see Figure. 9.1) which belongs to two triangular elements, a moving least squares (MLS) procedure [2] is adopted to calculate $\mathbf{s}$. In this case, we have

$$\mathbf{B} = \begin{bmatrix} N_{1,x} & 0 & N_{2,x} & 0 & N_{3,x} & 0 & N_{4,x} & 0 \\ 0 & N_{1,y} & 0 & N_{2,y} & 0 & N_{3,y} & 0 & N_{4,y} \\ \frac{1}{2}N_{1,y} & \frac{1}{2}N_{1,x} & \frac{1}{2}N_{2,y} & \frac{1}{2}N_{2,x} & \frac{1}{2}N_{3,y} & \frac{1}{2}N_{3,x} & \frac{1}{2}N_{4,y} & \frac{1}{2}N_{4,x} \end{bmatrix} \tag{9.11}$$

$$\mathbf{u} = \left[u_1, v_1, u_2, v_2, u_3, v_3, u_4, v_4\right]^{\mathrm{T}} \tag{9.12}$$

where $N_{i,x}$ and $N_{i,y}$ are the diffusive derivatives given by

$$N_{i,x} = \frac{w_i}{d} \sum_{j \neq i} \sum_{k > j, k \neq i} w_j w_k (y_j - y_k) \Theta\left(\mathbf{x}_i, \mathbf{x}_j, \mathbf{x}_k\right) \tag{9.13}$$

$$N_{i,y} = \frac{w_i}{d} \sum_{j \neq i} \sum_{k > j, k \neq i} w_j w_k (x_k - x_j) \Theta\left(\mathbf{x}_i, \mathbf{x}_j, \mathbf{x}_k\right) \tag{9.14}$$

with

$$\Theta\left(\mathbf{x}_i, \mathbf{x}_j, \mathbf{x}_k\right) = -x_j y_i + x_k y_i + x_i y_j - x_k y_j - x_i y_k + x_j y_k$$

$$d = \sum_{i=1,2} \sum_{j=i+1,3} \sum_{k=j+1,4} w_i w_j w_k \left(\Theta\left(\mathbf{x}_i, \mathbf{x}_j, \mathbf{x}_k\right)\right)^2$$

The weight function w used in this paper is

$$w(r) = e^{\left(-3\hat{r}^2\right)} \tag{9.15}$$

where $\hat{r} = r / r_{\max}$ with $r = \sqrt{\left(x_\mathrm{m} - x\right)^2 + \left(y_\mathrm{m} - y\right)^2}$ and $\left(x_\mathrm{m}, y_\mathrm{m}\right)$ being the reference point (the center of the bond in this chapter).

The strain energy stored in each bond is

$$\Pi_\mathrm{b} = \frac{1}{2} \hat{\mathbf{u}} \mathbf{K}^\mathrm{bond} \hat{\mathbf{u}}^\mathrm{T} \tag{9.16}$$

The global stiffness matrix contributed by each bond is obtained as

$$\mathbf{K}^\mathrm{b} = \left[\frac{\partial^2 \Pi_\mathrm{b}}{\partial u_i \partial u_j} \right] = \left(\mathbf{TB}\right)^T \mathbf{K}^\mathrm{bond} \mathbf{TB} \tag{9.17}$$

Finally, the global stiffness matrix is assembled bond by bond. The boundary conditions specified by displacement or force are treated in the same method as in the standard FEM.

9.2 Numerical Examples

9.2.1 Beam subjected to bending

The geometry and boundary conditions of this plain-stress problem are described in Figure 9.2. The left side of the beam is fixed in the x direction and the left-bottom corner is fixed in both x and y directions. A shear stress equals to $1\mathrm{Mpa}$ is applied on the right side of the beam. The top and bottom boundaries are subject to the stress free condition. The elastic constants of the material and the corresponding spring parameters for the proposed DLSM are given in Table 9.1.

Table 9.1. Material constants, model parameters and numerical errors of CLSM and DLSM compared with FEM results for the beam bending problem.

E (MPa)	ν	α^{2D}	k_n (MN/m)	k_s (MN/m)	Err_1 (%)	Err_2 (%)
10000	0.1000	3.6447	6097.1021	3879.9741	88.2	2.8
10000	0.2000	3.6447	6859.2398	2286.4133	84.8	1.5
10000	0.3000	3.6447	7839.1313	603.0101	71.2	2.1
10000	0.3333	3.6447	8231.0878	0.0	2.5	2.0

The final algebraic equation assembled from the bond stiffness matrix given by Equation (9.17) with the implementation of the boundary conditions is solved by a direct method for sparse matrix. The lattice size is 4m, which corresponds to a total of 1250 lattice nodes approximately. Figure 9.3 shows the displacement results predicted by FEM, CLSM and DLSM with the Poisson's ratio of 0.1. The results of DLSM are in good agreement with those obtained by FEM, while this is not true for the results of CLSM. Compared to the displacement results obtained by FEM, the maximal relative errors of CLSM and DLSM (denoted as Err_1 and Err_2) are given in Table 9.1 for four different values of the Poisson's ratio. In all cases the errors of DLSM are rather small, while the errors of CLSM are very large except for the case of Poisson's ratio equal to 1/3 where shear spring is absent. Therefore, it can be concluded that shear spring must be introduced by preserving rotational invariance as done in DLSM in order to reproduce reasonably the elastic solutions for the Poisson's ratios other than 1/3.

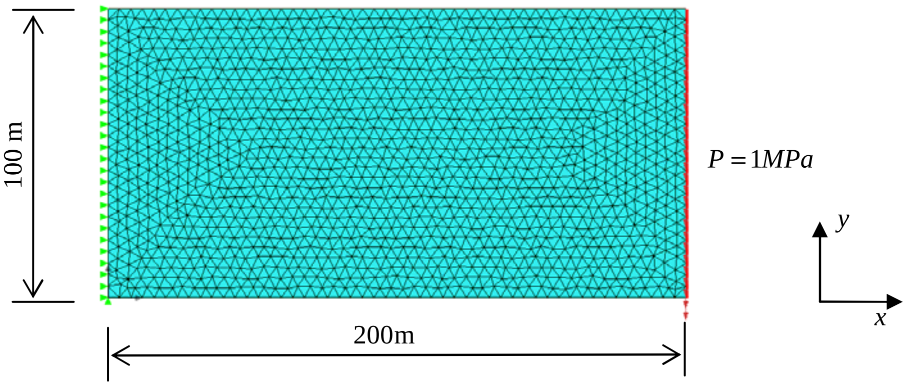

Figure 9.2. The geometry and boundary conditions for the beam bending problem.

The convergence of DLSM is studied by solving the same problem with different lattice sizes. Figure 9.4 shows that when lattice size becomes smaller and smaller, the result of DLSM gets closer and closer to the reference one obtained by FEM with a fine mesh. The influence of lattice type is also studied by comparing the results of four different lattice structures as shown in Figure 9.5, in which structure *a* is made of particles with a slight irregular distribution, structure *b* consists of particles with a regular distribution, and structures *c* and *d* are obtained by randomly moving the particles in structures *a* and *b* respectively.

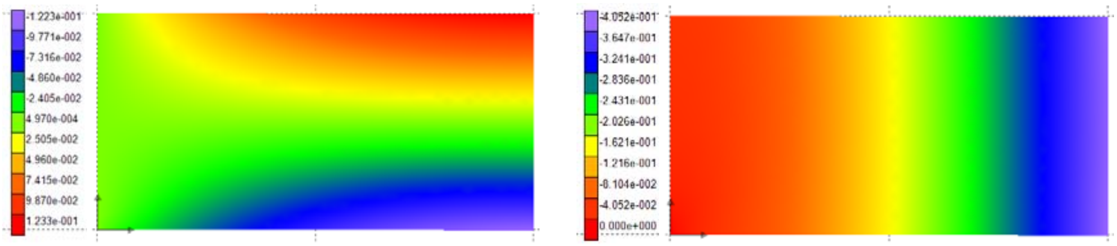

(a) The x-direction displacement (FEM) (b) The y-direction displacement (FEM)

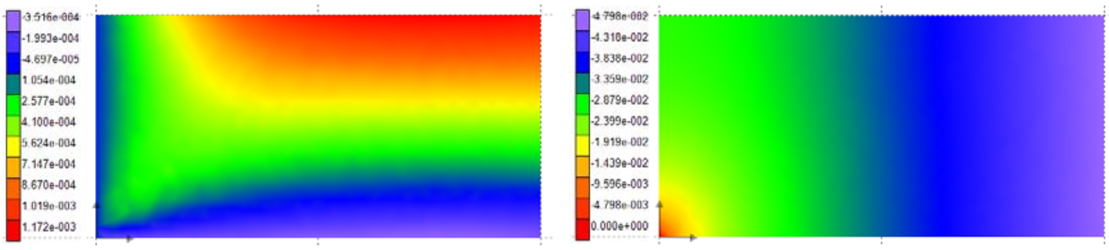

(c) The x-direction displacement (CLSM) (d) The y-direction displacement (CLSM)

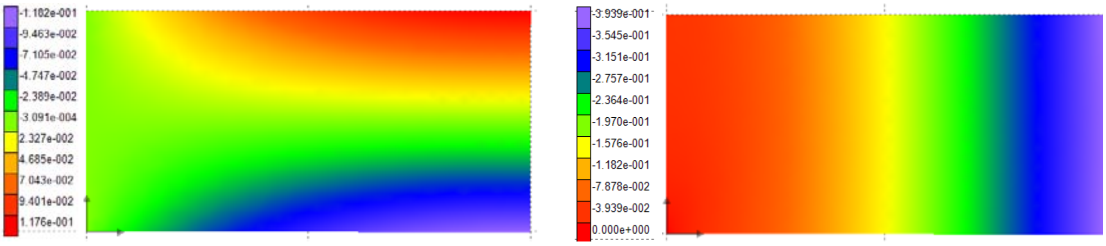

(e) The x-direction displacement (DLSM) (f) The y-direction displacement (DLSM)

Figure 9.3. Contour plot of the displacement results predicted by FEM, CLSM and DLSM for the beam bending problem.

The model parameters and the results for this study are summarized in Table 9.2, from which it is observed that the random lattice model gives better results than that given by regular lattice model. The reason is that the relationship between the model parameters and the material constants is derived based on the assumption that the bond orientation distribution is uniform. Hence, a random lattice is preferable when applying the relationship to obtain the model parameters from the material constants.

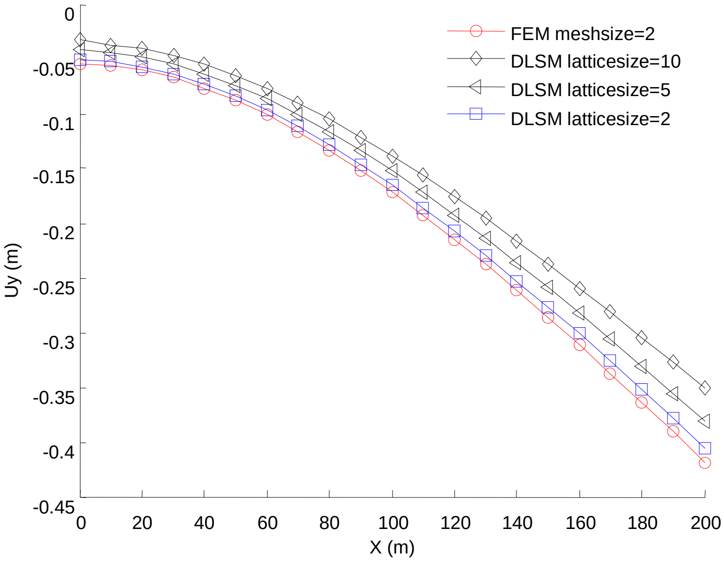

Figure 9.4. The y-direction displacement along the top surface predicted by DLSM with different lattice sizes for the beam bending problem.

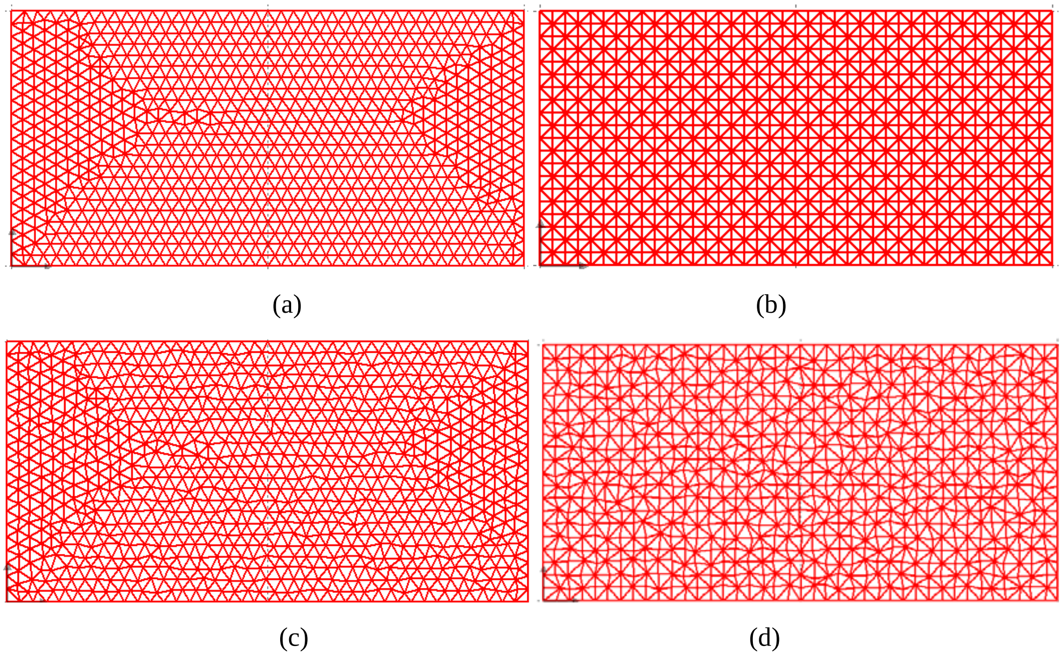
(a)

(b)

(c)

(d)

Figure 9.5. Different lattice structures for the beam bending problem.

Table 9.2. Material constants, model parameters and numerical errors of DLSM for the beam bending problem with different lattice structures.

Structure	E (MPa)	ν	α^{2D}	k_n (MN/m)	k_s (MN/m)	Err_2 (%)
a	10000	0.2000	3.5596	7023.1976	2341.0659	6.01
b	10000	0.2000	4.0750	6134.9693	2044.9898	6.23
c	10000	0.2000	3.6447	6859.2398	2286.4133	1.46
d	10000	0.2000	4.2213	5922.3862	1974.1287	3.11

9.2.2 Square hole subjected to compression

In this subsection, a more complex plain-stress problem is solved by DLSM. Figure 9.6 shows the geometry, the loading condition, and the lattice structure for this problem. The elastic constants are $E = 10^3\text{MPa}$ and $\nu = 0.2$ or 0.4. The results are presented in Figure 9.7 and Figure 9.8. Again, a good match between the results by DLSM and the elastic solutions by FEM is observed. Like FEM, the proposed method cannot solve the case of $\nu = 0.5$. However, this is not a deficiency of the method, because incompressible solid materials do not exist.

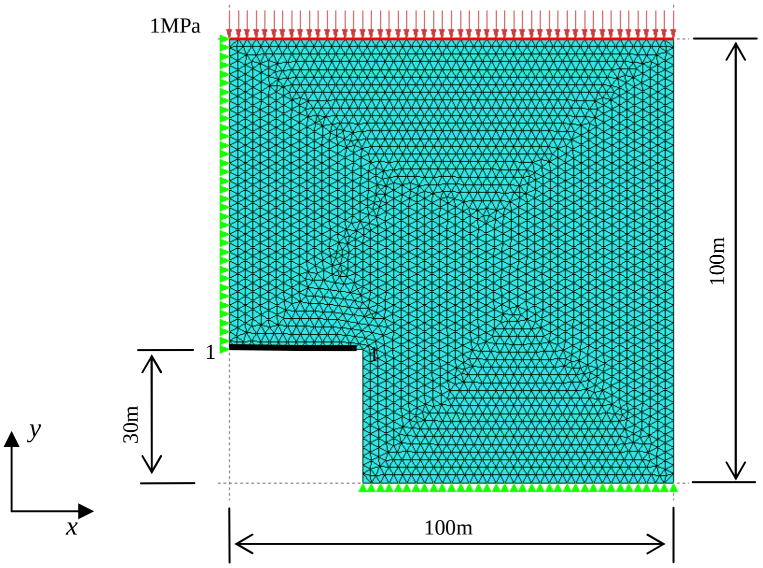

Figure 9.6. The geometry and boundary conditions for the square hole problem.

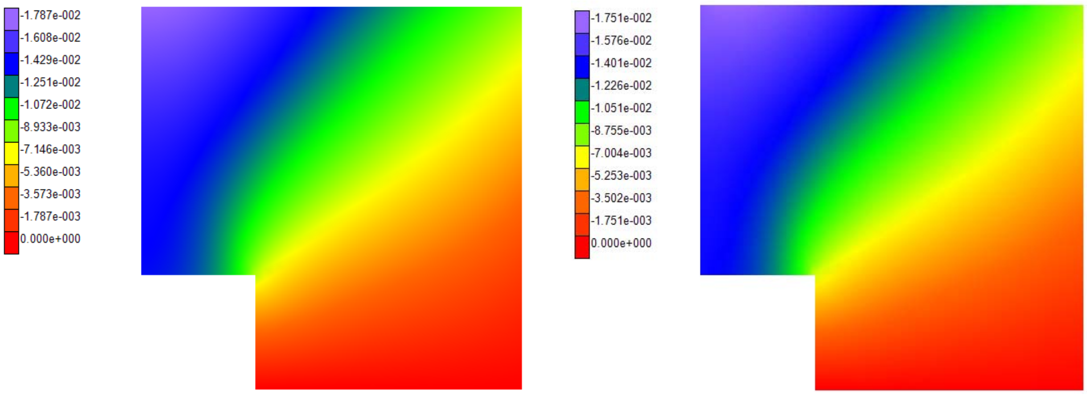

(a) FEM (b) DLSM

Figure 9.7. Contour plot of the y-direction displacement results for the square hole problem.

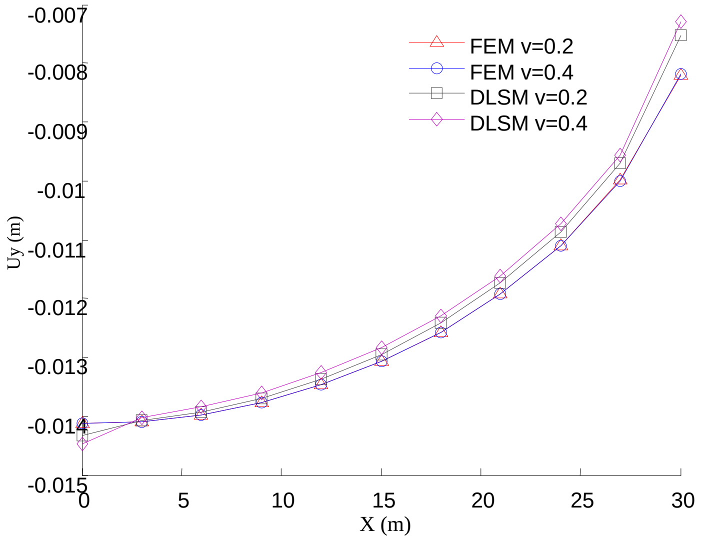

Figure 9.8. The y-direction displacement along the top surface of the square hole.

9.2.3 Fracture simulation

The proposed model is applied to the fracture simulation of a solid specimen with a side notch subjected to quasi-static tensile loading in the plain-stress condition. The geometry and the loading setup are shown in Figure 9.9. The controlled displacement on the top is 10^{-2}m. The elastic constants of the material are $E = 10^3$MPa and $\nu = 0.2$.

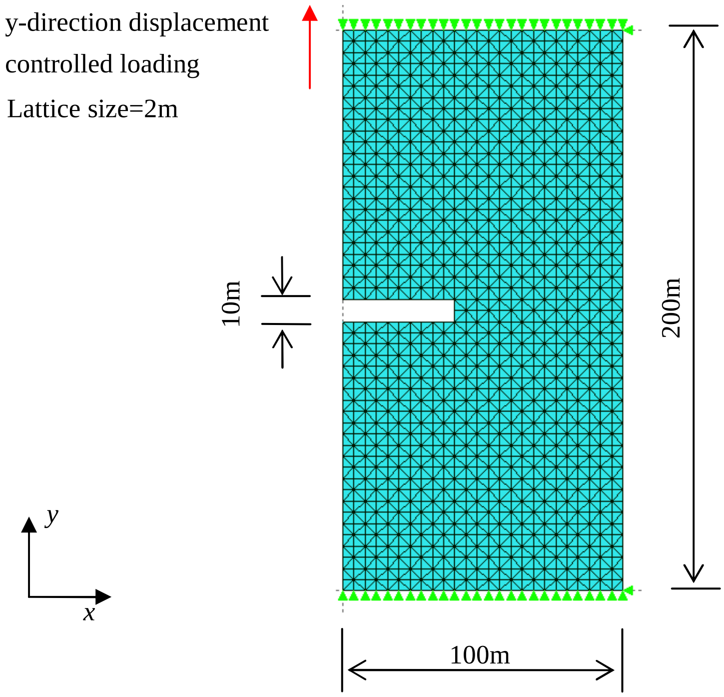

Figure 9.9 . The geometry and boundary conditions for the fracture simulation of a notched specimen under uniaxial tensile loading.

The purpose of this example is to demonstrate the easy feature of the model for fracture simulation; we only consider the tensile failure of bond, which occurs when

$$-F_n > F_t$$

where F_n is the normal force of the bond and $F_t = u_n^* k_n$ is the tensile strength of the bond with u_n^* being the limit value of the bond's stretching. Whenever a bond fails, it is deleted from the calculation procedure. The simulation was performed using $u_n^* = 0.0003$. The damage pattern is presented in Figure 9.10 for four stages. The bond in which failure occurs is marked by double red lines around the center of the bond. With regard to the crack patterns obtained, the simulation gives a realistic description of the fracture process of the notched solid specimen under tensile loading.

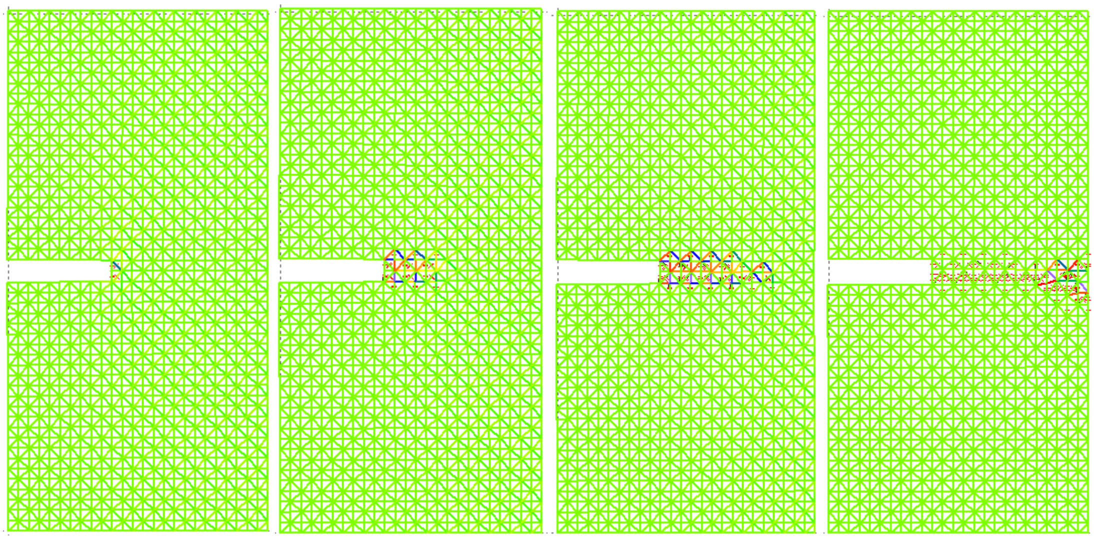

(a) step=50 (b) step=60 (c) step=70 (d) step=100

Figure 9.10. The fracture process predicted by implicit DLSM.

9.3 Conclusions

The implicit DLSM is developed and compared with FEM solutions. Results show that the DLSM system equations are numerically stable even when the negative shear spring is used. In this sense, the DLSM can also be used as a meshless method like EFG and FPM. Moreover, DLSM have advantages over exiting meshless methods, e.g., EFG, FPM and SPH, on stability, no integration requirement and easy to deal with heterogeneity problems. Results provide confidence on further development of implicit dynamic DLSM 3D code for quasi-dynamic/quasi-static analysis.

9.4 References

1. G.F. Zhao, J. Fang, and J. Zhao. A MLS-based lattice spring model for simulating elasticity of materials. Int J Comput Meth, 2010 (accepted).
2. Breitkopf P, Rassineux A, Touzot G, Villon P. Explicit form and efficient computation of MLS shape functions and their derivatives. Int J Numer Methods Eng 2000; 48(3):451-66.

Chapter 10

Conclusions and further development

10.1 Summary and conclusions

A micro-macro and continuum-discontinuum coupled model and corresponding computer codes have been developed in this thesis. The goal is to provide a suitable numerical tool which satisfies all the requirements mentioned in Chapter 1 dedicated to the rock dynamics study. This goal has been preliminarily achieved through seven integrated, yet relatively independent works, which are summarized in the following.

1) A new microstructure based model, RMIB, is proposed to describe the elastic continuum. The model has an underlying microstructure consisting of discrete particles connected by normal and shear springs. Based on the Cauchy-Born rules and the hyperelastic theory, relationships between the micromechanical parameters and the macro material constants are derived. Relationship between micro failure law and macro failure law is preliminarily investigated. The results reveal the importance of building the corresponding numerical model.

2) Based on the RMIB theory, a numerical model DLSM is proposed. DLSM is different from the conventional lattice spring models in that a shear spring is introduced to model the multi-body force through the spring deformation. The method of evaluating the shear displacement is proven to be able to keep rotational invariance. By doing this, the DLSM model can represent the diversity of the Poisson’s ratio. Microscopic spring parameters are directly obtained from macroscopic material constants based on the RMIB theory. Numerical examples are presented to show the abilities and properties of DLSM in modeling elastic and simple dynamic failure problems.

3) A multi-scale model, m-DLSM, is proposed to combine DLSM with NMM. An inter-element model is proposed to couple these different methods. The coupling procedure and technique are presented. The model includes three-layer structures. During calculation, the inter-element model can be automatically transformed into the particle based model. Examples are given to demonstrate the feasibility of m-DLSM. The model can solve problems which are memory demanding for DLSM on normal PC.

4) The ability of DLSM on modeling dynamic failure is studied. A general form of constitutive law for the spring bond is developed based on the principle of damage. The proposed constitutive law includes linear, hardening and softening parts. Empirical equations relating tensile strength and fracture energy with the micro parameters are derived. Two examples on dynamic fracturing of PMMA and rock material are presented to illustrate the ability of solving this kind of problems.

5) The developed DLSM code is used to study wave propagation through rock material and jointed rock masses. Non-reflection boundary is implemented to enhance the DLSM modeling of wave propagation in infinite domain. Influence of particle size on numerical accuracy of DLSM modeling of wave propagation is investigated. Proper values for the mesh ratio used in DLSM modeling of P-wave and S-wave propagation are provided. To represent discontinuity in DLSM, the weak material layer method and the virtual joint plane method are proposed and implemented into the DLSM code. Wave attenuation through single joint is modeled and compared with analytical solution.

6) The parallelization of DLSM is studied. Two parallel codes, multi-core DLSM and cluster DLSM, are developed. The multi-core DLSM can fully utilize the computing resources of modern PC. It can provide a maximum speed-up of 4.68 on a quad-core PC. The cluster DLSM can achieve a maximum speed-up of 40.89 when 256 CPUs are used. It can be concluded that the DLSM model is suitable for parallelization on different platforms.

7) The implicit 2D DLSM for static analysis is developed. A mesh based methodology is used for strain computing and the solution can be directly obtained by solving linear

algebraic equations. Results are stable and consistent with FEM results.

10.2 Future research

As a newly developed numerical model and code, there still are substantial works to be done to improve. For example, further calibrations, model developments, and more broad applications are needed. The prospected research context includes:

Calibrating DLSM through experiments

In this thesis, the DLSM code is validated for both static and dynamic elastic problems. Preliminary applications in dynamic failure show that the code is capable of reproducing some experimental observations, e.g., the correct dynamic cracking velocity, cracking branching and dynamic fracture toughness. However, the experiments referred in this thesis are not specially designed for the validation of DLSM. Performing experiments on wave propagation and dynamic compressive failure and comparing the obtained data with the DLSM modeling results are needed.

Studying mechanisms of rock fracturing and failure

One of the main objectives of this thesis is to provide a better numerical tool for studying mechanisms in rock mechanics. DLSM is a microstructure based model which is made up of springs and based on the Newton’s second law. Failure law used in the model is also simple because it is based on the distance between two particles. For this reason, the model is suitable to study some mechanisms of rock mechanics, e.g., the loading rate effect of rock material failure and strength. However, DLSM modeling of the compressive failure is still not satisfactory. A possible solution for this problem is attempted, in which the model is built based on the microstructure information from digital picture (see Figure 10.1). The simulated strain stress curves of uniaxial tensile and compressive tests are shown in Figure 10.2. When explicitly considering the microstructure of rock material, the ratio of compressive strength to tensile strength predicted by DLSM is 12.35, which is also the typical value for rock materials.

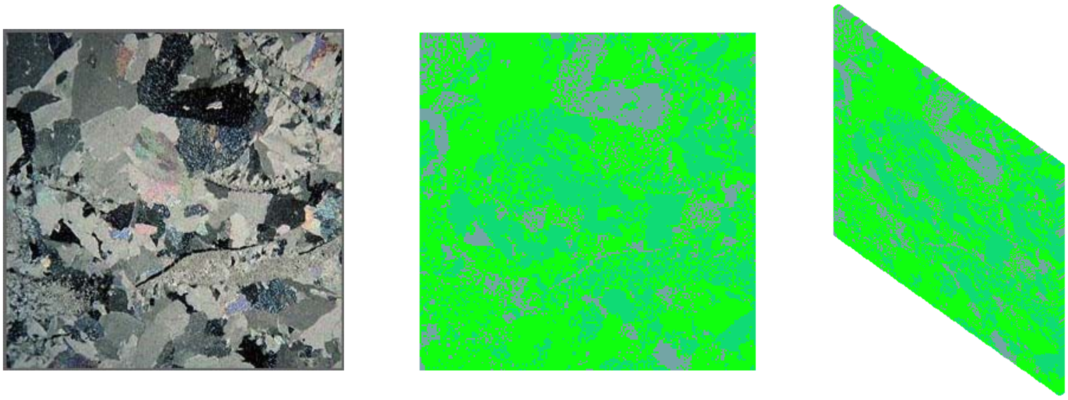

(a) Digital picture [1] (b) Plane view (c) 3D view

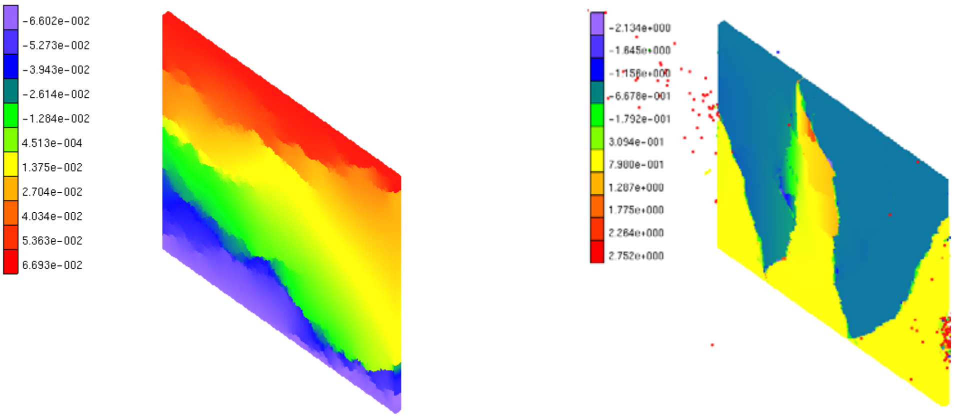

(d) Tensile failure (e) Compressive failure

Figure 10.1. The used microscopic model of rock material and the corresponding DLSM modeling of tensile and compressive failure under uniaxial loading.

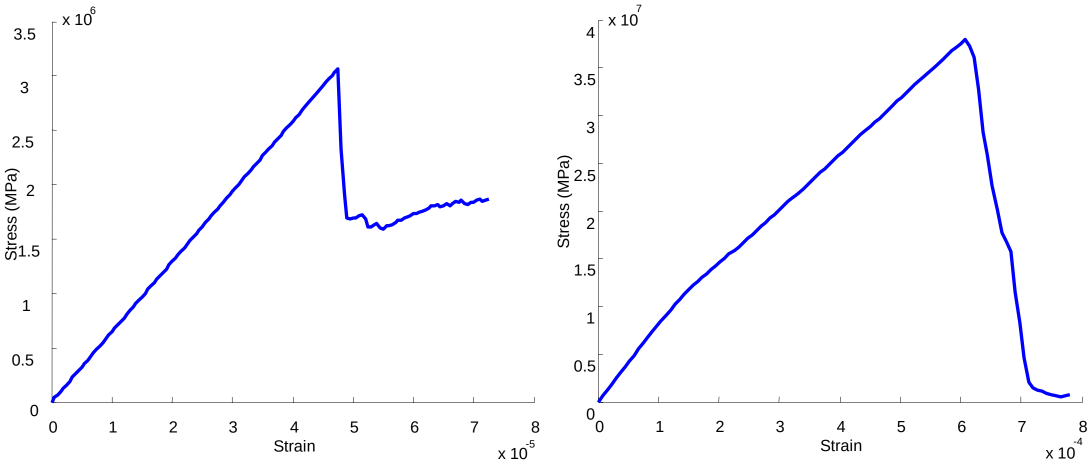

(a) Uniaxial tensile test (b) Uniaxial compressive test

Figure 10.2. The strain stress curves predicted by DLSM for the uniaxial tensile and compressive tests.

The multi-physical modeling is one of the challenges existing in material science and has been studied through various methods in different areas [2, 3, 4]. The classical LSM has already been successfully used in multi-physical simulations. The DLSM also has potential in this field. For example, the thermo-mechanical coupling is relatively easy to be implemented. The microscopic thermal parameters of the lattice spring can be obtained as

$$\eta = \frac{\sum l}{3Vk} \tag{10.1}$$

where η is the thermal resistance of the bond, l is the bond length, V is the volume of the model and k is the macroscopic heat conductive coefficient. This relation can be directly implemented in DLSM for the purpose of thermo-mechanical modeling.

Developing GPU based high performance DLSM code

The new GPU computing technique provides a powerful platform for parallelization of DLSM. The speed-up achieved in some GPU applications is reported to be more than hundreds [5]. To obtain the compressive results shown in Figure 10.2, the simulation takes ten days in the fastest PC (Intel Core i7 950) of LMR and one day in Pleiades2 when 64 CPUs is used. However, it may only need a few hours if the parallelization of DLSM is developed for GPU computing environment.

Developing implicit 3D DLSM

Chapter 9 presents an implicit DLSM model for two dimensional case. The model is based on a FEM mesh and MLS interpolation. Yet, the 3D implicit code is still not developed. The implicit 3D DLSM is more complex than the 2D DLSM. A prototype code, Ball3D, had been already developed, which is earlier than DLSM and based on implicit scheme. One of the applications of Ball3D is shown in Figure 10.3. Further development was given up as the code can only handle a few thousands of spheres. However, this kind of model has advantages on solving quasi-static problems as large time step can be used. So implementing the implicit 3D DLSM is another possible future work.

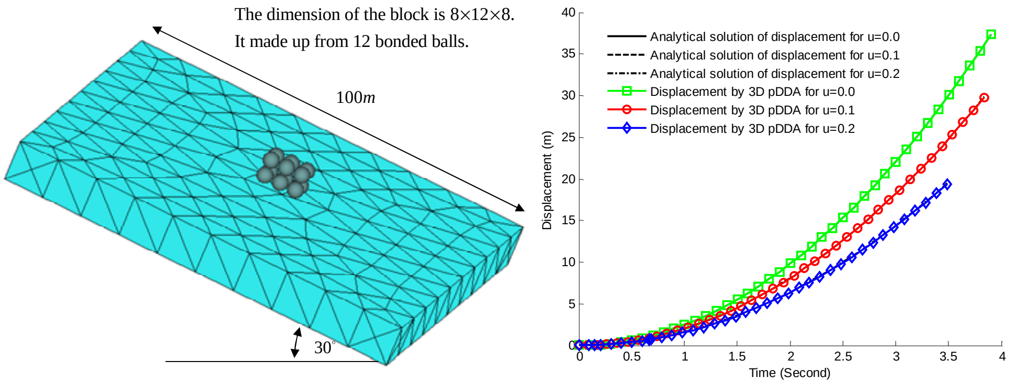

Figure 10.3. Application of the Ball3D code on modeling sliding block problem.

10.3 References

1. Walker I. An introduction to mineralogical terms and observations with the Leica CME. http://www.microscopy-uk.org.uk/mag/artfeb04/iwouslides.html, 2010.
2. De Borst R. Challenges in computational materials science: Multiple scales, multi-physics and evolving discontinuities. Computational Materials Science, 2008; 43(1): 1-15.
3. Laloui L, Leroueil S, Chalindar S. Modelling of the combined effect of strain rate and temperature on one-dimensional compression of soils. Canadian Geotechnical Journal, 2008;12(45):1765-1777.
4. Karalekas D, Cugnoni J, Botsis J. Monitoring of hyrgothermal ageing effects in an epoxy resin using FBG sensor: A methodological study, Composites Science & Technology, 2009; 69: 507-514.
5. Nvidia ltd., http://www.nvidia.com/cuda_home.html, 2010.

Appendix A

Proof of negative spring in RMIB

The proof of negative shear spring can be based on the potential functions used in MD simulation. It is known that the Poisson's ratio of silver is 0.37, which corresponds to negative shear spring stiffness in the RMIB model. The atomic lattice structure of sliver is shown in Figure A1.

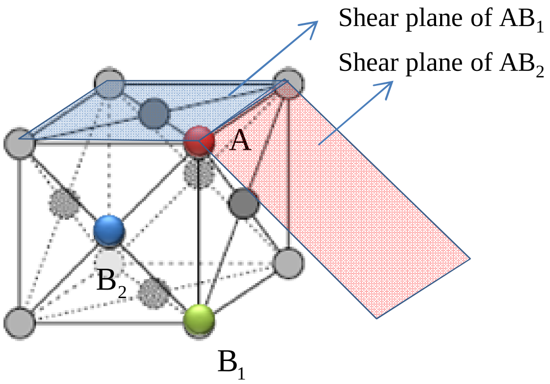

Figure A1. The cubic face-centered lattice (fcc) of silver.

The Finnis-Sinclair potential proposed by Sutton and Chen [1] can be used to describe silver, which can be written as

$$P_i = \varepsilon\left(\sum_{\substack{j=1 \\ j\neq i}}^{N}\left(\frac{\sigma}{r_{ij}}\right)^n - c\sqrt{\sum_{\substack{j=1 \\ j\neq i}}^{N}\left(\frac{\sigma}{r_{ij}}\right)^m}\right) \tag{A.1}$$

Both repulsive and attractive part included in this potential. The repulsive part is realized by a pair potential, while the attractive part is realized by a many-body potential. The material dependent parameters n, m, ε, σ and c are related to the material and specific type of lattice. The values of parameters which stand for silver are given in Table A1.

Table A1. The set of parameters of Finnis-Sinclair potential for silver.

m	n	ε	σ	c	l
6	12	2.5415×10^{-3}eV	4.09Å	144.41	1.21875 Å

The potential variation on atom B due to the movement of atom A in different shear planes (see Figure A1) can be calculated based on Equation (A.1) and the lattice structure information. The results for silver are shown in Figure A2. It can be seen that the shape of the potential variation function is exactly of the downward bowl shape, which indicates that the shear stiffness is negative. This is consistent with the fact that the Poisson's ratio of silver is greater than the critical value (0.25 for 3D).

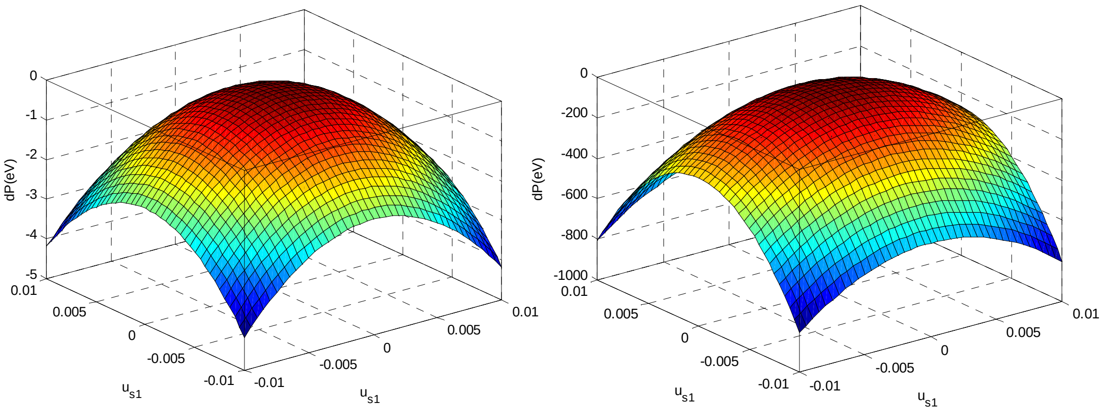

(a) B_1 atom

(b) B_2 atom

Figure A2. The variation of potential energy of silver at different atoms.

Reference

1.Sutton A, Chen J. Long-range Finnis-Sinclair potentials. Phil. Mag.Lett.,1990;61: 139–146.

Appendix B

Proof of rotation invariant in DLSM

In this appendix, Equation (4.7) used for evaluating the deformation of shear springs in DLSM is derived. First, consider a cubic unit volume containing a bond connecting two particles as shown in Figure A1.

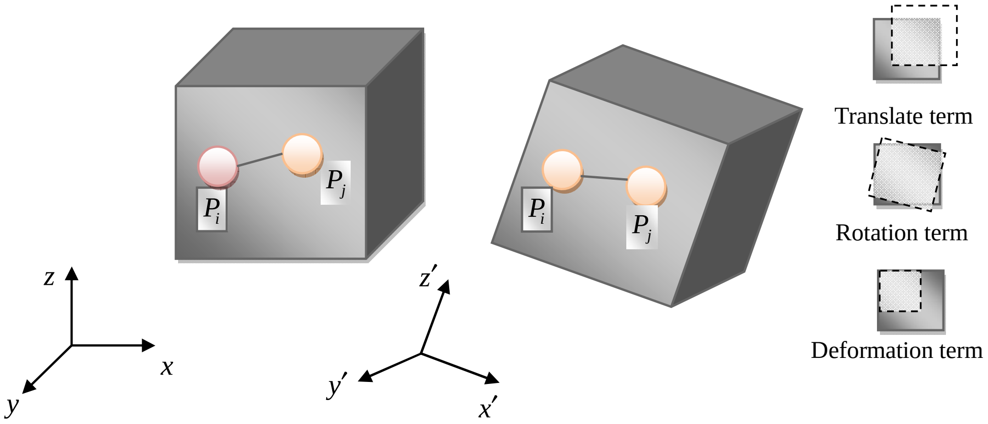

Figure B1. Illustration of the deformation of a cubic unit with a bond connecting two particles.

The complete 1st order displacement function of the cubic is

$$\begin{pmatrix} u_x \\ u_y \\ u_z \end{pmatrix} = \begin{pmatrix} a_0 & a_1 & a_2 & a_3 \\ b_0 & b_1 & b_2 & b_3 \\ c_0 & c_1 & c_2 & c_3 \end{pmatrix} \begin{pmatrix} 1 \\ x \\ y \\ z \end{pmatrix} \tag{B.1}$$

Assuming the center of the block at $\left(x_c, y_c, z_c\right)$, then its displacement is represented by

$$\begin{pmatrix} u_{cx} \\ u_{cy} \\ u_{cz} \end{pmatrix} = \begin{pmatrix} a_0 & a_1 & a_2 & a_3 \\ b_0 & b_1 & b_2 & b_3 \\ c_0 & c_1 & c_2 & c_3 \end{pmatrix} \begin{pmatrix} 1 \\ x_c \\ y_c \\ z_c \end{pmatrix} \tag{B.2}$$

Subtracting (B.2) from (B.1) gives

$$\begin{pmatrix} u_x \\ u_y \\ u_z \end{pmatrix} - \begin{pmatrix} u_{cx} \\ u_{cy} \\ u_{cz} \end{pmatrix} = \begin{pmatrix} a_0 & a_1 & a_2 & a_3 \\ b_0 & b_1 & b_2 & b_3 \\ c_0 & c_1 & c_2 & c_3 \end{pmatrix} \begin{pmatrix} 1 \\ x \\ y \\ z \end{pmatrix} - \begin{pmatrix} a_0 & a_1 & a_2 & a_3 \\ b_0 & b_1 & b_2 & b_3 \\ c_0 & c_1 & c_2 & c_3 \end{pmatrix} \begin{pmatrix} 1 \\ x_c \\ y_c \\ z_c \end{pmatrix} \tag{B.3}$$

Equation (B.3) can be further written as

$$\begin{pmatrix} u_x \\ u_y \\ u_z \end{pmatrix} = \begin{pmatrix} u_{cx} \\ u_{cy} \\ u_{cz} \end{pmatrix} + \begin{pmatrix} a_1 & 0 & 0 \\ 0 & b_2 & 0 \\ 0 & 0 & c_3 \end{pmatrix} \begin{pmatrix} x - x_c \\ y - y_c \\ z - z_c \end{pmatrix} + \begin{pmatrix} 0 & a_2 & a_3 \\ b_1 & 0 & b_3 \\ c_1 & c_2 & 0 \end{pmatrix} \begin{pmatrix} x - x_c \\ y - y_c \\ z - z_c \end{pmatrix} \tag{B.4}$$

From (B-4), we have

$$\varepsilon_{xx} = \frac{\partial u_x}{\partial x} = a_1$$

$$\varepsilon_{yy} = \frac{\partial u_y}{\partial y} = b_2$$

$$\varepsilon_{zz} = \frac{\partial u_z}{\partial z} = c_3$$

$$\omega_x = \frac{1}{2}\left(\frac{\partial u_z}{\partial y} - \frac{\partial u_y}{\partial z} \right) = \frac{1}{2}\left(c_2 - b_3 \right)$$

$$\omega_y = \frac{1}{2}\left(\frac{\partial u_x}{\partial z} - \frac{\partial u_z}{\partial x} \right) = \frac{1}{2}\left(a_3 - c_1 \right)$$

$$\omega_z = \frac{1}{2}\left(\frac{\partial u_y}{\partial x} - \frac{\partial u_x}{\partial y} \right) = \frac{1}{2}\left(b_1 - a_2 \right)$$

$$\varepsilon_{yz} = \frac{1}{2}\left(\frac{\partial u_z}{\partial y} + \frac{\partial u_y}{\partial z} \right) = \frac{1}{2}\left(c_2 + b_3 \right)$$

$$\varepsilon_{zx} = \frac{1}{2}\left(\frac{\partial u_x}{\partial z} + \frac{\partial u_z}{\partial x} \right) = \frac{1}{2}\left(a_3 + c_1 \right)$$

$$\varepsilon_{xy} = \frac{1}{2}\left(\frac{\partial u_y}{\partial x} + \frac{\partial u_x}{\partial y}\right) = \frac{1}{2}(b_1 + a_2)$$

Using the above relations, Equation (B.4) can be transformed into

$$\begin{pmatrix} u_x \\ u_y \\ u_z \end{pmatrix} = [\mathrm{D}_0]\begin{pmatrix} u_{cx} \\ u_{cy} \\ u_{cz} \end{pmatrix} + [\mathrm{D}_1]\begin{pmatrix} \omega_x \\ \omega_y \\ \omega_z \end{pmatrix} + [\mathrm{D}_2]\begin{pmatrix} \varepsilon_{xx} \\ \varepsilon_{yy} \\ \varepsilon_{zz} \end{pmatrix} + [\mathrm{D}_3]\begin{pmatrix} \varepsilon_{yz} \\ \varepsilon_{zx} \\ \varepsilon_{xy} \end{pmatrix} \tag{B.5}$$

where

$$[\mathrm{D}_0] = \begin{pmatrix} 1 & 0 & 0 \\ 0 & 1 & 0 \\ 0 & 0 & 1 \end{pmatrix}$$

$$[\mathrm{D}_1] = \begin{pmatrix} 0 & z - z_c & -(y - y_c) \\ -(z - z_c) & 0 & x - x_c \\ y - y_c & -(x - x_c) & 0 \end{pmatrix}$$

$$[\mathrm{D}_2] = \begin{pmatrix} x - x_c & 0 & 0 \\ 0 & y - y_c & 0 \\ 0 & 0 & z - z_c \end{pmatrix}$$

$$[\mathrm{D}_3] = \begin{pmatrix} 0 & z - z_c & y - y_c \\ z - z_c & 0 & x - x_c \\ y - y_c & x - x_c & 0 \end{pmatrix}$$

Denoting the coordinates of the two particles in the cubic as (x_1, y_1, z_1) and (x_2, y_2, z_2) and the displacement of them as (u_1, v_1, w_1) and (u_2, v_2, w_2), the relative displacement vector between the two particles is

$$\begin{pmatrix} u_{12x} \\ u_{12y} \\ u_{12z} \end{pmatrix} = \begin{pmatrix} u_{2x} - u_{1x} \\ u_{2y} - u_{1y} \\ u_{2z} - u_{1z} \end{pmatrix} \tag{B.6}$$

and the normal unit vector is

$$\begin{pmatrix} n_x \\ n_y \\ n_z \end{pmatrix} = \begin{pmatrix} \dfrac{x_2 - x_1}{l} \\ \dfrac{y_2 - y_1}{l} \\ \dfrac{z_2 - z_1}{l} \end{pmatrix} \tag{B.7}$$

where l is the length of the bond. The relative normal displacement vector is defined as

$$\begin{pmatrix} u_{12x}^n \\ u_{12y}^n \\ u_{12z}^n \end{pmatrix} = \left(\begin{pmatrix} u_{12x} \\ u_{12y} \\ u_{12z} \end{pmatrix}^T \begin{pmatrix} n_x \\ n_y \\ n_z \end{pmatrix} \right) \begin{pmatrix} n_x \\ n_y \\ n_z \end{pmatrix} \tag{B.8}$$

By vector operation, the relative shear displacement vector is obtained as

$$\begin{pmatrix} u_{12x}^s \\ u_{12y}^s \\ u_{12z}^s \end{pmatrix} = \begin{pmatrix} u_{12x} \\ u_{12y} \\ u_{12z} \end{pmatrix} - \begin{pmatrix} u_{12x}^n \\ u_{12y}^n \\ u_{12z}^n \end{pmatrix} = \begin{pmatrix} u_{12x} \\ u_{12y} \\ u_{12z} \end{pmatrix} - \left(\begin{pmatrix} u_{12x} \\ u_{12y} \\ u_{12z} \end{pmatrix}^T \begin{pmatrix} n_x \\ n_y \\ n_z \end{pmatrix} \right) \begin{pmatrix} n_x \\ n_y \\ n_z \end{pmatrix} \tag{B.9}$$

Now, applying the equation (B.5) , the relative displacement vector can be represented as

$$\begin{aligned} \begin{pmatrix} u_{2x} - u_{1x} \\ u_{2y} - u_{1y} \\ u_{2z} - u_{1z} \end{pmatrix} = {} & \underbrace{\begin{pmatrix} x_2 - x_1 & 0 & 0 \\ 0 & y_2 - y_1 & 0 \\ 0 & 0 & z_2 - z_1 \end{pmatrix} \begin{pmatrix} \varepsilon_{xx} \\ \varepsilon_{yy} \\ \varepsilon_{zz} \end{pmatrix} + \begin{pmatrix} 0 & z_2 - z_1 & y_2 - y_1 \\ z_2 - z_1 & 0 & x_2 - x_1 \\ y_2 - y_1 & x_2 - x_1 & 0 \end{pmatrix} \begin{pmatrix} \varepsilon_{yz} \\ \varepsilon_{zx} \\ \varepsilon_{xy} \end{pmatrix}}_{\text{strain related term}} \\ & + \underbrace{\begin{pmatrix} 0 & z_2 - z_1 & -(y_2 - y_1) \\ -(z_2 - z_1) & 0 & x_2 - x_1 \\ y_2 - y_1 & -(x_2 - x_1) & 0 \end{pmatrix} \begin{pmatrix} \omega_x \\ \omega_y \\ \omega_z \end{pmatrix}}_{\text{rotation related term}} \end{aligned} \tag{B.10}$$

With the above equation, it is straightforward to show that the relative normal displacement vector is only dependant on the strain related term because of the following equivalence

$$\begin{pmatrix} 0 & z_2 - z_1 & -(y_2 - y_1) \\ -(z_2 - z_1) & 0 & x_2 - x_1 \\ y_2 - y_1 & -(x_2 - x_1) & 0 \end{pmatrix} \begin{pmatrix} x_2 - x_1 \\ y_2 - y_1 \\ z_2 - z_1 \end{pmatrix} = 0$$

However, for the relative shear displacement vector, if we directly substitute (B.10) into (B.9), the rotation related term will not vanish. It is known that rigid rotation of the cubic should not produce strain energy. Therefore, in DLSM, the rotation related term is removed from the calculation of the relative shear displacement vector, namely, the relative displacement vector in (B.9) is not calculated anymore by using (B.10) or (B.6), but by the following

$$\begin{aligned} \begin{pmatrix} \hat{u}_{12x} \\ \hat{u}_{12y} \\ \hat{u}_{12z} \end{pmatrix} &= \begin{pmatrix} x_2 - x_1 & 0 & 0 \\ 0 & y_2 - y_1 & 0 \\ 0 & 0 & z_2 - z_1 \end{pmatrix} \begin{pmatrix} \varepsilon_{xx} \\ \varepsilon_{yy} \\ \varepsilon_{zz} \end{pmatrix} + \begin{pmatrix} 0 & z_2 - z_1 & y_2 - y_1 \\ z_2 - z_1 & 0 & x_2 - x_1 \\ y_2 - y_1 & x_2 - x_1 & 0 \end{pmatrix} \begin{pmatrix} \varepsilon_{yz} \\ \varepsilon_{zx} \\ \varepsilon_{xy} \end{pmatrix} \\ &= \begin{pmatrix} \varepsilon_{xx} & \varepsilon_{xy} & \varepsilon_{zx} \\ \varepsilon_{xy} & \varepsilon_{yy} & \varepsilon_{yz} \\ \varepsilon_{zx} & \varepsilon_{yz} & \varepsilon_{zz} \end{pmatrix} \begin{pmatrix} x_2 - x_1 \\ y_2 - y_1 \\ z_2 - z_1 \end{pmatrix} \end{aligned} \tag{B.11}$$

Writing (B.11) in the vector form, we get

$$\hat{\mathbf{u}}_{\mathrm{ij}} = [\boldsymbol{\varepsilon}] \cdot \mathbf{n} l \tag{B.12}$$

Finally, the relative shear displacement vector (the vector form of (B.9)) can be written as

$$\hat{\mathbf{u}}_{ij}^{s} = [\boldsymbol{\varepsilon}] \cdot \mathbf{n} l \text{-} \Big(\big([\boldsymbol{\varepsilon}] \cdot \mathbf{n} l \big) \cdot \mathbf{n} \Big) \mathbf{n} \tag{B.13}$$

which is the equation (4.7) in the context.

Moreover, consider one rigid body rotation defined by

$$\mathbf{u}(\mathbf{x}) = \boldsymbol{\omega} \times \mathbf{x} \tag{B.14}$$

where $\boldsymbol{\omega}$ is the angular displacement vector with components $\left[\omega_x, \omega_y, \omega_z\right]^{\mathrm{T}}$. By simple derivation, the true gradient of this displacement field is found to be

$$\nabla \mathbf{u} = \begin{pmatrix} 0 & -\omega_z & \omega_y \\ \omega_z & 0 & -\omega_x \\ -\omega_y & \omega_x & 0 \end{pmatrix} \tag{B.15}$$

It is obvious that the strain tensor $\boldsymbol{\varepsilon} = (\nabla \mathbf{u} + \nabla \mathbf{u}^{\mathrm{T}})/2$ vanishes given the skew nature of $\nabla \mathbf{u}$. The least square approximation adopted in DLSM to calculate the gradient of the displacement field is first-order consistent, i.e., it is able to reproduce any linear function and its gradient, so the correct skew nature of $\nabla \mathbf{u}$ is kept numerically. Therefore the calculated strain $\boldsymbol{\varepsilon}$ is also invariant with respect to the rigid body rotation.

Overall, it is ensured that the DLSM model is rotationally invariant in the sense that the strain energy is independent of rigid rotation.

Appendix C

Shape functions used in m-DLSM

Table C1. Shape functions and their derivatives at different nodes of the 8-node 3D FEM element.

i	$N_i\left(x,y,z\right)=1-\frac{(x-x_i)(y-y_i)(z-z_i)}{L^3}$	$N_{i,x}\left(x,y,z\right)=-\frac{(y-y_i)(z-z_i)}{L^3}$
	$N_{i,y}\left(x,y,z\right)=-\frac{(x-x_i)(z-z_i)}{L^3}$	$N_{i,z}\left(x,y,z\right)=-\frac{(x-x_i)(y-y_i)}{L^3}$
j	$N_j\left(x,y,z\right)=1+\frac{(x-x_j)(y-y_j)(z-z_j)}{L^3}$	$N_{j,x}\left(x,y,z\right)=\frac{(y-y_j)(z-z_j)}{L^3}$
	$N_{i,y}\left(x,y,z\right)=-\frac{(x-x_i)(z-z_i)}{L^3}$	$N_{i,z}\left(x,y,z\right)=-\frac{(x-x_i)(y-y_i)}{L^3}$
k	$N_k\left(x,y,z\right)=1-\frac{(x-x_k)(y-y_k)(z-z_k)}{L^3}$	$N_{k,x}\left(x,y,z\right)=-\frac{(y-y_k)(z-z_k)}{L^3}$
	$N_{k,y}\left(x,y,z\right)=-\frac{(x-x_k)(z-z_k)}{L^3}$	$N_{k,z}\left(x,y,z\right)=-\frac{(x-x_k)(y-y_k)}{L^3}$
l	$N_l\left(x,y,z\right)=1+\frac{(x-x_l)(y-y_l)(z-z_l)}{L^3}$	$N_{l,x}\left(x,y,z\right)=\frac{(y-y_l)(z-z_l)}{L^3}$
	$N_{l,y}\left(x,y,z\right)=\frac{(x-x_l)(z-z_l)}{L^3}$	$N_{l,z}\left(x,y,z\right)=\frac{(x-x_l)(y-y_l)}{L^3}$
m	$N_m\left(x,y,z\right)=1+\frac{(x-x_m)(y-y_m)(z-z_m)}{L^3}$	$N_{m,x}\left(x,y,z\right)=\frac{(y-y_m)(z-z_m)}{L^3}$
	$N_{m,y}\left(x,y,z\right)=\frac{(x-x_m)(z-z_m)}{L^3}$	$N_{m,z}\left(x,y,z\right)=\frac{(x-x_m)(y-y_m)}{L^3}$

n	$N_n\left(x,y,z\right)=1-\frac{(x-x_n)(y-y_n)(z-z_n)}{L^3}$	$N_{n,x}\left(x,y,z\right)=-\frac{(y-y_n)(z-z_n)}{L^3}$
	$N_{n,y}\left(x,y,z\right)=-\frac{(x-x_n)(z-z_n)}{L^3}$	$N_{n,z}\left(x,y,z\right)=-\frac{(x-x_n)(y-y_n)}{L^3}$
o	$N_o\left(x,y,z\right)=1+\frac{(x-x_o)(y-y_o)(z-z_o)}{L^3}$	$N_{o,x}\left(x,y,z\right)=\frac{(y-y_o)(z-z_o)}{L^3}$
	$N_{o,y}\left(x,y,z\right)=\frac{(x-x_o)(z-z_o)}{L^3}$	$N_{o,z}\left(x,y,z\right)=\frac{(x-x_o)(y-y_o)}{L^3}$
p	$N_p\left(x,y,z\right)=1-\frac{(x-x_p)(y-y_p)(z-z_p)}{L^3}$	$N_{p,x}\left(x,y,z\right)=-\frac{(y-y_p)(z-z_p)}{L^3}$
	$N_{p,y}\left(x,y,z\right)=-\frac{(x-x_p)(z-z_p)}{L^3}$	$N_{p,z}\left(x,y,z\right)=-\frac{(x-x_p)(y-y_p)}{L^3}$

Note: L is the length of the cubic element.

Curriculum Vitae

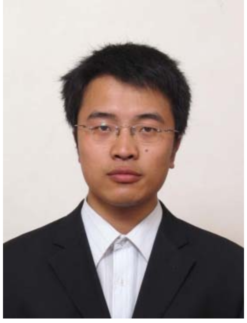

Legal Family Name: ZHAO

First Name: GaoFeng

Sex: Male

Address: EPFL ENAC IIC LMR
GC D1 414 (Bâtiment GC)
Station 18
CH-1015 Lausanne Switzerland

Postal Code: 1015

Email: gaofeng.zhao@epfl.ch

EDUCATION

Master of engineering 9/04-7/07

- Institution name: China University of Mining and Technology
- Major field of study: Bridge and tunnel engineering
- Dates attended from 9.2004 to 7.2007
- Number of years:3

Bachelor of engineering 9/00-7/04

- Institution name: China University of Mining and Technology
- Major field of study: Structure engineering
- Dates attended from 9.2000 to 7.2004
- Number of years:4

EMPLOYMENT

2007- now, Rock Mechanics Laboratory, Ecole Polytechnique Fédérale de Lausanne(EPFL), Switzerland.

2008.11-2009.01, School of Civil and Environmental Engineering, Nanyang Technological University, Singapore.

HONORS

2006	Second prize in National Graduate Student Mathematical Contest in Modeling .
2005	Third prize of National Graduate Student Mathematical Contest in Modeling.
2004	Outstanding graduate student in civil engineering of JiangSu province in China.
2003	Outstanding student of China University of Mining and Technology.
2002	Outstanding student of China University of Mining and Technology.

PUBLICATIONS

Journal Articles

published

- ✧ Zhao GF, Fang J, Zhao J. A 3D distinct lattice spring model for elasticity and dynamic failure, International Journal for Numerical and Analytical Methods in Geomechanics, 2010; DOI: 10.1002/nag.930.
- ✧ ZhaoGF, Ma GW, Zhang HH, Zhao J. A numerical manifold method for plane micropolar elasticity, International Journal of Computational Methods, 2010, 7:151–166.

- Fang JN, Zhao GF, Zhao J. Parriaux A. On the truly meshless solution of heat conduction problems in heterogeneous media,In Numerical heat Transfer Part B-Fundamentals, volume 55, number 1, pages 1-13, 2009.
- Kazerani T, Zhao GF, Zhao J. Dynamic fracturing simulation of brittle material using the Distinct Lattice Spring Model (DLSM) with a full rate-dependent cohesive law, Rock mechanics and rock engineering, 2010 ; DOI: 10.1007/s00603-010-0099-0.
- Zhao GF, Fang JN, Zhao J. A MLS-based lattice spring model for simulating elasticity of materials, International Journal of Computational Methods. 2010 (accepted).
- Xiao L, Li XZ, Hu ZH, Zhao XB, Zhao GF, Chen LG. The Influences of the Soil Structure on the Calculation Model of Thermal Conductivity, Geological Review 2009, 55(4):598-605 (In chinese).

Submitted

- Zhao GF, Fang JN, Zhao J. A new microstructure-based constitutive model for failure modeling of elastic continuum, European Journal of Mechanics - A/Solids. 2009 submitted).
- Zhao GF, Zhao XB, Zhu JB, Ma GW, Zhao J. Application of numerical manifold method for modeling stress wave propagation in jointed rock. International Journal of Rock Mechanics and Mining Sciences. 2010 (submitted).
- Zhao GF, Kazerani T, Man K, Zhao J .Numerical study of the semi-circular bend dynamic fracture toughness test by using discrete element models. Engineering Fracture Mechanics 2010 (submitted).
- Zhu JB, Zhao XB, Zhao GF. Li JC, Zhao J. Obliquely Incident Wave Propagation across One Joint Set with Virtual Wave Source Method, Journal of Geophysical Research, 2010 (submitted).
- Zhu JB, Zhao GF, Zhao XB, Zhao J, Calibration study of Distinct Lattice Spring Model (DLSM) on P-wave propagation across multiple parallel joints, preparing for Computer and geotechnique (submitted).

Conference paper

- Zhao GF, Xu, T, Zhao, J, Gao MZ. Microscopic back analysis method of Continuum Damage Model based FEM, Proc, Euro09, Rock Engineering in Difficult Ground Conditions Soft Rocks and Karst, 2009; 419-424.
- Zhao GF, Zhao J. Microscopic numerical modelling of the dynamic strength of brittle rock. Proc. ICADD9 Analysis of Discontinuous Deformation: New Developments and Applications 2009; 633-640.
- Zhao GF, Sun L, Zhu JB, Fang JN. OpenMP Parallelization of the three-dimensional distinct lattice spring model. Proc, Euro10, Rock Mechanics in Civil and Environmental Engineering 2010; 177-180.
- Zhao GF. A microstructure based model for rock materials. Proc, 1st EPFL Doctoral Conference in Mechanics, Advances in modern aspects of mechanics. 2010; 37-40.
- Zhu JB, Zhao GF, Zhao XB, Li JC. Analytical study of S-wave propagation across saturated joints in rock masses. Proc, Euro10, Rock Mechanics in Civil and Environmental Engineering, 2010; 289-292.
- Xu T, Zhao J, Zhao GF, Yuan L, Liu P. Modeling of shallow spallation of rock slope under dynamic loading, ISRS, 2010 (accepted).
- Zhao SF, Zhao GF. Modeling the cutting process of coal under single blade through Distinct Lattice Spring Model (DLSM). ICACTE 2010 (accepted).